Modeling atmospheres of classical novae in X-rays with `PHOENIX`

Dissertation
zur Erlangung des Doktorgrades
des Fachbereichs Physik
der Universität Hamburg

vorgelegt von
Alexander Petz
aus Schorndorf

Hamburg
Oktober, 2005

Gutachter der Dissertation: Prof. Dr. P. H. Hauschildt
Prof. Dr. S. Starrfield

Gutachter der Disputation: Prof. Dr. P. H. Hauschildt
Prof. Dr. J. H. M. M. Schmitt

Datum der Disputation: 2. 12. 2005

Vorsitzender des Prüfungsausschusses: Dr. habil. F.-J. Zickgraf

Vorsitzender des Promotionsausschusses: Prof. Dr. G. Huber

Dekan des Fachbereichs Physik: Prof. Dr. G. Huber

MODELING ATMOSPHERES OF CLASSICAL NOVAE IN X-RAYS WITH `PHOENIX`

by

ALEXANDER PETZ

(PhD Thesis under the direction of Peter H. Hauschildt)

ABSTRACT

`PHOENIX` has been used to calculate model atmospheres of classical novae in the X-ray spectral range. The models account for an expanding, one-dimensional spherically symmetric medium in full non-local thermodynamic equilibrium. Nova atmospheres have been modeled with `PHOENIX` since the early 90's to fit the early nova spectra in the ultraviolet and infrared spectral ranges. In this work the `PHOENIX`-code has been enhanced to also model X-ray spectra. This was accomplished by accounting for atomic data and physical processes.

The synthetic spectra were compared to observations from the LETGS onboard the CHANDRA X-ray satellite. The template is the observation of nova V4743 Sagittarii in March 2003. The spectrum is very spectacular because of the nova brightness and CHANDRA's spectral resolution. Further observations from July 2003, September 2003, and February 2004 were taken.

Models with solar and non-solar abundances have been calculated and the synthetic spectra have been fitted to the four observations. The fits were used to discuss discrepancies between models and observations. The effective temperature of the atmosphere, the hydrogen column density, and the abundances of helium, carbon, nitrogen, oxygen, and iron in the shell were determined by the fits. It was examined how the parameters evolve with time. With the models the atmosphere structure and NLTE effects were determined. The models were compared to the previous nova model atmospheres from `PHOENIX`.

Effects of different atomic data on the determined abundances have been examined. The abundances depend strongly on the atomic data and there are large errors in the abundance analysis. However, it could be shown that the abundances were changing between the March and July 2003 observation. From the fit parameters and the atmosphere structure a model for the emission and evolution of X-rays in nova V4743 Sgr was developed.

Models were also calculated for the nova V1494 Aquilae and for the supersoft X-ray binary sources CAL 83 and CAL 87. Supersoft X-ray binary sources are related to classical novae. The synthetic spectra cannot successfully fit the three observations as in the case of nova V4743 Sgr.

MODELLIERUNG VON ATMOSPHÄREN KLASSISCHER NOVAE IM RÖNTGENBEREICH MIT `PHOENIX`

von

ALEXANDER PETZ

(Dissertation unter der Anleitung von Peter H. Hauschildt)

KURZFASSUNG

Es wurden Modellatmosphären klassischer Novae im Röntgenbereich mit `PHOENIX` berechnet. Die Modelle behandeln ein expandierendes, eindimensionales sphärisches System, das komplett im nicht-lokalen thermodynamischen Gleichgewicht ist. Atmosphären von Novae werden seit den 90er Jahren mit `PHOENIX` für die frühen Phasen nach dem Ausbruch im ultravioletten und infraroten Spektralbereich modelliert. In dieser Arbeit soll der `PHOENIX`-Code in den Röntgenbereich erweitert werden, wobei Atomdaten und physikalische Prozesse implementiert wurden, die im Röntgenbereich wichtig sind.

Die Modellspektren wurden mit Beobachtungen des LETGS an Bord des CHANDRA Satelliten verglichen. Als Muster diente die März 2003 Beobachtung von Nova V4743 Sagittarii. Das Spektrum ist sehr bemerkenswert, da es sehr gut aufgelöst und die Nova sehr hell ist. Weitere Beobachtungen von Juli 2003, September 2003 und Februar 2004 wurden verwendet.

Es wurden Modelle mit solaren und nicht-solaren Häufigkeiten berechnet und die Modellspektren den vier Beobachtungen angepasst. Anhand der Fits wurden Unterschiede zwischen den Modellen und Beobachtungen diskutiert. Die Effektivtemperatur der Atmosphäre, die Wasserstoff-Säulendichte und die Elementhäufigkeiten von Helium, Kohlenstoff, Stickstoff, Sauerstoff und Eisen sind bestimmt worden. Eine zeitliche Entwicklung der Parameter sowie die Struktur der Atmosphäre und die NLTE Effekte wurden untersucht. Die Modelle im Röntgenbereich sind mit den früheren `PHOENIX`-Modellen von Nova Atmosphären verglichen worden.

Die Effekte verschiedener Atomdaten auf die bestimmten Häufigkeiten wurden untersucht. Die Häufigkeiten hängen stark von den Atomdaten ab und eine Analyse ist daher sehr ungenau. Dennoch war es möglich zu bestimmen, dass eine Änderung der Häufigkeiten zwischen März und Juli 2003 stattfand. Mit Hilfe der Fit-Parameter und der Atmosphärenstruktur ließ sich eine Theorie für die Emission und Entwicklung von Röntgenstrahlen in Nova V4743 Sgr bestimmen.

Modellatmosphären wurden auch für die Nova V1494 Aquilae und für zwei Superweiche Röntgen-Doppelsysteme berechnet, wobei die Modellspektren schlechter zu den drei Beobachtungen passen, als im Fall von V4743 Sgr.

Contents

List of Figures

Chapter 1

Introduction

1.1 Classical novae

Ancient astronomers who observed the sky with their naked eye and suddenly found a star which has not been observed previously had believed that it was a newly formed star. Tycho Brahe called it “nova stella” or shortly nova in 1572. Today it is known that novae are not newly formed stars but they are thermonuclear outbursts on top of a massive white dwarf (WD) which belongs to a binary stellar system, a cataclysmic variable (CV, Starrfield 1989; Warner 1989; King 1989). A CV contains a WD as the primary component and a late type main sequence star as the secondary component. A classical nova (CN) is a nova that has not previously been seen to erupt.

The secondary fills its Roche Lobe and the WD accretes hydrogen-rich material via an accretion disk onto its surface. This material becomes degenerated similar to interior WD material. The WD forms an electron-degenerated envelope around its core. Once a critical mass is accreted, explosive hydrogen burning through a non-equilibrium CNO-cycle starts. Due to electron degeneration, the released energy leads to a huge rise in temperature but the hot material cannot expand. After a critical temperature is reached the degeneration breaks down and the gas starts to behave like an ideal gas. The hydrogen rich envelope expands very rapidly and is ejected in a wind. The evolution to the outburst depends upon the mass and luminosity of the WD, the rate of mass accretion, the composition of the accreted material, and the chemical composition in the reacting layers (Starrfield 1989; Gehrz et al. 1998). The released energy causes an enormous increase in the luminosity and the outer parts of the envelope will be blown away. This is accompanied with a spectacular increase in brightness which can be observed at later stages also in the X-ray spectral range.

Observations imply and theory demands that core material be dredged-up into the accreted envelope and the gases be thoroughly mixed before being ejected into space (Starrfield et al. 1998; Gehrz et al. 1998). Thus, the chemical composition of the ejected material reflects a nuclear processed mixture of WD core plus accreted material. Abundance studies of the ejecta carried out with the IUE satellite have established that the underlying WDs are either carbon-oxygen (CO) or oxygen, neon, and magnesium (ONeMg) WDs. CNe are expected to be the major source of ^{15}N and ^{17}O in the Galaxy and to contribute to the abundances of other isotopes in this mass range.

Previous X-ray studies of CNe in outburst show that no other wavelength region provides unambiguous information on the evolution and characteristics of the underlying WD (Drake et al. 2003; Krautter et al. 1996, 2002; Ness et al. 2003). For example, the ROSAT studies discovered a "soft" component in CNe and placed them at, or near, the bright end of the class of supersoft sources (SSS). The "soft" component has been identified as emission from the hot nuclear burning photosphere of the WD and theoretical studies show that a determination of the temperature and lifetime is a measure of the mass of the WD. Stellar atmosphere analyses of the photosphere can provide abundances of the material remaining on the WD. CNe at optical maximum are luminous, $L_{\rm bol} \geq 10^5 L_\odot$ and evolve to X-ray maximum where $T_{\rm eff}$ ranges from 3×10^5 K to 6×10^5 K or higher (Krautter et al. 1996; Balman et al. 1998; Orio et al. 2002, 2003).

X-ray emission during the CN outburst can be divided into three phases (Krautter 2002). The first is the early fireball phase, in which the hot atmosphere of the white dwarf is expanding and cooling adiabatically. The peak temperature of the white dwarf is predicted to exceed $T = 10^6$ K (depending on the mass of the white dwarf: Starrfield et al. 1996) so, if detected in this phase, it would be an extremely hot source. Nevertheless, the expanding shell cools rapidly and becomes more opaque in X-rays within a few hours. Therefore, for the first few hours of the outburst, after the shell has cooled sufficiently, the nova is probably undetectable by an X-ray satellite. However, after a few days, the expanding shell starts to become ionized and the copious X-rays from the inner layers partially penetrate the shell and X-ray observations of novae during this phase show emission lines from the expanding gas (Mukai & Ishida 2001; Orio et al. 2002, 2003). This is the second phase.

The third is the constant bolometric luminosity phase when the system again becomes observable as a "soft" source. This phase occurs because as both observational and theoretical studies of CNe show that not the complete envelope is ejected during the explosive phase of the outburst. Some fraction remains on the WD and rapidly returns to hydrostatic equilibrium. This material provides sufficient fuel so that the enlarged WD remains hot and luminous for months to years (Krautter et al. 1996). It is predicted that the duration of this phase lasts shorter for more massive WDs (Krautter et al. 1996) so that a determination of how long a nova is "on" in X-rays can provide an estimate of the WD mass. Moreover, since the burning WD is hot, with nuclear burning ongoing close to its surface layers, its characteristics closely resemble those of the SSS.

CNe are related to the Super Soft Binary X-ray Sources (SSBS) which are probably progenitors of SN Ia explosions (Kahabka & van den Heuvel 1997) and which are thought to be the result of thermonuclear explosions in the cores of mass-accreting white dwarfs in close binary systems (Hillebrandt & Niemeyer 2000; Leibundgut 2001). The association of CNe and SSBS is important both because of the cosmological implications of SN Ia (currently the best standard candles for determining cosmological distances) and because SN Ia are thought to be responsible for the abundance of iron in the solar system. CAL 83 is the prototype of SSBS and another well studied SSBS is CAL 87 (Starrfield et al. 2004).

1.2 The CHANDRA data of classical novae

The template X-ray spectrum of classical novae is the observation of nova V4743 Sagittarii (V4743 Sgr) on 2003 March 19 (Ness et al. 2003). It was observed for 24.7 ksec with the Low Energy Transmission Grating Spectrometer (LETGS) onboard the CHANDRA satellite. The spectrum is very spectacular because of the nova brightness and spectral resolution of CHANDRA. It shows a strong X-ray continuum with strong absorption features between $\lambda \sim 18\,\text{Å}$ and $\lambda \sim 55\,\text{Å}$. The strongest lines are from the two highest ionization stages of carbon, nitrogen, and oxygen. An extensive analysis of the spectrum has been carried out by Ness et al. (2003).

A long term observation of V4743 Sgr has been carried out (Ness et al. 2006). It was further observed on 2003 July 18, 2003 September 25, and 2004 February 28. The quality of the July and September 2003 observations is as good as in March 2003. In March and July 2003 the nova is similar in brightness. In September 2003 it became fainter and even more so in February 2004. The count rate dropped from March 2003 to February 2004 by one order of magnitude. The spectral lines become fainter between March and July and stay similar in line strength until September. In the four observations V4743 Sgr fulfills the criteria of a SSS. The observations imply a cooling of the WD (drop of the continuum flux) and a thinning of the nova wind due to expansion (weakening of the spectral lines).

Another well observed nova in the SSS phase is nova V1494 Aquilae (V1494 Aql). It was observed with the LETGS on 2000 September 28 and 2000 October 1. The spectra are dominated by a strong soft continuum component with superimposed emission features. So far, none of the emission features could be identified with any known emission lines. Hauschildt et al. (1992) and Hauschildt et al. (1997b) observed spectra in the UV with the same characteristics but identified them as absorption spectra. The spectrum also could be an absorption spectrum with less absorption at the wavelengths where the emission features appear. In order to determine the nature of the spectrum of V1494 Aql suitable model atmospheres are necessary.

1.3 Modeling nova atmospheres with `PHOENIX`

Model atmospheres of novae have been calculated with `PHOENIX` since the early '90s. `PHOENIX` is a generalized stellar atmosphere code which can calculate atmospheres of main sequence stars, giants, brown dwarfs, irradiated planets, supernovae, novae, etc. Nova model atmospheres are treated as expanding, one-dimensional spherically symmetric shells and in full non-local thermodynamic equilibrium (NLTE). The spherical, co-moving frame radiative transfer equation for expanding media is solved for lines and continua, coupled with the NLTE statistical equilibrium equations (Hauschildt & Baron 1999). Nova atmospheres are far from LTE, therefore, all models have to include NLTE for as many atoms and energy levels as feasible.

The radiative transfer problem is coupled to the energy conservation through the equation of radiative equilibrium (in the co-moving frame) and, therefore, a temperature correction procedure (Hauschildt et al. 2003) is used to iteratively correct the structure so that energy is conserved. Mechanical energy sources, due to the expansion of the nova envelope, as well as convection are negligible for the conditions found in nova atmospheres.

The density profile and the velocity field of the expanding medium are taken from hydrodynamic simulations (Shara 1989; Starrfield 1989). In this case, the radiation transport problem effectively decouples from the hydrodynamic equations and the problem is dramatically simplified. Earlier nova models in other wavelength ranges had shown that there are satisfactory results by the use of these simulations (Hauschildt & Starrfield 1995).

The nova atmosphere is approximated by an expanding but stationary (in time) structure. This implies that the explicit time dependencies in the radiation transfer and hydrodynamics (or in the given density profile and velocity field) can be neglected and that the time evolution of the nova atmosphere can be represented by a sequence of snapshot models.

In order to account for LTE and NLTE line blanketing, the opacities of all important spectral lines have to be included. This also includes the handling of line blends, e.g., due to line broadening. Doppler broadening due to the large scale velocity field is handled through the co-moving frame radiation transport and the Lorentz transformation of the radiation field is used to obtain the observed spectrum in the Euler frame. The line radiative transfer equations are solved without using approximations such as the Sobolev method (see Grinin 2001, and ref. therein) and a large number of wavelength points is required. All depth-dependent spectral line profiles have to be calculated in the Lagrangian frame.

The generation of a model is very time consuming due to the complexity of the problem. The construction of detailed models is possible only through the use of parallel algorithms in the `PHOENIX` code (Hauschildt et al. 1997a; Baron & Hauschildt 1998; Hauschildt et al. 2001). Therefore, modern parallel computers are used to allow more complex, more sophisticated, and more realistic models.

1.4 The topic of this work

So far, nova spectra have been calculated with `PHOENIX` to fit early nova spectra in the ultraviolet and infrared spectral ranges (e. g., Hauschildt et al. 1992; Hauschildt & Starrfield 1995). In this work, X-ray spectra of CNe in the constant bolometric luminosity phase will be modeled. Therefore, the `PHOENIX`-code first must be enhanced by the implementation of atomic data and processes which are important at the energies of the X-ray spectral range.

Atomic data for `PHOENIX` are taken from databases which must provide transition probabilities and, if available, collision strengths for electrons and protons. Quantities like the emissivity of spectral lines must be calculated with `PHOENIX` directly. The CHIANTI Version 4 (Dere et al. 2001), CHIANTI Version 5 (Landi et al. 2006), and APED[1] databases are implemented in the `PHOENIX`-code. These databases contain many spectral lines in the X-ray range (below $\lambda \sim 100\,\text{Å}$). New physical processes like proton collisions, relativistic and non-relativistic thermal bremsstrahlung, and two-photon continuum emission can be calculated with the data.

The synthetic spectra can be compared with observations by the CHANDRA X-ray satellite, specifically, the four LETGS observations of V4743 Sgr. The effective temperature of the atmosphere and the abundances of helium, carbon, nitrogen, oxygen, and iron in the nova shell, and the hydrogen column density will be determined from the fits. NLTE effects on the

---

[1] `http://cxc.harvard.edu/atomdb/`

synthetic spectra and the atmosphere structure will be examined. Results from the models in X-rays will be compared with results from the previous nova model atmospheres which were calculated with `PHOENIX`.

Calculations with different atomic data may influence the abundance analysis and errors must be estimated. From the comparison of the fit parameters and from the atmosphere structure a model for the emission mechanism and the evolution of X-rays in nova V4743 Sgr will be developed. This has to be treated with caution because there are uncertainties in the observations. Discrepancies between models and observations will be discussed together with possible approaches for future work.

Furthermore, the CHANDRA observation of nova V1494 Aquilae will be modeled and the nature of the spectrum will be examined. Finally, model atmospheres for the SSBS CAL 83 and CAL 87 will be calculated and it will be examined if a possible relation between CNe and SSBS exits. The results for these three objects however, turn out to be not sufficient and more work has to be done in future.

1.5 Chapter overview

In chapter 2 the physics of classical novae will be outlined. Observations of novae with ROSAT, CHANDRA, and XMM and the physics and observations of SSBS with CHANDRA will be presented. Chapter 3 gives an overview of the CHANDRA detectors and the observations of nova V4743 Sgr. In chapter 4 the principle of modeling atmospheres with `PHOENIX` will be explained and this theory will be adopted to nova atmospheres in chapter 5. Results of the previous nova model atmospheres in the UV and IR will be presented.

The newly implemented atomic databases and physical processes will be shown in chapter 6. Finally, the models for the atmosphere of nova V4743 Sgr will be presented in chapter 7. The models were calculated with solar and non-solar abundances and the atmosphere structure will be examined with models which were calculated with solar abundances. The observations were also fitted with models which were calculated with the CHIANTI and APED databases and results due to different atomic data will be studied. From the models the emission mechanism and the evolution of X-rays in novae will be examined. Finally, the `PHOENIX` models can be compared with plane parallel, static, NLTE models of `TMAP` (Rauch et al. 2005).

In chapter 8 models for nova V1494 Aquilae and for the SSBS CAL 83 and CAL 87 will be calculated. An outlook will be given in chapter 9. In the appendix plots with spectra of different T_{eff} and plots to examine the structure of atmospheres with different abundances can be found.

Chapter 2

The physics of novae

This chapter gives an overview about the physics of novae. It is not limited to the X-ray range because the entire spectral range from the radio to gamma rays is needed to describe the rates and distributions, the speed classes, and especially the light curves, the spectral evolution, the outburst, and the chemical composition of classical novae (section 2.1.1 - 2.1.6).

For example, abundance analyses have been done very extensively using ultraviolet observations (Cassatella & Gonzalez-Riestra 1990). As shown in this work, X-ray spectra are also very useful for this kind of analysis. The ultraviolet and X-ray spectral ranges provide important keys to improve the understanding of the nova outburst since very high energies are involved. Furthermore, the infrared is very important to describe the light curve and spectral evolution during dust formation in a later stage after the outburst (Bode & Evans 1989). With radio observations it is possible to determine the geometry of the shell as well as the distance of the nova (Seaquist 1989).

The origin of the X-ray emission of classical novae is not quite clear. In section 2.2 two possible theories for the X-ray emission mechanisms of classical novae are described. The results of the model atmospheres calculated in this work are used to test these ideas. Therefore, X-ray observations have been taken to compare the synthetic spectra and the results from these models. Section 2.3 is an overview about the X-ray observations of novae with the ROSAT, CHANDRA, and XMM-Newton observatories. The CHANDRA observations of nova V4743 Sgr are important for this work and will be described together with the functionality of the detector in chapter 3.

Supersoft X-ray binary sources (SSBS) are related to novae. They are possible candidates for progenitors of supernovae type Ia which are of general importance in astrophysics and cosmology. Section 2.4 describes the physics of SSBS. The X-ray spectra of the SSBS CAL 83 and CAL 87 were observed with CHANDRA and will be described in section 2.5.

2.1 Physical properties of classical novae

A nova occurs through a thermonuclear outburst on a white dwarf with a spectacular increase in brightness and a violent ejection of matter. Afterwards a decline in brightness over several months to years can be observed.

The term nova (plural: novae) was coined by Tycho Brahe who observed a “new star” with his naked eye in 1572. It was a supernova. Today it is known that a supernova is an exploding star, not a newly formed star, and that a nova is a variable star with a sudden brightness increase between ~ 7 to 16^m.

A classical nova (CN) is a nova that has not previously been seen to erupt. Each nova can undergo several outbursts with time and becomes a recurrent nova (RN). The lightcurves and the spectral evolutions of RNe are different to CNe (Anupama 1995).

2.1.1 Rate and distribution of classical novae

In the seventeenth and eighteenth centuries only the novae CK Vul (1670) and WY Sge (1783) had been discovered (Warner 1989). In the nineteenth century V841 Oph (1848) was the first observed nova. Between 1900 and 1975 only ten novae with an apparent magnitude brighter than 3^m were detected.

In order to estimate the nova rate in our galaxy, it must be allowed for selection effects and incompleteness of the surveys (Allen 1954). Selection effects are caused, e. g., by obscuration by interstellar gas and dust in our galaxy. The observations, corrected for these effects, give an estimated galactic CNe rate of about 100 per year, which is certainly too high. The nova rate in the Andromeda galaxy M31 is about 26 ± 4 CNe per year (Arp 1956) and from theory it is supposed that there are around 35 CN explosions in our galaxy but only about five are observed.

CNe emanate from two different stellar populations (della Valle 2002). There are fast evolving novae (fast novae, section 2.1.2) related to Population I stars (Pop I) which are located in the galactic plane with a strong concentration towards the center. A few novae are related to Population II stars (Pop II) and can be located in globular clusters, dwarf E galaxies, and elliptical galaxies. These are slow evolving objects (slow novae, section 2.1.2). In addition, planetary nebulae (which belong to Pop II) have similar galactic longitudinal distributions like Pop II CNe (Minkowski 1948). Figure 2.1 shows the nova distribution in the milky way (Warner 1989).

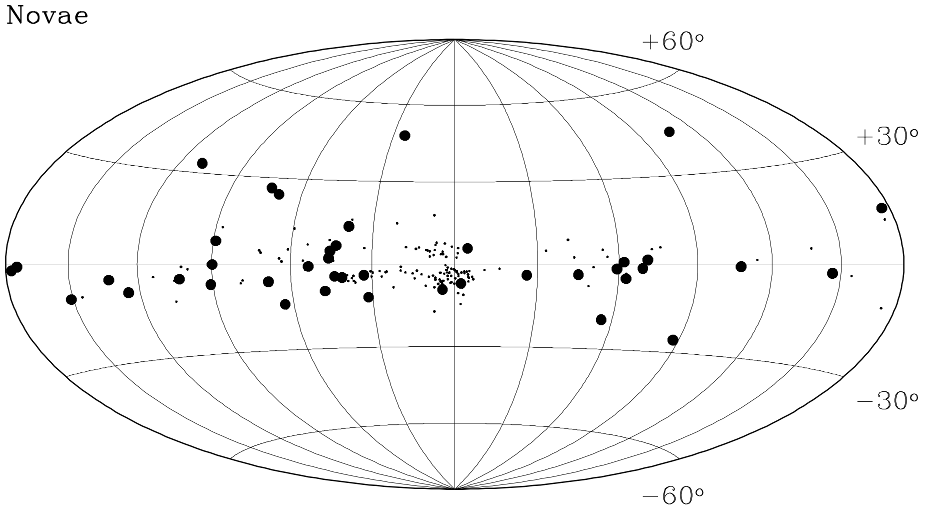

Figure 2.1: Nova distribution in the milky way (Warner 1989). Most of the novae are distributed in the galactic plane with a strong concentration towards the galactic center. Thick marks indicate slow and thin marks indicate moderate and fast novae (section 2.1.2).

2.1.2 The speed class of classical novae

The outbursts of all CNe are similar but the timescales and behavior of the decline allow to distinguish between different nova types. Therefore, CNe are divided into speed classes (Gaposchkin 1964). The characteristical quantity for the speed class is the time, t_2, for a nova to decline by 2^m below its maximum visual brightness (table 2.1). The time t_3 for a decrease by 3^m is also used to classify the speed classes.

There is a correlation between the absolute magnitude and the speed class:

$$M = b \log(t_2) - a \quad , \tag{2.1}$$

with, e. g., $a = -10.42 \pm 0.38$ and $b = 1.76 \pm 0.31$ for the absolute magnitude in the visual (Cohen 1985). This correlation implies that fast novae are brighter than slow novae. Therefore, fast novae are more energetic and their outburst is more violent. Moreover, a relationship between the speed class and the expansion velocity of novae shows higher velocities for fast novae. In section 2.1.5 the outburst of CNe and the physical mechanism to produce a fast nova are discussed. According to section 2.1.1 and figure 2.1 fast and moderate novae occur near the galactic plane. Their progenitors are more massive than those of slow novae which can occur at high galactic latitudes.

Speed class	t_2 (days)	dV/dt (mag day^{-1})
Very fast	< 10	> 0.20
Fast	11 - 25	0.18 - 0.08
Moderately fast	26 - 80	0.07 - 0.025
Slow	81 - 150	0.024 - 0.013
Very slow	151 - 250	0.013 - 0.008

Table 2.1: Classification of the speed of a nova with t_2 which is the time taken for a nova to diminish by 2^m below maximum visual brightness (Gaposchkin 1964). Another useful quantity is dV/dt, the declined visual magnitude per day.

2.1.3 The lightcurve of classical novae

Due to the similarities in the outburst of CNe it is possible to sketch a morphological visual lightcurve which has been done by McLaughlin (1960), cf. figure 2.2. The following description of the lightcurve is for the visual spectral range.

In the pre-nova stage there is a significant rise in brightness for 1-5 years prior to the outburst. Due to the definition of a CN, observations of pre-nova objects are only available from general sky surveys. But for most CNe the pre-nova is too faint to be discovered. Very few pre-novae have been observed so far.

The initial rise until 2^m below maximum takes place within 2-3 days even for slow novae. In many novae there is a pause of a few hours in fast novae to a few days in slow novae, the pre-maximum halt. Then the final rise follows where the nova brightens to maximum in one or two days for fast novae and up to several weeks for slow novae.

After maximum the early decline begins. This is a smooth drop off, except for slow novae which show an irregular lightcurve with variations of 1-20 days Slow novae show larger variations in their light curves than fast novae because slow novae run through their spectral variations (section 2.1.4) more slowly. At about 3 to 4^m below maximum there is a "transition region" where novae show different behaviors in the spectral range. Some novae pass into a minimum which is 7 to 10^m deep and stay there for 2-3 months before brightening again. Other novae enter into large scale oscillations. Only a few novae pass through the "transition region" without a noticeable peculiarity. The oscillations in the "transition region" are due to the formation of dust which absorbs optical light and reemits it in the infrared.

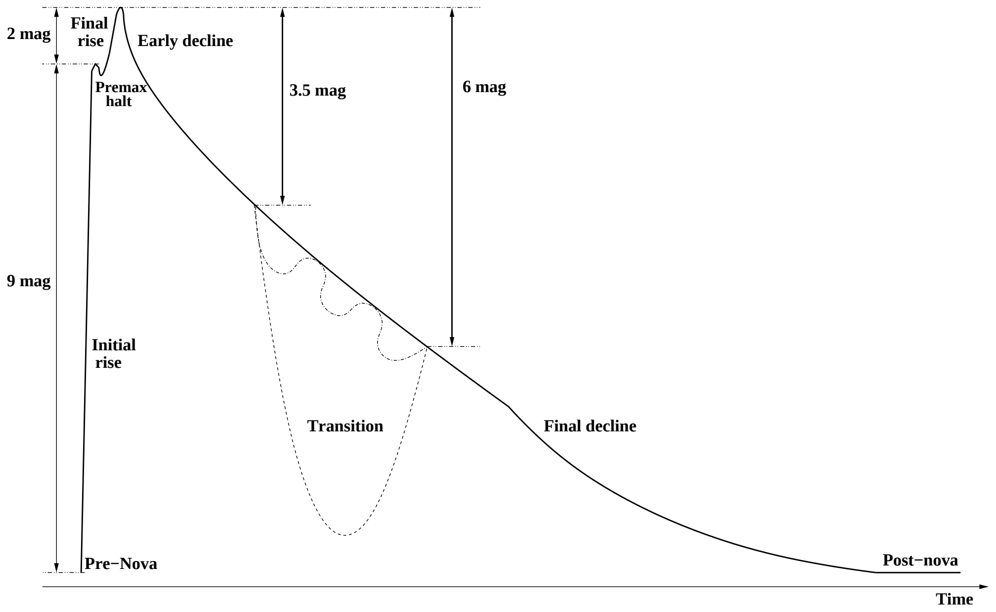

Figure 2.2: Morphological visual lightcurve of a CN (after McLaughlin 1960)

The final decline shows only small fluctuations in brightness and the nova enters the post-nova state. Post-novae remain constant in brightness, reaching minimum light or they vary irregularly through 1 to 2^m for many years.

After about 8-80 years a nova can show an outburst again becoming a recurrent nova (RN) (Anupama 1995). RNe can be distinguished from CNe due to the duration of their outburst. A RN returns to minimum brightness in less than one year and it fades very rapidly during the first week after maximum. In addition, the amplitude of a RN is much smaller and there are features in the spectra of RNe not known from CNe.

2.1.4 The spectral evolution of classical novae

McLaughlin was the first to characterize nova spectra (McLaughlin 1960) and subsequent studies have proven that there is no necessity for major modifications of his scheme. The following text shows results from McLaughlin (1960). Spectra of novae in different stages can be found in this reference.

During the initial rise there is the pre-maximum spectrum. It is dominated by broad blue-shifted absorption lines with velocities from 72 to 1300 km s^{-1} from slow to very fast novae and it resembles a spectrum of an early type star. Due to the expansion of the nova shell towards to the observer the spectral lines are blue-shifted. At maximum light the spectral type is between B5 and F0 and evolves to a later type with time. Fast novae show earlier spectral types and larger blue-shifts than slow novae, indicating a more violent outburst in fast novae. The widths of the spectral lines are approximately equal to the expansion velocity which remains almost constant or decreases slightly up to the maximum. The absorption lines from carbon, nitrogen, and oxygen are usually much stronger than in the spectrum of a supergiant. From observations it is known that the pre-maximum phase of a nova outburst is a period of uniform expansion of an optically thick envelope which cools with time.

At visual maximum the principal spectrum is observed. It resembles a spectrum of an A or F supergiant with line enhancement of carbon, nitrogen, and oxygen and strong absorption lines with a larger blue-shift than in the pre-maximum spectrum. In this stage multiple substructures which vary greatly from component to component and which are different from nova to nova begin to get prominent in the spectrum. At or after maximum the absorption lines develop a P Cygni structure indicating a strong wind. The strongest lines are formed by hydrogen, Ca I, Na I, and Fe II. After a few days, forbidden lines from [O I], [O III], and [N II] appear in the spectrum.

Shortly after the maximum light (from 1-20 days or 0.4 to 2.3^m below maximum from fast to slow novae) a third sequence of absorption lines appears: the diffuse enhanced spectrum. These lines are broad and blue-shifted by about twice the velocity of the principal spectrum (700 to 2200 km s^{-1} according to the speed class). At first they are usually diffuse and later they develop into several separate components. The diffuse enhanced spectrum lasts two weeks for fast novae to $\sim$ 100 days for slow novae.

After 1 to 2^m below visual maximum the nova spectrum is a mixture of the principal and diffuse enhanced absorption line spectrum and of an emission line spectrum. Additionally, another component appears: the so called Orion spectrum. It is also an absorption line spectrum which is blueward displaced by 1000 to 2700 km s^{-1}, with increasing velocities up to $\sim$ 4200 km s^{-1} before the Orion spectrum disappears. The Orion spectrum consists of absorption lines from H I, O II, N II, N III, and C II accompanied by broad emission lines which become more prominent and the various absorption systems decrease in strength as the nova declines.

As the Orion spectrum fades out, the spectrum consists of emission and forbidden lines with the same widths as the absorption lines in the principal spectrum. In the optical region, the spectrum evolves towards a planetary nebula spectrum. This is called the “nebula stage” of the nova. The spectrum remains an emission line spectrum during the slow return to pre-outburst brightness.

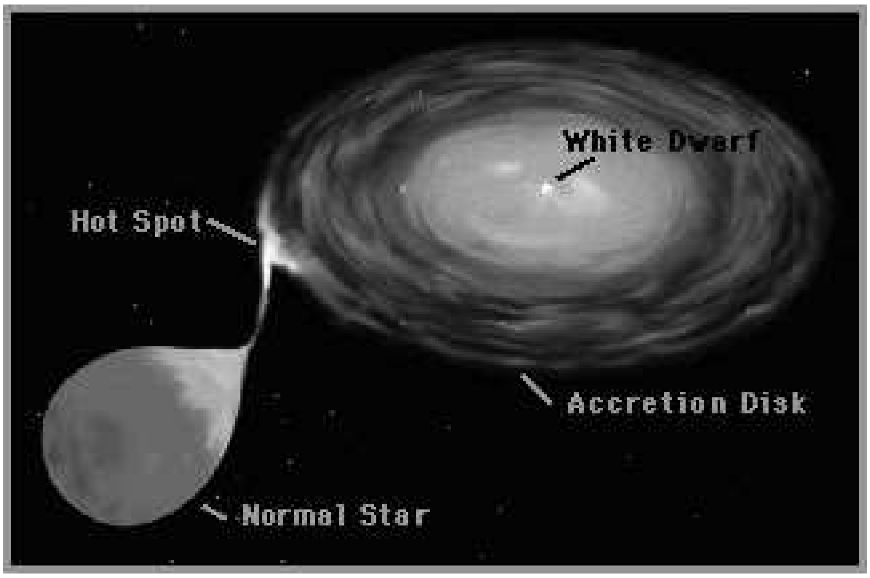

Figure 2.3: Sketch of a nova system before the outburst
(from `http://www.aip.de/groups/turbulence/pic/DiskIllus2.gif`).

2.1.5 The outburst of a classical nova

A nova outburst is caused by thermonuclear reactions on the top of a white dwarf (WD) (Kraft 1964). Novae belong to the class of cataclysmic variables (CV)[1], a binary system with a WD as the primary and a late type main-sequence star as the secondary component. The binarity of nova systems was first discovered by Walker (1954) for Nova DQ Her (Her 1934). He observed a short eclipsing binary with a 71s oscillation in the lightcurve and interpreted this as the presence of a compact object.

The secondary component fills its Roche lobe and hydrogen rich material, flows through the inner Lagrangian point to the surface of the WD. Due to the angular momentum of this material it cannot fall directly onto the WD and, therefore, it forms an accretion disk around the WD (figure 2.3). The mass transfer and the physics of the accretion disk is described e.g. in King (1989).

The WD accretes more and more material and the accreted envelope becomes hotter and denser. In stars the temperature increase is regulated by a simultaneous expansion but in WDs the electrons are degenerated and the material cannot expand. The degeneration pressure is the dominant pressure. It arises from the fact that electrons are fermions which obey the Pauli exclusion principle. At the temperatures and densities in WDs, all of the

---

[1] from Greek $\kappa\alpha\tau\alpha\kappa\lambda\upsilon\sigma\mu\acute{o}\zeta \mathrel{\hat{=}}$ flood

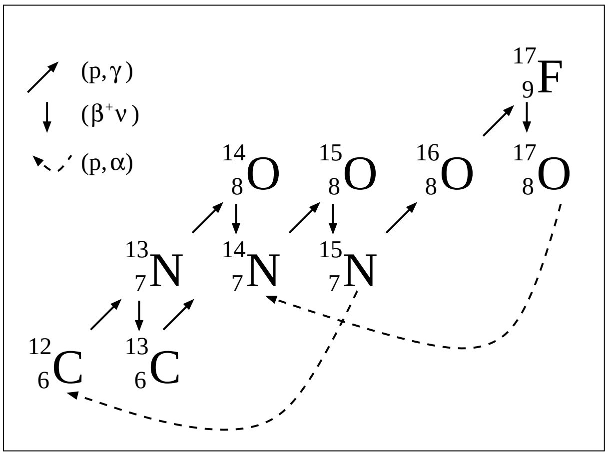

Figure 2.4: Illustration of the nuclear processes during the CNO cycle. Above $T \sim 10^8$ K the proton capture time decreases and the abundance of the β^+-unstable nuclei (^{13}N, ^{14}O, ^{15}O, and ^{17}F) increases.

lowest energy states are filled and there are electrons with higher momenta than given by a Maxwellian velocity distribution. Therefore, the degeneration pressure is higher than the thermal pressure and the pressure does not depend on the temperature. The temperature and the energy production increase. This effect is called a thermonuclear runaway (TNR, Gallagher & Starrfield 1978; Starrfield 1989).

The evolution of the TNR depends on the mass and luminosity of the WD, the mass transfer rate, and the chemical composition of the reacting layers (Starrfield 1989; Gehrz et al. 1998). If the accretion rate is too high, the accreted material will not become degenerated before the temperature is high enough to initiate hydrogen burning. From theoretical calculations and from observations of old novae accretion rates of $\dot{M} \sim 10^{-9}\,\mathrm{M}_\odot\,\mathrm{year}^{-1}$ are obtained (King 1989; Warner 1995).

At temperatures of $T \sim 10^7$ K the CNO cycle starts which is in non-equilibrium. With a nuclear energy production rate of $\epsilon_{nuc} \propto T^{18}$ the temperature dependence of the CNO cycle is high and the energy production increases quickly (The proton-proton chain which takes place at temperatures around $T = 10^6$ K has a lower temperature dependence of $\epsilon_{nuc} \propto T^4$). Figure 2.4 shows a diagram of the nuclear processes during the CNO cycle. In the early evolution, the lifetime of the nuclei against proton capture is much longer than the β^+-decay time. With increasing temperature the proton capture time continually decreases. At temperatures of $T \sim 10^8$ K it is similar to the β^+-decay time and the abundance of the β^+-unstable nuclei increases.

During the evolution to peak temperature, a convection zone is formed in the deepest layers of the accreted envelope and grows through the whole envelope due to further temperature increase. The convective turnover timescale of the envelope is in the order of $\tau_{\mathrm{ct}} \sim 100\,\mathrm{s}$ (Starrfield 1989) and shorter than the half-life of the β^+-unstable nuclei ($\tau(^{13}\mathrm{N}) = 863\,\mathrm{s}$, $\tau(^{14}\mathrm{O}) = 102\,\mathrm{s}$, $\tau(^{15}\mathrm{O}) = 176\,\mathrm{s}$, $\tau(^{17}\mathrm{F}) = 92\,\mathrm{s}$). Therefore, these nuclei are transported to the outer part of the envelope and the β^+-decays release enough energy to eject material with expansion velocities in agreement with the observed values. The predicted lightcurve produced by the expanding material agrees quite closely with the observations (section 2.1.3). Accordingly, if the abundance of the CNO nuclei is higher, the outburst will be more violent and a faster nova is produced. This also affects the chemical composition of the nova ejecta (see section 2.1.6 for more details).

Above $T \sim 10^8\,\mathrm{K}$ the velocity distribution of the electrons becomes Maxwellian again. Degeneration is lifted and the pressure depends on the temperature. The envelope starts to expand. The mass of the accreted material is a decreasing function of the WD mass (for a given mass loss rate) and WD luminosity. Properties of WDs of various masses can be found in table 3.1 of Starrfield (1989) and critical accretion rates and luminosities for the nova outburst are listed in table 3.2 of Starrfield (1989).

The strength of the outburst is determined by a pressure at the core-envelope interface (CEI) (Fujimoto 1982; MacDonald 1983):

$$P_{\mathrm{CEI}} = \frac{GM_1}{R_1^2}\frac{M_e}{4\pi R_1^2} \quad , \tag{2.2}$$

where M_e is the mass of the envelope and M_1 and R_1 are the mass and radius of the WD. In order to produce a fast nova (section 2.1.2), a pressure of $P_{\mathrm{CEI}} \sim 10^{20}\,\mathrm{dyn\,cm^{-2}}$ is necessary. With known pressure and the mass-radius relation for WDs (Chandrasekhar 1967) the envelope mass M_e, necessary to produce an outburst of a given strength, can be determined. Therefore, M_e can be decreased if the WD mass M_1 is increased and it becomes easier to produce a nova outburst.

2.1.6 The chemical composition of nova ejecta

In order to produce a fast nova outburst in agreement with the observations, β^+-unstable nuclei have to be transported to the outer part of the accreted envelope as described above. The higher the abundance of these nuclei, the more violent the nova outburst. This is one of the first predictions of the TNR theory for the outburst.

Nova ejecta have a high abundance of carbon, nitrogen, and oxygen relative to the sun. But if one considers the chemical composition in the outer layers of a late main sequence star, where the carbon, nitrogen, and oxygen abundances are in the order of the solar values, where is the origin of the nuclei in the accreted envelope? One possible process to enhance the abundance of the CNO nuclei is a core mixing mechanism which dredges material from the interior of the WD into the envelope (Starrfield et al. 1972). Observations yield an additional enhancement over the solar abundance of other heavy elements, e. g., neon, magnesium, sulfur, and iron. Studies of abundances with the IUE (International Ultraviolet Explorer) satellite have established that the underlying WDs are either carbon-oxygen (CO) or oxygen-neon-magnesium (ONeMg) WDs (Starrfield et al. 1998; Gehrz et al. 1998). Hydrodynamical studies by Politano et al. (1995) show that the elements neon, magnesium, and sulfur can originate from the core of a ONeMg WD. A trend among the ejected abundances in their models is the increase of the mass fraction of heavier nuclei with increasing WD mass. ONeMg WDs are, in general, more massive than CO WDs and the outburst of a CN with an underlying ONeMg WD is more violent.

Today it is known that the core mixing mechanism has to exist but we do not know how it works exactly. A possible mechanism is shear mixing, the coupling of large scale flows like convection or accretion with breaking interfacial waves at the WD surface (Alexakis et al. 2003).

The ejected shell from a nova outburst has chemical abundances which are far from solar abundances and the isotope fractions are also different from the sun. The chemical composition in the ejected material reflects a TNR processed mixture of WD core plus accreted material. CNe are expected to be the major source of ^{15}N, ^{17}O, and ^{26}Al in the Galaxy and to contribute to the abundances of other isotopes in this atomic mass range. Detectable γ-ray emission from the decay of ^{22}Na should be produced by CNe in certain cases (Politano et al. 1995). A summary about element abundances of eleven CNe studied with UV and optical spectra can be found in Andrea et al. (1993).

2.2 X-ray emission of classical novae

So far, only a few CNe have been observed in X-rays (section 2.3) and the observed spectra and lightcurves of each nova look different. Therefore, no observational basis to classify the X-ray emission is known. Possible emission mechanisms exist from a theoretical point of view.

There are two main possible X-ray emission mechanisms of CNe: emission from hot circumstellar material and emission from shocks in the nova shell.

In order to describe the emission from hot circumstellar material, it has to be distinguished between three different phases (Krautter 2002). The first is the early fireball phase in which the hot atmosphere of the WD is expanding and cooling adiabatically. The peak temperature of the WD is predicted to exceed $T = 10^6\,\mathrm{K}$ (depending on the mass of the WD: Starrfield et al. 1996). If detected in this phase, the CV would be an extremely hot source. The expanding shell cools rapidly and becomes more opaque in X-rays within a few hours. Therefore, for the first few hours of the outburst the nova is probably undetectable by an X-ray satellite. However, after a few days the expanding shell starts to become ionized and the copious X-rays from the inner layers partially penetrate the shell. X-ray observations of novae during this phase show emission lines from the expanding gas (Mukai & Ishida 2001; Orio et al. 2002, 2003). This is the second phase. It has a duration of several months.

The third phase is the constant bolometric luminosity phase when the system becomes observable as a “soft” X-ray source once again. This phase occurs because the envelope is not ejected completely during the explosive phase of the outburst, as shown by observational and theoretical studies of CNe. Some fraction remains on the WD and rapidly returns to hydrostatic equilibrium. This material provides sufficient fuel so that the enlarged WD still burns hydrogen and remains hot and luminous for months to years (Krautter et al. 1996). It is predicted that the duration of this phase is an inverse function of the mass of the WD so that a determination of how long a nova is “on” in X-rays can provide an estimate of the WD mass. Moreover, since the burning WD is hot with nuclear burning ongoing in its surface layers its characteristics closely resemble those of supersoft X-ray sources (SSS).

From the second X-ray emission mechanism (emission from shocks in the nova shell) hard X-rays with a soft bremsstrahlung emission are expected. There are different ways to produce shocks (Balman et al. 1998). Shocks can be produced by the interaction of the expanding shell with circumstellar material like an old nova shell, interstellar matter or the wind of the main sequence star. Alternatively, shocks can originate from inhomogeneities within the expanding shell. The hard X-ray emission should be similar to the X-ray emission of stellar wind from OB stars. Another shock mechanism is the collision of a fast wind with preexisting slow wind material from the WD. This produces a spectrum which looks like coronal line emission from a hot plasma.

2.3 Observations of novae in X-rays

This section gives an overview about X-ray observations of classical novae. First the results of the ROSAT satellite[2] (Aschenbach et al. 1981) are summarized. In contrast to the X-ray satellites EINSTEIN[3] (Giacconi et al. 1979) and EXOSAT[4] (Bradt et al. 1992), ROSAT had a few times larger area and a better angular and energy resolution ($E/\Delta E \sim 50\%$ in the energy range of 0.1 to 2.4 keV or 124.0 to 5.2 Å of the Position Sensitive Proportional Counter). Longer exposure times and a systematic program of monitoring novae throughout their outburst were possible. Nevertheless, the spectral resolution of ROSAT was too low to be useful for this work. The observations are summarized here because there are some important discoveries concerning the X-ray emission of CNe, e. g., the length of the constant bolometric luminosity phase.

In the second part of this section, observations of CNe with CHANDRA[5] are outlined. The CHANDRA detectors are described in more detail in section 3.1. There are two grating spectrometers onboard the CHANDRA satellite: the Low and the High Energy Transmission Grating Spectrometer (LETGS and HETGS). Additional instruments are the Advanced CCD Imaging Spectrometer (ACIS), and a high resolution camera (HRC) (Weisskopf et al. 2002). The resolutions of the grating spectrometers surpass all previous X-ray spectrometers by more than two orders of magnitude. The LETGS covers a wavelength range from 6.1 to 155.0 Å (2 to 0.08 keV) with the complete soft X-ray spectrum. Together with the HRC, a wavelength resolution of $(\Delta\lambda)_{\mathrm{FWHM}} = 0.05\,\text{Å}$ for the full width at half maximum is obtained. Therefore, LETG spectra detected with the HRC are used in this work to fit the modeled spectra.

Another powerful X-ray observatory is XMM-Newton[6] (Jansen et al. 2001). It has three X-ray telescopes on board, each with an European Photon Imaging Camera (EPIC).There are two Reflecting Spectrometers (RGS1 and RGS2) mounted in the light path of the EPICs. Although the angle and energy resolution of XMM is comparable with CHANDRA and even though XMM has a larger mirror area and is not as much limited in detecting faint sources like CHANDRA, none of the XMM grating spectrometers cover the long X-ray wavelength range like the CHANDRA LETGS (for the RGSs the resolution is only satisfactory up to $\lambda \sim 35\,\text{Å}$). Therefore, XMM data is not

---

[2] Röntgensatellit, a german project

[3] in honor of Albert Einstein

[4] European X-ray Observatory Satellite

[5] in honor of Subrahmanyan Chandrasekhar

[6] X-ray Multi-Mirror Mission, in honor of Sir Isaac Newton

useful for this work but for completeness some XMM observations of CNe are summarized in the last part of this section.

Due to the low X-ray luminosity of CNe all observations are limited by interstellar dust absorption. It is strongest in the galactic plane where most of the CNe are located (figure 2.1). The hydrogen absorption mostly affects the soft component ($\lambda \gtrsim 30\,\text{Å}$) of the X-ray spectrum.

2.3.1 ROSAT observations of classical novae

In the ROSAT All-Sky Survey (RASS) about 283 positions of known novae and nova-like objects were examined in X-rays (Oegelman & Orio 1995). Only seven CNe were detected. Six show CV-like emission from old novae and one nova, GQ Mus (Nova Muscae 1983), was a recent nova. Nova GQ Mus was already detected by EXOSAT about 460 days after the outburst on 1983 January 18 (Oegelman et al. 1984). ROSAT detected GQ Mus with a count rate of 0.143 ± 0.035 counts s^{-1} on 1992 February 25 (day 3118 of the RASS), six years after EXOSAT observed it last and about nine years after the outburst (Oegelman et al. 1993). In the following years several observations were carried out and a decreasing count rate from 0.127 ± 0.006 counts s^{-1} on day 3322 to 0.007 ± 0.002 counts s^{-1} on day 3871 was observed (Shanley et al. 1995).

Balman & Krautter (2001) carried out an analysis with CO-enhanced LTE atmosphere models. They conclude that only the RASS data on day 3118 show evidence for ongoing hydrogen burning in the accreted layers on the top of the WD and on day 3322 the hydrogen burning has already turned off. GQ Mus is the nova with the longest hydrogen burning phase known of about 8.5-9.1 years.

Another very extensive study with ROSAT has been done for nova V1974 Cygni (1992) (Krautter et al. 1996). This nova is the prototype of CNe from the ROSAT data to show the basic X-ray properties of CNe. V1974 Cyg was discovered in outburst on 1992 February 20 and first observed with ROSAT on 1992 April 20 when it entered the ROSAT field of view. Subsequently, the nova was observed with ROSAT over nearly two years on a total of 18 occasions. The lightcurve of the total count rate of V1974 Cyg in the 0.1 to 2.4 keV (124.0 Å to 5.2 Å) band is described in Krautter et al. (1996). This is the first nova with completely covered X-ray lightcurve.

In the first observation, the X-ray spectrum of V1974 Cyg was a highly absorbed hard spectrum with essentially no photons below 0.7 keV ($> 17.7\,\text{Å}$). In later observations an increasingly soft component appeared. Finally, before the decline, the spectrum consisted of a strong soft component whose spectral energy distribution exhibited the general characteristics of a supersoft X-ray source (SSS) and the hard component was still present. V1974 Cyg was the by far strongest SSS ever observed with ROSAT.

Fits with a black body energy distribution give several thousand Eddington luminosities L_{edd} for a $1M_\odot$ WD. With the assumption of $L_{\mathrm{bol}} = L_{\mathrm{edd}}$ the fits are not reasonable. These results can be generalized for other SSS (Kahabka & van den Heuvel 1997). In order to fit the X-ray spectra of SSS more realistic model atmospheres have to be calculated.

Balman et al. (1998) concluded from their analysis that the soft component follows an evolution as predicted from the phase of constant bolometric luminosity (section 2.2). The effective temperature increases with decreasing radius at constant luminosity and there is a strong decrease of T_{eff} and L during the decline phase. When the hard component of the spectrum is analyzed, the temporal evolution of the hard X-ray flux and the plasma temperatures imply a shock origin of the hard X-ray emission but the data did not allow to distinguish between the three possible shock origins describes in section 2.2.

The temporal evolution of the soft spectral range shows clear evidence for a decreasing circumstellar absorption in the expanding shell described by a hydrogen column density n_h. Due to the fact that the effect of n_h is strongest in the soft spectral range, the high n_h during the early phases is the reason for the absence of soft X-ray emission in the first observations. Once the expanding shell has become optically thin for soft X-ray radiation, the X-ray flux remains constant. It declines only if the hydrogen burning switches off, as seen in the last observations.

There are other novae detected by ROSAT during their outburst stage, e. g., nova Herculis 1991 (Lloyd et al. 1992; Szkody & Hoard 1994) and nova Pup 1991 (Orio et al. 1996). These observations do not contribute essential insight for this work and are not presented here.

2.3.2 CHANDRA observations of classical novae

Nova V382 Velorum (Nova Vel 1999) was observed in X-rays with CHANDRA. It is a fast ONeMg nova with $t_3 \sim 10\,$days (Shore et al. 1999a,b) and was discovered on 1999 May 22. With a maximum brightness of $V_{\mathrm{max}} = 2.6^m$ it was one of the brightest novae of the last century. An ACIS observation on 1999 December 30 showed a strong soft component and that the nova was still in the SSS phase (Burwitz et al. 2002). In a high resolution observation with the LETGS on 2000 February 14 a spectrum with a wealth of coronal emission lines of different elements and different ionization stages appeared (Fig 2.5). Thus the nova had evolved to the emission line phase. The strong soft component had totally disappeared which indicates that hydrogen burn-

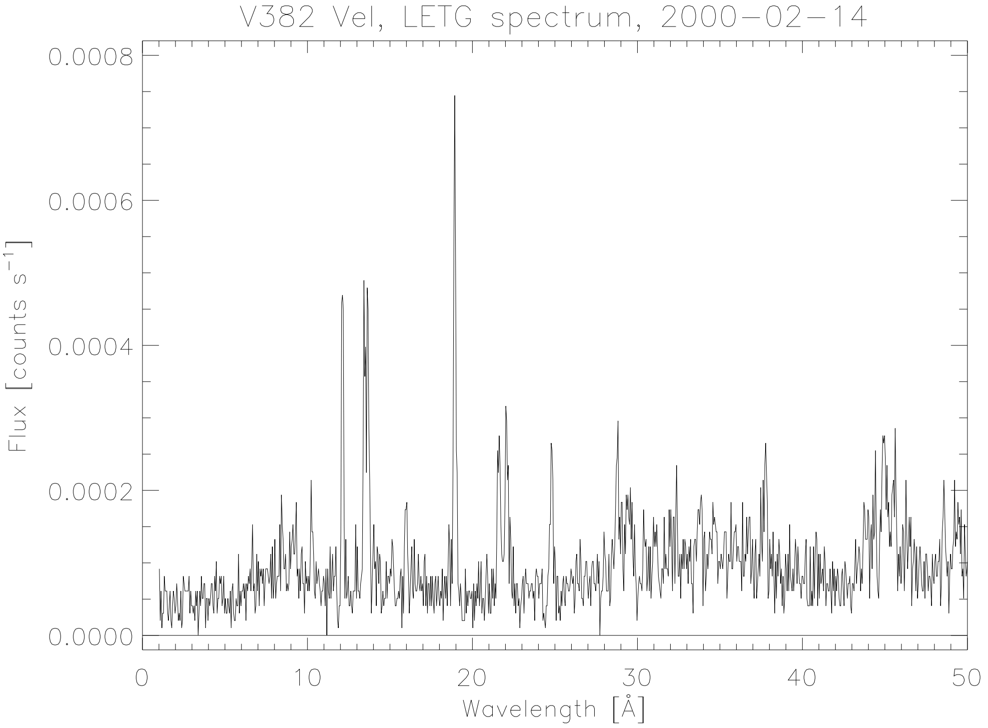

Figure 2.5: CHANDRA LETGS observation of nova V382 Velorum 1999 on 2000 February 14 (OBSID 958, data taken from the CHANDRA archive: `http://cxc.harvard.edu/cgi-gen/cda/retrieve5.pl`).

ing in the accreted layers atop the WD had been turned off between 1999 December 30 and 2000 February 14. The short duration of the SSS phase (less than 4 months) implies that the WD in V382 has to be massive, which is consistent with its ONeMg nature and with the speed class of the nova.

Another CN observed with CHANDRA is V1494 Aquilae (Starrfield et al. 2001) whose outburst occurred on 1999 December 2 with $V_{\rm max} = 4^m$. The first two observations where obtained with the ACIS on 2000 April 15 and 2000 June 7. A hard spectrum with emission lines and no soft component was observed. On 2000 September 28 (Fig 2.6) and 2000 October 1 two LETGS observations were carried out. These spectra are dominated by a strong soft continuum component with superimposed emission features which implies that V1494 Aql is a SSS. So far, none of the emission features could be identified with any known emission lines. Hauschildt et al. (1992) and Hauschildt et al. (1997b) observed spectra in the UV with the same characteristics and identified them as absorption spectra. Therefore, it is not clear if the spectrum is an emission or an absorption spectrum with less absorp-

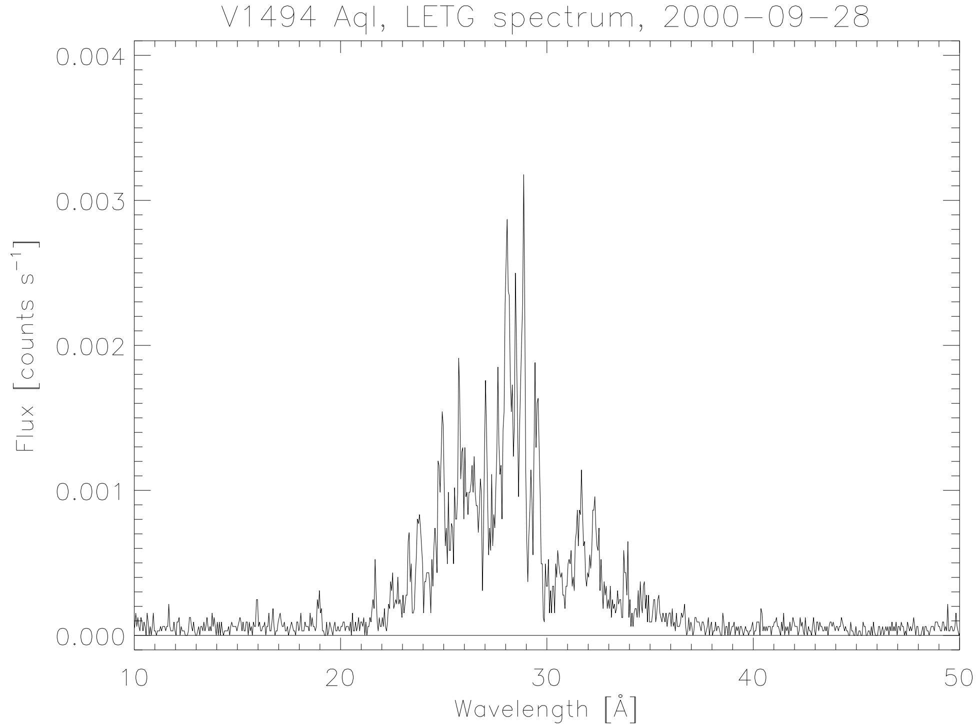

Figure 2.6: CHANDRA LETGS observation of nova V1494 Aquilae on 2000 September 28 (OBSID 2308, data taken from the CHANDRA archive: `http://cxc.harvard.edu/cgi-gen/cda/retrieve5.pl`).

tion at the wavelengths where the emission features appear. Suitable model atmospheres are needed to clarify the nature of the spectrum. Results of model calculations for V1494 Aql with `PHOENIX` will be shown in section 8.1.

The first long term observation of a CN with CHANDRA had been done for the nova V4743 Sagittarii. The spectra are optically thick absorption spectra from a strong supersoft component. They are very spectacular because of their high spectral resolution and the brightness of the nova. Therefore, this data will be used in this work as a template X-ray observation of CNe. The observations will be described in section 3.2.

2.3.3 XMM-Newton observations of classical novae

Out of several classical novae observed with XMM-Newton some are interesting and bright X-ray sources, for example Nova V4633 Sagittarii (Nova Sgr 1998) and Nova V2487 Ophiuchi (Nova Oph 1998) (Sala 2004). Their X-ray emission is over the whole energy range of the EPIC cameras (0.2 to 8 keV).

The observations were made between two and five years after the outburst and show that hydrogen burning has turned off in the WD envelope. This indicates turn-off times which are shorter than approximately three years (Sala 2004).

The X-ray spectrum of Nova V4633 Sgr is dominated by emission from a shock-heated expanding shell or from the reestablishment of accretion in the CV. In Nova V2487 Oph the accretion had been reestablished on the WD less than 1000 days after the outburst and the spectrum is also dominated by emission. There is an additional excess of thermal plasma emission at $\sim 6.4\,\mathrm{keV}$ from the Kα line of iron. In the spectrum of V2487 Oph a soft X-ray emission can be found which is due to a fraction of the WD surface heated by hard X-rays from the accretion shock region. In addition, the high temperature and large X-ray luminosity of the nova indicate that Nova V2487 Oph had probably occurred on a magnetic white dwarf. The CV which hosts V2487 Oph already has been observed in the RASS. Accordingly the nova was the first CN detected in the X-ray before and after the outburst which supports the CV scenario of CNe.

2.4 Supersoft X-ray binary sources

Supersoft X-ray binary sources (SSBS) are a subclass of SSS. It is assumed that they are candidates for the progenitors of Supernovae Ia (SNe Ia, Li & van den Heuvel 1997). SNe Ia are of general importance in astrophysics and cosmology. They are important for our understanding of the evolution of the Universe and for the formation of iron in the Galaxy and they are recognized as standard candles[7] for the extragalactic distance scale.

The assumption exists that SNe Ia arise from a thermonuclear runaway in the cores of CO WDs which have accreted material from a binary companion until their masses reach the Chandrasekhar mass M_{Ch} (Leibundgut 2001; Hillebrandt & Niemeyer 2000).

There exist two main mechanisms producing a SN Ia: two merging WDs in a binary star system (Webbink 1984) and a single WD which accretes material from a main sequence star. The first mechanism can explain the missing hydrogen lines in spectra of SN Ia but it cannot explain why SNe Ia behaves like so called standard candles because the explosion should depend on the properties of the WD. Some theoretical modeling has indicated that this mechanism should lead to a accretion induced collapse and not to a SN Ia explosion (Segretain et al. 1997). The second mechanism is favored to produce a SN Ia. One of the first suggestions was that this mechanism occurs

---

[7] All SNe Ia have nearly the same absolute magnitude.

in a CN system but the amount of core material ejected during the outburst implies that the WD is decreasing in mass as a result of the outburst (Gehrz et al. 1998; Starrfield 2003). Therefore, it is suggested that SSBS are the progenitors of SNe Ia. The WD mass and the accretion rate is so high that a thermonuclear runaway and finally a nova outburst cannot occur (section 2.1.5). The question is if this objects can reach M_{Ch} to finally undergo an explosion to a SN Ia.

Nomoto et al. (1979) pointed out that only a relatively small amount of accreted material is necessary to ignite the hydrogen shell-burning and a weak shell-flash on the WD occurs. Later more and more mass is accreted which is not compressed but it is accumulated layer by layer and the atmosphere of the WD gets a radius like a supergiant star. This envelope can fill the inner and the outer critical Roche lobe. A common envelope can be formed around the orbit of the WD and its companion. This leads to the formation of a very compact binary with a CO WD and a He WD. A SN Ia cannot be produced.

This changes if an optically thick wind is formed (Hachisu et al. 1996). This is a continuum-radiation driven wind in which the acceleration occurs deep inside the photosphere (Kato & Hachisu 1994). A part of the accreted matter is lost by the wind and the rest remains on the WD and burns to helium. During the further evolution the mass accretion rate drops. When it decreases below the critical value of $\dot{M}_{crit} = 9.0 \times 10^{-7}(M_{WD}/M_{\odot} - 0.5)M_{\odot}\,\mathrm{year}^{-1}$, the optically thick wind stops. Weather it is possible for the WD to reach M_{Ch}, depends on the mass which was accreted before this point because stronger flashes will develop at lower accretion rates. If $\dot{M}_{crit} < 0.5 M_{\odot}\,\mathrm{year}^{-1}$ before the WD reaches $1.38 M_{\odot}$, hydrogen shell flashes on the WD will eject the accreted matter and the WD cannot grow further. During this described evolution the WD is a SSBS.

Starrfield et al. (2004) have demonstrated via self-consistent calculations of accretion onto hot, luminous, and massive WDs that their mass can grow beyond M_{Ch}. In contrast to the situation in CNe this simulations show that no or only a small fraction of the accreted material is ejected. A hydrogen TNR cannot occur because hydrogen burns immediately to helium in the surface layers. Depending on the WD mass and accretion rate, the helium is burned to carbon and higher mass nuclei. This can explain the absence of hydrogen and helium in the spectra of SNe Ia. Furthermore, the evolution occurs for mass accretion rates which are observed in CVs.

Observations of SSBS revealed that they contain a WD and burn hydrogen in a shell with a very thin hot atmosphere. SSBS have bolometric luminosities between $L_{\mathrm{bol}} = 10^{36}$ and $L_{\mathrm{bol}} = 10^{38}\,\mathrm{erg\ s}^{-1}$ and their radiation is almost completely emitted in the energy band below 0.5 keV. They are

Instrument	OBSID	Date	Exp. time [ksec]	state
LETGS	77	1999-11-29	52.3	off-state
ACIS-S	84	1999-11-30	2.1	off-state
LETGS	1900	2001-08-15	35.4	detected
LETGS	3402	2001-10-03	61.6	off-state

Table 2.2: Observations of CAL 83 with CHANDRA. In the first two and in the last observation CAL 83 was in an off-state.

variable on timescales from hours to years (Greiner 1995).

The prototype of a SSBS is CAL 83 which was observed by different X-ray observatories. It is the brightest SSBS at X-ray wavelengths and has optical properties (luminosity and periodicity) very similar to the properties of low-mass X-ray binaries (Crampton et al. 1987). Kahabka et al. (1996) discovered CAL 83 in an X-ray off-state with ROSAT in April 1996. Observations from ~ 20 days earlier and ~ 100 days later found CAL 83 in its normal X-ray brightness which implies a duration of the off-state of less than 120 days (Kahabka 1998). Alcock et al. (1997) observed an optical minimum which precedes the X-ray off-state by $\sim 10 - 15$ days. They conclude that this sequence of events is similar to the decline phase of novae. Alternatively the observed X-ray variability is assumed to originate from variations in the temperature of the WD envelope due to expansion and contraction (Kahabka 1998). CAL 83 was also observed in X-rays with CHANDRA. Another well studied SSBS is CAL 87. The CHANDRA data of CAL 83 and CAL 87 will be described in the following and results of model calculations will be discussed in section 8.3.

2.5 CHANDRA observations of supersoft X-ray binary sources

2.5.1 CHANDRA observations of CAL 83

The supersoft X-ray binary source CAL 83 was observed four times with CHANDRA (table 2.2). The second was a very short observation with the ACIS-S and the other three were carried out with the high resolution grating spectrometry (LETGS). In the first two observation CAL 83 remained undetected. For the ACIS-S observation, the 3σ upper limit is 0.004 counts s^{-1} and for the first observation it is of the same order of magnitude (Greiner & Stefano 2002). CAL 83 was in an off-state in the first two observations.

In the third observation on 2001 August 15, CAL 83 was clearly detected. The observation was interrupted by solar flare activity after $\sim 35\,\mathrm{ksec}$ and in an observation in October 2001, which was rescheduled for completion, CAL 83 was in an off-state again. This off-state corresponds to an upper limit for the X-ray luminosity of $L_\mathrm{X} < 9.2 \times 10^{34}\,\mathrm{erg\ s^{-1}}$ (Lanz et al. 2005) similar to that during the 1999 off-state (Greiner & Stefano 2002). By assuming a constant bolometric luminosity there is a temperature limit of $T \lesssim 1.7 \times 10^5\,\mathrm{K}$.

From the original 1996 off-state observed by ROSAT Alcock et al. (1997) developed a model in which a cessation of the steady nuclear burning is related to a drop in the accretion rate. The observed off-states can be explained if the WD cools quickly. From the timescale of the off-states results a high WD mass. On the other hand if the off-states are caused by increased accretion which results in the swelling and the cooling of the WD atmosphere (Kahabka 1998) and if an adiabatic expansion at constant luminosity and a realistic accretion rate of $\dot{M} \approx 10^{-6}\,\mathrm{M_\odot\ yr^{-1}}$ are assumed, then it follows from the characteristic timescale of the off-states that the WD has to be massive with $M_\mathrm{WD} \gtrsim 1.2\,\mathrm{M_\odot}$.

In contrast to the model by Alcock et al. (1997) Greiner & Stefano (2002) assume that the WD mass has to be close to the Chandrasekhar limit if cessation of nuclear burning takes place. With the assumption of a constant luminosity they explain the off-states by an increase of the photospheric radius or by circumstellar absorption. In both cases the emission is shifted towards longer wavelength.

The spectrum of the August 2001 observation of CAL 83 can be seen in figure 2.7. The spectrum has been analyzed and NLTE models have been calculated with TLUSTY by Lanz et al. (2005). TLUSTY can compute static and plane parallel NLTE model atmospheres in radiative and hydrostatic equilibria. The models include ions from hydrogen, helium, carbon, nitrogen, oxygen, neon, magnesium, silicon, sulfur, argon, calcium, and iron but only photoionization from the ground state of each ion is considered. Auger inner-shell photoionization and dielectronic recombination are considered, too.

Between $\lambda = 40\,\mathrm{Å}$ and $\lambda = 43\,\mathrm{Å}$ the observed spectrum is very noisy. The spectral features are blends of many spectral lines mostly from Si XII, S XI, S XII, Ar X, Ar XI, Ar XII, Ca XII, and Fe XVI. It is impractical and, with only theoretical atomic data for wavelengths, it is difficult to identify these features individually. Therefore, an overall match to the observed spectrum has been attempted. Lanz et al. (2005) found the best fit at $T_\mathrm{eff} = 5.5 \pm 0.25 \times 10^5\,\mathrm{K}$ and $\log(g) = 8.5 \pm 0.1$. For the WD they determined a radius of $R_\mathrm{WD} = 0.01 \pm 0.001\,\mathrm{R_\odot}$, a luminosity of $L_\mathrm{WD} = 9 \pm 3 \times 10^3\,\mathrm{L_\odot}$, and a mass of $M_\mathrm{WD} = 1.3 \pm 0.3\,\mathrm{M_\odot}$. Thus the WD is very massive. The upper limit is above

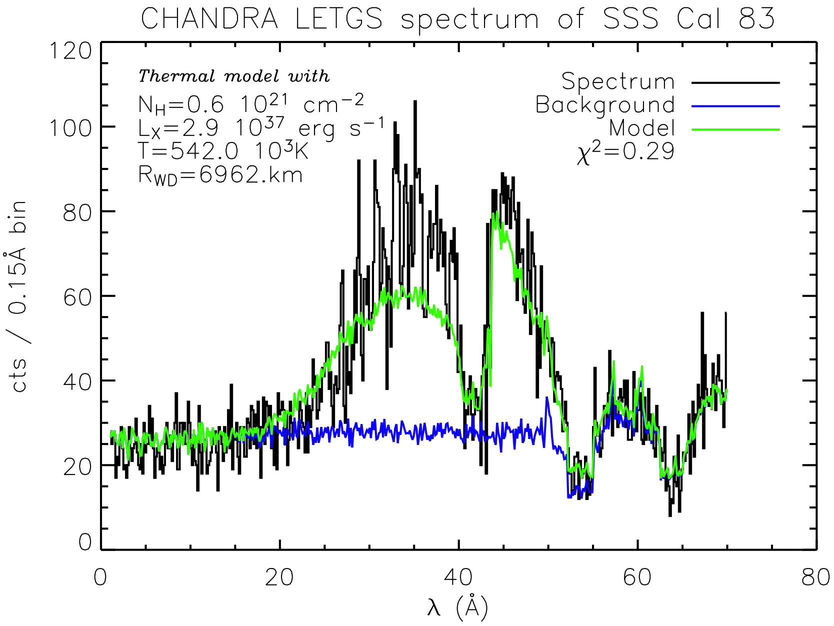

Figure 2.7: A blackbody fit (light curve) to the observed spectrum (black curve) from 2001 August 15 of CAL 83 (Ness 2004).

the Chandrasekhar mass but the lower mass limit is curtly below. CAL 83 is a possible progenitor of a SN Ia if its real mass is at the Chandrasekhar limit.

The models do not reveal any evidence of an outflow from the WD. Within the models of a SN Ia progenitor by Hachisu et al. (1996) the models by Lanz et al. (2005) would place CAL 83 in a late stage after the strong accretion and wind phase when the accretion rate drops below the critical limit for sustaining steady nuclear burning. Following this argument CAL 83 is a very likely candidate for a future SN Ia event.

Ness (2004) has fitted a blackbody spectrum to the observed CAL 83 spectrum (figure 2.7). With the assumption for the WD radius of $R_{\mathrm{WD}} = 6962\,\mathrm{km}$ the X-ray luminosity of $L_{\mathrm{X}} = 2.9 \times 10^{37}\,\mathrm{erg\,s^{-1}}$ and with an hydrogen column density of $n_h = 0.6 \times 10^{21}\,\mathrm{cm^{-2}}$ he determined an effective temperature of $T_{\mathrm{eff}} = 542.0 \times 10^3\,\mathrm{K}$. This temperature is much smaller than the temperature determined by Lanz et al. (2005) which shows that more improved models are needed. In this work, unlike the models of Lanz et al. (2005), spherically symmetric expanding model atmospheres are calculated, which, in addition, account for improved treatment of atomic data and NLTE effects.

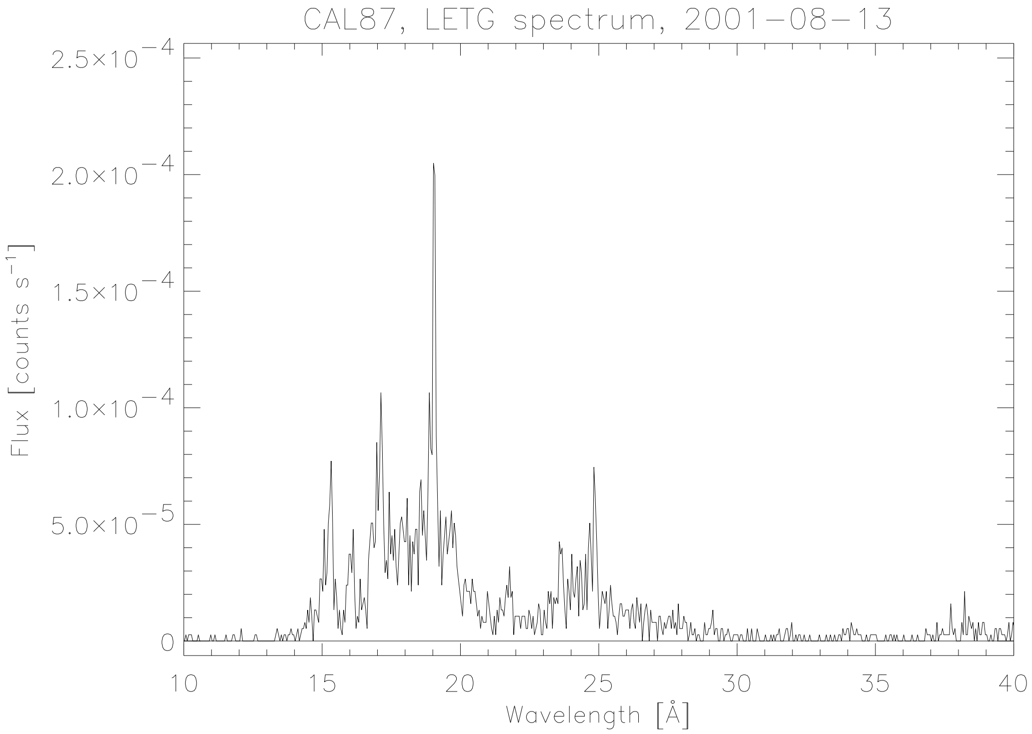

Figure 2.8: CHANDRA LETGS observation of CAL 87 on 2001 August 13 (OBSID 1896, data taken from the CHANDRA archive: `http://cxc.harvard.edu/cgi-gen/cda/retrieve5.pl`).

2.5.2 CHANDRA observations of CAL 87

CAL 87 was observed with CHANDRA on 2001 August 13 for ∼ 100 ksec. The spectrum is shown in figure 2.8.

CAL 87 was apparently less luminous than CAL 83 but hotter. From an observation with BeppoSAX, the effective temperature was assumed with $T_{\text{eff}} = (6 - 9) \times 10^5\,\text{K}$ and the luminosity with $L = (3 - 5) \times 10^{36}\,\text{erg s}^{-1}$ by Parmar et al. (1997). The orbital period of 10.6 h was longer than for CAL 83 of 1.04 h. Both periods are longer than for typical CNe (except, e. g., GK Per). Accordingly, the secondary must be evolved to fill its Roche Lobe and there is a large mass transfer for steady burning (Starrfield et al. 2004).

Chapter 3

The CHANDRA data

The results of the computed model atmospheres are compared with observed X-ray spectra of classical novae and supersoft X-ray binary sources. As explained in section 2.3, CHANDRA is the best satellite for this purpose because older satellites like ROSAT have a non sufficient energy and spectral resolution and XMM-Newton does not cover the soft X-ray spectral range which is necessary to fit the model to the data.

Section 3.1 presents the CHANDRA observatory, especially the instruments which have observed the data used in this work. In Section 3.2 the CHANDRA data of nova V4743 Sgr (2002) which consists of five observations from November 2002 to February 2004 will be describes. These observations will be taken as a template and model atmospheres of V4743 Sgr will be calculated in chapter 7.

3.1 Description of the CHANDRA observatory

The CHANDRA X-ray Observatory (CXO, figure. 3.1) is one of the newest X-ray facilities and like XMM-Newton (Weisskopf et al. 2002) it has a yet unsurpassed efficiency. CHANDRA provides the ability for sub-arcsecond imaging, spectroscopic imaging, and high-resolution dispersive spectroscopy over the range of 0.08 to 10 keV (155.0 to 1.2 Å).

CHANDRA was launched on 1999 July 23 with a specified lifetime of five years. Its orbit is at 140 000 km apogee and 10 000 km perigee with a 28.5° inclination in respect to the ecliptic. This highly elliptical orbit has a period of 63.5 hours and yields a high observing efficiency because the fraction of the sky occulted by Earth and the fraction of the time when the detector is in the Earth's radiation belt are both small. Therefore, more than 70% of

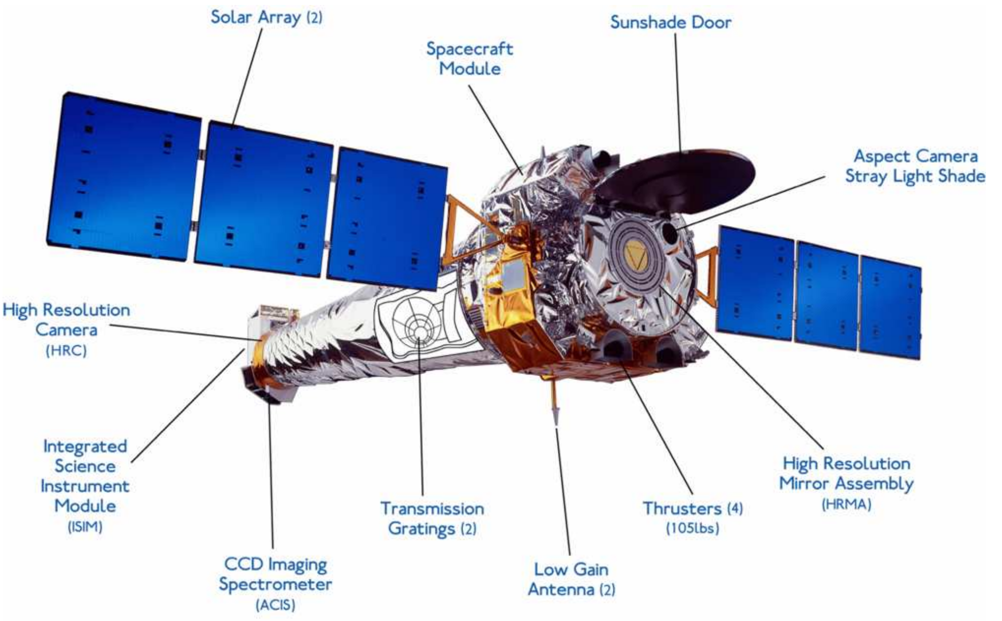

Figure 3.1: Draft of the CHANDRA satellite
(from `http://jelley.wustl.edu/x-ray/obs.shtml`).

the time is usable for observation and an undisturbed observation over more than two days is possible.

Due to relevance, only the X-ray subsystems shall be explained in more detail here. They consist of the High-Resolution Mirror Assembly (HRMA), the Low- and the High-Energy Transmission Gratings (LETG and HETG), the High-Resolution Camera (HRC), and the Advanced CCD Imaging-Spectrometer (ACIS).

The HRMA consists of four mirror pairs with a focal length of 10 m. They are coated with Iridium which has a high X-ray reflectivity and chemical stability. A forward contamination cover with 16 radioactive sources is used to verify transfer of the flux scale from the ground to the orbit.

Behind the HRMA are the LETG and HETG. Each of these Objective Transmission Grating Spectrometers (OTGs) can be inserted into the converging beam by a position mechanism where they disperse the X-rays onto the focal plane. The LETG consists of 180 modules with 3 grating facets in each module. Four rings of the LETG can be seen in figure 3.2. With free-standing "gold bars" of about 991 nm period the LETG provides high-resolution spectroscopy from 0.08 to 2 keV (155.0 to 6.2 Å). The primary use of the LETG is intended to be for on-axis observations of point sources which produce a zero-order image and a dispersed spectrum.

Figure 3.2: Four rings of the LETG
(from `http://wave.xray.mpe.mpg.de/technologies/letg`).

The HETG consists of two grating facets which are orientated at different dispersion directions: the Medium Energy Gratings (MEGs) and the High Energy Gratings (HEGs). The MEGs and the HEGs are mounted behind the HRMA's two outermost and two innermost shells and they consist of polyimide-supported gold bars of 400 and 200 nm periods respectively. The HETG provides high-resolution spectroscopy from 0.4 to 4 keV (31.0 to 3.1 Å).

The HRC is made of a single 10 cm^2 microchannel plate. It provides an imaging detector (I, combined to HRC-I) and a spectroscopy detector (S, combined to HRC-S). The spectroscopy detector S is especially designed to supply a readout for the photons dispersed by the OTGs. The HRC-S is the primary readout detector for the LETG. The HRC-I provides high resolution imaging over a 31' square field of view. Both the HRC-I and HRC-S are coated with a cesium-iodide photocathode and are covered with aluminized-polyimide UV/ion shields.

Like the HRC, the ACIS provides a spectroscopy detector S and an imaging detector I (ACIS-S and ACIS-I). ACIS-S is made of a 2×2 array of large-format, front-illuminated CCDs with an area of 2.5 cm^2. It provides high-resolution imaging over a 17' square field of view. The ACIS-S is a

6×1 array of four front-illuminated CCDs and two back-illuminated CCDs mounted along the dispersion direction of the OTGs. It is the primary readout detector for the HETG and provides high-resolution spectroscopic imaging over a 8' square field of view (smaller than ACIS-I). Both, ACIS-I and ACIS-S are covered with aluminized-polyimide optical blocking filters.

Data of the LETG combined with the HRC-S are used in this work. The LETG has a spectral resolution of $(\Delta\lambda)_{\rm FWHM} = 0.05\,\text{Å}$. Together with the HRC-S it works in a wavelength range of 1.2 - 175 Å (10.3 - 0.07 keV) and the energy resolution is $E/\Delta E \geq 1000$ for $50 \leq \lambda \leq 160\,\text{Å}$ and $E/\Delta E = 20 \times \lambda$ for $3 \leq \lambda \leq 50\,\text{Å}$. After filtering, the background is ~ 0.04 counts/pixel/100-ksec.

CHANDRA detects the photon flux in particle counts. In order to compare the observed spectra with modeled spectra it is necessary to convert the count fluxes into energy fluxes. It is assumed that each photon with wavelength λ has an energy of $E = hc/\lambda$ where h is the Planck constant and c is the speed of light. The detector counts N photons in the observation time t. For the energy flux per wavelength interval follows:

$$F(\lambda) = \frac{N}{t} \cdot \frac{h \cdot c}{\lambda} \cdot \frac{1}{R_{\rm eff}(\lambda) \cdot \lambda} \qquad [\mathrm{erg\,s^{-1}\,cm^{-2}\,cm^{-1}}] \ . \tag{3.1}$$

$R_{\rm eff}$ is the effective area of the detector. It contains all properties of the detector like the efficiency and converts the instrumental count rate in a photon count rate. Data exist for closely lying wavelength points from which the effective area can be interpolated linearly for each required wavelength.

The grating spectrometry accounts for the high angle resolution and not for the energy resolution of the detector. The efficiency depends on the position in the diffraction pattern and the effective area is a function of the distance from zero order where the distance is converted to a wavelength with the lattice constant. Therefore, the effective area depends on the wavelength of the impinging photon and the diffraction order. For any diffraction order it is equal to the product of the effective area of the HRMA, the net efficiency of the LETG for that order, and the overall detector efficiency. The overall detector efficiency varies slightly depending on exactly where the diffracted spectrum falls on the detector.

The effective area of order zero of the LETG is plotted in figure 3.3. The curve was determined with the CIAO software package (CHANDRA Interactive Analysis of Observations[1]) version 3.0 from an observation in March 2003. The effective area is measured in each observation. It changes with time because of the varying efficiency of the mirrors and the change in

---

[1] `http://cxc.harvard.edu/ciao/`

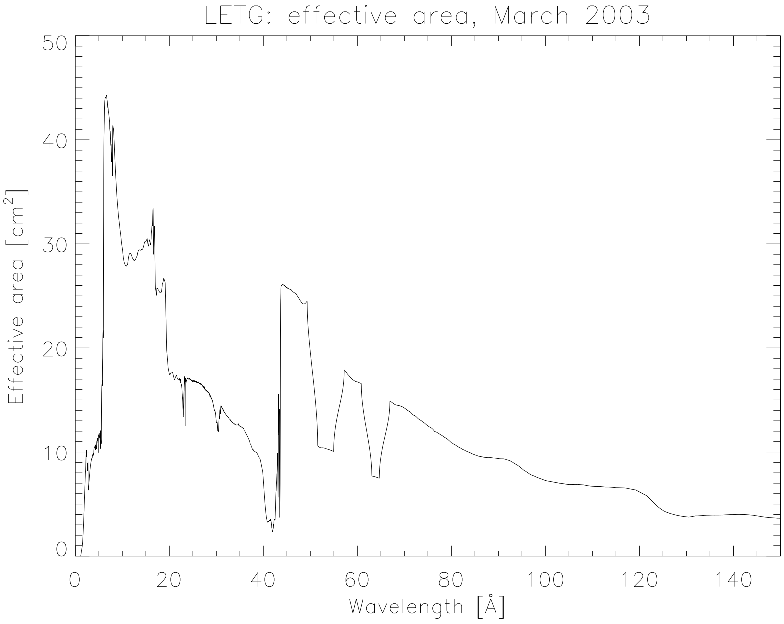

Figure 3.3: Effective area of the LETG for zero order determined from an observation in March 2003 with the CIAO software package version 3.0.

the detector coating. But this effect is only very weak (figure 3.4). There are differences at wavelengths where jumps in the effective area exist (between $\lambda \sim 45$ Å and $\lambda \sim 70$ Å). From measurement to measurement these jumps are shifted a little bit in wavelength and the strength of these shifts differs (compare the top and the bottom panel in figure 3.4). In addition there is a very minor difference in the depth of the valleys at around $\lambda \sim 52$ Å and $\lambda \sim 65$ Å.

The effective area is largest at small wavelengths ($\lambda \lesssim 22.5$ Å) and there is a minimum around $\lambda = 43.6$ Å, the carbon K-edge. Between 50-60 Å, depending on the position of zero order, there are two valleys in the effective area due to the boundary of two grating facets (There are two boundaries due to the three grating facets per module).

The instrumental absorption edges are listed in table 3.1[2]. They can be seen in the effective area curve where the area decreases or increases. All edges in the table are due to material of the HRC. Edges of the LETG are at lower wavelengths and edges of the ACIS are not listed. Both are not important for this work. To measure the effective area near the edges at good accuracy is very difficult and there are large uncertainties in these regions.

---

[2] data taken from `http://cxc.harvard.edu/proposer/POG/html/LETG.html`

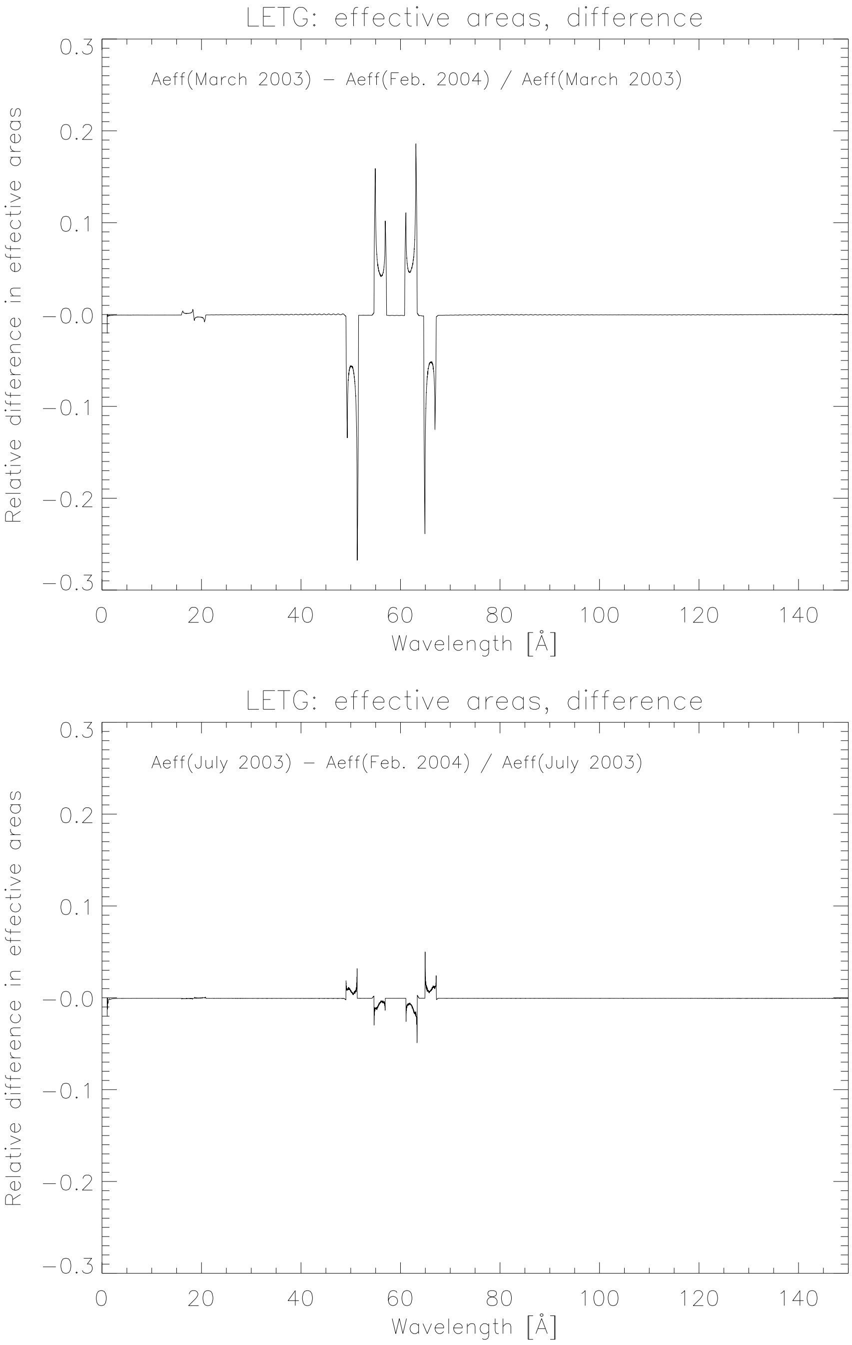

Figure 3.4: Relative differences of the effective areas of the LETG between an observation in March 2003 and February 2004 (top), and July 2003 and February 2004 (bottom).

Element	Edge	Wavelength [Å]
Si	K	6.742
Al	K	7.953
Cs	M	10.24
I	M	11.56
Cs	M	11.58
Cs	M	12.36
I	M	13.32
I	M	14.17
Cs	M	16.74
Cs	M	17.06
I	M	19.65
I	M	20.20
O	K	23.30
N	K	30.50
C	K	43.60

Table 3.1: Instrumental absorption edges between $\lambda = 6.7$ Å and $\lambda = 43.6$ Å. All edges are due to material of the HRC. Edges of the LETG are at lower wavelengths and edges of the ACIS are neglected.

3.2 Observations of nova V4743 Sgr

Nova V4743 Sgr (2002) was first detected on 2002 September 20 by Haseda et al. (2002) at $m_V = 5^m$. An accurate position is RA(J2000) = $19^h01^m09^s.38$, DEC(J2000) = $-22°00'05''.9$ (Tanaka et al. 2002). From the optical light curve the nova was classified as very fast. A velocity of $2400\,\mathrm{km\ s^{-1}}$ was estimated from the full width at half maximum (FWHM) of the Hα emission line (Kato et al. 2002) indicating that the expansion velocities are $v \sim 1200\,\mathrm{km\,s^{-1}}$. Nielbock & Schmidtobreik (2003) determined a distance to the nova between 400 and 1600 pc and a larger distance of 6.3 kpc was obtained from infrared observations by Lyke et al. (2002).

V4743 Sgr was the first nova monitored with CHANDRA over a long period of several months (Ness et al. 2003, 2006). With the analysis of the spectra and lightcurves it should be possible to determine the development of all physical parameters and the X-ray emission mechanism. The observations are listed in table 3.2. The used instrument, the observation ID, the date of the observation, and the exposure time are indicated there.

The first CHANDRA observation of V4743 Sgr has been carried out with the ACIS-S on 2002 November 19. The nova was found in an emission line state. With an exposure time of 5.3 ksec the observation was very short and only to establish a flux level. The first observation with the grating spectrometry was carried out on 2003 March 19. The nova had brightened considerably and the spectrum shows strong absorption. The observed spectrum was very spectacular and the light curve showed clear oscillations with an unexpected drop in count rate. Therefore, a long term observing program

Instrument	OBSID	Date	Exp. time [ksec]
ACIS-S	3774	2002-11-09	5.30
LETGS	3775	2003-03-19	25.0
LETGS	3776	2003-07-18	11.7
LETGS	4435	2003-09-25	11.9
LETGS	5292	2004-02-28	10.3

Table 3.2: Observations of nova V4743 Sgr with CHANDRA.

was carried out for every few months.

The light curves of the five CHANDRA observations are plotted in figure 3.5 in units of LETGS counts/s and over a bin size of 25 sec. The ACIS-S count rate was converted to the LETGS count rate by scaling with the ACIS and LETG effective areas. The ACIS-S observation was very faint. In order to fit in the graph, the count rate in the ACIS-S light curve is stretched by a factor of 20. The observation from July and the first 13 ksec (time before the drop in brightness) of the March 2003 observation are similar in brightness. In September 2003 the nova became fainter and even more so in February 2004. The count rate dropped from March 2003 to February 2004 by one order of magnitude.

The clearest oscillations with a high amplitude can be seen in the light curve of March 2003. At $\sim$ 13 ksec there was a sudden decrease in brightness possibly due to an eclipse by the main sequence star. But the decrease in brightness was accompanied by a decrease in hardness which disagree an eclipse scenario where the hard emission would be located in the outer layers (Ness et al. 2003). However, there was no similar event in the other observations.

Also the other light curves showed an oscillatory behavior of the source. The amplitude of the oscillations dropped significantly in July 2003 but became stronger in September 2003 suggesting a more effective pulsation. In February 2004 the amplitude was similar to the July 2003 observation. In contrast to the amplitude the period of the oscillations seemed to be similar in all observations. The length of the period was around 1300 sec.

Due to its low spectral resolution the results of the ACIS-S are not important for this work and the spectrum of the first observation in November 2002 will not be discussed here (for a discussion see Ness et al. 2006). The spectra of the four LETGS observations, plotted in units of energy fluxes, can be seen in the figures 3.6 and 3.7. The spectrum of March was plotted only for the first 13 ksec of the observation when there was no decline in the light curve. All spectra are background substracted. The spectra all exhibit

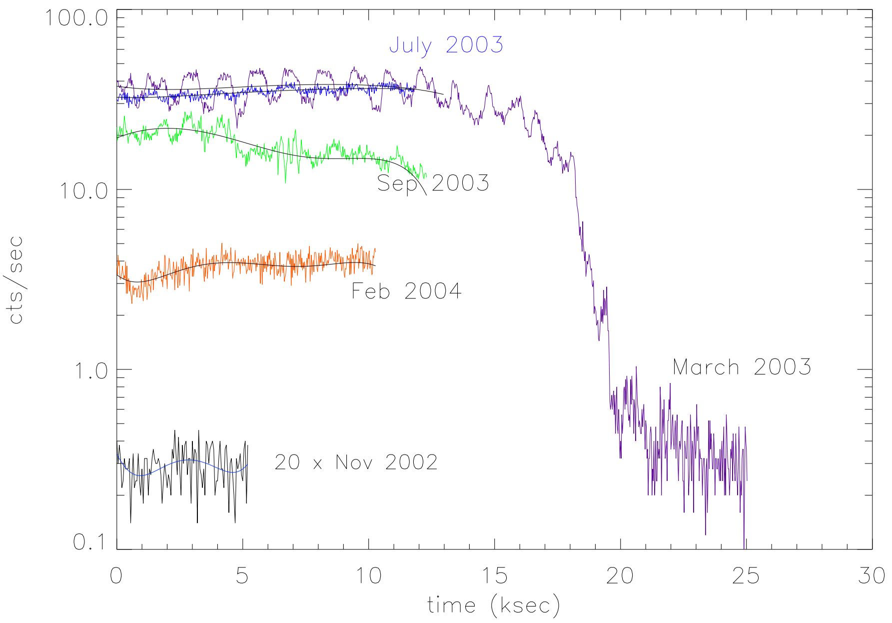

Figure 3.5: Light curves of the five CHANDRA observations of nova V4743 Sgr (Ness et al. 2006). The observed counts of the November 2002 observation with the ACIS-S is stretched by a factor of 20 in order to fit in the graph.

strong continuum emission with line absorption where the strongest lines are from the two highest ionization stages of carbon, nitrogen, and oxygen. In the March 2003 spectrum the strongest identified lines are indicated.

The count ratios for the observations are plotted in figure 3.8 for each spectral bin. Count ratios are equivalent to flux ratios since effective areas and wavelengths are identical in numerator and denominator (see equation 3.1). In all cases the ratios relative to the March observation are taken. A ratio larger than unity indicates stronger continuum emission or weaker line absorption in the considered observation compared with the March observation.

Concerning the total flux, the March and July 2003 observations are very similar with a little more emission below $\lambda \sim 24\,\text{Å}$ in July. This is due to a weaker hard emission in March or an additional hard component in July (Ness et al. 2003). The September 2003 observation is fainter with apparently the same spectral shape but it is remarkably softer. This may be due to the cooling of the surface of the white dwarf which is responsible for the continuum emission. Both in July and September the line absorption is weaker than in March due to the expansion and, therefore, thinning of the

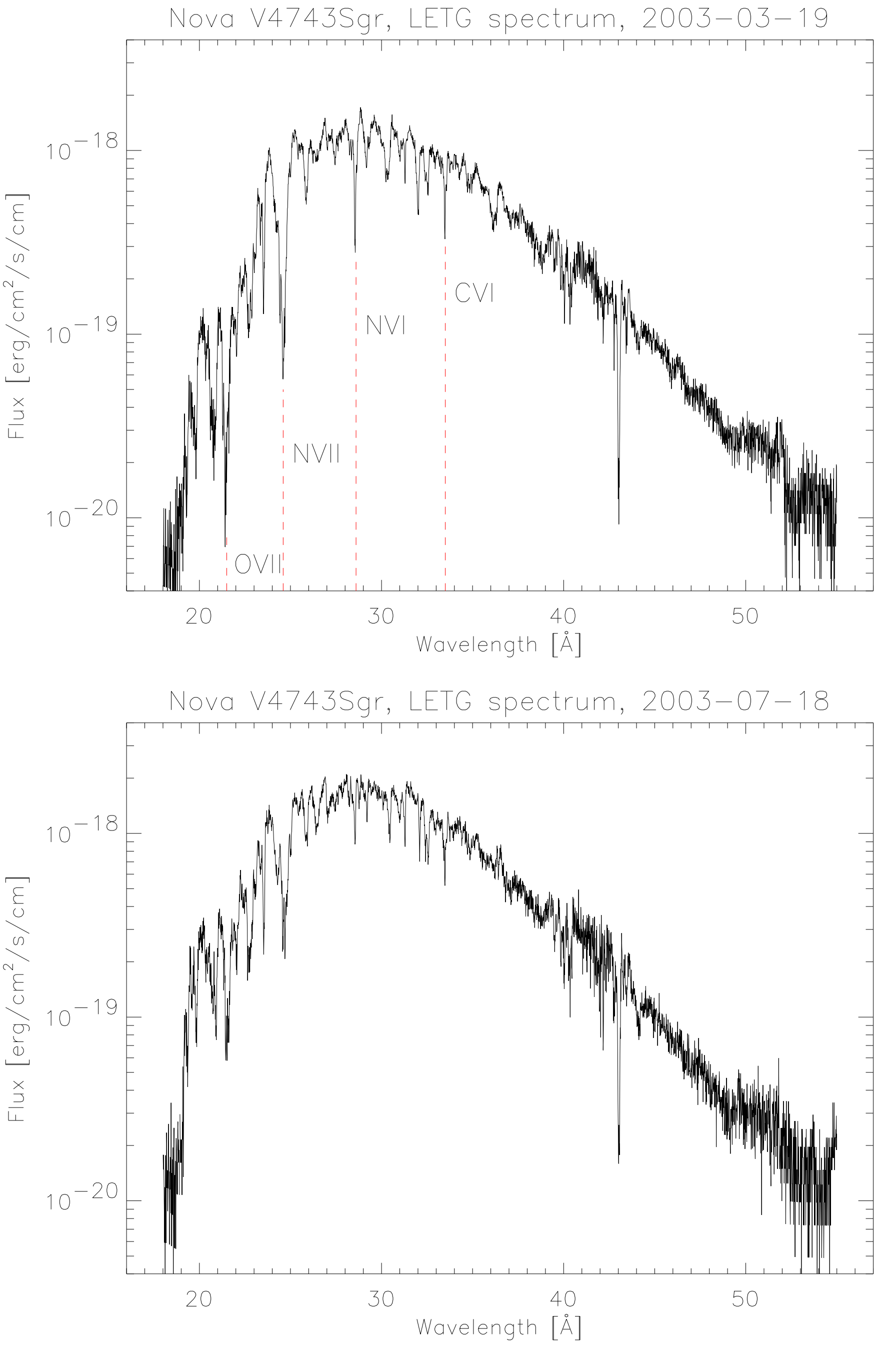

Figure 3.6: The observations from March and July 2003 of nova V4743 Sgr with the LETGS.

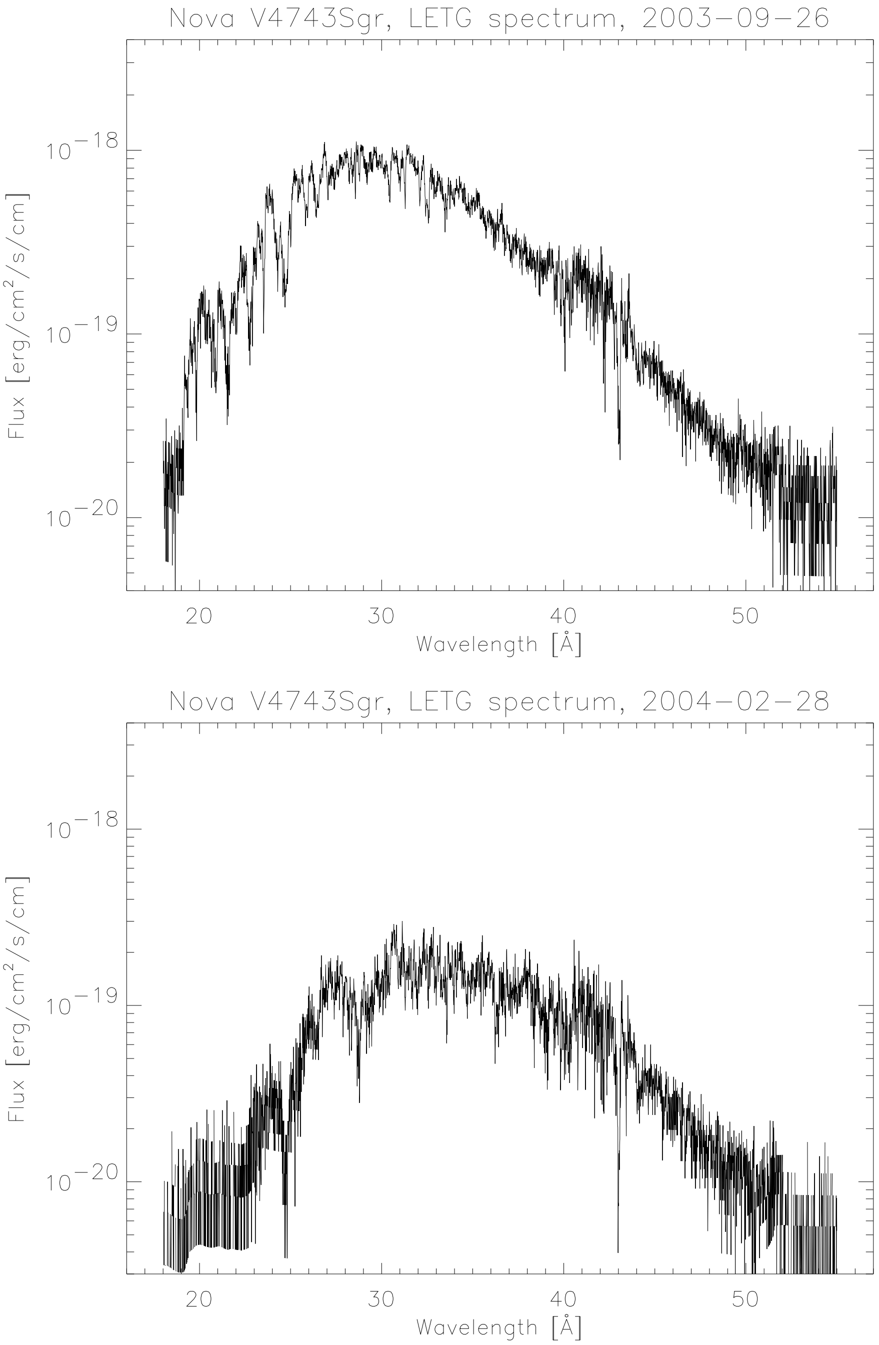

Figure 3.7: The observations from September 2003 and February 2004 of nova V4743 Sgr with the LETGS.

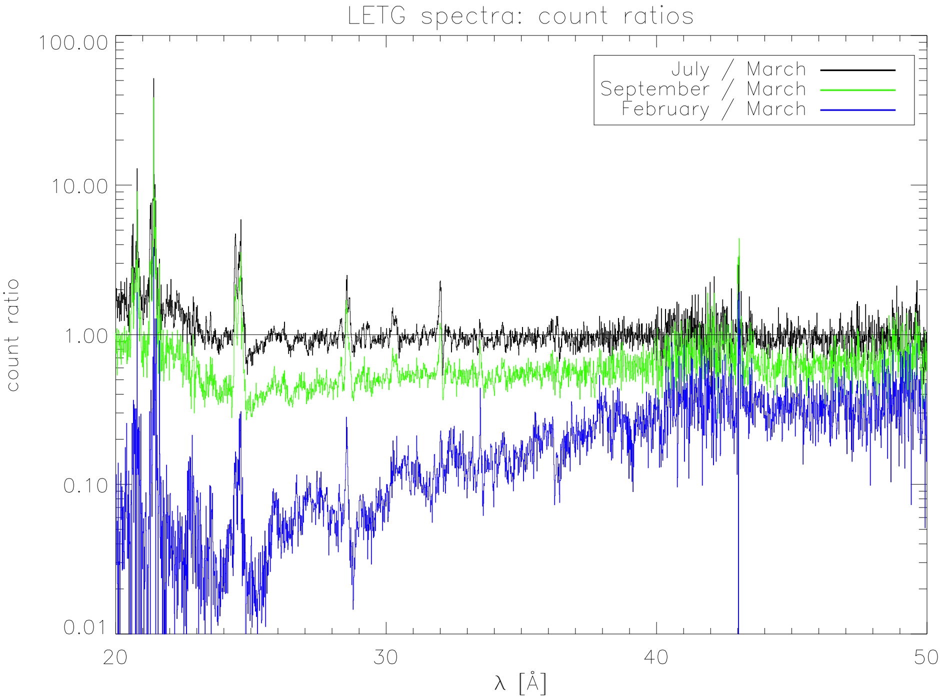

Figure 3.8: Count ratios of the four LETG spectra of nova V4743 Sgr.

nova shell. Between July and September the line absorption changes only marginally. However, the February 2004 observation has a reduced count rate and is softer. In all observations the surface of the white dwarf is expected to be still in the phase of hydrogen burning.

For a detailed understanding of the run of the physical parameters suitable model atmospheres are required. Simple blackbody fits (figure 7.22) give no adequate results and it is necessary to calculate more elaborated models with `PHOENIX` (chapter 7).

During the occultation in the March 2003 observation the residual emission formed an emission line spectrum (figure 7 of Ness et al. 2006). This spectrum has arisen from an optically thin region and there is no need to model it with `PHOENIX` because much simpler software tools like APEC (Atomic Plasma Emission Code) or CHIANTI software package provide good results. However, it presents the material ejected by the explosion. Emission lines from carbon, nitrogen, oxygen, magnesium, argon, sulfur, and silicon can be identified in the spectrum (table 3 in Ness et al. 2006). These elements should be considered in synthetic spectra for all observations. The spectrum during the occultation is discussed in detail in section 3.3 in Ness et al. (2006).

Chapter 4

The `PHOENIX`-code

Before describing the generation of a nova model atmosphere with `PHOENIX`, the main physical steps and equations to calculate a model atmosphere will be outlined in this chapter. The description is kept general enough that it can be applied not only to novae but also to all expanding stellar atmospheres or shells. A general description of the physics of stellar atmospheres can be found for example in Mihalas (1978) and Boehm-Vitense (1989).

First the modeling of stellar atmospheres with `PHOENIX` is introduced in a general way and the main steps of the calculation are presented (section 4.1). The following section describes the solution of the radiation transport equation for expanding media. In section 4.3 the treatment of NLTE processes are described and in section 4.4 the temperature correction procedure is outlined. How these calculations can be applied to nova shells will be described in chapter 5.

4.1 Stellar model atmosphere with `PHOENIX`

`PHOENIX` is a generalized stellar atmosphere code[1]. It can calculate models of static stellar atmospheres, i. e., normal main sequence stars, giants, dwarfs, white dwarfs, irradiated planets (Allard et al. 2000; Barman et al. 2000, 2001) and of expanding stellar atmospheres like nova and supernova shells (Hauschildt & Baron 1999; Baron & Hauschildt 2004). The models can be calculated in non-local thermodynamic equilibrium (NLTE) for as many atoms and energy levels as computationally feasible. Line blanketing is considered by the direct calculation of opacities for a given atmosphere structure for as many spectral lines as possible (if atomic line data exists) even if they are blended by other lines. In cool atmospheres, millions of molecular lines

---

[1] `http://www.hs.uni-hamburg.de/phoenix`

and dust can be considered. In expanding atmospheres, the radiation transfer and the radiative equilibrium are considered in the Lagrangian (co-moving) frame (the observers or rest frame is the Eulerian frame). The models can be calculated with a standard velocity law (equation 5.3) or a β-wind law:

$$v(r) = v_{\mathrm{out}}\,(1 - r_{\mathrm{ref}}/r)^{\beta} \quad . \tag{4.1}$$

v_{out} is the outer velocity in the shell, r_{ref} is a reference radius as described below, and β is the velocity exponent. In the following the model construction for an expanding atmosphere is described.

The combined radiation transfer, radiative equilibrium, and NLTE rate equations for an expanding shell are solved. The radiation transfer is treated as special relativistic and in a one-dimensional spherical, expanding geometry. If the standard velocity field is used, the density profile and velocity law of the expanding atmosphere structure are taken from hydrodynamic simulations (Shara 1989; Starrfield 1989). Therefore, the hydrodynamic calculations are effectively decoupled from the solution of the radiation transfer and the problem is dramatically simplified.

Approximations like the Sobolev method (see Grinin 2001, and references therein) are not appropriate because of the complicated interaction of overlapping lines and the continua as well as the velocity field in the line forming region. Rather up to 500 000 wavelength points are required because the line blanketing needs an accurate description of the Lagrangian radiation field and the energy balance by the radiative equilibrium should be fulfilled as accurate as possible.

The atmosphere is divided into a number of layers (at least 50 layers to provide a good resolution). For each layer a set of physical variables like temperature, density, velocity field, population number of each atomic level, and the radiation field have to be calculated and all required equations have to be simultaneously fulfilled in each layer. The layers must be distributed in the atmosphere. An optical depth grid τ_{std} for the continuum at a standard wavelength λ_{std} have to be calculated. For cool atmospheres a standard wavelength of $\lambda_{\mathrm{std}} = 1.2\,\mu$m is selected but for hot atmospheres as calculated in this work the optimal λ_{std} depends on the effective temperature and density structure of the atmosphere. If the atmosphere structure converges as fast as possible, the λ_{std} is optimally selected. The optimal standard wavelength must be determined with continuum models before starting the model generation (section 7.1.1). Finally, the points of the optical depth grid are distributed in a logarithmic scale over the atmospheric layers from a maximal (inner boundary of the atmosphere) to a minimal (outer boundary of the atmosphere) optical depth. The maximal optical depth has to be large enough in order to achieve thermalization of the radiation field.

As an alternative to the standard optical depth grid, a Rosseland optical depth grid, τ_{Ross}, can be used to scale the atmosphere. Before starting a model calculation, a grid of Rosseland opacities must be calculated for a set of temperatures and gas pressures for each effective temperature and chemical composition, a so called opacity table. The Rosseland opacity is defined as a mean opacity (for example, Mihalas 1978):

$$\bar{\kappa}_{\text{Ross}} = \frac{4\sigma T^3}{\pi \int\limits_0^\infty \frac{1}{\kappa_\nu} \frac{\partial B_\nu}{\partial T} d\nu} \quad . \tag{4.2}$$

κ_ν and B_ν are the opacity and the Planck function at frequency ν, σ is the Stefan-Boltzmann constant, and T the temperature. During the model calculation the Rosseland opacity can be interpolated from the opacity table for each atmosphere layer. Finally the Rosseland optical depth can be calculated:

$$d\bar{\tau}_{\text{Ross}} = -\rho \bar{\kappa}_{\text{Ross}} dr \quad , \tag{4.3}$$

where ρ is the density and dr is the path length in the atmosphere. In the following, all equations are noted for a standard optical depth grid.

The model calculation consists of a sequence of iterations. At the beginning of each iteration the temperature structure $T(\tau_{\text{std}})$, the opacities, and the NLTE departure coefficients are obtained for each layer from a previous iteration. The departure coefficients describe the relative fractions of level population numbers calculated in NLTE to LTE (see section 4.3). If starting a model construction from scratch, the temperature structure and the opacities are obtained from a gray atmosphere. A gray atmosphere has opacities which are independent of the wavelength, for example a Rosseland opacity. In most cases this is an adequate assumption to start off.

The radial grid (radius from the center of the star to each layer) of the expanding atmosphere is calculated by integrating the equation:

$$\frac{dr}{d\tau_{\text{std}}} = -\frac{1}{\kappa_{\text{std}} + \sigma_{\text{std}}} \quad . \tag{4.4}$$

κ_{std} and σ_{std} are the opacities from thermal and scattering processes. The boundary of an expanding atmosphere is determined by an outer radius and an outer density. The outer radius r_{out} is a reference radius r_{ref} and it is iterated to satisfy the condition:

$$r_{\text{ref}} = r(\tau_{\text{std}} = 1) \quad , \tag{4.5}$$

with τ_{std} as defined above. In order to solve the atmosphere problem, a set of physical variables $\{T, P_{\text{gas}}, n_i\}$ for each radial point (T is the temperature,

P_{gas} is the gas pressure, and n_i are the level populations) has to be found. The gas pressure can be calculated by solving the equation of state, $P_{\text{gas}} = P_{\text{gas}}(\rho, T)$. ρ is known from the given density profile and the temperature T from a previous iteration. The n_i can be updated for the new P_{gas}.

Next the radiation transport is solved by the Accelerated Lambda Iteration (ALI) method for all wavelength points. This will be described in section 4.2. The radiation field for all wavelength points is obtained for each layer. In addition, the flux at each wavelength, a synthetic spectrum, can be calculated and converted into the Eulerian frame.

In NLTE the radiation is not assumed to be in equilibrium with matter as in LTE. Rather the matter is coupled with the radiation and the radiation field must be known to calculate the NLTE occupation numbers of the atomic levels by solving the NLTE rate equations (section 4.3). Opacities can be obtained. In turn these opacities have to be known in the radiation transfer (coupling of the radiation transfer equation and the NLTE rate equations). The opacities are used in the next iteration to solve the radiation transfer again and to obtain a better radiation field and better NLTE occupation numbers. Now a new electron pressure can be calculated and the n_i can be updated which are used in the next iteration to solve the radiation transfer.

In order to obtain a correct temperature structure, energy equilibrium has to be fulfilled in the atmosphere. This is obtained by a temperature correction procedure at the end of each iteration (section 4.4). Separating the radiation transfer, the calculation of the NLTE rate equations, and the temperature correction procedure from each other corresponds to a nested iteration scheme. It allows to compute more detailed model atmospheres because the coupling between important variables is directly considered and the indirect coupling between sets of variables is iteratively considered. The whole problem is splitten into a large number of small problems with only a few variables. This works well because of the difference in the level of coupling of the variables. The solution of the radiation transfer, the NLTE rate equations, and the temperature correction is done for many iterations. This corresponds to a self-consistent solution of the radiation transfer in non-local thermodynamic equilibrium.

The model is converged if the corrected temperatures depart from the temperatures of the previous iteration by a value lower than a specific fraction. For the models calculated in this work the fraction should be below 1%. Furthermore, it has to be examined if the NLTE departure coefficients are converged. This can be done by checking the behavior of the departure coefficients from iteration to iteration. The number of iterations which is necessary for a complete convergence depends on the model. Examples can be found in chapter 7.1.1.

The calculations outlined above are very time consuming especially if a large set of ions is treated in the NLTE rate equations or if a very large number of wavelength points is calculated in the radiation transfer. Therefore, the whole `PHOENIX` code is parallelized in order to use large supercomputers (Hauschildt et al. 1997a; Baron & Hauschildt 1998; Hauschildt et al. 2001). Both data and task parallelism must be applied for reasonable parallel speedups.

For example the calculations at different wavelength points are parallelized. The coupling of wavelength points in expanding media makes this parallelization very complex. Therefore, a set of wavelength points is distributed in "wavelength clusters" onto a different set of nodes (Baron & Hauschildt 1998). Another example is the parallelization of the NLTE calculations where the three following parts are parallelized: the calculation of the NLTE opacities, the calculation of the rates at each wavelength point, and the solution of the NLTE rate and statistical equilibrium equations (Baron & Hauschildt 1998).

In the following the radiation transport in expanding media, the solution of the NLTE rate equations, and the temperature correction procedure are described.

4.2 Radiation transport in expanding media

4.2.1 The radiation transfer equation

The 1-dimensional spherically symmetric, special relativistic radiation transfer equation (SSRT) for expanding media is given by Mihalas & Weibel-Mihalas (1984) (all time dependent terms are canceled out):

$$\begin{aligned}
&\gamma(\mu+\beta)\frac{\partial I_\nu}{\partial r} + \frac{\partial}{\partial \mu}\left\{\gamma(1-\mu^2)\left[\frac{1+\beta\mu}{r} - \gamma^2(\mu+\beta)\frac{\partial \beta}{\partial r}\right] I_\nu\right\} \\
&-\frac{\partial}{\partial \nu}\left\{\gamma\nu\left[\frac{\beta(1-\mu^2)}{r} + \gamma^2\mu(\mu+\beta)\frac{\partial \beta}{\partial r}\right] I_\nu\right\} \\
&+4\gamma\left[\frac{\beta(1-\mu^2)}{r} + \gamma^2\mu(\mu+\beta)\frac{\partial \beta}{\partial r}\right] I_\nu \\
&= \eta_\nu - \chi_\nu I_\nu \quad . \qquad (4.6)
\end{aligned}$$

$\mu = \cos\theta$ is the cosine of the angle θ between a ray and the direction normal to the surface, ν is the frequency of the radiation, and $I_\nu = I(r,\mu,\nu)$ is the specific intensity at radius r and frequency ν in the direction $\arccos\mu = \theta$ in the Lagrangian frame. $\beta = v(r)/c$ is the velocity measured in units of lightspeed and $\gamma = 1/(1-\beta^2)^{1/2}$ is the usual Lorentz factor.

On the right hand side of equation (4.6) $\chi_\nu = \chi(r,\nu)$ is the extinction coefficient. It is the sum of thermal absorption and absorption by scattering. $\eta_\nu = \eta(r,\nu)$ contains contributions from scattering terms for the continuum and spectral lines:

$$\eta_\nu = \kappa_\nu S_\nu + \sigma_\nu J_\nu + \frac{1}{2}\sum_{lines}\left(\sigma_l(\nu)\int \phi_l \int\limits_{-1}^{1} d\mu I_\nu d\nu\right) \quad . \tag{4.7}$$

$J_\nu = J(r,\nu)$ is the mean intensity. It is expressed as the zeroth angular moment of I_ν:

$$J_\nu = \frac{1}{2}\int\limits_{-1}^{1} d\mu I_\nu \quad . \tag{4.8}$$

In equation (4.7) κ_ν is the thermal absorption coefficient, S_ν is the source function, σ_ν is the continuum scattering coefficient, $\sigma_l(\nu)$ is the line scattering coefficient, and $\phi_l(\nu)$ is the line profile.

The SSRT incorporates all relativistic effects like advection and aberration. With equation (4.7) the SSRT becomes an integro-differential equation. It is time independent ($\partial I_\nu/\partial t = 0$) and its velocity field is monotonic. Therefore, the SSRT becomes a boundary value problem in spatial coordinates and an initial value problem in frequency coordinates. Equivalently, all quantities in the above equations can be expressed in wavelengths with $\lambda = c/\nu$. In the following it will be switched to wavelengths.

The SSRT (equation 4.6) is solved with the Accelerated Lambda Iteration (ALI) method as described in Hauschildt (1992). In the following, a short outline is given.

4.2.2 The Accelerated Lambda Iteration

The mean intensity J_λ has to be solved. This is obtained with the source function S_λ by a formal solution of the radiation transport equation (RTE) by using the so called Lambda operator Λ_λ:

$$J_\lambda = \Lambda_\lambda S_\lambda \quad . \tag{4.9}$$

The usual Lambda iteration method:

$$\begin{aligned} J_{\text{new}} &= \Lambda S_{\text{old}} \quad , & (4.10)\\ S_{\text{new}} &= (1-\epsilon)J_{\text{new}} + \epsilon B \quad , & (4.11) \end{aligned}$$

fails in the case of large optical depths and small ϵ (thermal coupling parameter, B is the Planck function). This can be seen for example in the case of LTE. Then the source function is equal to the Planck function: $J_\lambda = \Lambda_\lambda B_\lambda(T)$. The range of the Lambda operator is only in the order of $\Delta\tau \sim 1$. At large optical depths the mean intensity calculated with the Lambda iteration must be $J_\lambda = B_\lambda + O(e^{-\tau_\lambda})$ and the convergence is infinitely slow. If there are high opacities in certain wavebands, J_λ is equal B_λ and the convergence is too slow again.

Therefore, an approximate Lambda Operator Λ^* is used. It can be obtained by the operator splitting method:

$$\Lambda = \Lambda^* + (\Lambda - \Lambda^*) \quad . \tag{4.12}$$

Thus equation (4.9) can be written as:

$$J_{\text{new}} = \Lambda^* S_{\text{new}} + (\Lambda - \Lambda^*) S_{\text{old}} \quad , \tag{4.13}$$

and with equation (4.11) it follows:

$$\left[1 - \Lambda^*(1-\epsilon)\right] J_{\text{new}} = J_{\text{fs}} - \Lambda^*(1-\epsilon) J_{\text{old}} \quad , \tag{4.14}$$

where $J_{\text{fs}} = \Lambda S_{\text{old}}$ is the formal solution. With equations (4.12) - (4.14) new values of the mean intensity J_{new} can be obtained and with equation (4.11) the new source function can be calculated. The new problem is to compute the approximate Lambda Operator Λ^*.

4.2.3 Computation of the approximate Lambda Operator

For a fast computation of equation (4.14) the calculation and structure of Λ^* should be simple. Fastest convergence is obtained with $\Lambda = \Lambda^*$ but to construct Λ is more time consuming than to construct a simpler Λ^*. The diagonal or tri-diagonal form of the exact Λ matrix is optimal for a fast convergence and computation of Λ^*.

The formal solution is performed along characteristic rays by the short-characteristic method of Olson & Kunasz (1987). In an expanding medium the characteristic rays are curved. Before the SSRT can be solved they have to be calculated. The source function is interpolated piecewise linearly or parabolically along each ray. For the specific intensity $I(\tau_i)$ the following expressions are obtained along a ray k:

$$\begin{aligned} I^k(\tau_i^k) &= I^k(\tau_{i-1}^k)\exp(\tau_{i-1}^k - \tau_i^k) + \int\limits_{\tau_{i-1}^k}^{\tau_i^k} \hat{S}(\tau)\exp(\tau - \tau_i^k)d\tau \quad , & (4.15) \\ I_i^k &\equiv I_{i-1}^k \exp(-\Delta\tau_{i-1}^k) + \Delta I_i^k \quad . & (4.16) \end{aligned}$$

τ_i^k is the optical depth along ray k with i as the running index of the optical depth points. With $\tau_1 = 0$ and $\tau_{i-1}^k \leq \tau_i^k$ it follows for the calculation of τ^k:

$$\Delta\tau_{i-1}^k = (\hat{\chi}_{i-1} + \hat{\chi}_i)|s_{i-1}^k - s_i^k|/2 \quad . \tag{4.17}$$

$\hat{\chi}_i$ is the extinction coefficient at point i and $|s_{i-1}^k - s_i^k|$ is the geometrical path length between point i and $i-1$ along the ray k.

For ΔI_i^k the following expression applies:

$$\Delta I_i^k = \alpha_i^k \hat{S}_{i-1} + \beta_i^k \hat{S}_i + \gamma_i^k \hat{S}_{i+1} \quad . \tag{4.18}$$

α_i^k, β_i^k, and γ_i^k are interpolation coefficients. When computing this coefficients it has to be distinguished between parabolic and linear interpolation of the source function $\hat{S}$. The expressions for the coefficients can be found in equations (23) to (25) in Hauschildt (1992).

The Λ^* operator has to be splitten into two parts:

$$\Lambda^* = \Lambda^t + \Lambda^c \quad . \tag{4.19}$$

Λ^t is the part for rays tangential to the core and Λ^c for core intersecting rays. Equations to compute the parts of Λ^t and Λ^c are in equations (27) to (32) of Hauschildt (1992). With this equations it follows for the expression of the full Λ-matrix:

$$\Lambda_{ij} = \sum_k \left(\sum_l w_{l,j}^k \lambda_{l,j}^k + \sum_{l'} w_{2(k+1)-l',j}^k \hat{\lambda}_{2(k+1)-l',j}^k \right) \quad . \tag{4.20}$$

$w_{i,j}^k$ are the angular quadrature weights, $\{l\}$ is the set $\{i \leq k+1\}$, and $\{l'\}$ is the set $\{i > k+1\}$. The coefficients $\lambda_{l,j}^k$ and $\hat{\lambda}_{l,j}^k$ depend on the interpolation coefficients α_i^k, β_i^k, and γ_i^k. How many coefficients have to be computed depends on the bandwidth of the Λ-matrix. The CPU time required for a computation of the full Λ-matrix can be reduced with a smaller bandwidth.

4.3 Modeling NLTE

4.3.1 The Rate equations

In order to solve the SSRT (equation 4.6) the emissivity, η_λ, and the opacity, κ_λ, have to be known. η_λ and κ_λ depend on the NLTE level populations which are calculated with the rate equations. On the other hand the rate equations depend on the radiation field calculated by the SSRT. Therefore, the SSRT and the rate equations have to be solved simultaneously or with the nested iteration scheme described above.

The rate equations are of the form:

$$\begin{aligned}&\sum_{j<i} n_j(R_{ji}+C_{ji})\\ &-n_i\left\{\sum_{j<i}\left(\frac{n_j^*}{n_i^*}\right)(R_{ij}+C_{ji})+\sum_{j>i}(R_{ij}+C_{ij})\right\}\\ &+\sum_{j>i} n_j\left(\frac{n_i^*}{n_j^*}\right)(R_{ji}+C_{ij})=0 \quad . \end{aligned} \tag{4.21}$$

n_i is the actual NLTE population density of level i and n_i^* is the LTE population density of level i which is calculated by the Saha-Boltzmann Equation (for example equation 3.127 in Lang 1999). In the calculation of the n_i^*, the value of the population density for the ground state of the next higher ionization stage is the NLTE value. The NLTE departure coefficient for level i can be defined as $b_i = \frac{n_i}{n_i^*}$ which describes the relative fraction of the population of level i calculated in NLTE to the level population calculated in LTE. The more this coefficient differs from unity in both directions the stronger are the NLTE effects on level i.

In equation (4.21) R_{ij} is the upward radiative rate or absorption coefficient ($i < j$):

$$R_{ij} = \frac{4\pi}{hc}\int_0^\infty \alpha_{ij}(\lambda)J(\lambda)\lambda d\lambda \quad , \tag{4.22}$$

and R_{ji} is the downward radiative rate or emission coefficient ($j > i$):

$$R_{ji} = \frac{4\pi}{hc}\int_0^\infty \alpha_{ji}(\lambda)\left(\frac{2hc^2}{\lambda^5}+J(\lambda)\right)\exp\left(-\frac{hc}{k\lambda T}\right)\lambda d\lambda \quad . \tag{4.23}$$

$\alpha_{ij}(\lambda)$ and $\alpha_{ji}(\lambda)$ are the cross-sections of the transitions $i \rightarrow j$ and $j \rightarrow i$. It is assumed that the cross-sections are the same for absorption and emission and that the upward and downward radiative rates are in detailed balance. The cross sections are taken from atomic databases (chapter 6). $J(\lambda)$ is the mean intensity which is calculated from the SSRT (equation 4.6). h, c, and k are the Planck constant, the lightspeed, and the Boltzmann constant and T is the electron temperature.

C_{ij} and C_{ji} from equation (4.21) are the collisional rate coefficients for absorption and emission. They are taken from atomic databases (section 6.3). The sums in equation (4.21) are over all levels in the model atoms and depend on the number of data entries in the databases (section 6.1). The system of rate equations is closed by the conservation of the nuclei and charges described by the statistical equations.

The rate equations in (4.21) are non-linear with respect to the population densities and to the electron density via the collision rate. They are solved with an extension of the operator splitting method. The rate equations are written in the form of an operator equation. Like the approximate Lambda Operator, an approximate Rate Operator is introduced and the rate and statistical equations can be solved iteratively by an operator splitting method. This is described in detail in Hauschildt (1993) and should be outlined here very short.

4.3.2 The rate operator and the linearized rate equation

The rate operator $[R_{ij}]$ is defined as:

$$R_{ij} = [R_{ij}][n] \quad . \tag{4.24}$$

$[n]$ is the population density operator, a vector of the population densities of all levels in all layers. With the rate operator the rate equations in (4.21) can be written in the form:

$$\begin{aligned} & \sum_{j<i} n_j([R_{ji}][n] + C_{ji}) + \sum_{j>i} n_j \left(\frac{n_i^*}{n_j^*}\right) ([R_{ji}][n] + C_{ij}) \\ - \quad & n_i \left\{ \sum_{j<i} \left(\frac{n_j^*}{n_i^*}\right) ([R_{ij}][n] + C_{ji}) + \sum_{j>i} ([R_{ij}][n] + C_{ij}) \right\} = 0 \quad . \end{aligned} \tag{4.25}$$

Here the definition of the departure coefficients is used.

In analogy to equation (4.12) the rate operator $[R_{ij}]$ is splitten (the same holds for $[R_{ji}]$) as:

$$\begin{aligned} [R_{ij}] &= [R_{ij}^*] + ([R_{ij}] - [R_{ij}^*]) = [R_{ij}^*] + [\Delta R_{ij}] \quad , \\ R_{ij} &= [R_{ij}^*][n_{\mathrm{new}}] + [\Delta R_{ij}][n_{\mathrm{old}}] \quad . \end{aligned} \tag{4.26}$$

$[n_{\mathrm{old}}]$ are the current and $[n_{\mathrm{new}}]$ are the updated population densities to be calculated. Now the $[R^*_{ij}]$ and $[R^*_{ji}]$ are linear functions of the population density operator $[n]$. They contain informations about the influence of a particular level on all radiative transitions. With equations (4.21) and (4.26) the following equation is obtained:

$$\begin{aligned}
& \sum_{j<i} n_{j,\mathrm{new}}([R^*_{ji}][n_{\mathrm{new}}] + [\Delta R_{ji}][n_{\mathrm{old}}] + C_{ji}) \\
+ & \sum_{j>i} n_{j,\mathrm{new}} \left(\frac{n^*_i}{n^*_j}\right) ([R^*_{ji}][n_{\mathrm{new}}] + [\Delta R_{ji}][n_{\mathrm{old}}] + C_{ij}) \\
- & \; n_{i,\mathrm{new}} \left\{ \sum_{j<i} \left(\frac{n^*_j}{n^*_i}\right) ([R^*_{ij}][n_{\mathrm{new}}] + [\Delta R_{ij}][n_{\mathrm{old}}] + C_{ji}) \right. \\
+ & \left. \sum_{j>i} ([R^*_{ij}][n_{\mathrm{new}}] + [\Delta R_{ij}][n_{\mathrm{old}}] + C_{ij}) \right\} = 0 \quad . \qquad (4.27)
\end{aligned}$$

$[n_{\mathrm{new}}]$ is non-linear with respect to $n_{i,\mathrm{new}}$ and n_e. In order to linearize the equation, the terms $(n_{j,\mathrm{new}}[R^*_{ij}][n_{\mathrm{new}}])$ are replaced by $(n_{j,\mathrm{old}}[R^*_{ij}][n_{\mathrm{new}}])$. Then the equation is only non-linear with respect to n_e.

Not all levels are strongly coupled to the other levels. With the known electron density the linearized rate equation can be solved for each element separately. Therefore, the calculation of the electron density must be done before the linearized rate equation is solved. This is a crucial assumption because NLTE effects may affect the electron density. Changes of the electron density are considered only in the next iteration. But the advantage is that the described method requires the solution of a large linear system for the population densities and only a low-dimensional non-linear system for the electron density. Therefore, the solution is more stable and many more atomic levels can be treated.

The solution of the NLTE problem during one iteration is summarized as following: After the solution of the radiation transfer with given n_i and n_e the radiative rates and the approximated rate operator are updated. Next the linear systems of the linearized rate equation are solved for each element with the old electron density. From the new population densities new departure coefficients b_i can be calculated which are used in the next iteration. Finally a new electron density is calculated. If the new electron density is not converged, the rate equations are solved again. Otherwise the iteration is finished. The NLTE structure of the model is converged if the n_i and n_e or the b_i have a prescribed accuracy.

4.4 The temperature correction

At the end of each iteration the temperature structure must be examined to satisfy the energy conservation. This can be achieved with a temperature correction procedure. In the calculation of expanding atmospheres a generalization of the Unsöld-Lucy temperature correction scheme to spherical geometry and NLTE model calculations is used (Hauschildt et al. 2003). This works very well even in extreme physical conditions like in nova or supernova shells.

The Unsöld-Lucy correction works on the principle that the ratios of wavelength-averaged absorption and emission coefficients depend much less on values of the independent variables than do the averages themselves. To obtain radiative equilibrium, the Planck function B has to be corrected:

$$\begin{aligned}\delta B(r) = \; & \frac{1}{\kappa_P}\{\kappa_J J - \kappa_P B + \dot{S}/(4\pi)\} - \{2(H(\tau=0) - H_0(\tau=0)) \\ & - \frac{1}{fqr^2}\int\limits_r^R qr'^2\chi_F(H(r') - H_0(r'))dr'\} \quad , \qquad (4.28)\end{aligned}$$

with:

$$\begin{aligned}\kappa_P = & \left(\int\limits_0^\infty \kappa_\lambda B_l d\lambda\right)/B \quad , \kappa_J = \left(\int\limits_0^\infty \kappa_\lambda J_l d\lambda\right)/J \quad , \\ \chi_J = & \left(\int\limits_0^\infty \chi_\lambda F_l d\lambda\right)/F \quad , \qquad (4.29)\end{aligned}$$

as the wavelength-averaged absorption and emission coefficients. B is the Planck function, J is the averaged intensity, and F is the radiation flux. $H = F/4\pi$, $H_0(\tau)$ is the target luminosity, and q is the sphericity factor:

$$q = \frac{1}{r^2}\exp\left(\int\limits_{r_{core}}^{r}\frac{3f-1}{r'f}dr'\right) \quad , \qquad (4.30)$$

where r_{core} is the inner radius. R is the total radius of the atmosphere. $f(\tau) = K(\tau)/J(\tau)$ is the Eddington factor with $K = \int \mu^2 I d\mu$ as the second angular moment of the intensity I. $\dot{S}$ is the sum over all additional sources of energy, e. g., mechanical energy. The first term of equation (4.28) is dominant in the outer parts of the atmosphere and the second term in the inner parts. From the corrected Planck function the corrected temperature structure can be obtained.

Chapter 5

Modeling nova atmospheres with `PHOENIX`

After having explained the `PHOENIX` code in chapter 4, it is now time to describe how stellar atmospheres can be modeled in general. In this chapter the theory is applied to nova model atmospheres. The expanding wind of a nova which is optically thick can be treated as an expanding stellar atmosphere and the hot white dwarf below can be considered as an energy source which produces a strong continuum. The secondary star of the nova system will be neglected because its emission is too weak to affect the atmosphere structure and the synthetic spectra.

In section 5.1 the model assumptions are described and the model parameters are listed. These are the general assumptions for all nova model atmospheres: for the previous nova model atmospheres calculated with `PHOENIX` and for the nova model atmospheres in the X-ray calculated in this work. The results from previous nova model atmospheres, which were calculated for the ultraviolet and infrared spectral range are described in section 5.2. Comparing these results with results for model atmospheres of nova in the X-ray spectral range which are in the constant bolometric luminosity phase (section 2.2) represents a part of the motivation of this work.

Before nova model atmospheres in the X-ray spectral range can be calculated, the microphysics of `PHOENIX` has to be expanded. For example new atomic data has to be implemented in the code to treat emission and absorption processes in the X-ray wavelength range. This will be described in chapter 6 and the results from the model atmosphere calculations will be presented in the chapters 7 and 8.

5.1 Model assumptions and parameters

The nova model atmospheres calculated with the `PHOENIX` code are one-dimensional spherically symmetric, expanding, line blanketed, NLTE model atmospheres. Therefore, the spherical, special relativistic, co-moving frame radiative transfer equation (SSRT) for expanding media (Equation 4.6) has to be solved for lines and continua. The special relativistic terms like advection and aberration are not important in nova model atmospheres but they do not decelerate the model calculation (Hauschildt et al. 1992).

Due to the high temperatures and relatively low densities in nova winds, nova atmospheres are far from LTE. All models have to include NLTE for as many atoms and energy levels as feasible. In order to fulfill the assumption of NLTE, the SSRT equation has to be coupled with the NLTE statistical equilibrium equations (Equation 4.21). As described in section 4.2 and 4.3, the numerical solution of the radiation transport and multi-level NLTE problems are based on an operator splitting (ALI) method.

The radiation transfer problem is coupled to the energy conservation through the equation of radiative equilibrium (in the Lagrangian frame). The temperature correction procedure described in section 4.4 is used to iteratively correct the structure so that energy is conserved. Mechanical energy sources due to the expansion of the nova envelope as well as convection and radioactive decays are negligible for the conditions found in nova atmospheres. This holds for all temperature ranges so far modeled with `PHOENIX`.

As described in section 4.1, the density profile and the velocity field of the expanding medium are taken from hydrodynamic simulations (Shara 1989; Starrfield 1989). Earlier nova model atmospheres in other wavelength ranges have shown that satisfactory results can be produced by the use of these simulations (section 5.2). Therefore, the results of the hydrodynamic simulations are also used in this work as a first assumption. More elaborated models with a more complicated velocity law must be calculated in a future work.

The nova atmosphere is approximated by an expanding but stationary structure. Therefore, the outer layers of the nova must behave like a steady state, spherical, expanding wind which is a good approximation in the early stage of the nova outburst. This implies that the explicit time dependencies in the radiation transfer and hydrodynamics (or in the given density profile and velocity field) can be neglected. Consequently, the time evolution of the nova atmosphere can be represented by a sequence of snapshot models. The assumption of time independence is valid since the hydrodynamic time scale is much larger than the radiative time scale and the excitation and ionization equilibrium time scales (Bath & Shaviv 1976).

In order to account for LTE and NLTE line blanketing, the opacities of all important spectral lines have to be included. This also includes the handling of line blends due to line broadening. Doppler broadening from the large scale velocity field is handled through the calculation of line profiles in the Lagrangian frame. The Lorentz transformation of the radiation field is used to obtain the observed spectrum in the Euler frame. `PHOENIX` includes a large number of NLTE lines as well as LTE background lines of species not treated in NLTE (Hauschildt 1993; Hauschildt & Baron 1995). All depth-dependent spectral line profiles have to be calculated in the Lagrangian frame. This in turn requires a large number of wavelength points ($\sim$ 400 000 for the models presented in this work).

In addition to the assumptions described above, there is a set of model parameters. First there is the effective temperature T_{eff}. Together with the reference radius r_{ref} it is defined by the bolometric luminosity of the nova via:

$$L_{\text{bol}} = 4\pi\sigma T_{\text{eff}}^4 r_{\text{ref}}^2 \quad . \tag{5.1}$$

σ is the Stefan-Boltzmann constant. The definition of L_{bol} is only used as a convenient parameterization.

The reference radius r_{ref} is defined as the radius at the optical depth $\tau_{\text{std}} = 1$ (section 4.1). There is ample evidence from modeling of the outburst that the nova wind is driven by radiation pressure (Hauschildt & Starrfield 1994). In this case the static Eddington luminosity L_{edd} cannot be used as an upper limit. Thus the luminosity of the nova has to be considered as a free parameter or taken from hydrodynamical simulations.

The density profile of the nova atmosphere can be parameterized as a power law of the form:

$$\rho(r) \propto r^{-n} \quad , \tag{5.2}$$

where n is the density exponent. The velocity profile of the nova wind $v(r)$ follows directly from the requirement that the mass loss rate $\dot{M}(r,t)$ is constant in space (and time as described above):

$$v(r) = \frac{\dot{M}}{4\pi r^2 \rho(r)} \quad . \tag{5.3}$$

The assumption of a constant mass loss rate is crucial because it determines the run of the velocity in the atmosphere but detailed numerical hydrodynamic calculations which assume a diffusion approximation for the radiative transfer show that the assumption of a constant mass loss rate is indeed reasonable (Bath & Shaviv 1976).

Like the reference radius, the reference point of this equation is set at $\tau_{\text{std}} = 1$. At this point, the outer velocity v_{out} and the outer density ρ_{out}

are model parameters. $\rho_{\rm out}$ determines the outer edge of the envelope and is given by an outer pressure $p_{\rm out}$ under the assumption that the ideal gas equation is valid.

Another set of model parameters are the abundances of the elements in the atmosphere. Each abundance can be varied individually. They are set constant through all the atmosphere layers (homogene abundances). The models contain 40 elements with all astrophysical important elements up to ^{55}Cs included. Due to the high temperatures of the nova atmospheres modeled in this work molecules and dust cannot form and are not considered in the models.

The models include bound-bound, bound-free, and free-free transitions, as well as Rayleigh and Thomson scattering. In the calculation of the line profiles, natural, thermal, collisional, Doppler, and Stark broadening are considered. If there is line data for a specific ion in the implemented atomic databases, it is possible to specify how many atomic levels of this ion will be treated explicitly in the NLTE equations. Then collisions with electrons and protons for this ion can be included in the calculations. There are different atomic databases in `PHOENIX` with different sets of data from various literature sources (section 6). It is possible to decide for each ionization stage which database and data set is used in the model.

Currently nova model atmospheres are lacking the treatment of inhomogeneities and density clumps in the shell. From the morphology of nova shells it is known that they can be very inhomogeneous. Inhomogeneities may have a strong influence on the X-ray spectrum because absorption is very important in the soft X-ray range. Furthermore magnetic fields are missing in the models. Although magnetic fields of the order of $10^5 - 10^8$ G are very common in white dwarfs it is not crucial that magnetic fields are not treated in the model calculations because a magnetic field influences the accretion process and may suppress a nova outburst (Livio 1995). Therefore, magnetic fields have to be small in the novae analyzed in this work and their effects on the nova shell are negligible. If a strong magnetic field is present, its main effects on cataclysmic variables are an enhanced mass loss of the main sequence star and the shaping of the nova shell. It is difficult to determine magnetic field strengths in nova systems and observations of the rates and the decline of novae do not show any clear evidence for the existence of magnetic fields.

5.2 Previous nova model atmospheres

Nova atmospheres have been modeled since the early '90s with `PHOENIX` (Hauschildt et al. 1992; Hauschildt & Starrfield 1994; Hauschildt et al. 1994; Hauschildt & Starrfield 1995; Hauschildt et al. 1996, 1997b; Schwarz et al. 1997; Short et al. 1999, 2001). They have been developed in order to understand the newly available high quality UV and IR spectra for novae in outburst especially for the early stage of the outburst when the expanding envelope is still optically thick. Many spectroscopic features were unexplained and there were unidentified strong spectral lines in the UV.

Before the `PHOENIX` models, abundances were determined from the nova spectra in the late nebular phase. Ideally they have to be independent from the abundances in the early phase of the outburst which can be determined by modeling early nova spectra with `PHOENIX`. The models can also help to better understand the outburst mechanism. By modeling a sequence of observed spectra of a nova it is possible to determine the effective temperature, the velocity and density distribution, and the radius of the expanding material as a function of time. It is also important to model novae in other galaxies like in the Large Magellanic Cloud (LMC) to determine the effects of different metallicity in the accreted material on the evolution of the outburst.

The agreement of synthetic and observed spectra are very good from the optical to the ultraviolet even with solar abundances in the models (Hauschildt & Starrfield 1995). The main results of the nova model atmospheres are the following (see references above):

Extension and energy budget: The atmospheres of novae are more geometrically extended than in other objects, for example giants and SNe. A typically geometrical extension is $R_{\rm out}/R_{\rm in} \approx 100...1000$ (Hauschildt & Starrfield 1995, it is ~ 2 for regular giants). Curvature terms in the radiation transfer equation are very important. In the early stages of the outburst the spectrum is formed in an optically very thick shell (in lines and continua) with a flat density profile. This leads to a very extended line and continuum forming region. Due to a large variation of physical conditions in the spectrum forming region (see next point) the term "photosphere" is not appropriate for novae. Therefore, nova atmospheres are different from other stellar atmospheres even from the atmospheres of SNe. SN spectra show continuously decreasing color temperatures and decreasing bolometric luminosities (except in the plateau phase which is very short compared to the total lifetime of SNe) on the other hand the color temperatures of novae increase with time and the bolometric luminosities are constant. This is due to the continuing presence of a central energy and matter source in novae, which is the WD, missing in SNe where the only energy sources are the radioactive decays of nickel and cobalt nuclei.

Temperature stratification: In the inner part of the atmosphere the temperature rises very fast inwards and in the outer parts $T \propto r^{1/2}$ as a consequence of geometric dilution. For example the electron temperature for a model with $T_{\rm eff} = 1.5 \times 10^4\,{\rm K}$ ranges from $T = 4 \times 10^3\,{\rm K}$ to $T = 150 \times 10^3\,{\rm K}$ (Hauschildt & Starrfield 1995). Consequently, there are multiple ionization stages for all elements simultaneously present in the nova shell. The temperature in the outermost layers is low enough for molecule and dust formation as observed (Gehrz 1988).

Density distribution: In the optical phase, the densities in the outer layers of the nova shell are very low and photons from great depths can reach the surface where large depths of the nova shell are visible at some wavelengths. The radiative rates dominate the collision rates and the radiation field is very nongray. This leads to a strong departure from LTE in the line and continuum forming region and NLTE effects must be included self-consistently

NLTE effects: The NLTE effects are strongest for high effective temperatures ($T_{\rm eff} \geq 2 \times 10^4\,{\rm K}$) and for short wavelengths, particular in the UV (Hauschildt et al. 1996). The major NLTE effect is overionization, for example from Fe II to Fe III, caused by the strong UV radiation field which keeps Fe III from recombining to Fe II. Due to this effect it is important to include all required ionization stages of an element in the NLTE calculations simultaniously to calculate the line strengths as correct as possible. Furthermore, NLTE contributes electrons to the e^- reservoir by a partial ionization and this affects any ion of any element. In general, NLTE has to be incorporated in the calculations as complete as possible.

Strength of NLTE: The NLTE departure coefficients (section 4.3) differ from unity in the line forming region of the shell (the relative radial extension of the line and continuum forming regions is about 100, Hauschildt et al. 1994) but the effects of NLTE on the temperature structure of the atmosphere are quite small. The deviations from LTE are large in the outer parts of the atmosphere and influence the profiles of strong lines. But the temperature structure is dominated by the effects of the UV lines on the radiative equilibrium and consequently the temperature differences between the LTE and NLTE models are small.

Line blanketing: The effects of line blanketing on the spectra and the temperature structure of the atmosphere are very large and black body fits to observed spectra lead to wrong effective temperatures. The line blanketing effects are strongest for cooler models where Fe II is the dominant ionization stage of iron because the wealth of Fe II lines form a quasi-continuum in the UV range, the so called "Fe II forest". The expansion of the shell leads to an increase of overlap in lines and continua due to the doppler effect. In hotter models Fe II is ionized to Fe III, a ionization stage of iron with much less lines. Most of the emission lines in the observed spectra have remained unidentified because they are not emission lines but transparent regions between overlapping absorption from the "Fe II forest". Line blanketing also leads to a strong wavelength redistribution of the radiative energy and the temperature structure of the atmosphere must be calculated including the effects of line blanketing.

Non-solar abundances: The effects of enhanced CNO abundances is only visible in relative small regions of the spectrum. An abundance analysis on Nova Cyg 1992 shows a strong hydrogen depletion. The Fe/H ratio is about twice the solar value, and the CNO elements are probably enhanced by a factor of 10 compared to the solar values (Hauschildt & Starrfield 1994). The hydrogen depletion can be explained by a mixing of metal rich white dwarf core material into the ejected shell during the thermonuclear runaway or by burning of hydrogen to helium during the TNR or possibly both. In Nova Cas 1993 an abundance analysis results in a hydrogen depletion of a factor of two and CO is enhanced by a factor of 100 compared to the solar composition (Hauschildt & Starrfield 1994). In contrast, an analysis of Nova OS Andromedae 1986 shows that the observation can be fitted best by models with solar abundances and no metal enhancement (Schwarz et al. 1997). Furthermore, the fit is better with decreased Mg abundance compared to the solar value. A possible explanation is that the secondary star of this nova system is a Galactic halo subdwarf and that metal poor material was accreted on the WD before the outburst.

Radiation pressure: During most of the outburst the material is accelerated by radiation pressure which is higher than the deceleration by gravitation from the central star. Therefore, the material can reach the high velocities observed in novae by radiation pressure alone.

Luminosity and velocity field: The synthetic spectra are insensitive to changes in the luminosity of the nova. This is consistent with the results from Pistinner et al. (1995). But they are sensitive to the form of the velocity field and an enhanced field, e. g. a β-wind law, has to be applied to get a better fit.

X-ray emitting novae have high effective temperatures from $T_{\mathrm{eff}} \sim 10^5\,\mathrm{K}$ to $T_{\mathrm{eff}} \sim 10^6\,\mathrm{K}$. In this work the model atmospheres for novae in the early phase are extended to model atmospheres of novae in the constant bolometric luminosity phase which emit in X-rays (chapter 7). All above points have to be proven if they are consistent in the X-ray range. E. g. there is a forest of iron lines for Fe XVII to XXVI at X-ray wavelengths and line blanketing is expected to be important there, too. Another question is the strength of the NLTE effects and the invariance of the spectrum to different luminosities. In addition, the structure of the atmosphere must be examined at such high temperatures.

Furthermore, the model atmospheres can help to better understand the mechanism of the nova outburst. For this purpose, the X-ray spectral range is more suitable than the other spectral ranges modeled with `PHOENIX`. The X-ray emission mechanmism and the evolution of the X-ray radiation of novae has to be understood (section 7.4). The models are also used to determine the abundance of elements like from helium, carbon, nitrogen, oxygen, and iron in the nova shell (section 7.2). Nova V4743 Sgr (section 3.2) is very convenient for this kind of analysis because a long term observation of this nova has been done and the quality of the data is excelent.

Before it is possible to calculate such models, additional atomic data and microphysics for atomic transitions in the X-ray range are necessary. New atomic databases and X-ray emission and absorption processes have to be implemented in the code first (chapter 6).

Chapter 6

New microphysics in `PHOENIX`

The calculation of the X-ray emission and spectral features of a hot stellar plasma requires atomic transition rates and energy levels of highly ionized elements, particularly for the elements which are strongly abundant in such astrophysical media. The hydrogen-like and helium-like isoelectronic sequences and their satellites are very important at these energies. The data are collected in atomic databases but only the latest versions of these databases are extended to the X-ray (high energy) range.

In earlier versions of `PHOENIX` the CHIANTI Version 3 (hereafter CHIANTI3) database (Dere et al. 1997) and the line lists of Kurucz (Kurucz & Bell 1995) are implemented. For this work, the `PHOENIX`-code was extended to use the CHIANTI Version 4 (hereafter CHIANTI4) (Dere et al. 2001), CHIANTI Version 5 (hereafter CHIANTI5) (Landi et al. 2006), and the APED[1] Version 1.3.1 databases. For each ion the database can be selected individually. Therefore, the results can be compared when the database is changed.

In order to implement a new database in the `PHOENIX`-code, it is important that the data are available in a compatible format. The code needs to read the following data in ASCII-format (The data tables of the APED database are in fits-format and has to be converted into the ASCII-format after downloading from the web):

- energies of the atomic levels
- degeneracies of the atomic levels
- one of the Einstein coefficients for the atomic transitions (for example the A-value)

---

[1] `http://cxc.harvard.edu/atomdb/`

- electron collision excitation rates
- proton collision rates (only if available)

Some atomic databases like XSTAR (Bautista & Kallman 2001) provide line emissivities and opacities for optically thin media. They are not useful because these quantities must be calculated in `PHOENIX` directly.

The new databases provide the following extensions compared to previous `PHOENIX` versions:

- NLTE model atom data for highly ionized species or species with large ionization potential
- many new spectral lines in the X-ray waveband down to 1 Å
- improved data for electron collision rates
- new data for proton collision rates
- better data for thermal bremsstrahlung (relativistic, non-relativistic)
- two-photon continuum emission for the hydrogen and helium isoelectronic sequence

Additionally data for dielectronic recombination and the inverse process, autoionization, exist. These processes produce X-ray satellite lines and may be important for X-ray spectra of novae. The data can be implemented in the code easily if they are taken from the CHIANTI5 database. But CHIANTI5 was available only a few weeks before this work was completed and there was no time to implement the data in the `PHOENIX`-code. This will be done in the future.

The extensions to the `PHOENIX`-code are discussed in the following.

6.1 Ions in the databases

Table 6.1 is a list of all ions in the CHIANTI4, CHIANTI5, and APED databases. There are some ions which do not appear in all databases. They are marked with a 'C' if they appear in CHIANTI4 and CHIANTI5, with a 'C5' if they appear in CHIANTI5 and with an 'A' if they appear in APED only.

There are no data for the lowest ionization stages of high-z elements. These ions are not important for calculations in the X-ray spectral range because in hot plasmas the lowest ions of an element are less abundant and

Ion	I	II	III	IV	V	VI	VII	VIII	IX	X	XI	XII	XIII	XIV	XV	XVI
^{1}H	X															
^{2}He	X	X														
^{6}C		**X**	**X**	X	X	X										
^{7}N	C	**X**	**X**	**X**	X	X	X									
^{8}O		X	**X**	**X**	**X**	X	X	X								
^{9}F									A							
^{10}Ne		**X**	**X**	X	**X**	**X**	**X**	X	X	X						
^{11}Na			**C**	**C**	C	C	C	C	C	C	C					
^{12}Mg		X	**A**	**X**	**X**	**X**	**X**	**X**	**X**	X	X	X				
^{13}Al		C5	X		**C**	**X**	X	X	**X**	**X**	X	X	X			
^{14}Si		**X**	**X**	X	**X**	**X**	**X**	**X**	**X**	**X**	**X**	X	X	X		
^{15}P					C		**C**	**C**	C	C	C	C	C			
^{16}S		X	C	**X**	**X**	X	**X**	**X**	**X**	X	**X**	**X**	**X**	X	X	X
^{17}Cl		C5								C5	C5	C5		C		C5
^{18}Ar				C			**X**	X	**X**	**X**	**X**	X	**X**	**X**	**X**	X
^{19}K					C5				C		C	C	C	C	C	C
^{20}Ca							C5	C5	**X**	X	**X**	**X**	**X**	X	**X**	**X**
^{22}Ti											C	C		**C**	**C**	**C**
^{24}Cr													C	C		**C**
^{25}Mn															C	
^{26}Fe		X				C	C	X	X	**X**	**X**	**X**	**X**	**X**	**X**	X
^{27}Co																
^{28}Ni												**X**	**X**		**X**	**X**
^{30}Zn																

Ion	XVII	XVIII	IXX	XX	XXI	XXII	XXIII	XXIV	XXV	XXVI	XXVII	XXVIII
^{17}Cl	C5											
^{18}Ar	X	X										
^{19}K	C	C5	C5									
^{20}Ca	**X**	X	X	X								
^{22}Ti	**C**	**C**	**C**	C								
^{24}Cr	**C**	**C**	**C**	**C**	**C**	C						
^{25}Mn	C	C	C	C	**C**	C	C					
^{26}Fe	**X**	**X**	**X**	**X**	**X**	**X**	**X**	X	X	X		
^{27}Co	C		C		C	C	C	C	C			
^{28}Ni	X	X	**X**	**X**	**X**	**X**	**X**	**X**	**X**	X	X	X
^{30}Zn				C			C5	C	C		C	C

Table 6.1: Ion content of the CHIANTI4, CHIANTI5, and APED databases. 'X' marks an ion which appears in all three databases, 'C' if it appears only in CHIANTI4 and CHIANTI5, 'C5' if it appears only in CHIANTI5, and 'A' if it appears only in APED. Proton collisions data are available for the bold printed ions.

there is not enough opacity to form spectral lines from transitions of these ions. However, in the case of astrophysically interesting elements, data for the highest and for all important ionization stages exist in the databases.

database	X-ray lines	all lines
CHIANTI3	$\approx$ 13 600	$\approx$ 32 700
CHIANTI4	$\approx$ 22 500	$\approx$ 62 000
CHIANTI5	$\approx$ 102 000	$\approx$ 193 300
APED (total)	$\approx$ 326 000	$\approx$ 463 200
APED (unique)	$\approx$ 178 000	$\approx$ 310 400

Table 6.2: Number of spectral lines from the atomic databases. The number of X-ray lines (defined as lines with wavelengths $\lambda \leq 100\,\text{Å}$) and the sum of all lines over the whole spectral range (up to $\lambda \approx 10^7\,\text{Å}$) are listed. In the APED database entries for the same transition with different data from different sources are possible. In the last row the number of unique lines are specified.

6.2 Spectral lines

Table 6.2 shows the number of spectral lines in the X-ray range (wavelengths $\lambda \leq 100\,\text{Å}$) and the sum of all lines over the full spectral range (up to $\lambda \approx 10^7\,\text{Å}$) in the CHIANTI and APED databases for all ions. The APED database contains multiple spectral lines with different data from several data sources which is designated in the last two rows of the table.

A vast improvement to CHIANTI4 is the CHIANTI5 database. With the numbers in table 6.2 it is obvious that the CHIANTI4, CHIANTI5 and especially the APED database are very good extensions to the available number of spectral lines. The effects of the different databases and the different data sets in the APED database on the synthetic spectra will be examined in section 7.3.

6.3 Electron collision rates

Electron collision rates are obtained from theoretical calculations and cannot easily be measured like some of the spectral line data. The accuracy of the calculations depends on two main factors: the representation of the target wave function and the type of scattering approximation.

In order to represent the target wave function, configuration interaction must be taken into account and intermediate coupling for the higher states of ionization must be allowed. There are three different approximations for the electron-ion collision strength: the Close Coupling (CC), the Coulomb Bethe (CBe), and the Distorted Wave (DW) approximation. The CC approximation is the most accurate. In the CC approximation the significant contribution of resonance structures to the excitation rate has been taken into account, in particular for forbidden and intersystem lines. Spin orbit effects and other relativistic corrections to the target wavefunctions are also important in electron scattering calculations.

By using one of these approximations for the collision strength, the electron collisional excitation rate coefficient can be written as:

$$C^e_{i,j} = \frac{8.63 \times 10^{-6}}{T_e^{1/2}} \frac{\Upsilon_{i,j}(T_e)}{\omega_i} \exp\left(\frac{-E_{i,j}}{kT_e}\right) \quad . \tag{6.1}$$

A Maxwellian electron velocity distribution with T_e as the electron temperature is assumed. ω_i is the statistical weight of the level i, $E_{i,j}$ is the energy difference between levels i and j, k is the Boltzmann constant, and $\Upsilon_{i,j}$ is the thermal-averaged collision strength:

$$\Upsilon_{i,j}(T_e) = \int_0^\infty \Omega_{i,j} \exp\left(-\frac{E_j}{kT_e}\right) \mathrm{d}\left(\frac{E_j}{kT_e}\right) \quad . \tag{6.2}$$

E_j is the energy of the scattered electron relative to the final energy state of the ion. The collision strength Ω is a symmetric ($\Omega_{i,j} = \Omega_{j,i}$) and a dimensionless quantity.

The databases contain the thermal-averaged collision strength Υ. With equation (6.1) the collisional excitation rates can be calculated and the de-excitation rates can be obtained by applying the principle of detailed balance.

The electron collision data in the databases are taken from several data sources where authors provide their data in different formats, for example Ω as a function of energy or Υ as a function of temperature. In order to provide the data in an uniform, compressed, and easily accessible format, the method of Burgess & Tully (1992) has been applied by Dere et al. (1997). This method is based on scaling the incident electron energy and the collision strength in such a way that they both fall within a given, finite range. There are different types of transitions: electronic dipole, non-electronic dipole, non-exchange, and exchange transitions. Each has to be treated differently. The scaled values can often be approximated by a straight line. Therefore, the extrapolation of the collision strength to threshold and to infinite energy becomes relatively straightforward.

With the knowledge of the collision strength Ω over the full energy range the integration over the Maxwellian velocity distribution is possible (equation 6.2) and is carried out with the Gauss-Laguerre method. The collision strengths Ω are finally expressed as a n-point spline fit to the scaled collision strengths Υ. In the CHIANTI3 database the spline fit is always expressed with $n = 5$ points. If it is necessary to improve the accuracy of the electron collision data, the fit will be extended to $n = 9$ points in the CHIANTI4, CHIANTI5, and APED databases.

6.4 Proton collision rates

The proton collision rates are accessible from the databases in the same format as the electron collision rates. Due to accuracy requirements, nearly all fits are splines with $n = 9$ points. Otherwise, the splines use $n = 5$ points. Only transitions within the ground configuration of an ion are important. Compared to the electron collision data, relatively little data is required for proton collisions. Whereas electron collision data is usually published in the form of collision strengths, proton collision data is generally directly published as rate coefficients. Proton collision data is a new feature in the `PHOENIX`-code and provided only if the CHIANTI4, CHIANTI5 or APED databases are used.

The proton rates can become comparable to the electron excitation rates for transitions with $\Delta E \ll kT$. This has been shown by Seaton (1964) for the Fe XIV ion in solar coronal conditions. The rate coefficient drops to zero at the threshold energy for the transition because protons are repelled by positively charged ions. The electron and proton rate coefficients of the transitions $2p^5\,{}^2P_{3/2} \rightarrow {}^2P_{1/2}$ in Fe XVIII and $2p^3P_0 \rightarrow {}^3P_1$ in O V are plotted against the plasma temperature in figure 6.1. The rates have been calculated with data from the CHIANTI4 database with a proton to electron ratio of $p/e \sim 1$. The proton rates are comparable in strength to the electron rates at the temperature of maximum ionization T_{max} of the ion and become stronger at higher temperatures. From figure 6.1 it follows $\log T_{\rm max} \approx 7.0$ for Fe XVIII and $\log T_{\rm max} \approx 5.4$ for O V. In section 7.1.4 an analysis of the effects of the proton collision rates on the atmospheric structure is given.

6.5 Thermal bremsstrahlung

The free-free emissivity can be calculated by:

$$\epsilon(\nu, T) = f \cdot \frac{\exp(-u)}{\sqrt{T_e}} \cdot n_e \cdot \sum_{ions,z} \left[n_{ion} \cdot z^2 \cdot g_{\rm ff}(z, u) \right] \quad , \tag{6.3}$$

with $u = \frac{h\nu}{kT_e}$ as the ratio of the energy of the emitted photon to the thermal energy of the electron. The dimensionless factor f has a value of

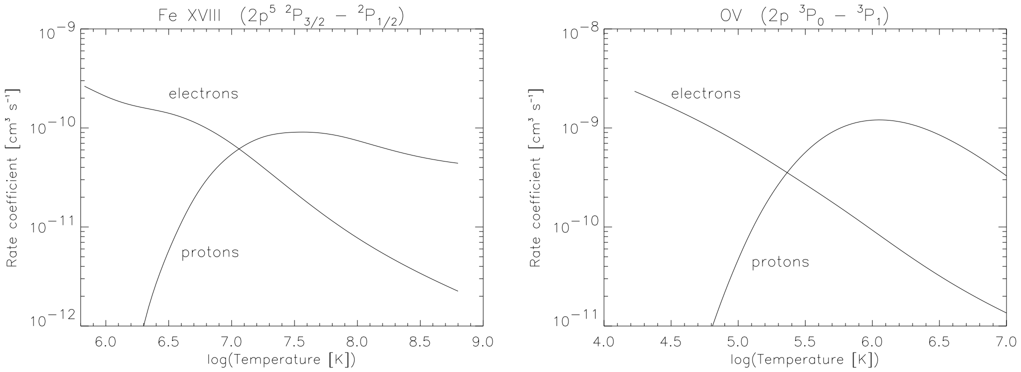

Figure 6.1: Electron and proton collision rates calculated with CHIANTI4 data for a transition in Fe XVIII and O V plotted against the plasma temperature.

$f = 1.42554 \times 10^{-27}$. n_e is the electron number density, n_{ion} is the number density of the ion with the charge Z, ν is the frequency of the emitted photon, and $g_{\rm ff}$ are the free-free gaunt factors, which depend on Z and u.

Except of the gaunt factors all values in equation (6.3) can be calculated with `PHOENIX`. The gaunt factors have to be read from a database as a function of the ion-charge Z and the ratio u. Earlier versions of `PHOENIX` only considered free-free emission from H, Mg, and Si. The CHIANTI4 and CHIANTI5 databases provide gaunt factors for all ions of elements up to $Z = 30$.

The gaunt factors for these elements are either relativistic or non-relativistic. Therefore, two ranges of T_e and u have to be distinguished. In the range $6.0 \leq \log(T_e) \leq 8.5$ and $-4.0 \leq \log(u) \leq 1.0$ the fitting formula for relativistic gaunt factors of Itoh et al. (2000) and for $\log(T_e) < 6.0$ and $\log(u) > 1.0$ the non-relativistic gaunt factors of Sutherland (1998) are used. The transition from relativistic to non-relativistic gaunt factors is so smooth that no effects are visible in the models and synthetic spectra. Interpolation procedures would be very time consuming and are not necessary. Therefore, they have not been implemented in the `PHOENIX`-code. If bremsstrahlung is important in nova atmospheres in X-rays, will be examined in section 7.1.1.

6.6 Two-photon continuum emission

Two-photon continuum emission has been implemented in `PHOENIX`. The process is valid for the first excited level in hydrogen isoelectronic ions and for the second excited levels in helium isoelectronic ions. These levels can only decay through a forbidden magnetic dipole or a two-photon transition. In the case of hydrogen the importance of the magnetic dipole transition increases with Z, but for nickel ($Z = 28$) the two-photon transition rate is about five times that of the magnetic dipole transition rate.

The two-photon continuum emission in (erg cm^{-3} s^{-1} Å^{-1}) for a transition from level i to level j is calculated by:

$$\epsilon_{ij}(\lambda, T) = \frac{hc}{4\pi\lambda} A_{ij} N_j \phi \left(\frac{\lambda_0}{\lambda} \right) \quad . \tag{6.4}$$

A_{ij} is the Einstein A-coefficient for the transition, N_j is the number density of the level j of the ion involved in the transition, and ϕ is the spectral distribution function.

Like in the case of the free-free gaunt factors for bremsstrahlung, ϕ and A_{ij} have to be taken from an atomic database. These data is included in CHIANTI4 and CHIANTI5 (Young et al. 2003). In the case of the hydrogen isoelectronic sequence, CHIANTI contains data from Parpia & Johnson (1982) for the magnetic-dipole and two-photon transition rates and the spectral distribution function for Z = 1, 20, 40, 60, 80, and 92 is taken from the tables in Goldman & Drake (1981). Interpolation for values of $Z \leq 28$ should be fairly accurate. For the helium isoelectronic sequence the rates have been calculated by Drake (1986) and the spectral distribution function by Drake et al. (1969) for $2 \leq Z \leq 10$. At $Z = 10$ the shape of the distribution function does not appear to be changing too fast with Z and for $Z > 10$ the distribution function for $Z = 10$ is used.

The importance of two-photon continuum emission from hydrogen has been examined by Drake & Ulrich (1981) with data from the IUE (International Ultraviolet Explorer) for the ultraviolet spectral range and moderately dense plasmas. The two-photon emission depends on the temperature of the gas, the optical depth in the Lyman α continuum, and the photoionization out of the ground state. In plasmas at moderate densities two-photon emission occurs more readily at lower temperatures ($T = 5 \times 10^3$ K to $T = 1 \times 10^4$ K) than at higher ones because, at higher temperatures, collisions on the first excited level of hydrogen reduce its population at densities $N_e \approx 10^{11}$ cm^{-3}. The optical depth in the Lyman α continuum has to be high to counteract the collisions. If the ground state photoionization rate is low, the first excited level can be populated by collisions and two-photon emission is favored. The importance of the two-photon emission in the X-rays spectral range, at temperatures and densities in nova atmospheres, will be examined in section 7.1.4.

Chapter 7

Analysis of nova V4743 Sgr

In this chapter the results of the model atmospheres of the nova V4743 Sagittarii are presented. The models were calculated with solar abundances (section 7.1). There are discrepancies between models and observations which are due to the use of solar abundances. Therefore, models with non-solar abundances are discussed in section 7.2 to obtain the best fits to the observations.

The effective temperature and the chemical composition of the nova atmosphere, and the hydrogen column density for the best fit can be determined. From fitting all observations of V4743 Sgr the variations of the fit parameters are examined. It is possible to develop a model for the emission and evolution of X-ray radiation in nova V4743 Sgr (section 7.4). But before doing so, the effects of the different atomic data (chapter 6) on the quality of the fits have to be examined and the errors on the fit parameters must be determined (section 7.3). All main results and the comparison to the results from the previous nova model atmospheres which were calculated with `PHOENIX` to fit early nova spectra in the infrared (IR) and ultraviolet (UV) spectral ranges (section 5.2) are summarized in section 7.4. In section 7.5 the results of `PHOENIX` will be compared with models from TMAP for a XMM-Newton observation of nova V4743 Sgr.

7.1 Models with solar abundances

With the new microphysics described in chapter 6 nova model atmospheres with high effective temperatures can be calculated. In this section atomic data from the "standard dataset" of APED (section 7.3.2) have been used in the model calculations. Differences to models calculated with atomic data from the CHIANTI databases will be discussed in section 7.3.

In order to narrow the parameter space, the first models for nova V4743 Sgr were calculated with solar abundances. They are also useful to test if the `PHOENIX`-code can produce reliable results for hot nova atmospheres in the X-ray spectral region. Models with non-solar abundances will be described in section 7.2. From observations and from theory it is known that the assumption of solar abundances in nova ejecta is wrong (section 2.1.6). It will be shown in section 7.1.3 that nova model atmospheres with solar abundances can produce results which are close to the observations but there are discrepancies between the observed and modeled line strengths and in the continuum emission. Therefore, the models with solar abundances are used to show differences to models with non-solar abundances. Furthermore, they are useful to determine NLTE effects and the structure of nova atmosphere in the X-ray (section 7.1.4) which are qualitatively the same as for models with non-solar abundances.

The solar abundances were taken from Anders & Grevesse (1989). They are sufficient for this work since the revised abundances from Asplund et al. (2005) are not yet generally accepted. The models were calculated for effective temperatures in the range of $T_{\rm eff} = 10^5 - 10^6\,{\rm K}$. For the bolometric luminosity a value of $L_{\rm bol} = 5 \times 10^4 L_\odot$ is assumed. This value implies a white dwarf mass close to the Chandrasekhar limit. As described in section 5.2, nova model atmospheres for earlier phases of the outburst have shown very little dependence of the spectrum on the bolometric luminosity (Hauschildt & Starrfield 1995). This is has been tested for the models presented in this work. The shape of the spectra does not depend on the luminosity and the models are parameterized by $T_{\rm eff}$ for equal luminosities.

For nova V4743 Sgr the density exponent is taken as $n = 3$ (see section 5.1), which is typical for nova atmospheres, as determined from the hydrodynamic simulations of the nova outburst (Starrfield 1993). For the velocity field, the observed value of $v_{\rm out} = 2500\,{\rm km\ s^{-1}}$ (Kato et al. 2002) is used. A reasonable value for the outer pressure to produce the best and fastest convergence lies at $p_{\rm out} = 10^{-2}\,{\rm dyn\ cm^{-2}}$ and $p_{\rm out} = 10^{-1}\,{\rm dyn\ cm^{-2}}$, depending on $T_{\rm eff}$ of the model (table 7.2).

There are different steps during the generation of a model as described in the following.

7.1.1 Modeling steps for hot nova atmospheres

The calculation of a nova model atmosphere with a high $T_{\rm eff}$ and with all atomic transitions simultaneously treated in NLTE is very difficult. In order to avoid only apparent and to obtain true convergence the calculation must be divided in different steps where the physical input changes only slightly. After each step the model must converge. The main steps are the calculation of continuum models, models in LTE, and mixed LTE and NLTE models. The first step, the continuum model, starts the model calculation from scratch.

The complexity of the models complicates the calculation of models with different T_{eff} . For each T_{eff} the calculation has to be started with the continuum model from scratch.

Continuum models

Continuum models are calculated by ignoring all spectral lines (bound-bound transitions). Only bound-free, free-free, and free-bound transitions are accounted for. The bound-free transitions are calculated with photoionization cross sections from Verner & Yakovlev (1994). Cross sections for all neutral atoms from helium to zinc and about 70% of all ions of elements with atomic number $Z \leq 30$ are used. They are determined with analytic fits to the partial photoionization cross sections which were calculated by the Hartree-Dirac-Slater method (Verner & Yakovlev 1995). This data is relatively old and not as accurate as the line data from chapter 6. But it is adequate to calculate continuum models because these models are only starting approximations and in the final NLTE models the improved data from chapter 6 are used.

The continuum models are used to determine the optimal standard wavelength $\lambda_{\text{std}}^{\text{opt}}$ which is the standard wavelength λ_{std} for which the models converge fastest (λ_{std} is the wavelength to define the optical depth grid, section 4.1). This standard wavelength can be used for all steps of a specific model because changes in $\lambda_{\text{std}}^{\text{opt}}$ are small enough that all model steps can converge with the same standard wavelength. $\lambda_{\text{std}}^{\text{opt}}$ depends on T_{eff} of the model. Therefore, a grid of models with different λ_{std} was calculated for different T_{eff}. For each model it was determined how many iterations were necessary for convergence, i. e. if the temperature correction produced a temperature difference of less than 1% in each layer according to the last iteration. Then $\lambda_{\text{std}}^{\text{opt}}$ is the λ_{std} of the model with the minimal number of iterations iter_{min} necessary for convergence.

Results for $T_{\text{eff}} = 6.0 \times 10^5\,\text{K}$ are shown in table 7.1. Fastest convergence is achieved, e. g., at $\lambda_{\text{std}} = \lambda_{\text{std}}^{\text{opt}} = 600\,\text{Å}$. Accordingly, this λ_{std} is optimal to calculate a model atmosphere with $T_{\text{eff}} = 6.0 \times 10^5\,\text{K}$. For the wavelength grid, the increment of $\Delta\lambda = 50\,\text{Å}$ is small enough to determine $\lambda_{\text{std}}^{\text{opt}}$ because the results for iter_{min} changed only slightly around $\lambda_{\text{std}}^{\text{opt}}$ if λ_{std} changes by $\Delta\lambda = 50\,\text{Å}$. The determination of $\lambda_{\text{std}}^{\text{opt}}$ for different T_{eff} from $T_{\text{eff}} = 10^5\,\text{K}$ to $T_{\text{eff}} = 10^6\,\text{K}$ can be found in table 7.2. $\lambda_{\text{std}}^{\text{opt}}$ decreases with higher T_{eff} because the spectral energy maximum increases with T_{eff}.

$\lambda_{\rm std}$ in Å	iter$_{\rm min}$	$\lambda_{\rm std}$ in Å	iter$_{\rm min}$
50	nc	550	18
100	nc	600	17
150	nc	650	17
200	nc	700	17
250	26	750	17
300	25	800	18
350	25	850	18
400	23	900	18
450	23	950	23
500	23	1000	23

Table 7.1: Minimal number of iterations iter$_{\rm min}$ which is necessary for convergence. 'nc' means that the model is not converged. The models were calculated for $T_{\rm eff} = 6.0 \times 10^5$ K and different standard wavelengths $\lambda_{\rm std}$. Fastest convergence is achieved, e. g., at $\lambda_{\rm std} = \lambda_{\rm std}^{\rm opt} = 600$ Å.

$T_{\rm eff}$ [10^5 K]	$\lambda_{\rm std}^{\rm opt}$ [Å]	$p_{\rm out}$ [dyn cm^{-2}]	$T_{\rm eff}$ [10^5 K]	$\lambda_{\rm std}^{\rm opt}$ [Å]	$p_{\rm out}$ [dyn cm^{-2}]
1.0	4000	10^{-2}	6.0	600	10^{-1}
2.0	3500	10^{-2}	7.0	600	10^{-1}
3.0	3000	10^{-2}	8.0	450	10^{-1}
4.0	2800	10^{-2}	9.0	400	10^{-1}
5.0	1500	10^{-2}	10.0	400	10^{-1}

Table 7.2: Standard wavelength $\lambda_{\rm std}^{\rm opt}$ which is optimal for fastest convergence for models of different effective temperatures from $T_{\rm eff} = 10^5$ K to $T_{\rm eff} = 10^6$ K. The pressure $p_{\rm out}$, used for models at these temperatures, is given.

The choice of $\lambda_{\rm std}$ has no physical background and is only a numerical parameter which is necessary to calculate an atmosphere. The outer pressure $p_{\rm out}$ is a numerical parameter, too. As described in section 5.1, $p_{\rm out}$ determines the outer edge of the nova envelope. The $p_{\rm out}$ which is used to calculate models with different $T_{\rm eff}$ is given in the last column of table 7.2. For $T_{\rm eff} \geq 6.0 \times 10^5$ K, the outer pressure has to be switched from $p_{\rm out} = 10^{-2}$ to $p_{\rm out} = 10^{-1}$ dyn cm^{-2} in order to reach converge in the models.

Before the implementation of the thermal bremsstrahlung process from CHIANTI (section 6.5, in the following called 'new bremsstrahlung') has been done, there was only the 'old bremsstrahlung' process in `PHOENIX`. The

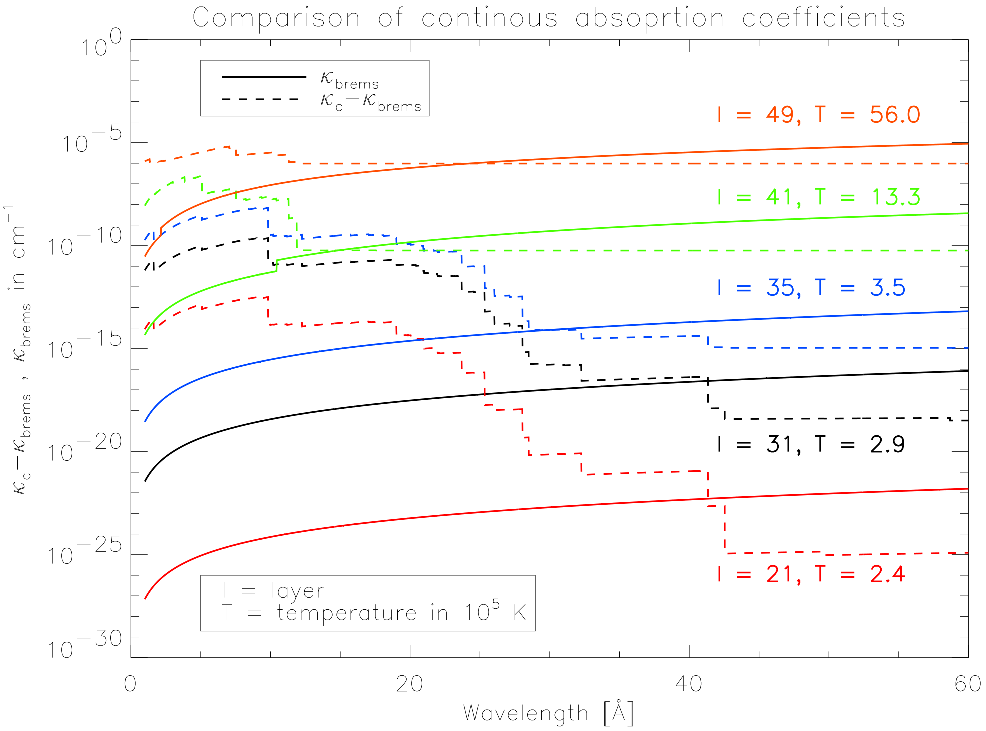

Figure 7.1: Continuous absorption coefficients for bremsstrahlung κ_{brems} (solid lines) and for all other continuous processes $\kappa_c - \kappa_{brems}$ (dashed lines) in different layers l, i. e. at different temperatures T. Layer $l = 50$ is at the bottom of the atmosphere.

'old bremsstrahlung' considers contributions from hydrogen and silicon, but in the 'new bremsstrahlung' there are contributions from all elements up to $Z = 30$.

In figure 7.1 is a comparison of the continuous absorption coefficients without bremsstrahlung (dashed lines) and from bremsstrahlung (solid lines) at different temperatures (in different atmosphere layers). The coefficients are plotted for wavelengths up to $\lambda = 60\,$Å since this wavelength range is important in this work (figures 3.6 and 3.7). At $T \sim 1.3 \times 10^6\,$K (layer 41) and for $\lambda \gtrsim 15\,$Å the bremsstrahlung absorption is stronger than all other continuous absorption processes. In all other layers the dominance of bremsstrahlung begins at larger wavelengths.

In figure 7.2 two test models calculated with the 'old' and the 'new bremsstrahlung' can be seen. Both are calculated for $T_{\rm eff} = 5.8 \times 10^5\,$K. In the spectrum with the 'old bremsstrahlung' iron lines are missing because of non-convergence when adding iron. There are only weak absorption and

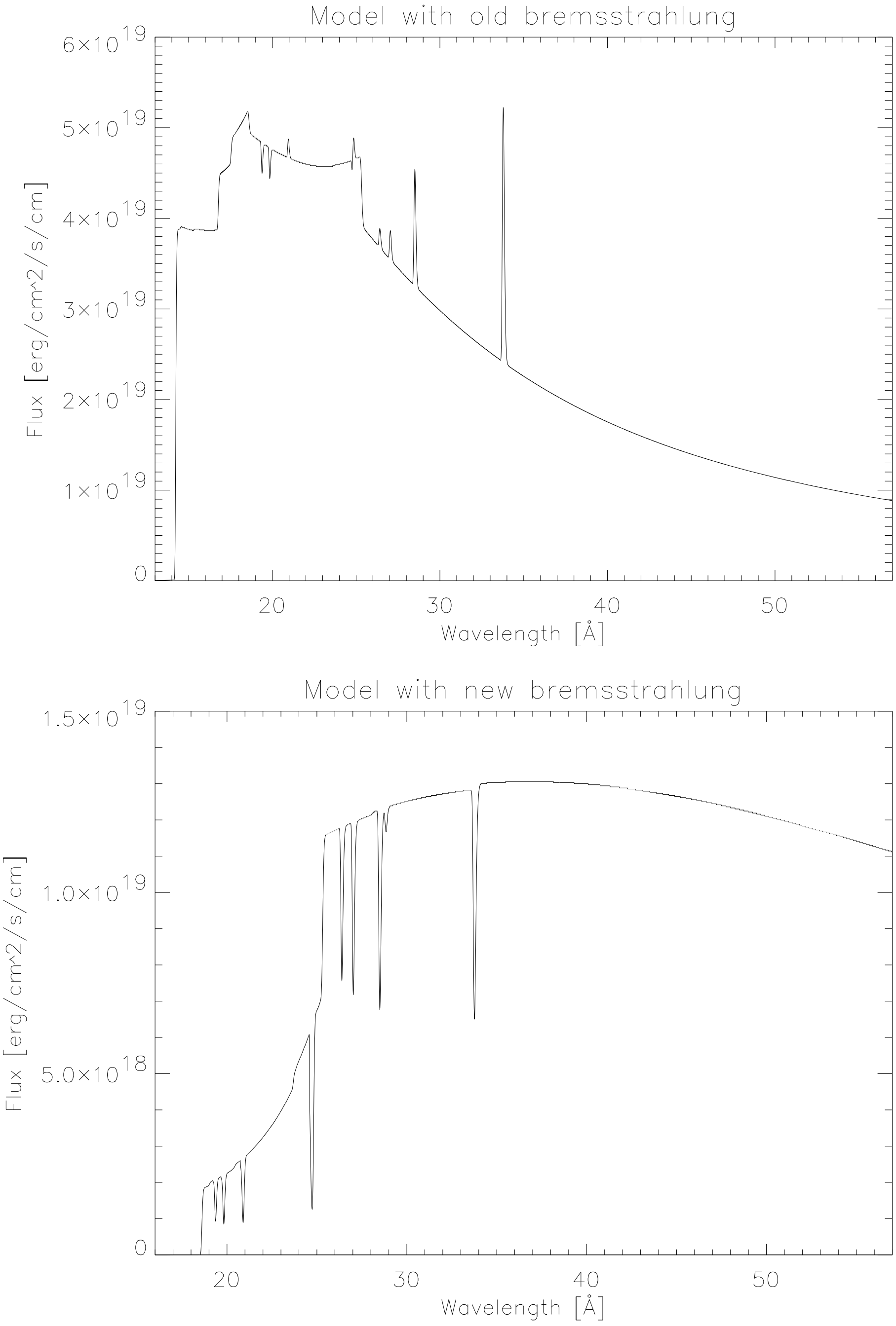

Figure 7.2: Two test models, calculated with the 'old' and the 'new bremsstrahlung'. The model atmosphere has an effective temperature of $T_{\text{eff}} = 5.8 \times 10^5\,\text{K}$.

very strong emission lines in the spectra with the 'old bremsstrahlung'. It is impossible to fit the observed spectra (figures 3.6 and 3.7) with a model spectrum calculated with the 'old bremsstrahlung'. As a conclusion, the bremsstrahlung emission is a dominant X-ray emission process in classical novae of the kind of V4743 Sgr and must properly be included in the modeling of the X-ray observations of these novae. This is an important result of this work and the consequences will be discussed in section 7.4.

Bremsstrahlung is a pure continuum process. Therefore, the correct bremsstrahlung process has to be used in the continuum models. E. g., calculations with the 'old' and the 'new bremsstrahlung' have shown that the correct process is crucial for the determination of $\lambda_{\mathrm{std}}^{\mathrm{opt}}$. Using the two bremsstrahlung processes, the results for $\lambda_{\mathrm{std}}^{\mathrm{opt}}$ are different for the same T_{eff}. E. g., $\lambda_{\mathrm{std}}^{\mathrm{opt}} = 850$ for $T_{\mathrm{eff}} = 5.0 \times 10^5\,\mathrm{K}$ if the 'old bremsstrahlung' is used and $\lambda_{\mathrm{std}}^{\mathrm{opt}} = 1500$ for the same T_{eff} and models with the 'new bremsstrahlung'. There is no such a trend in the run of the λ_{std} against T_{eff} like in table 7.2 if the 'old bremsstrahlung' is used.

Spectra of continuum models will be shown in section 7.1.2.

LTE and mixed LTE and NLTE models

After calculating continuum models as described above, models with LTE lines are calculated. The spectral lines from the lists of Kurucz & Bell (1995) can be added to the models but the line selection procedure in `PHOENIX`, where the lines are preselected depending on their contribution to the opacity (see below), ignores all of these lines. This is due to the high temperatures in the model atmospheres where only the highest ionized elements are present (e. g., C V, C VI, N VII, O VII, O VIII, Fe VIII - Fe XXVI, ...). There is no line data from these highly ionized elements in Kurucz & Bell (1995).

In the CHIANTI3 database, data for highly ionized elements exist but most of the weak spectral lines in the X-ray spectral range which are important for the line blanketing are missing. Therefore, the CHIANTI3 database is also not useful for this work. Therefore, only spectral lines of the CHIANTI4, CHIANTI5, and APED databases (section 6.1) are useful.

The species included in the models are listed in table 7.3. The ionization stages which are important in the atmosphere are treated in the NLTE calculations. In table 7.3 they are listed in the last column. Species are important in the atmosphere if the concentrations of their partial pressures are sufficiently large. If the probabilities for transitions in these species are also sufficiently large their opacity is important. The ionization stages contribute to the NLTE effects and all available transitions between all available levels of these ions must be treated in the NLTE rate equations (section 4.3).

element	Z	in LTE	in NLTE
H	1	—	I
He	2	—	I - II
C	6	I - III	IV - VI
N	7	I - IV	V - VII
O	8	I - V	VI - VIII
Ne	10	I - VI	VII - X
Mg	12	I - VIII	IX - XII
Al	13	I - IX	X - XIII
Si	14	I - IX	X - XIV
S	16	I - VIII	IX - XVI
Fe	26	I - XV	XVI - XXVI

Table 7.3: Species included in the LTE and NLTE calculations. Given are the ionization stages for each element. Z is the atomic number.

An example for oxygen can be seen in figure 7.3. The partial pressures of all oxygen ions (solid lines) and the total partial pressure of oxygen (sum of O I to O IX, dashed line) are plotted against the radius R of the atmosphere[1] ($R = 0\,\mathrm{cm}$ is at the center of the WD). Only O VII and O VIII have relatively high concentrations in comparison to the total partial pressure of oxygen. In order to treat the underionization effects the lower ionization stage O VI is treated in NLTE together with O VII and O VIII. The lines of all other species have only minor or no contributions to the opacities and are calculated in LTE. This is very fast in contrast to the NLTE calculations (solution of the rate equations) and there is vanishing waste of time from the calculation of line opacities which have no contributions. The model atmosphere has an effective temperature of $T_{\mathrm{eff}} = 6.0 \times 10^5\,\mathrm{K}$. For all other effective temperatures calculated here, the results in the case of oxygen are qualitatively the same. The partial pressures of other elements will be discussed in section 7.1.4.

In order to prevent pseudo-convergence, the lines from the species from table 7.3 have to be added to the models for one element after another, first in the LTE and then in the NLTE calculations. These are the mixed LTE and NLTE models. Calculating the lines in LTE first gives an estimate of the populations of the atomic levels n_i before the departure coefficients b_i (section 4.3) will be calculated and a better convergence is provided. In the following, the model which includes all species from table 7.3 is called a

---

[1] Physical quantities are plotted against the radius in order to be able to compare different models.

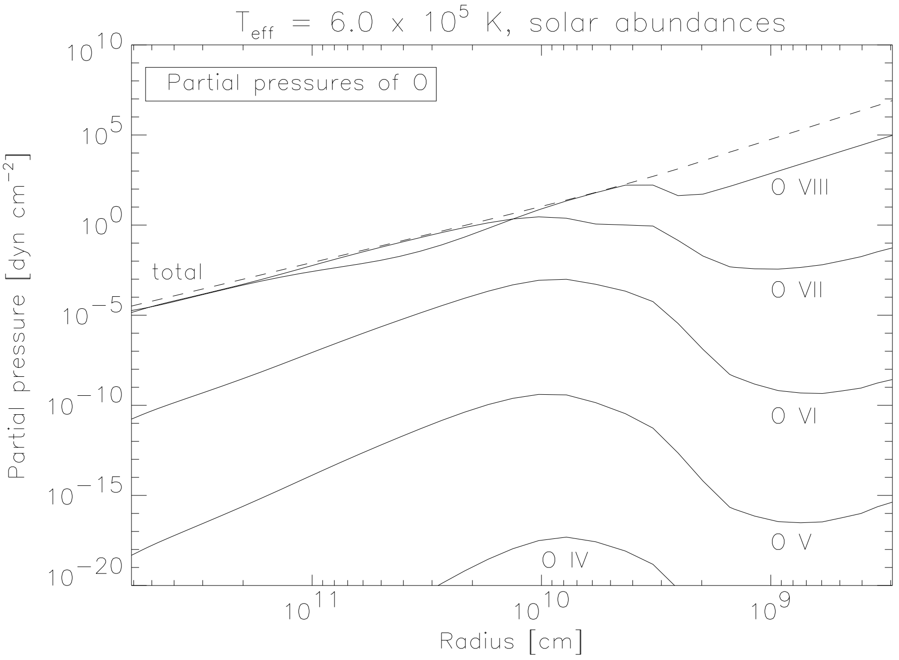

Figure 7.3: Partial pressures of all ions of oxygen (solid lines) and total partial pressure of O I to O IX (dashed line) plotted against the radius R of the atmosphere ($R = 0\,\mathrm{cm}$ is at the center of the WD). The model atmosphere has an effective temperature of $T_{\mathrm{eff}} = 6.0 \times 10^5\,\mathrm{K}$.

complete NLTE model. Figure 7.4 shows a flow-chart for the development of a complete NLTE model.

The Boltzmann and Saha-Boltzmann equations (e. g., equations 3.124 and 3.127 in Lang 1999) are no longer valid in NLTE. The ionization stages are over- or underpopulated in contrast to calculations by the Saha-Boltzmann equation. An over- or underpopulated ionization stage has effects on the neighboring ionization stages, if both are important in the atmosphere. Therefore, it is in principle necessary to calculate all transitions of all ionization stages of an element in the NLTE rate equations simultaneously.

In section 4.2 it was explained that the source function can be interpolated linearly or parabolically along a characteristic ray of the radiation field. In the `PHOENIX`-code it can be switched between parabolic and linear interpolation with the parameter `taulin`. If the optical depth between two points on the characteristic ray is smaller or equal to `taulin`, the source function will be interpolated linear between this two points. The higher `taulin`, more parts of the source function are interpolated linear. Although the most accurate result is achieved with the parabolic interpolation `taulin` must be chosen as small

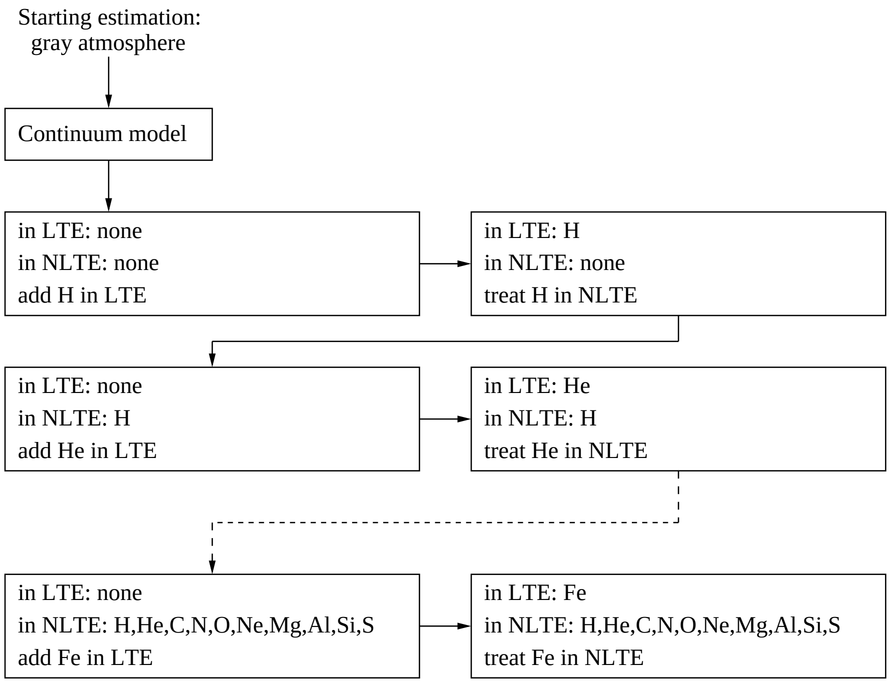

Figure 7.4: Different steps to calculate a complete NLTE model. For each step 30 iterations are used.

as possible. The value of `taulin` has a strong influence on the convergence of the NLTE structure. For all models in this work a value of taulin $= 10^{-2}$ is used to ensure convergence of the NLTE departure coefficients.

For each of the mixed LTE and NLTE models the energy equilibrium and the NLTE rate equations have to be converged before the next model can be calculated. The number of iterations which is necessary for convergence is different for each element and it depends on $T_{\rm eff}$ of the model. Except for the NLTE calculations of iron, the number of necessary iterations is between 20 and 30. For all model steps up to iron in LTE, the calculation of one iteration on a parallel computer used for this work takes less than five minutes. Therefore, 30 iterations are used for each step up to iron in LTE and there is no great waste due to time from some extra iterations after convergence is reached. In models with iron treated in NLTE the energy conservation and NLTE structure converge much faster because of the large number of spectral lines of iron. The coupling of the radiation field to the plasma is stronger and there is less scattering if lines of iron are included (this is only directly treated in NLTE calculations). Therefore, the temperature correction works faster. Ten iterations are needed for models with iron in NLTE. For the calculation of a full NLTE model, 670 iterations are used.

In this work, a selection routine has been implemented in the `PHOENIX`-code for spectral lines from the CHIANTI and APED databases. For all species, except for iron, the NLTE calculations are so fast that the lines do not have to be preselected so that the selection procedure is only used if iron is treated in NLTE. It works like the procedure for the lines from the database of Kurucz & Bell (1995). The absorption coefficient in the line center κ_l is calculated for every line and compared to the corresponding continuum absorption coefficient κ_c. If the ratio $r = \kappa_l/\kappa_c$ is smaller than a prespecified value the transition is treated in the NLTE rate equation, otherwise it is used as a NLTE background opacity.

A transition used as a NLTE background opacity is called a secondary NLTE line. For secondary lines either one level (the upper or the lower level) or both levels of the transition are calculated in LTE. If one level is calculated in LTE, the NLTE departure coefficient of the other level is set equal to the departure coefficient of the ground state. If both levels are calculated in LTE, the same approach as for LTE-lines is adopted except that the ground state departure coefficient is used, in order to include the effects of under- and overionization.

The secondary NLTE lines are very weak. In contrast to a detailed NLTE calculation the above approach does not influence the spectrum significantly and it saves much of computational time. Spectra for models with different r are calculated. They are consistent as long as $r <= 10^{-3}$.

In the following, spectra calculated in the different steps are shown and the NLTE effects on the spectrum can be examined.

7.1.2 Spectra with solar abundances

In the figures 7.5 to 7.21 the spectra for the different model steps in figure 7.4 are plotted for a model atmosphere with $T_{\rm eff} = 6.0 \times 10^5\,\rm K$. The discussion is qualitatively the same for the models with other $T_{\rm eff}$. More spectra of full NLTE models with different $T_{\rm eff}$ are shown in the figures A.1 to A.7 in appendix A. The synthetic spectra are plotted over the wavelength range of the observed spectra (figure2 3.6 and 3.7). In each figure there are two spectra (dashed and solid line). The dashed line is the spectrum plotted as a solid line in the figure before (except in figure 7.5). The spectral changes between two successive model steps can be determined by comparing the two spectra in a figure. The NLTE effects on the spectrum can be determined for each chemical element.

Test calculations have shown that there is no disadvantage in the convergence of the models if the lines of elements up to oxygen are added simultaneously as LTE-lines (lines calculated in LTE). This saves 120 iterations (see

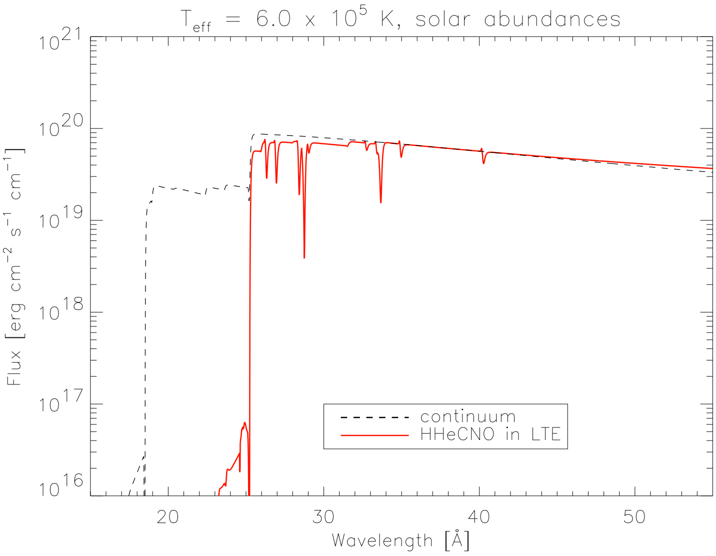

Figure 7.5: Spectra with solar abundances, comparing a continuum spectrum (dashed line) with a spectrum where hydrogen, helium, carbon, nitrogen, and oxygen are calculated in LTE (solid line).

above). This is not working for higher Z elements. If they are also added to the model in LTE before hydrogen, helium, carbon, nitrogen, and oxygen are treated in NLTE, the structure does not converge. As it can be seen below, the NLTE effects of carbon, nitrogen, and oxygen are very strong. The assumption of LTE is wrong for these elements and they have to be treated in NLTE before adding more elements to the model.

A continuum spectrum (dashed line) and a spectrum with LTE-lines of hydrogen, helium, carbon, nitrogen, and oxygen (solid line) are plotted in figure 7.5. There is very strong continuum absorption from carbon, nitrogen, and oxygen below $\lambda \sim 25\,\text{Å}$ and the continuum flux is vanishing. Above $\lambda \sim 25\,\text{Å}$ there are absorption lines from the highest ionization stages of carbon, nitrogen, and oxygen but there are no remarkable emission lines in the spectrum. The lines are assigned to their ions in the following discussion and are summarized in table 7.4 together with their Einstein A-values and the transition identifications.

When treating hydrogen in NLTE (figure 7.6), the continuum flux above $\lambda \sim 25\,\text{Å}$ increases. This is due to a change in the partition function from NLTE effects. The relative line strengths stay the same. No additional lines appear because of the lack of H-lines at such low wavelengths. Calculating helium in NLTE (figure 7.7) there is again no change in the spectral lines because like hydrogen, helium has no lines at small wavelengths.

ion	λ in Å	A-value in s^{-1}	transition identification
C V	40.34	8.83×10^{11}	$1s^2 \rightarrow 1s2p$
C VI	26.37	4.38×10^{10}	$1s\ ^2S_{1/2} \rightarrow 5p\ ^2P_{1/2}$
	26.37	2.19×10^{10}	$1s\ ^2S_{1/2} \rightarrow 5p\ ^2P_{3/2}$
	27.00	8.68×10^{10}	$1s\ ^2S_{1/2} \rightarrow 4p\ ^2P_{1/2}$
	27.00	4.35×10^{10}	$1s\ ^2S_{1/2} \rightarrow 4p\ ^2P_{3/2}$
	28.48	2.13×10^{10}	$1s\ ^2S_{1/2} \rightarrow 3p\ ^2P_{1/2}$
	28.48	1.07×10^{10}	$1s\ ^2S_{1/2} \rightarrow 3p\ ^2P_{1/2}$
	33.75	3.84×10^{5}	$1s\ ^2S_{1/2} \rightarrow 2s\ ^2S_{1/2}$
	33.75	7.98×10^{11}	$1s\ ^2S_{1/2} \rightarrow 2p\ ^2P_{1/2}$
	33.75	3.99×10^{11}	$1s\ ^2S_{1/2} \rightarrow 2p\ ^2S_{3/2}$
N VI	23.31	1.08×10^{11}	$1s^2 \rightarrow 1s5p$
	24.94	5.13×10^{11}	$1s^2 \rightarrow 1s3p$
	28.88	1.80×10^{12}	$1s^2 \rightarrow 1s2p$
N VII	19.37	8.11×10^{10}	$1s\ ^2S_{1/2} \rightarrow 5p\ ^2P_{1/2}$
	19.37	4.06×10^{11}	$1s\ ^2S_{1/2} \rightarrow 5p\ ^2P_{3/2}$
	19.84	1.61×10^{10}	$1s\ ^2S_{1/2} \rightarrow 4p\ ^2P_{1/2}$
	19.84	8.05×10^{10}	$1s\ ^2S_{1/2} \rightarrow 4p\ ^2P_{3/2}$
	20.92	3.94×10^{11}	$1s\ ^2S_{1/2} \rightarrow 3p\ ^2P_{1/2}$
	20.92	1.98×10^{11}	$1s\ ^2S_{1/2} \rightarrow 3p\ ^2P_{1/2}$
	24.80	9.88×10^{5}	$1s\ ^2S_{1/2} \rightarrow 2s\ ^2S_{1/2}$
	24.80	1.48×10^{12}	$1s\ ^2S_{1/2} \rightarrow 2p\ ^2P_{1/2}$
	24.80	7.40×10^{11}	$1s\ ^2S_{1/2} \rightarrow 2p\ ^2S_{3/2}$
O VII	18.65	9.33×10^{11}	$1s^2 \rightarrow 1s3p\ ^1P_1$
	21.63	3.30×10^{12}	$1s^2 \rightarrow 1s2p\ ^1P_1$
	21.88	5.56×10^{8}	$1s^2 \rightarrow 1s2p\ ^3P_1$
	21.88	3.33×10^{5}	$1s^2 \rightarrow 1s2p\ ^3P_2$
O VIII	18.99	2.16×10^{6}	$1s\ ^2S_{1/2} \rightarrow 2s\ ^2S_{1/2}$
	18.99	2.52×10^{12}	$1s\ ^2S_{1/2} \rightarrow 2p\ ^2P_{1/2}$
	18.99	1.26×10^{12}	$1s\ ^2S_{1/2} \rightarrow 2p\ ^2S_{3/2}$

Table 7.4: Strongest spectral lines from carbon, nitrogen, and oxygen in the synthetic spectrum. For each line the wavelength, the Einstein A-values and the transition identifications are given. The data are taken from the APED database.

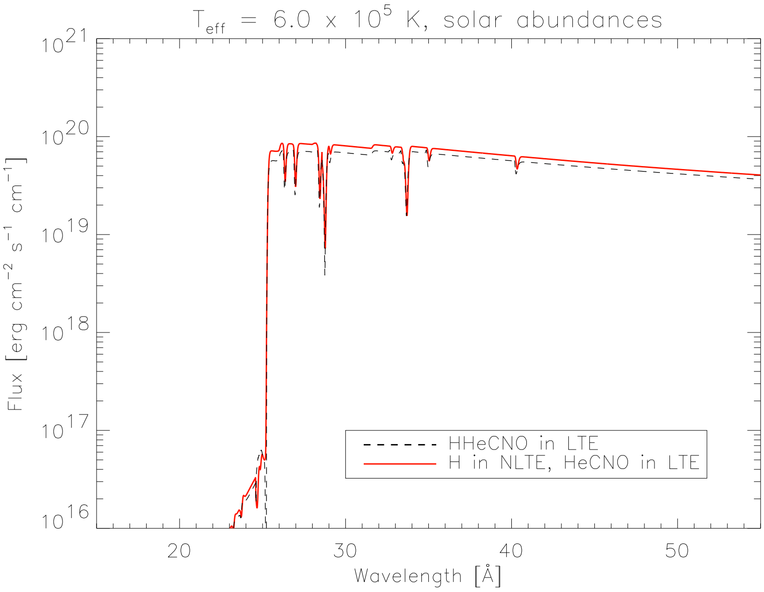

Figure 7.6: Spectra with solar abundances, comparing hydrogen calculated in LTE (dashed line) and treated in NLTE (solid line).

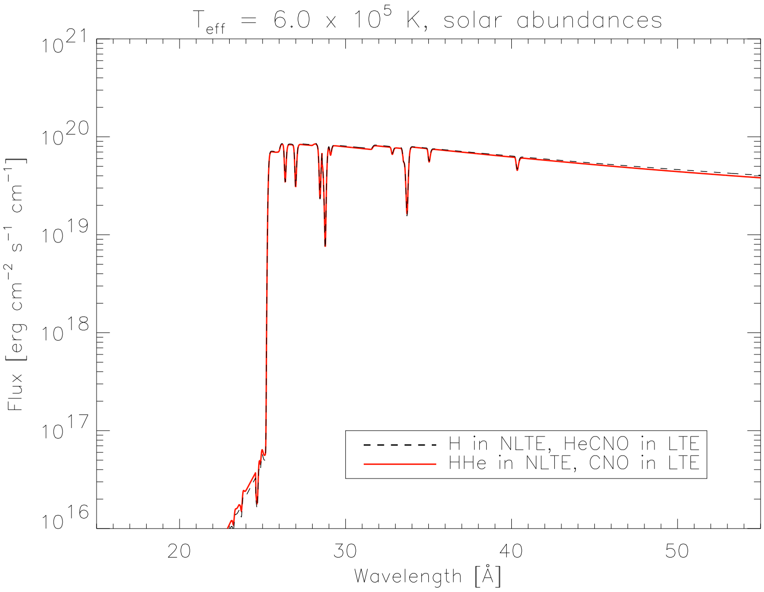

Figure 7.7: Spectra with solar abundances, comparing helium calculated in LTE (dashed line) and treated in NLTE (solid line).

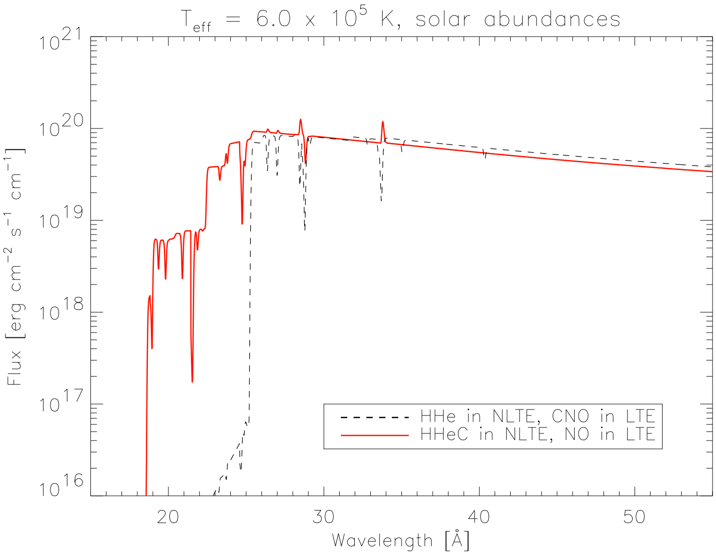

Figure 7.8: Spectra with solar abundances, comparing carbon calculated in LTE (dashed line) and treated in NLTE (solid line).

Stronger changes in the spectrum occur when carbon is treated in the NLTE calculations (figure 7.8). There arises continuum flux with strong absorption lines from N VI, N VII, O VII, and O VIII below $\lambda \sim 25$ Å. At higher wavelengths there are small changes in the continuum flux due to changes in the ionization balance of carbon. The change in the ionization balances of different elements will be examined in section 7.1.4 with the partial pressures (figures 7.39 to 7.42). The absorption lines from C VI at $\lambda \sim 26.3$ Å, $\lambda \sim 27.0$ Å, $\lambda \sim 28.5$ Å, and $\lambda \sim 33.8$ Å turn into emission lines. At $\lambda \sim 40.3$ Å the absorption line from C V disappears and at $\lambda \sim 28.8$ Å appears an absorption line from N VI which weakens in strength.

The continuum flux below $\lambda \sim 25$ Å increases further when N is treated in NLTE (figure 7.9). Between $\lambda \sim 18$ Å and $\lambda \sim 25$ Å are absorption lines from N V and N VI (at $\lambda \sim 19.4$ Å, $\lambda \sim 19.8$ Å, $\lambda \sim 20.9$ Å, $\lambda \sim 24.8$ Å, and $\lambda \sim 24.9$ Å), at $\lambda \sim 19.0$ Å is a line from O VIII, and at $\lambda \sim 18.7$ Å, $\lambda \sim 21.6$ Å, and $\lambda \sim 21.9$ Å are lines from O VII. The relative strength of the absorption lines from N V and N VI becomes relatively smaller but the O VII and O VIII lines stay same in relative strength. The absorption lines from N VI at $\lambda \sim 23.3$ Å and $\lambda \sim 28.8$ Å disappear and the emission line from C VI at $\lambda \sim 33.8$ Å increases in strength.

Treating oxygen in NLTE (figure 7.10) the continuum flux below $\lambda \sim 25$ Å increases even more and the spectral lines from oxygen weaken in relative line strength.

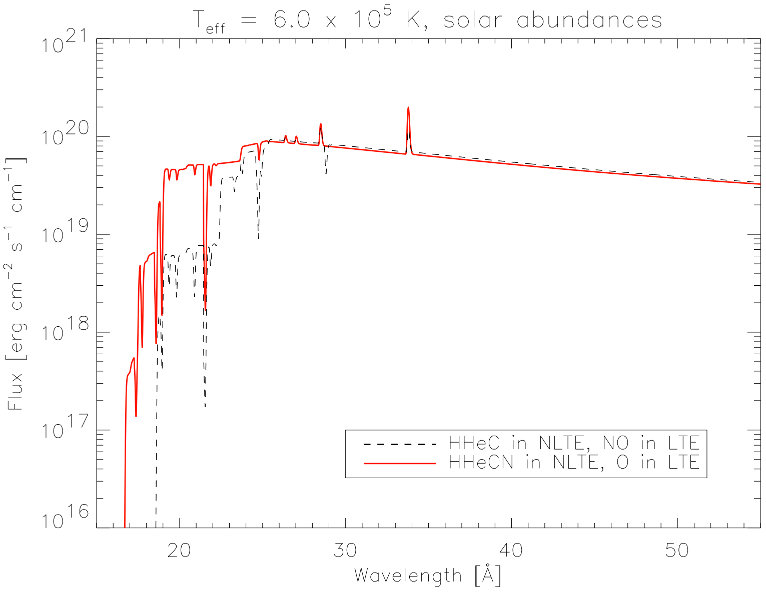

Figure 7.9: Spectra with solar abundances, comparing nitrogen calculated in LTE (dashed line) and treated in NLTE (solid line).

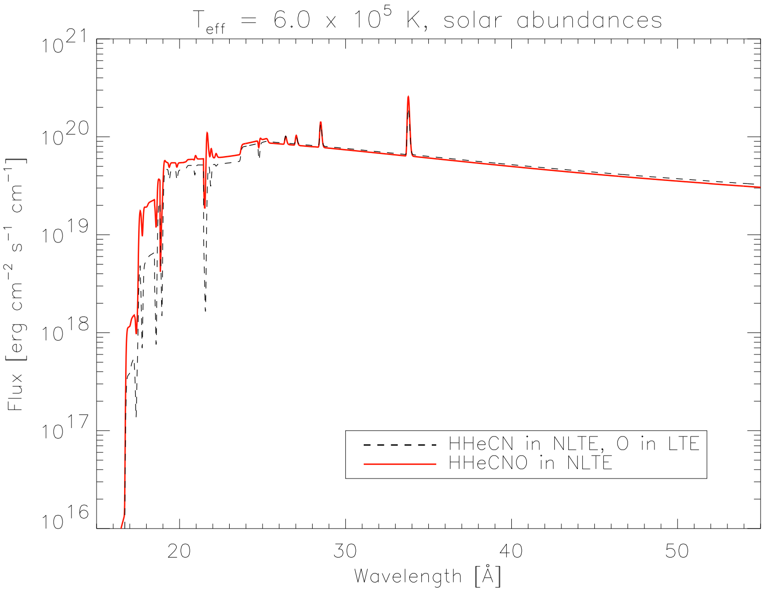

Figure 7.10: Spectra with solar abundances, comparing oxygen calculated in LTE (dashed line) and treated in NLTE (solid line).

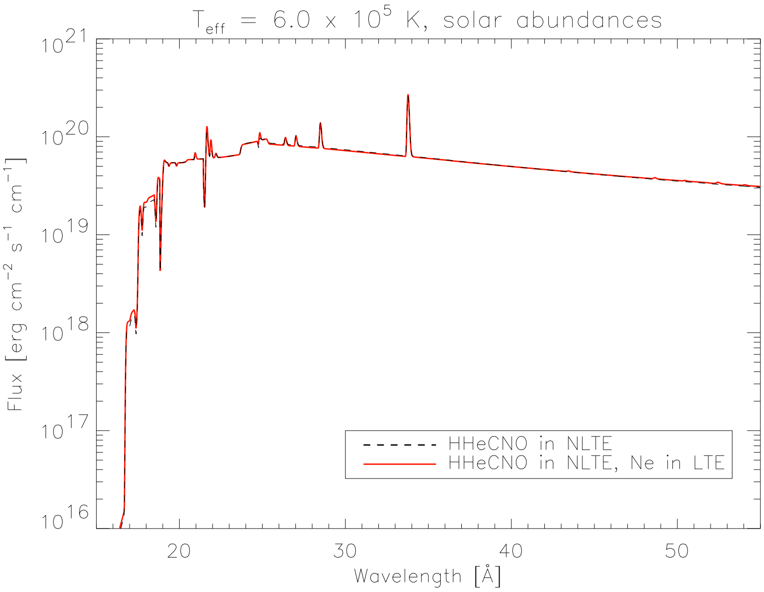

Figure 7.11: Spectra with solar abundances, comparing a spectrum calculated with neon in LTE (solid line) with a spectrum without neon (dashed line).

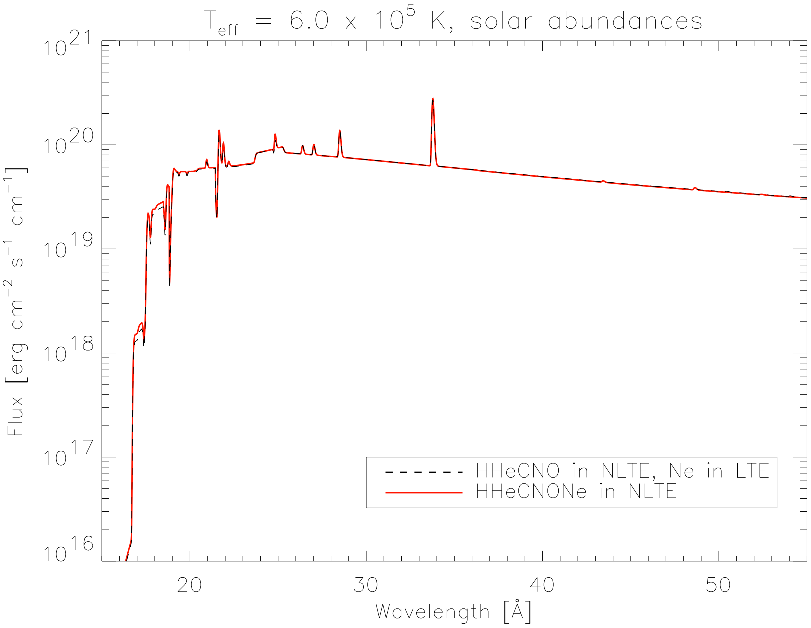

Figure 7.12: Spectra with solar abundances, comparing neon calculated in LTE (dashed line) and treated in NLTE (solid line).

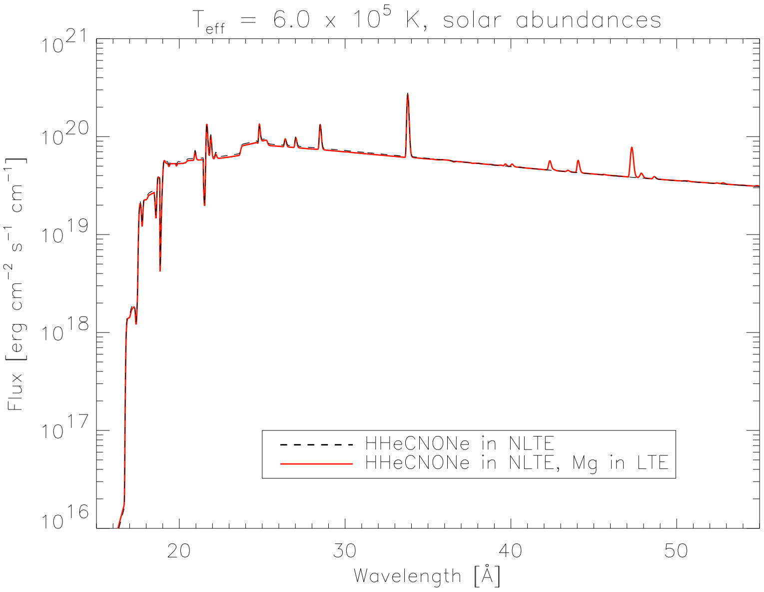

Figure 7.13: Spectra with solar abundances, comparing a spectrum calculated with magnesium in LTE (solid line) with a spectrum without magnesium (dashed line).

When neon is added in LTE to the model (figure 7.11) there is only a small change in the continuum flux between $\lambda \sim 17$ Å and $\lambda \sim 18$ Å and no neon lines appear. If neon is treated in NLTE (figure 7.12), the continuum flux between $\lambda \sim 17$ Å and $\lambda \sim 18$ Å increases again and lines from neon are still missing.

When magnesium is calculated in LTE, emission lines from the highest ionization stages of magnesium appear at wavelengths larger than $\lambda \sim 39$ Å (figure 7.13). These lines change to very weak absorption lines or disappear when magnesium is treated in NLTE (figure 7.14). In both cases there is no change in the continuum flux when magnesium is calculated in LTE and NLTE.

As in the case of magnesium, strong emission lines of aluminium at wavelengths larger $\lambda \sim 48$ Å appear when aluminium is added in LTE to the model (figure 7.15). Again as in the case of magnesium the lines are strongly weakened or disappear when aluminium is calculated in NLTE (figure 7.16).

Stronger changes appear when silicon is added to the model and calculated in LTE (figure 7.17). Due to strong silicon absorption the continuum flux decreases below $\lambda \sim 25$ Å. Between $\lambda \sim 30$ Å and $\lambda \sim 40$ Å strong emission lines and between $\lambda \sim 25.5$ Å and $\lambda \sim 33.5$ Å strong absorption lines from silicon appear. These effects are partially compensated when silicon is

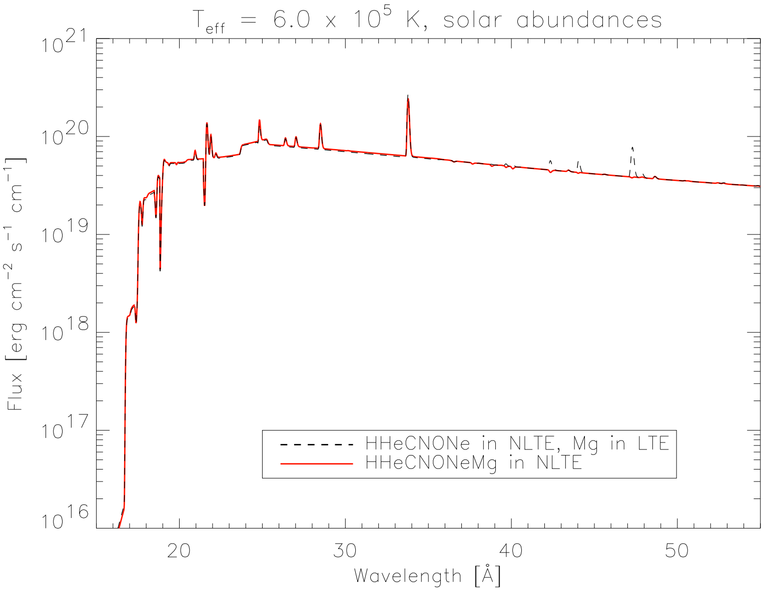

Figure 7.14: Spectra with solar abundances, comparing magnesium calculated in LTE (dashed line) and treated in NLTE (solid line).

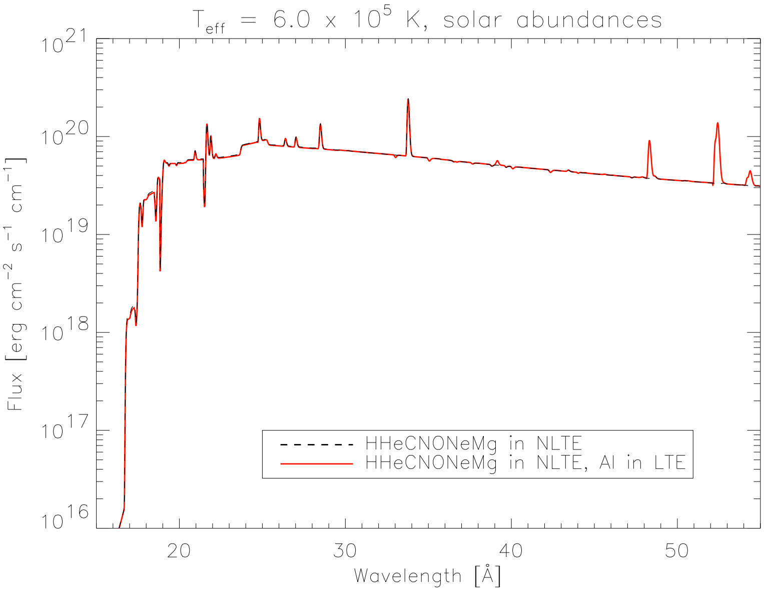

Figure 7.15: Spectra with solar abundances, comparing a spectrum calculated with aluminum in LTE (solid line) with a spectrum without aluminium (dashed line).

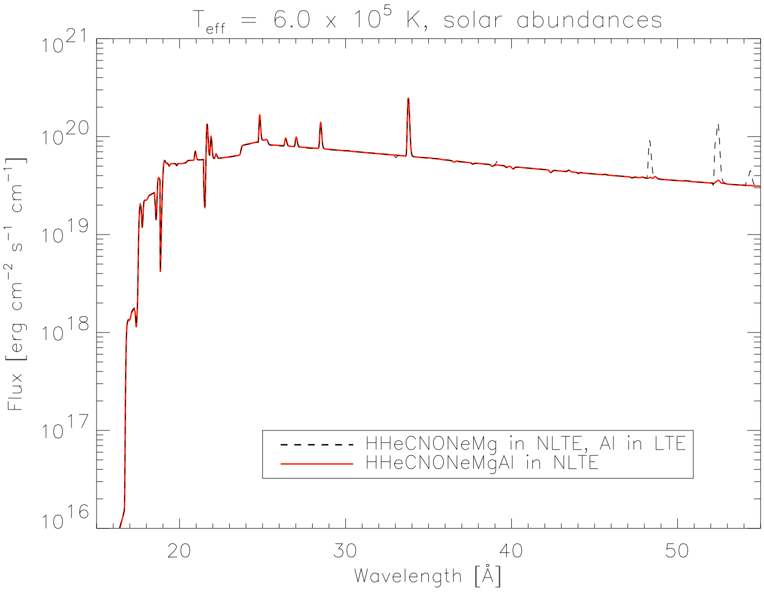

Figure 7.16: Spectra with solar abundances, comparing aluminium calculated in LTE (dashed line) and treated in NLTE (solid line).

treated in NLTE (figure 7.18). The continuum flux below $\lambda \sim 25$ Å increases again and the emission and absorption lines weaken or disappear.

When adding sulfur to the models the ions have to be treated in NLTE directly because the energy structure does not converge when calculating sulfur in LTE. This is due to the assumption of LTE which is just wrong. The continuum flux below $\lambda \sim 19$ Å increases. There are absorption lines from sulfur between $\lambda \sim 19$ Å and $\lambda \sim 33$ Å. At $\lambda \sim 20.7$ Å and $\lambda \sim 30.5$ Å emission lines from S XV and S XIV arise and around $\lambda \sim 33$ Å are multiple emission lines from S XIV. Above $\lambda \sim 48$ Å are very weak S-emission lines.

Including iron in the model has a very strong effect on the spectrum (figure 7.20) because there are several thousand iron lines in the plotted spectral range. Below $\lambda \sim 35$ Å there is a very strong decrease of the continuum flux and there are absorption lines from iron. At higher wavelength strong emission lines from iron appear, especially at $\lambda \gtrsim 46$ Å. The NLTE effects of iron on the spectrum are very strong (figure 7.21). When iron is treated in NLTE, the decrease in the continuum flux is partially compensated and the very strong emission lines are weakened. At $\lambda \sim 51$ Å the emission lines change to strong absorption lines.

From the discussion above it can be seen that the effects of carbon, nitrogen, oxygen, and iron on the spectrum are the largest, both in LTE and NLTE. Neon, magnesium, and aluminium affect the spectrum only slightly.

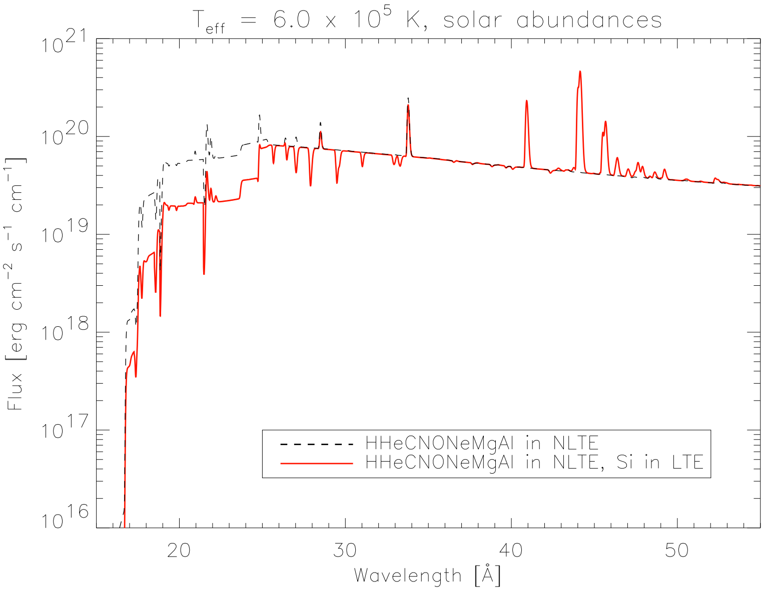

Figure 7.17: Spectra with solar abundances, comparing a spectrum calculated with silicon in LTE (solid line) with a spectrum without silicon (dashed line).

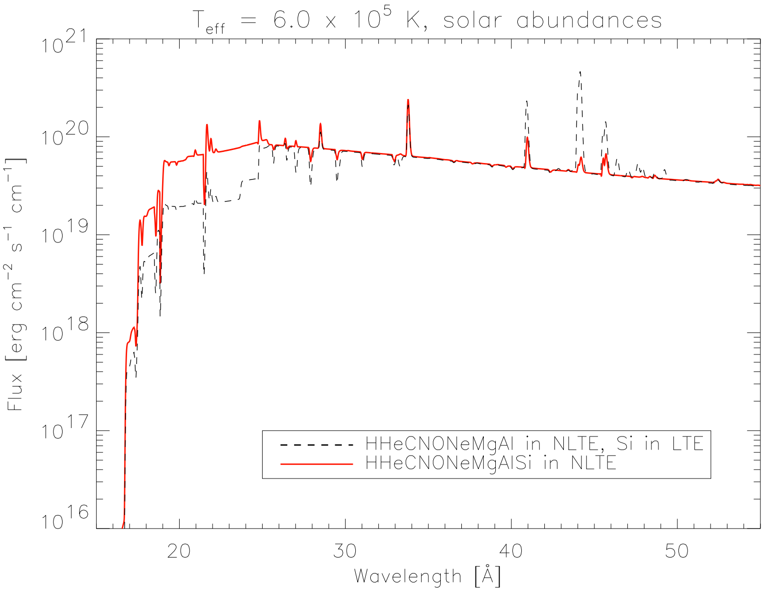

Figure 7.18: Spectra with solar abundances, comparing silicon calculated in LTE (dashed line) and treated in NLTE (solid line).

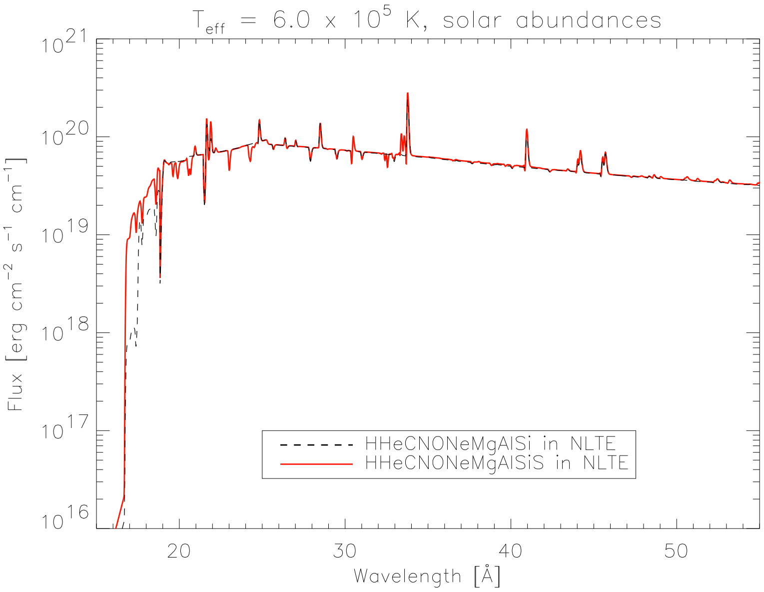

Figure 7.19: Spectra with solar abundances, calculated without sulfur (dashed line) and with sulfur (solid line).

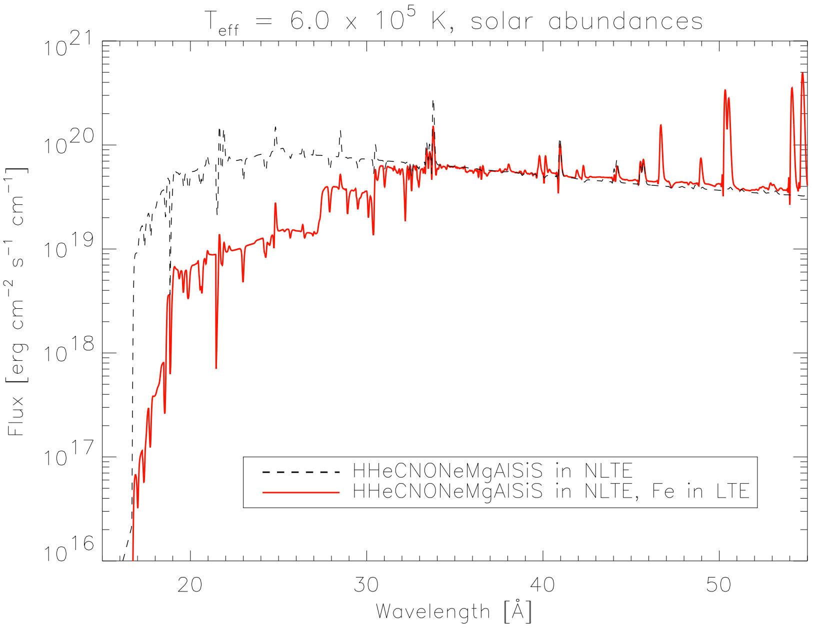

Figure 7.20: Spectra with solar abundances, comparing a spectrum calculated with iron in LTE (solid line) with a spectrum without iron (dashed line).

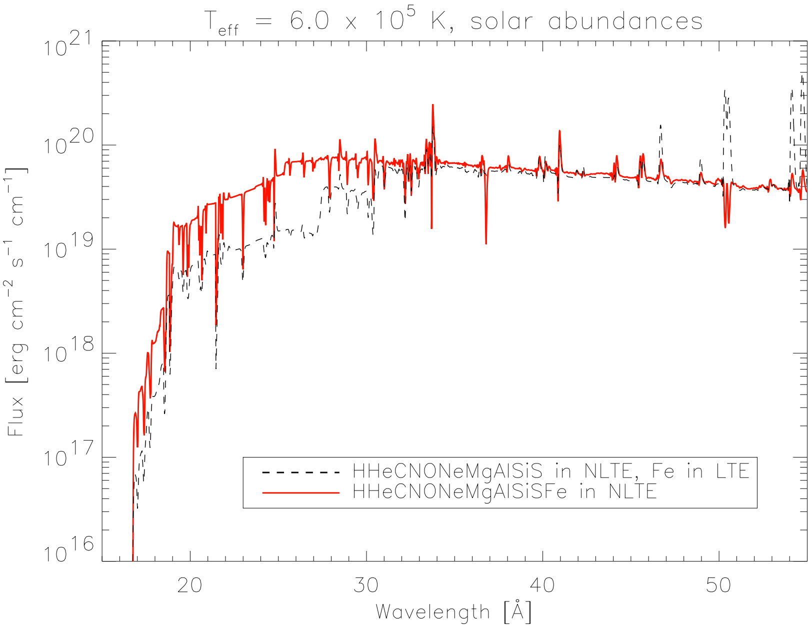

Figure 7.21: Spectra with solar abundances, comparing iron calculated in LTE (dashed line) and treated in NLTE (solid line).

The effects of silicon and sulfur are strong if these elements are calculated in LTE and they weaken in NLTE calculations but they are stronger than the effects of neon, magnesium, and aluminium and weaker than the effects of carbon, nitrogen, oxygen, and iron.

The NLTE effects change not only the relative line strengths but also the ionization balances. At small wavelengths (below $\lambda \sim 25$ Å) the effects are strongest. A similar result has been found for the previous nova model atmospheres in the UV and IR (see "NLTE effects" in section 5.2). The ionization edges which influence the synthetic spectra as strongest are below $\lambda = 25.3$ Å. A list of ionization edges between $\lambda = 18$ Å and $\lambda = 55$ Å is given in table 7.5. The largest effects are from the edges of C VI, N VI, N VII, and O VII. The ionization edge of O VIII lies at wavelengths where there is no flux in the observation. The effects of the edges of magnesium, aluminium, sulfur, and silicon are weak. Due to several thousand overlapping iron lines the effects of continuum and line absorption of iron cannot be distinguished and the strength of the effects of the iron edges on the continuum flux cannot be determined. As in the case of Fe II in the previous nova model atmospheres (see "line blanketing" in section 5.2), the lines of Fe XVII to Fe IXX form an "iron forest" and the effects of line blanketing on the spectrum are very large and have to be included into the calculations.

ion	λ_{edge} [Å]
C V	31.7
C VI	25.3
N VI	22.5
N VII	18.6
O VII	16.8
O VIII	14.2
Mg IX	37.8
Mg X	33.8
Al IX	37.6
Al X	31.1
Al XI	28.1
Si IX	35.3
Si X	30.9

ion	λ_{edge} [Å]
Si XI	26.1
Si XII	23.7
S IX	27.8
S X	24.6
S XI	22.0
S XII	19.0
S IX	17.5
Fe XII	37.5
Fe XIII	34.4
Fe XIV	31.6
Fe XV	27.2
Fe XVI	25.4

Table 7.5: Ionization edges which lie in the spectral range of the observed spectrum (Verner et al. 1996).

If spectral lines are calculated in NLTE, they weaken in relative line strength. In some cases, e. g., carbon and magnesium absorption lines can be changed to emission lines or vice versa due to NLTE effects.

7.1.3 Fits to the observations using solar abundances

In figure 7.22, a blackbody is fitted to the March observation of nova V4743 Sgr. The blackbody has a temperature of $T_{\text{bb}} = 7.0 \times 10^5\,\text{K}$ and can be fitted with $n_h = 5.0 \times 10^{21}\,\text{cm}^{-2}$. The fit to the observed continuum above $\lambda \sim 25\,\text{Å}$ is quite good. Below, the atmosphere is very nongray. This shows that more elaborated models than simple blackbodies have to be calculated to fit the observations.

The first fits with solar abundances to the observation of V4743 Sgr in March, 2003 were presented in Petz et al. (2005a). The models contain all ions of hydrogen, helium, carbon, nitrogen, and oxygen, and the ions Fe XXI - Fe XXVI. All other ions from table 7.3 were not included because at the stage of the first models convergence was not obtained when including more ions. The best fit can be seen in figure 7.23. The model atmosphere has an effective temperature of $T_{\text{eff}} = 5.8 \times 10^5\,\text{K}$. A hydrogen column density of $n_h = 4.0 \times 10^{21}\,\text{cm}^{-2}$ provides the best fit for the spectrum above $\lambda \sim 28\,\text{Å}$ which is influenced strongest by interstellar absorption.

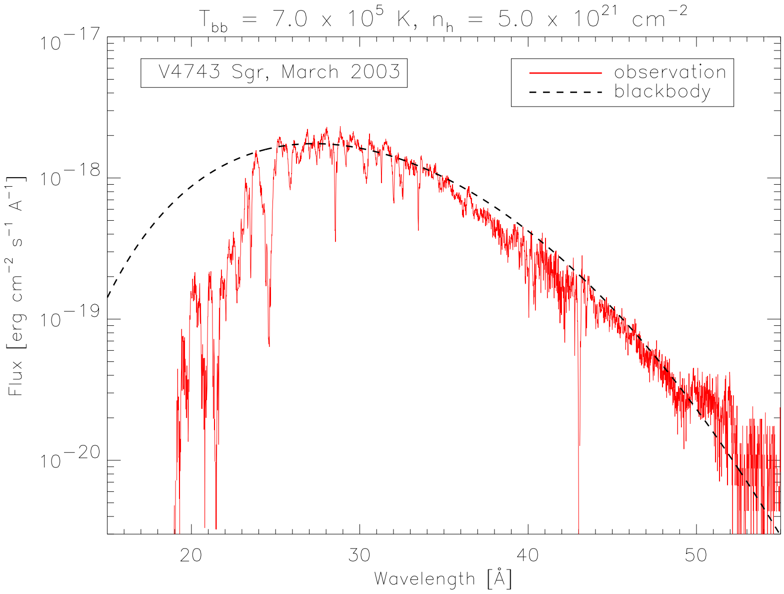

Figure 7.22: Fit of a blackbody spectrum (dashed lines) with a temperatures of $T_{\text{bb}} = 7.0 \times 10^5$ K for the March 2003 observation of nova V4743 Sgr (solid line). The used n_h is given in the plot.

There is a value from literature of $n_h = 1.41 \times 10^{21}\,\text{cm}^{-2}$ for V4743 Sgr given by Dickey & Lockman (1990). It is smaller than the hydrogen column density determined from the fit. The value from literature contains only the interstellar absorption. An additional circumstellar absorption can explain the discrepancy between the hydrogen column densities from literature and from the fits.

The fit seems to be good but close inspection of the observed spectrum reveals that some spectral lines are not reproduced well or are missing in the synthetic spectrum. Wrong line strengths could be due to the use of solar abundances in the model. Enhanced abundances of, e. g., the CNO elements, are generally observed in novae and predicted by the theory of the outburst (section 2.1.6). All absorption lines are too weak and there is too much emission around $\lambda \sim 24\,\text{Å}$ in the model. If the abundances are increased the absorption will be raised. This has been done in section 7.2.

The discrepancy of missing lines in the model which are present in the observations can also be explained because not all ions from table 7.3 have been included in the first models. After including all of these ions in the models, the fits with solar abundances are not improved. T_{eff} and the hydrogen column densities of the best fits do change because of strong changes in continuum and line opacities from the additional ions, especially due to

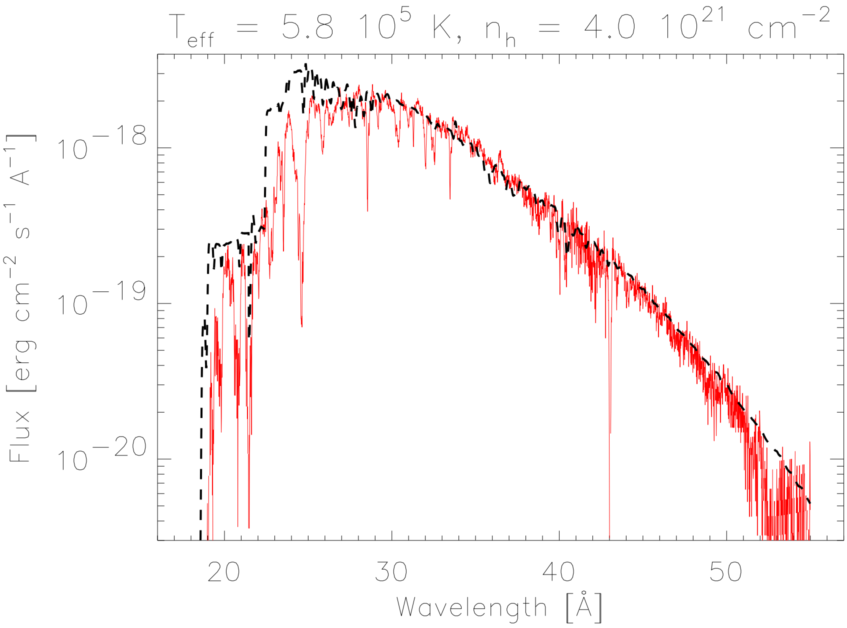

Figure 7.23: First fit with solar abundances for the March 2003 observation of nova V4743 Sgr (Petz et al. 2005a, figure 3). All ions of hydrogen, helium, carbon, nitrogen, and oxygen, and the ions Fe XXI - Fe XXVI were included in the models.

Fe XVII - Fe XX and silicon. The best fits are obtained with a spectrum of a model atmosphere with $T_{\rm eff} = 5.6 \times 10^5$ K and with $n_h = 4.2 \times 10^{21}$ cm^{-2} for the March, July, and September 2003 observations (figures 7.24 to 7.27). For the observation from February 2004 a spectrum of a model atmosphere with $T_{\rm eff} = 5.3 \times 10^5$ K and a $n_h = 4.0 \times 10^{21}$ cm^{-2} fits as best.

In order to compare fits of synthetic spectra with different $T_{\rm eff}$, they are plotted in figure 7.28 and 7.29 for model atmospheres with $T_{\rm eff} = 5.5 \times 10^5$ K, $T_{\rm eff} = 5.7 \times 10^5$ K, $T_{\rm eff} = 5.8 \times 10^5$ K, and $T_{\rm eff} = 6.0 \times 10^5$ K. The model spectra are always fitted to the March 2003 observations and comparing the fits in the figures 7.24 to 7.27 with the figures 7.28 and 7.29 reveals that the results are qualitatively the same for the other observations.

The possibility of fitting the first three observations with the same temperature is controversial to the theory that the temperature of the nova must change with time, obtained from the observations (section 3.2). Also the hydrogen column density has to decrease with time because the shell is expanding and the circumstellar material is thinning. The atmosphere of the fitted spectrum in the case of the observation from February 2004 is cooler and the n_h is lower but the fit is worse and not reliable.

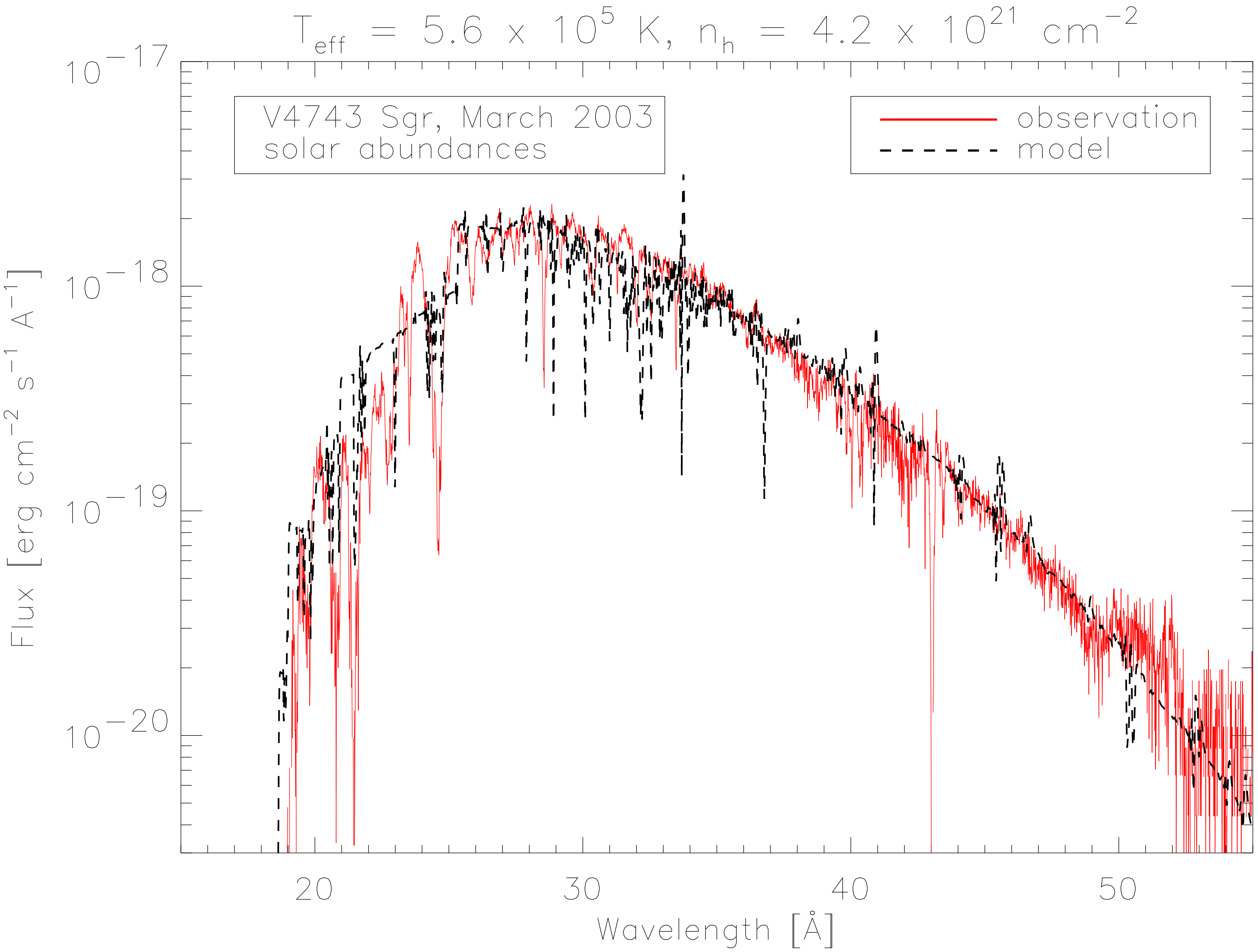

Figure 7.24: Fit of a model spectrum (dashed line) for the March 2003 observation of nova V4743 Sgr (solid line). The model atmosphere has $T_{\text{eff}} = 5.6 \times 10^5\,$K and from the fit $n_h = 4.2 \times 10^{21}\,\text{cm}^{-2}$ is obtained.

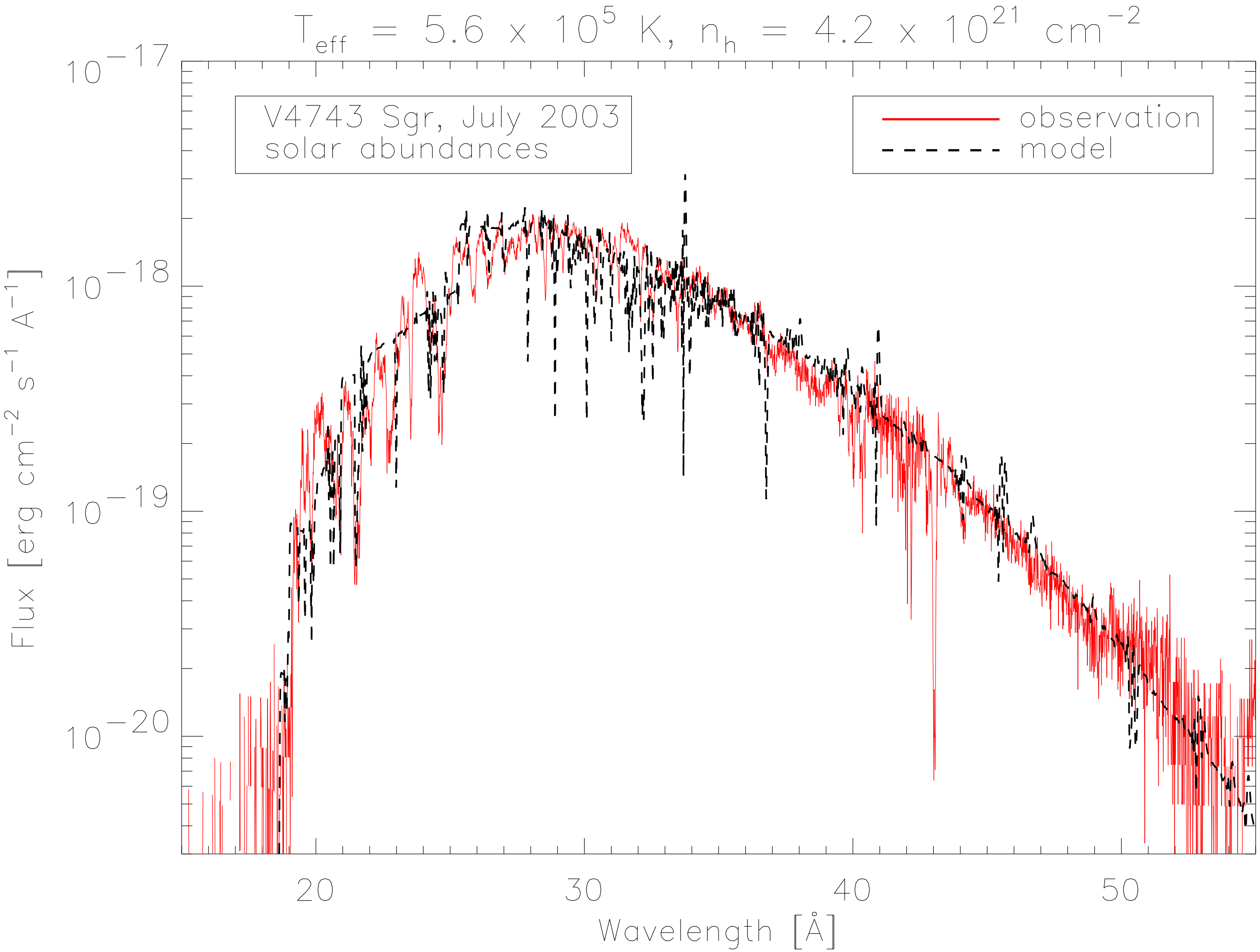

Figure 7.25: Fit of a model spectrum (dashed line) for the July 2003 observation of nova V4743 Sgr (solid line). The model atmosphere has $T_{\rm eff} = 5.6 \times 10^5$ K and from the fit $n_h = 4.2 \times 10^{21}$ cm^{-2} is obtained.

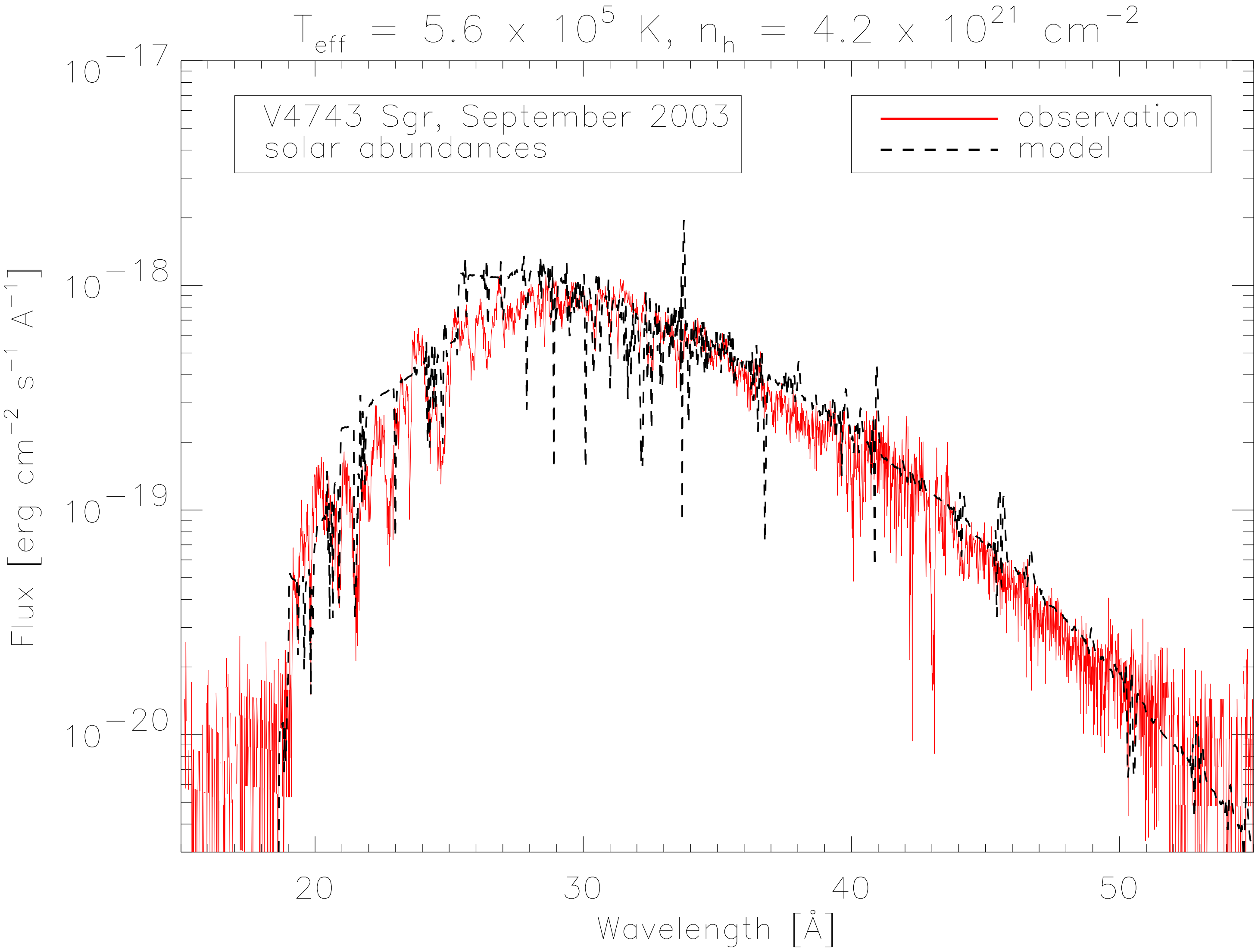

Figure 7.26: Fit of a model spectrum (dashed line) for the September 2003 observation of nova V4743 Sgr (solid line). The model atmosphere has $T_{\text{eff}} = 5.6 \times 10^5\,\text{K}$ and from the fit $n_h = 4.2 \times 10^{21}\,\text{cm}^{-2}$ is obtained.

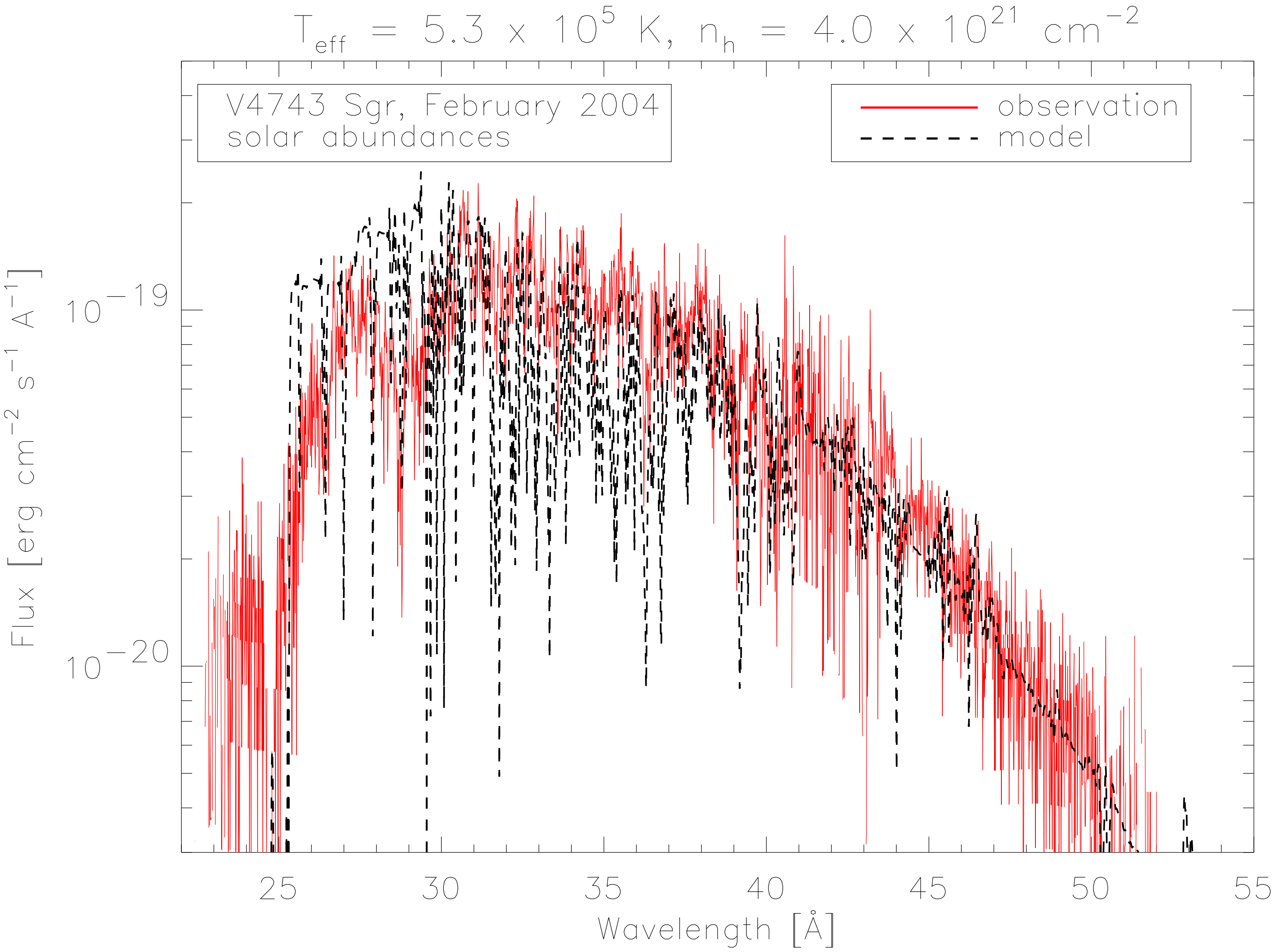

Figure 7.27: Fit of a model spectrum (dashed line) for the February 2004 observation of nova V4743 Sgr (solid line). The model atmosphere has $T_{\mathrm{eff}} = 5.3 \times 10^5\,\mathrm{K}$ and from the fit $n_h = 4.0 \times 10^{21}\,\mathrm{cm}^{-2}$ is obtained.

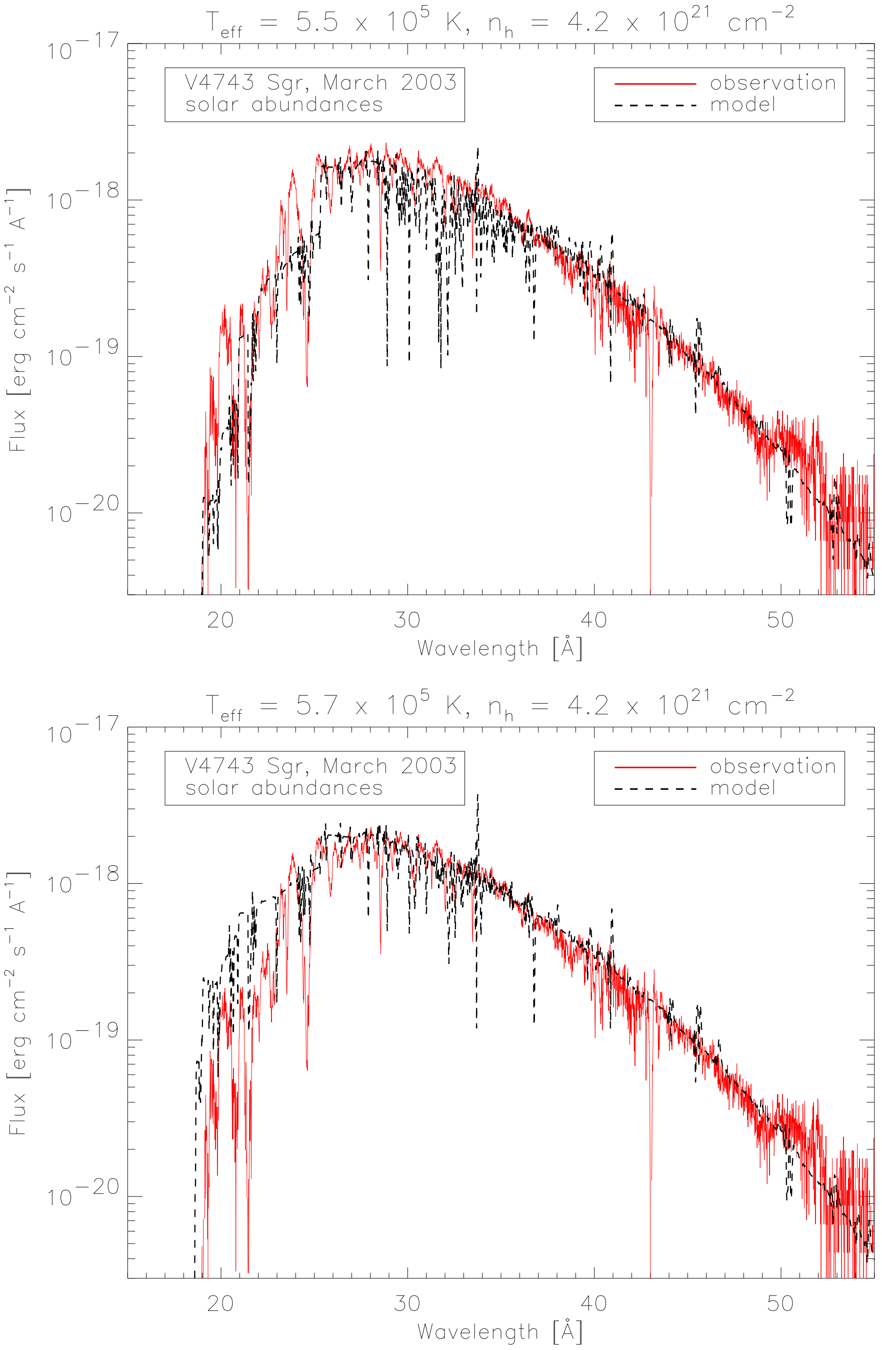

Figure 7.28: Fits of model spectra (dashed lines) with effective temperatures of $T_{\rm eff} = 5.5 \times 10^5$ K and $T_{\rm eff} = 5.7 \times 10^5$ K, and solar abundances for the March 2003 observation of nova V4743 Sgr (solid line).

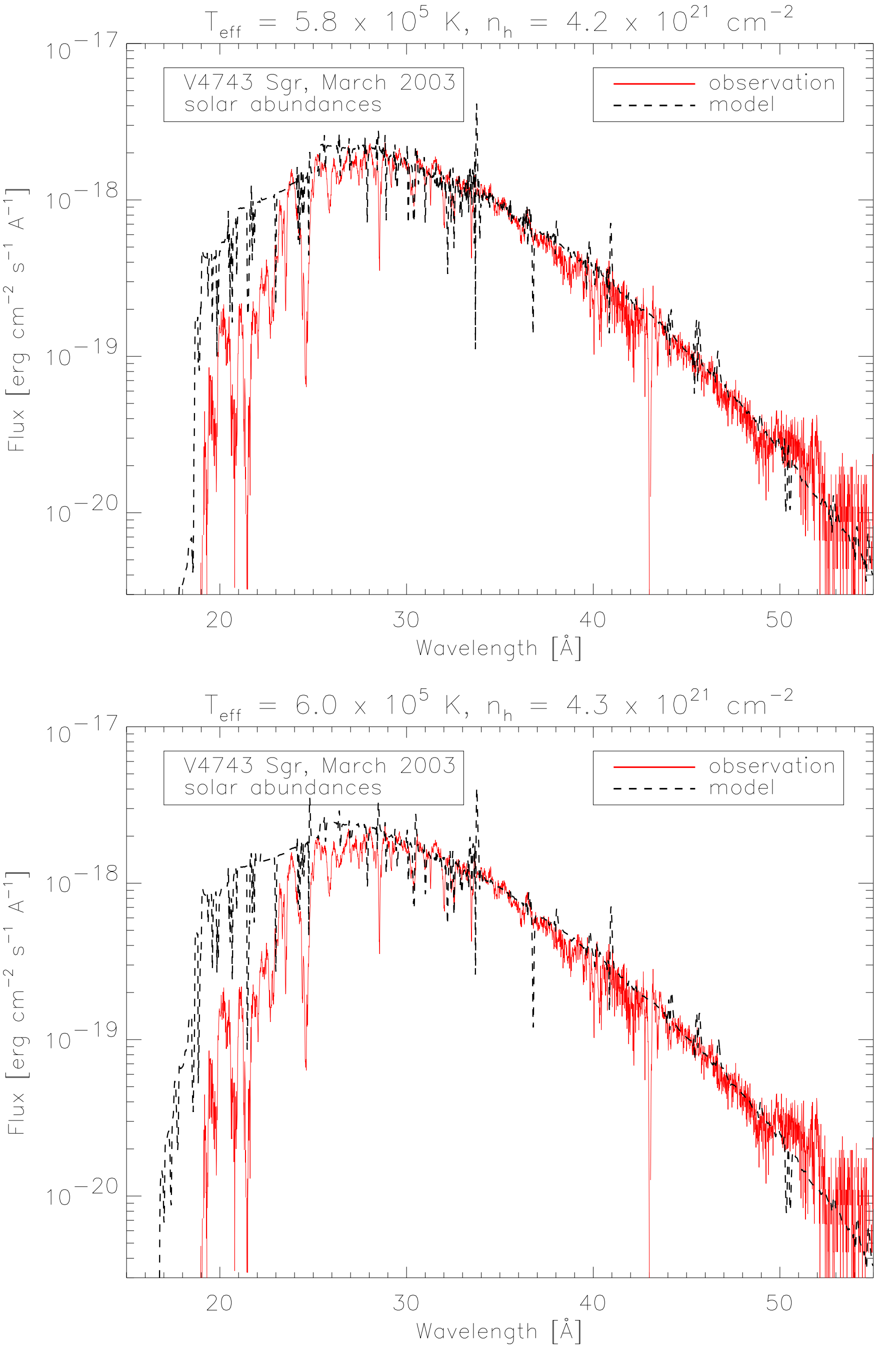

Figure 7.29: Fits of model spectra (dashed lines) with effective temperatures of $T_{\mathrm{eff}} = 5.8 \times 10^5\,\mathrm{K}$ and $T_{\mathrm{eff}} = 6.0 \times 10^5\,\mathrm{K}$, and solar abundances for the March 2003 observation of nova V4743 Sgr (solid line).

As in the first fits from Petz et al. (2005a), all spectral lines from carbon, nitrogen, and oxygen are too weak and the iron lines at $\lambda \gtrsim 27\,\text{Å}$ are too strong in the models. These iron lines are missing in the first models because the ionization stages below Fe XX were not included. Below $\lambda \sim 25\,\text{Å}$ the modeled continuum does not match the observations. At these wavelengths, there are ionization edges from carbon, nitrogen, and oxygen (table 7.5) which strongly contribute to the opacity and depend on the abundances.

Calculating models with non-solar abundances could solve these problems. From the discrepancies of the fits to the observations, the chemical abundances of carbon, nitrogen, and oxygen must be higher than the solar value and the abundance of iron has to be lower. Models with different sets of non-solar abundances have been computed and will be described in section 7.2.

7.1.4 Atmosphere structure

The following discussion is about a model atmosphere with an effective temperature of $T_{\text{eff}} = 6.0 \times 10^5\,\text{K}$. The results are qualitatively the same for other T_{eff} modeled and for non-solar abundances.

Temperature structure and geometrical extension

The change in the temperature structure when more species are added to the model was examined. In figure 7.30, the temperature is plotted against the radius R of the atmosphere ($R = 0\,\text{cm}$ is at the center of the WD) for models with hydrogen, helium, carbon, nitrogen, and oxygen in LTE (dashed line), with these elements treated in NLTE (dotted line), and for a complete NLTE model (solid line).

It can be seen that the atmosphere is geometrically very extended from $R_{\text{in}} \sim 3 \times 10^8\,\text{cm}$ to $R_{\text{out}} \sim 6 \times 10^{11}\,\text{cm}$ ($R_{\text{out}}/R_{\text{in}} = 2074$) and there is a large range of temperatures. For $R \lesssim 3 \times 10^9\,\text{cm}$ ($R/R_{\text{in}} \sim 10$) the temperature is dropping very steeply. In the rest of the atmosphere the temperature decrease is flat. For the complete NLTE model, the steep temperature decrease is in the order of one magnitude from $T \sim 6.8 \times 10^6\,\text{K}$ to $T \sim 5.8 \times 10^5\,\text{K}$ and the slow decreases is to $T \sim 2.4 \times 10^5\,\text{K}$.

An geometrically extended atmosphere with the same order of magnitude for $R_{\text{out}}/R_{\text{in}}$ was also found for the previous nova model atmospheres (see “Extension and energy budget” in section 5.2). Furthermore, like in previous nova model atmospheres, there is a large range of temperatures with the same run and there are multiple ionization stages for all elements simultaneously present in the nova shell (see “Temperature stratification” in section 5.2). In

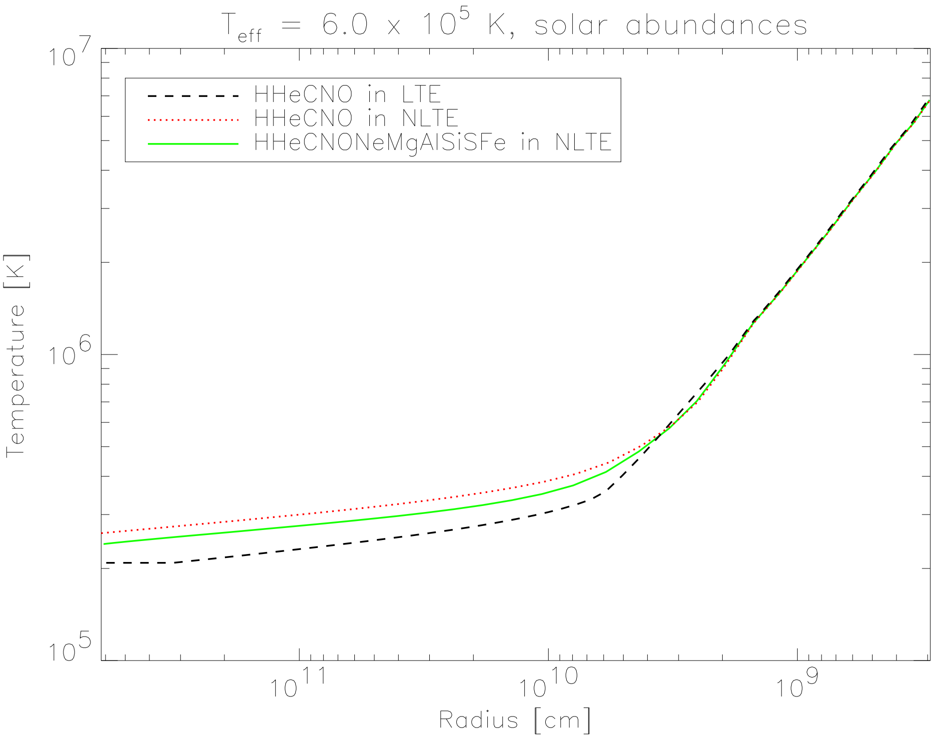

Figure 7.30: Temperature T of the atmosphere plotted against the radius R for different models: with the elements hydrogen, helium, carbon, nitrogen, and oxygen calculated in LTE (dashed line), with the same elements treated in NLTE (dotted line) and for a complete NLTE model (solid line).

this case these are the highest ionization stages (see below) because of the high temperatures of the model atmospheres.

If spectral lines are added to the models, there is no change in the temperature in the inner part of the atmosphere within $R \lesssim 10^9$ cm (figure 7.30). In the outer part (for $R \gtrsim 4 \times 10^9$ cm) the atmosphere is hotter by about 25% if hydrogen, helium, carbon, nitrogen, and oxygen are treated in the NLTE calculations (dotted line). Adding more elements to the model, the atmosphere cools again (solid line). Between $R \sim 1 \times 10^9$ cm and $R \sim 2 \times 10^9$ cm the atmosphere is only slightly cooler when the species are treated in NLTE and when higher Z species than oxygen are added to the model. As for the previous nova model atmospheres, the NLTE effects on the temperature structure are relatively small, particularly in the line and continuum forming region.

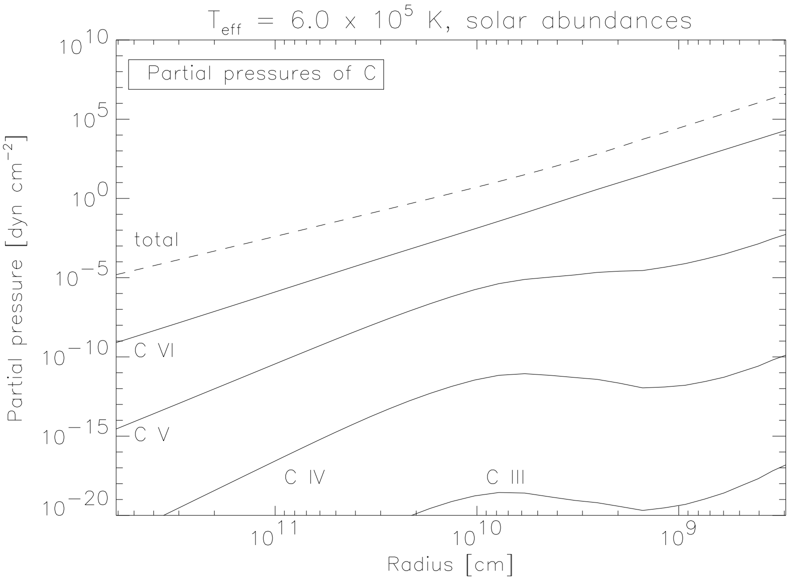

Figure 7.31: Partial pressures of C III to C VI (solid lines) and total partial pressure of C I to C VII (dashed line) plotted against the radius R of the atmosphere for a model atmosphere with $T_{\text{eff}} = 6.0 \times 10^5\,\text{K}$.

Partial pressures

In order to see that the highest ionization stages of an element are present in the atmosphere, the partial pressures of different elements are plotted against the radius R of the atmosphere in the figures 7.3 and 7.31 to 7.38.

For carbon and nitrogen the partial pressures are decreasing in all layers of the atmosphere with decreasing ionization stages (figures 7.31 and 7.32). If the total partial pressure of these elements (dashed line) is compared with the partial pressures of the ions, it can be seen that most of carbon and nitrogen is completely ionized to C VII and N VIII.

Most of the oxygen is only completely ionized in the inner part of the atmosphere within $R \lesssim 3 \times 10^9\,\text{cm}$ (figure 7.3). In the rest of the atmosphere, O VII and O VIII have partial pressures of approximately the same order of magnitude compared to the total partial pressure of oxygen (dashed line). The lower ionization stages behave like the ionization stages of carbon and nitrogen.

For neon, magnesium, aluminium, silicon, and sulfur, the ionization stage with one electron in the atomic shell is only abundant in the inner part of the atmosphere within $R \lesssim 2 \times 10^9\,\text{cm}$ (figure 7.33 to 7.37). In the rest of the atmosphere, the next lower ionization stage, and in the case of sulfur the

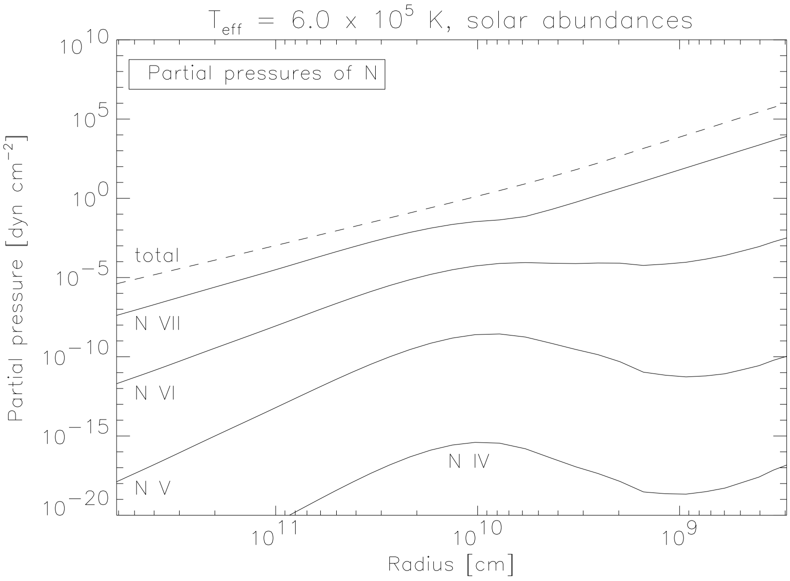

Figure 7.32: Partial pressures of N IV to N VII (solid lines) and total partial pressure of N I to N VIII (dashed line) plotted against the radius R of the atmosphere for a model atmosphere with $T_{\mathrm{eff}} = 6.0 \times 10^5\,\mathrm{K}$.

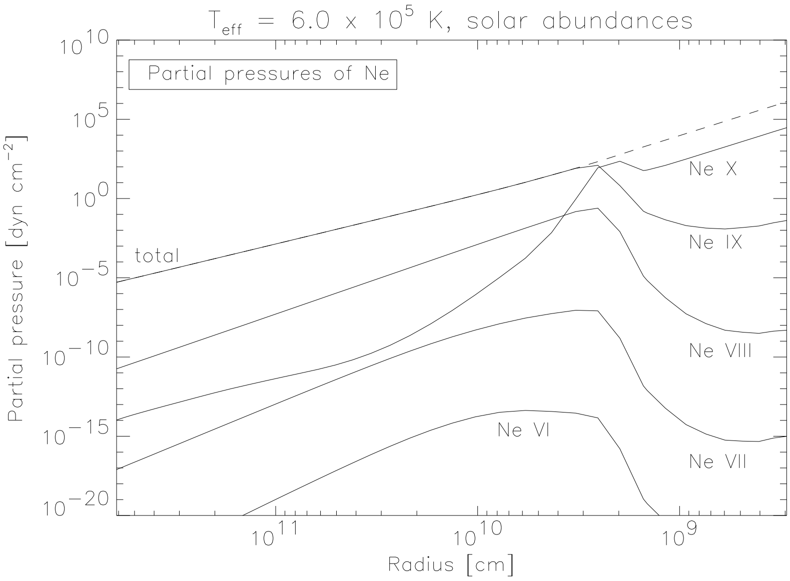

Figure 7.33: Partial pressures of Ne VI to Ne X (solid lines) and total partial pressure of Ne I to Ne XI (dashed line) plotted against the radius R of the atmosphere for a model atmosphere with $T_{\mathrm{eff}} = 6.0 \times 10^5\,\mathrm{K}$.

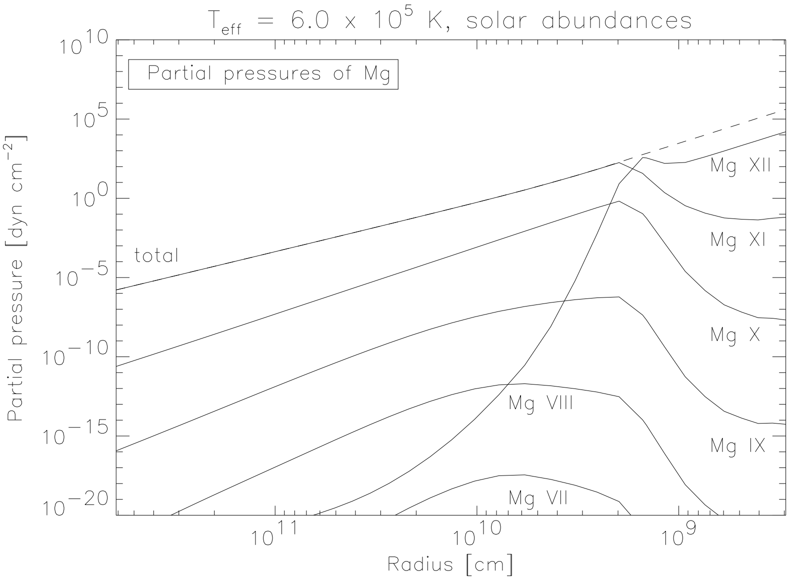

Figure 7.34: Partial pressures of Mg VII to Mg XII (solid lines) and total partial pressure of Mg I to Mg XIII (dashed line) plotted against the radius R of the atmosphere for a model atmosphere with $T_{\text{eff}} = 6.0 \times 10^5\,\text{K}$.

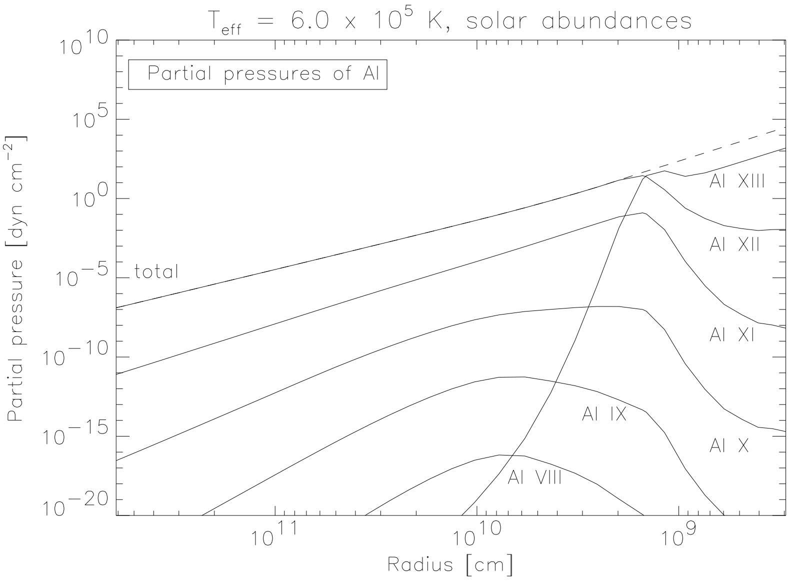

Figure 7.35: Partial pressures of Al VIII to Al XIII (solid lines) and total partial pressure of Al I to Al XIV (dashed line) plotted against the radius R of the atmosphere for a model atmosphere with $T_{\text{eff}} = 6.0 \times 10^5\,\text{K}$.

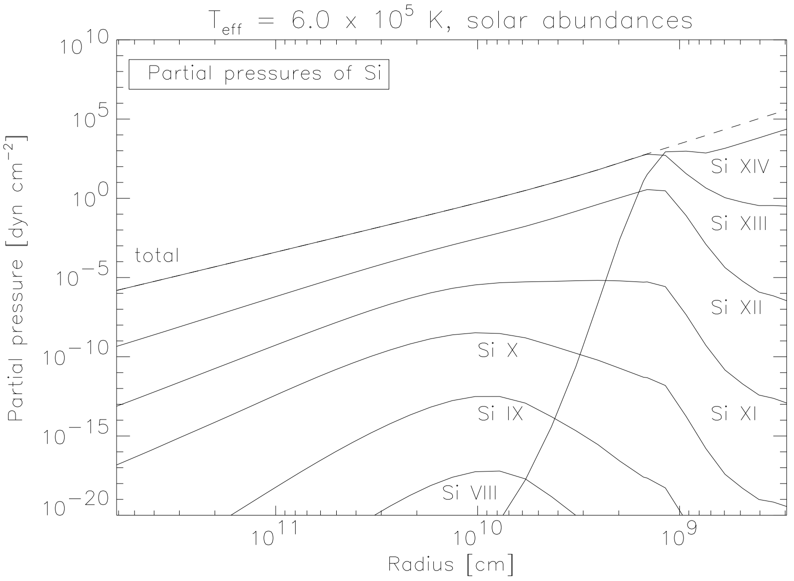

Figure 7.36: Partial pressures of Si VIII to Si XIV (solid lines) and total partial pressure of Si I to Si XV (dashed line) plotted against the radius R of the atmosphere for a model atmosphere with $T_{\text{eff}} = 6.0 \times 10^5\,$K.

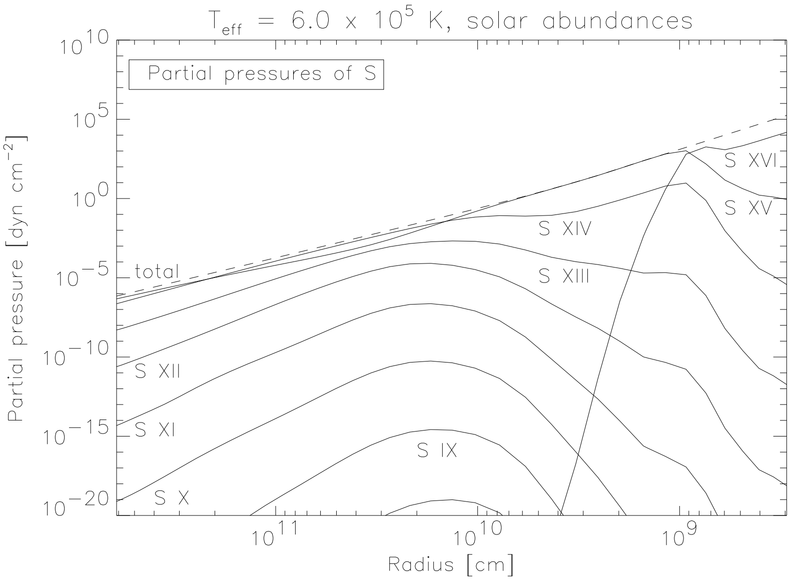

Figure 7.37: Partial pressures of S VIII to S XVI (solid lines) and total partial pressure of S I to S XVII (dashed line) plotted against the radius R of the atmosphere for a model atmosphere with $T_{\text{eff}} = 6.0 \times 10^5\,$K.

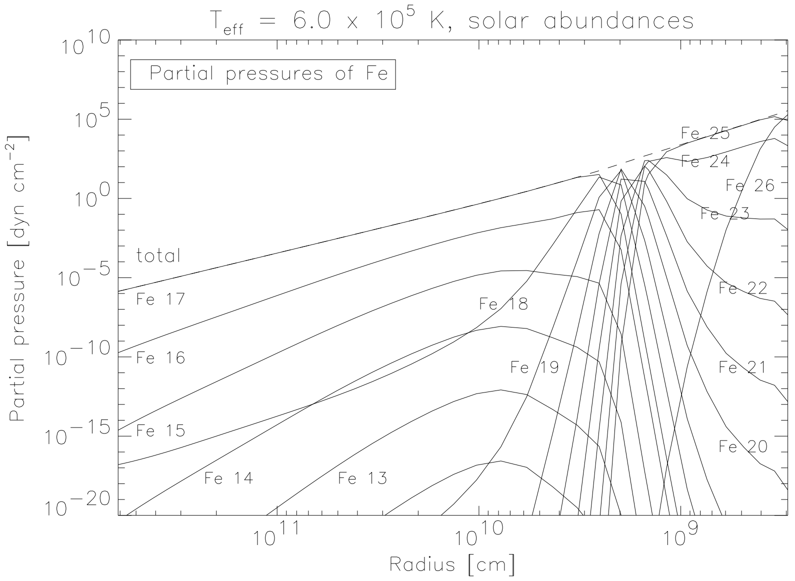

Figure 7.38: Partial pressures of Fe XII to Fe XXVI (solid lines) and total partial pressure of Fe I to Fe XXVII (dashed line) plotted against the radius R of the atmosphere for a model atmosphere with $T_{\text{eff}} = 6.0 \times 10^5\,\text{K}$.

succeeding two lower ionization stages, constitutes approximately the total partial pressure of the given element. Again, the lower ionization stages behave like the ionization stages of carbon and nitrogen.

For iron there are more ionization stages which are only important in the inner part of the atmosphere (figure 7.38). Fe XVII is the highest ionization stage which is significant in the outer part and it is approximately the total partial pressure of iron (dashed line).

One of the NLTE effects is the change of the ionization balances due to under- and overionization (section 7.1.2). This can be shown with the partial pressures. As an example, the case of carbon is plotted in figure 7.39. The dotted lines are the partial pressures of C III to C VI calculated in LTE and the solid lines are the partial pressures of C III to C VI in a model atmosphere where C IV to C VI are treated in NLTE (C III is always calculated in LTE). In the inner part of the atmosphere within $R \lesssim 1.5 \times 10^9\,\text{cm}$, the partial pressures of the ionization stages of carbon are not influenced by NLTE. At larger radii the partial pressures of all ionization stages are lower if the ions are treated in NLTE. The ions become overionized by NLTE effects. The total partial pressure of C I to C VII (dashed line) is the same for LTE and NLTE because NLTE does not change the total amount of carbon in the atmosphere.

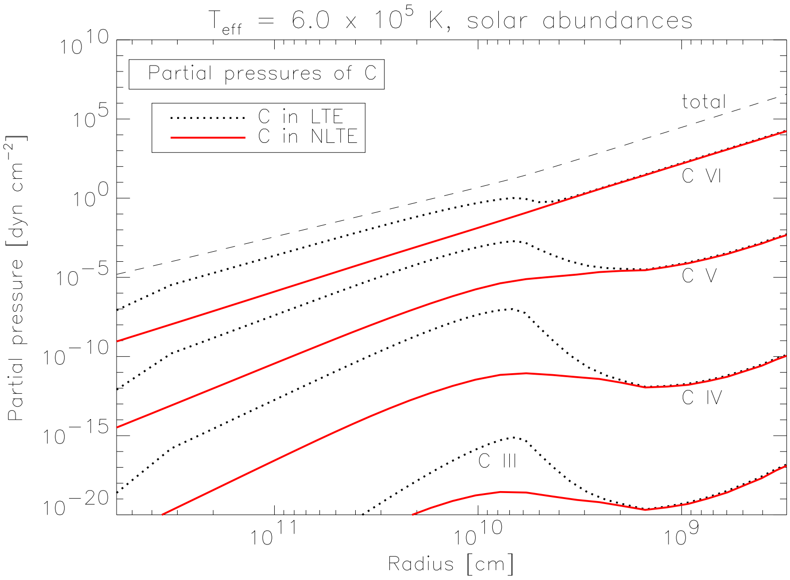

Figure 7.39: Partial pressures of C III to C VI calculated in LTE (dotted lines) and in NLTE (solid lines). The total partial pressure of C I to C VII (dashed line) is the same for LTE and NLTE.

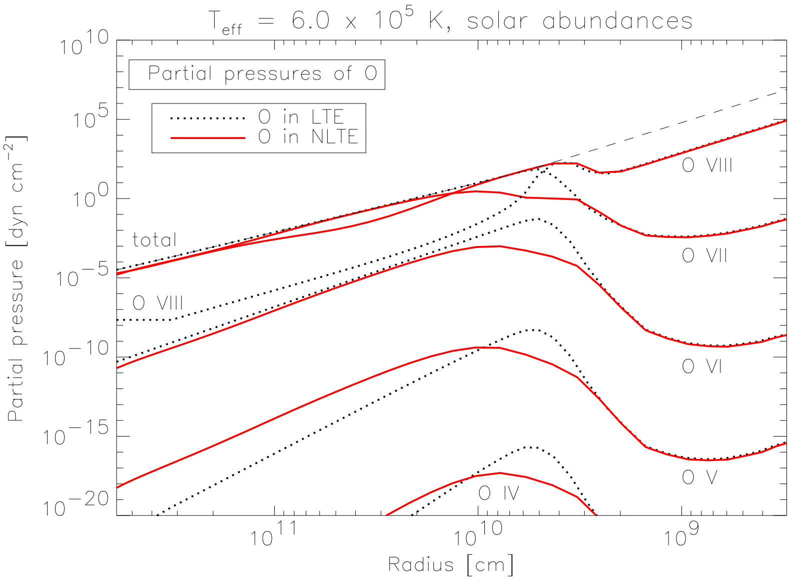

Figure 7.40: Partial pressures of O IV to O VIII calculated in LTE (dotted lines) and in NLTE (solid lines). The total partial pressure of O I to O IX (dashed line) is the same for LTE and NLTE.

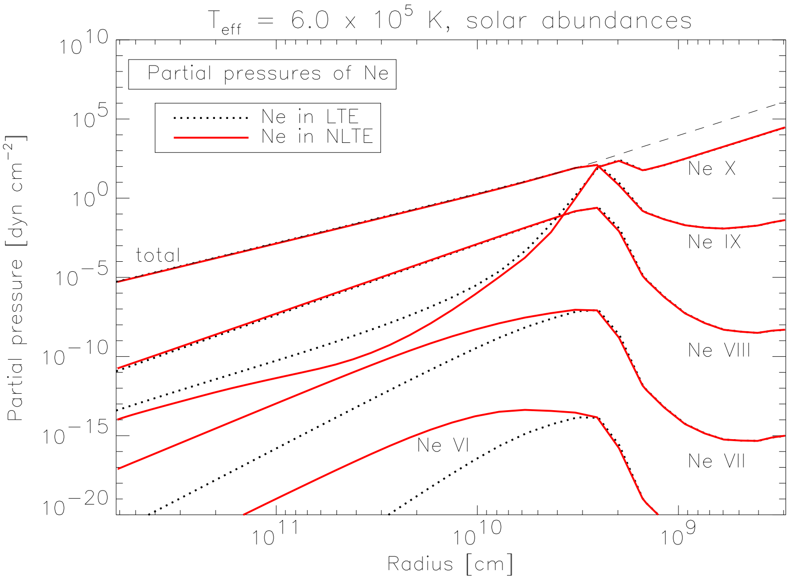

Figure 7.41: Partial pressures of Ne VI to Ne X calculated in LTE (dotted lines) and in NLTE (solid lines). The total partial pressure of Ne I to Ne XI (dashed line) is the same for LTE and NLTE.

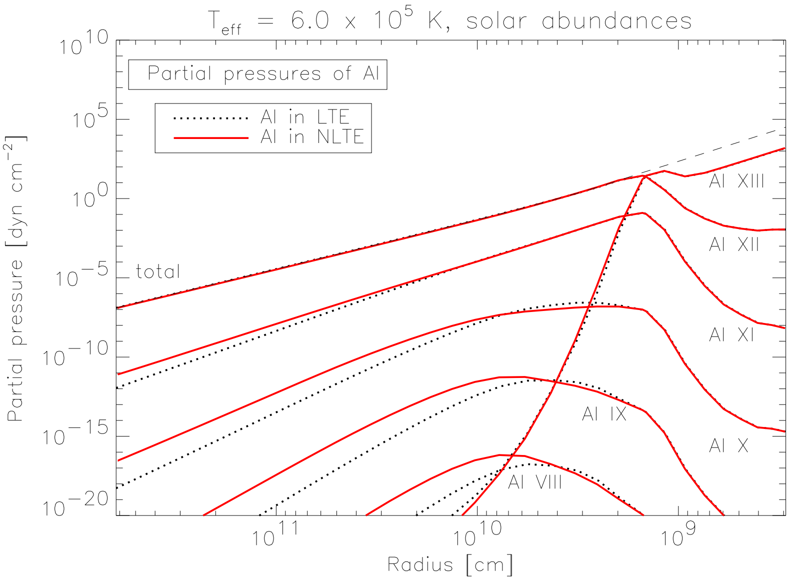

Figure 7.42: Partial pressures of Al VIII to Al XIII calculated in LTE (dotted lines) and in NLTE (solid lines). The total partial pressure of Al I to Al XIV (dashed line) is the same for LTE and NLTE.

The partial pressures of the ionization stages of oxygen show a different behavior (figure 7.40). O VII becomes overionized by NLTE effects in the outer part of the atmosphere and O VII becomes underionized. If the atmosphere is followed from the inner to the outer part, the ions O IV, O V, and O VII are not affected at first, then they are overionized, and finally underionized.

In figure 7.41 and 7.42 the behavior in LTE vs. NLTE of the partial pressures of neon and aluminium is compared. There are only small differences, particular for Ne X in the inner part and for Ne IX, Al XII, and Al XIII which are most important species in the atmosphere. This fact can explain why the NLTE effects of neon and aluminium on the spectrum are so small (section 7.1.2).

Density distribution

The gas density is plotted against the radius of the atmosphere in figure 7.43, upper panel, and against the temperature in figure 7.43, lower panel, for a model atmosphere with $T_{\text{eff}} = 6.0 \times 10^5\,\text{K}$. The density decreases from $\rho \sim 2.7 \times 10^{19}\,\text{cm}^{-3}$ in the inner part of the atmosphere to $\rho \sim 3.0 \times 10^9\,\text{cm}^{-3}$ in the outer part. The decrease in the inner part is very steep. The density is fallen to $\rho \sim 2.5 \times 10^{13}\,\text{cm}^{-3}$ at $R \sim 3 \times 10^{10}\,\text{cm}$ or $R/R_{\text{in}} \sim 100$ (compare with $R_{\text{out}}/R_{\text{in}} = 2074$). The density is relatively large at high temperatures (figure 7.43, lower panel) because the temperature falls also very steep in the inner part of the atmosphere (figure 7.30).

As for the previous nova model atmospheres (see "Density distribution" in section 5.2), the density is very low in the outer part of the atmosphere. Therefore, the radiative rates dominate the collision rates (figure 7.68) and departures from LTE in the line and continuum forming region are large. The effects of the departures from LTE on the spectrum has been shown in section 7.1.2 and the strength of the NLTE effects can be shown with the departure coefficients.

NLTE departure coefficients

The NLTE departure coefficients b_i of all levels and ionization stages in the elements of table 7.3 are plotted over the radius R for a model atmosphere with $T_{\text{eff}} = 6.0 \times 10^5\,\text{K}$ of the atmosphere in the figures 7.44 to 7.54. As expected, the departure coefficients are equal to unity in the inner part of the atmosphere within $R \lesssim 10^9\,\text{cm}$ and they increase in the outer part. For all elements there are very large and very small departure coefficients in respect to unity, from $b_i \sim 10^5$ to $b_i \sim 10^{-13}$. They are larger for atmospheres with

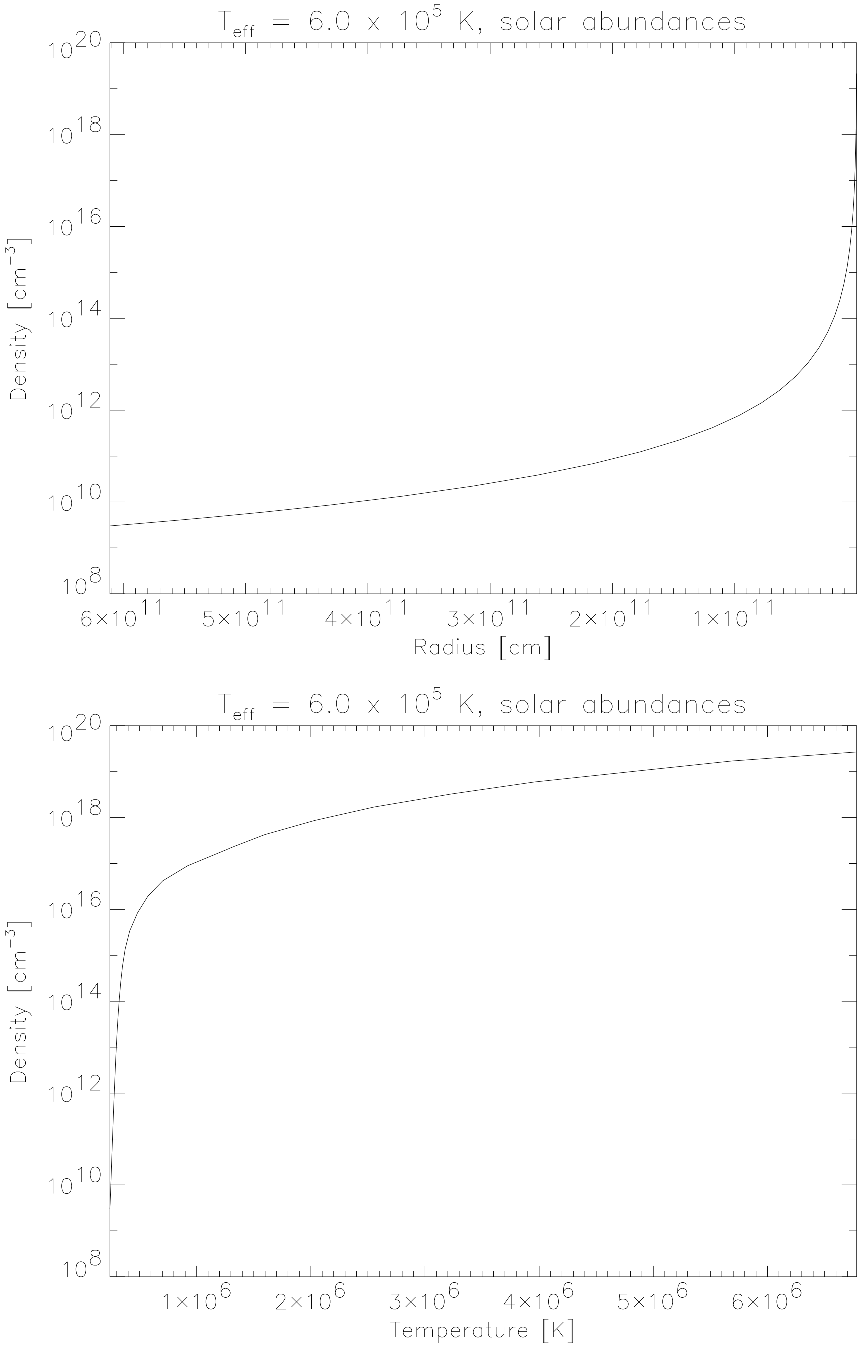

Figure 7.43: Gas density plotted against the radius of the atmosphere (upper panel) and against the temperature (lower panel).

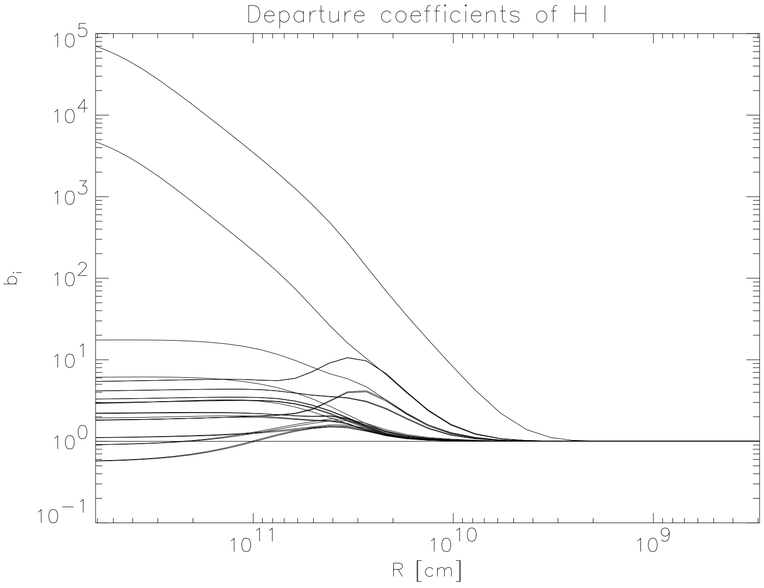

Figure 7.44: Departure coefficients b_i of all levels of H I plotted against the radius R of the atmosphere.

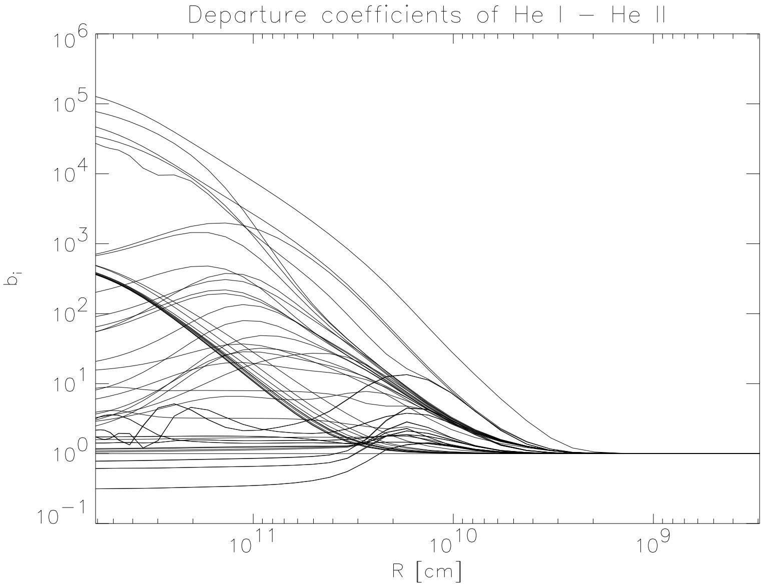

Figure 7.45: Departure coefficients b_i of all levels of He I and He II plotted against the radius R of the atmosphere.

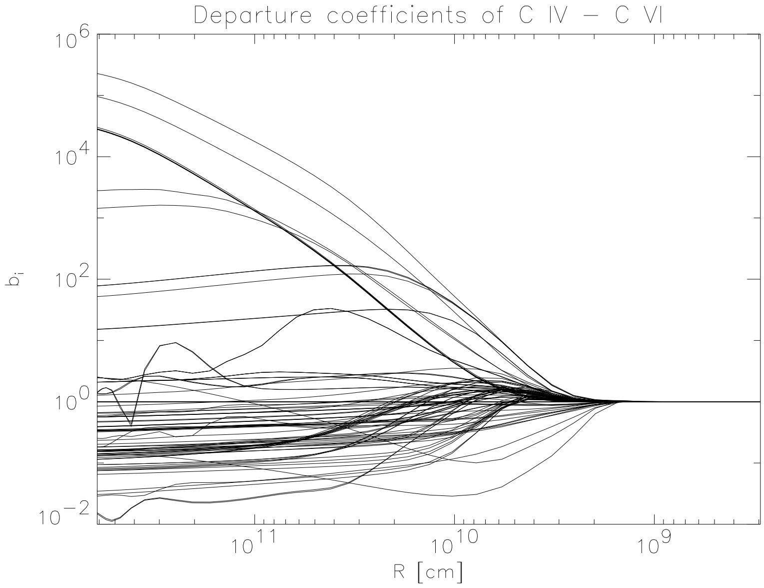

Figure 7.46: Departure coefficients b_i of all levels of C IV to C VI plotted against the radius R of the atmosphere.

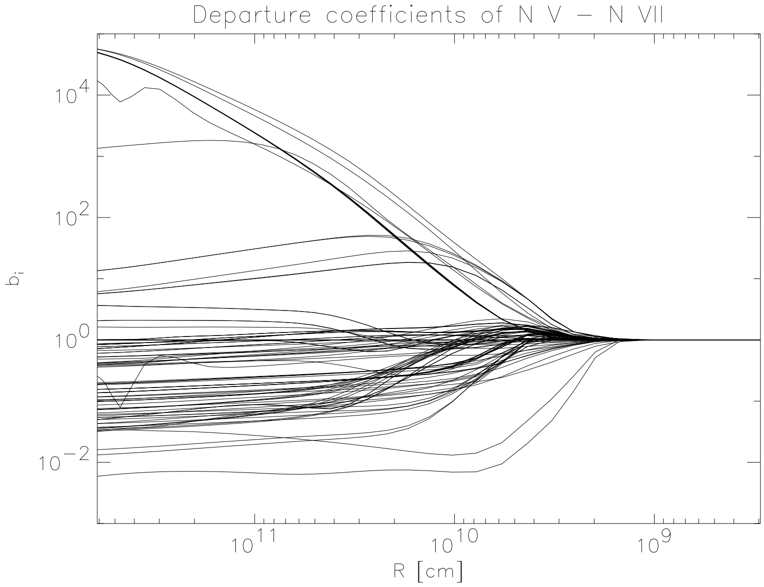

Figure 7.47: Departure coefficients b_i of all levels of N V to N VII plotted against the radius R of the atmosphere.

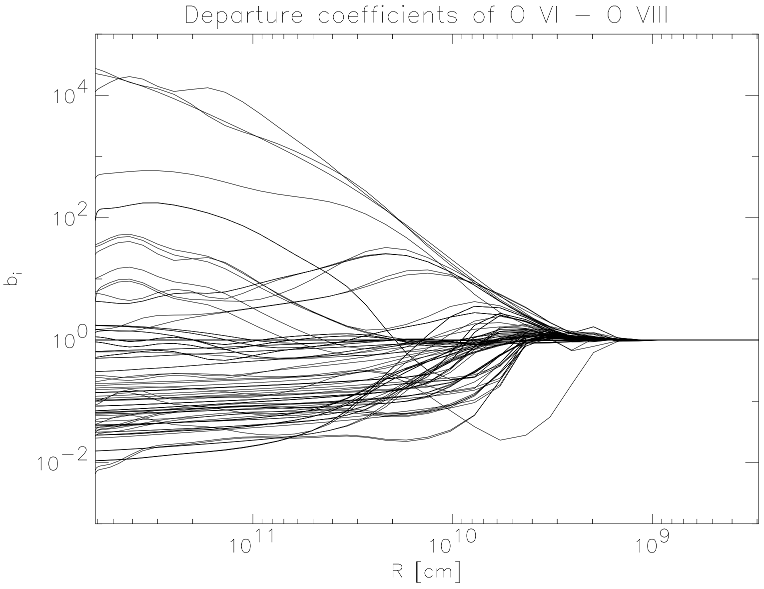

Figure 7.48: Departure coefficients b_i of all levels of O VI to O VIII plotted against the radius R of the atmosphere.

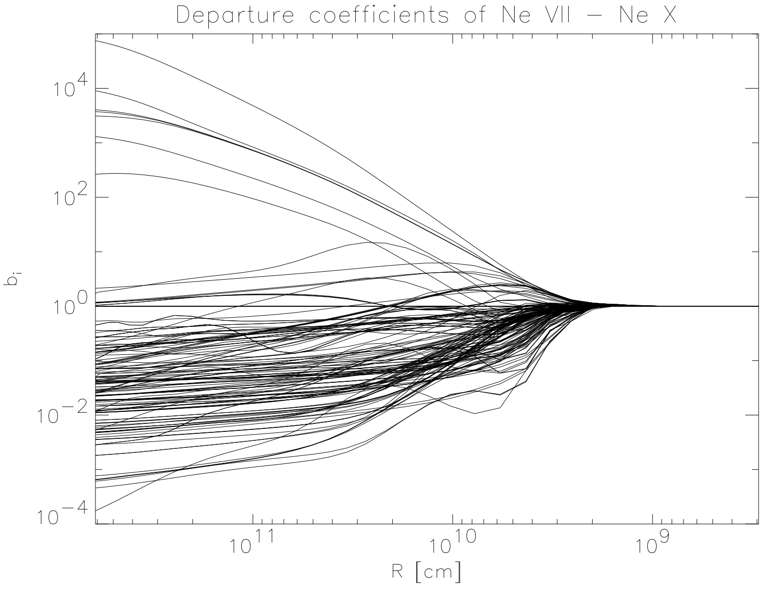

Figure 7.49: Departure coefficients b_i of all levels of Ne VII to Ne X plotted against the radius R of the atmosphere.

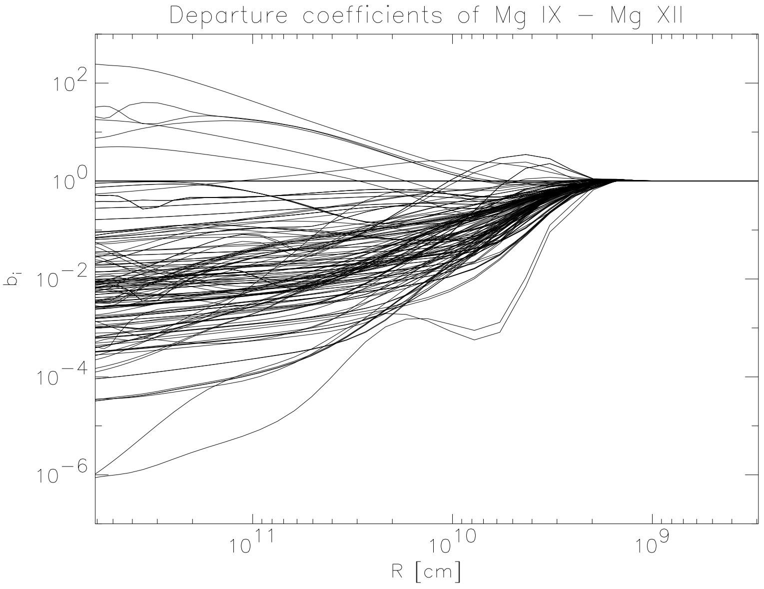

Figure 7.50: Departure coefficients b_i of all levels of Mg IX to Mg XII plotted against the radius R of the atmosphere.

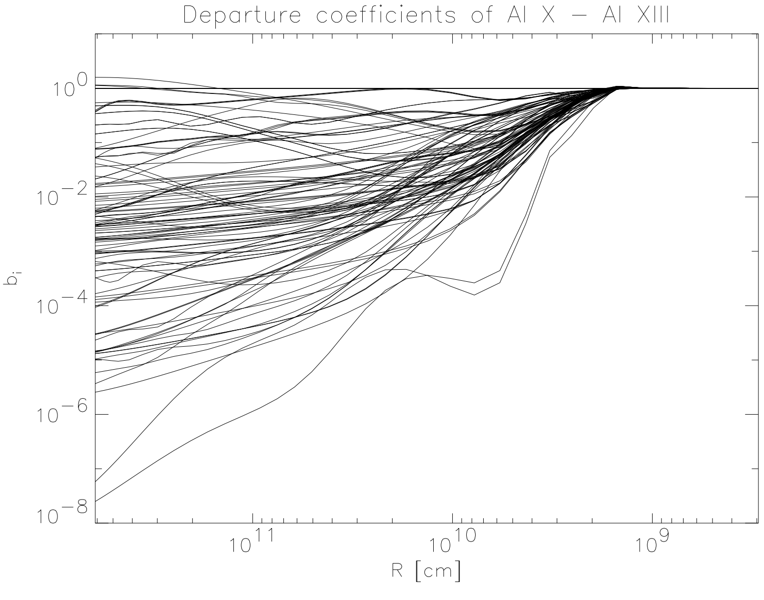

Figure 7.51: Departure coefficients b_i of all levels of Al X to Al XIII plotted against the radius R of the atmosphere.

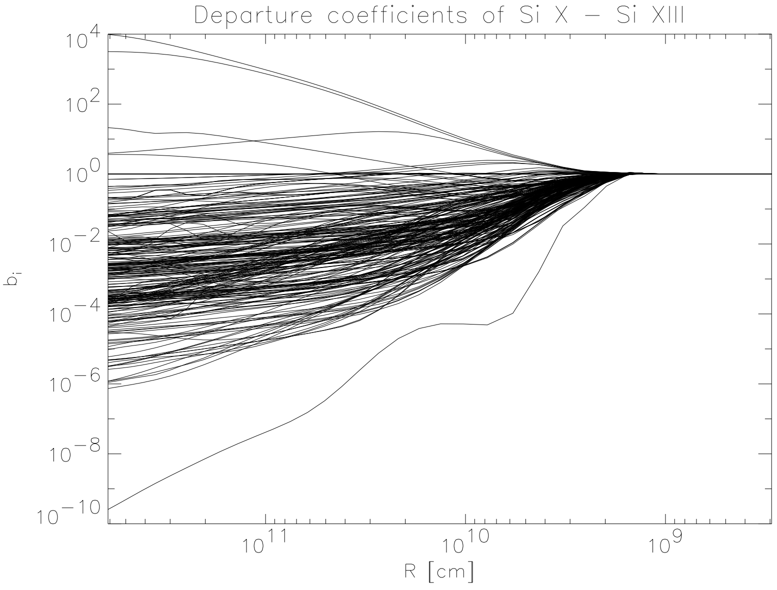

Figure 7.52: Departure coefficients b_i of all levels of Si X to Si XIII plotted against the radius R of the atmosphere.

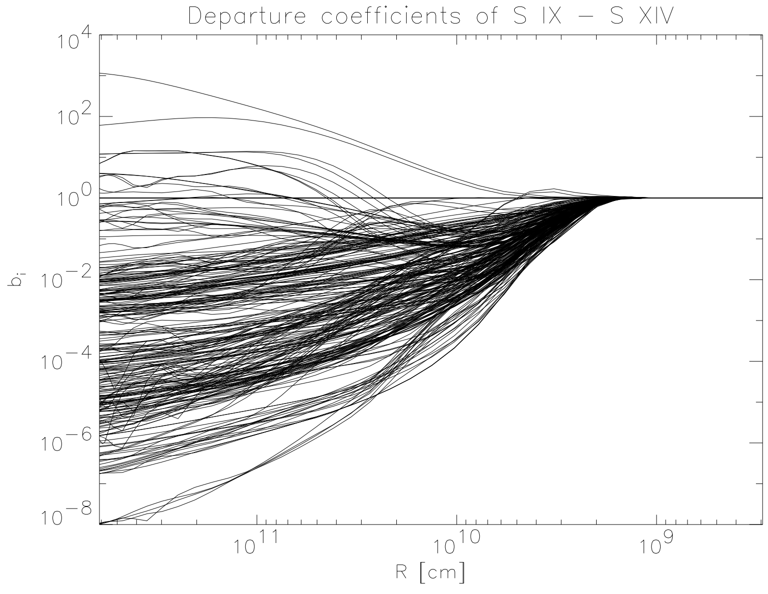

Figure 7.53: Departure coefficients b_i of all levels of S IX to S XIV plotted against the radius R of the atmosphere.

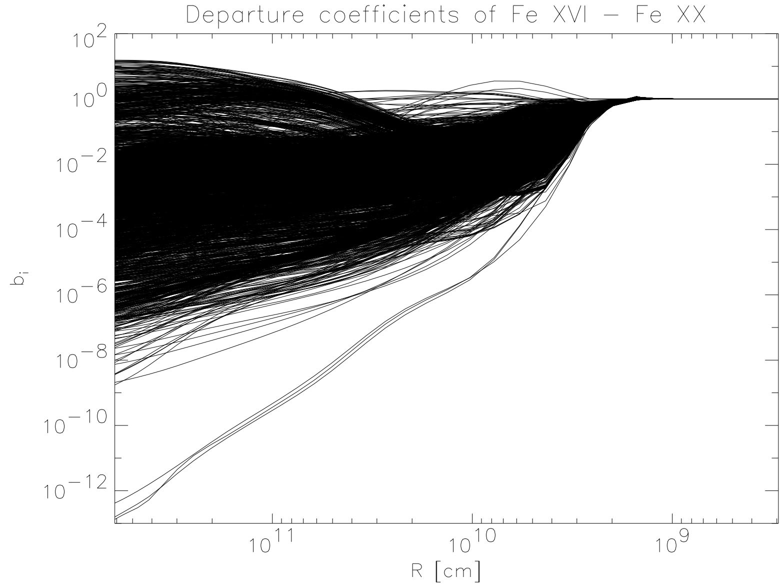

Figure 7.54: Departure coefficients b_i of all levels of Fe XVI to Fe XX plotted against the radius R of the atmosphere.

higher T_{eff}. The same result has been found for the previous nova model atmospheres in the UV and IR (see “NLTE effects” in section 5.2).

However, a departure coefficient of a specific level with a value far from unity does not always mean that the NLTE effects on this level are large. If the population of the level is very small, the opacity is very small, too (It is assumed here, that the level population is so small that the multiplication with the transition probabilities between this level and another results in a very small opacity). Then, NLTE has no significant effect, regardless of how strong the departure coefficient departs from unity.

For silicon, sulfur, and iron the departure coefficients of the levels in the highest ionization stages of these elements are not plotted in the figures 7.52, 7.53, and 7.54 (Si XIV, S XV, S XVI, and Fe XXI to Fe XXVI). There is a drop to unity in the inner part of the atmosphere where the departure coefficients should be large because the departure coefficients are no longer be calculated there. The concentrations of the highest ionization stages are very small in the outer part of the atmosphere (see figures 7.36 to 7.38) and the departure coefficients cannot be calculated. This is not crucial because in this case, the departure coefficients have no effect on the atmosphere structure.

Proton collision rates and two-photon continuum emission

Models with and without proton collision rates are calculated for model atmospheres with $T_{\text{eff}} = 6.0 \times 10^5$ K and $T_{\text{eff}} = 1 \times 10^6$ K, and for models with non-solar abundances (section 7.2). In section 6.4 it was described that the strength of the proton collision rates are comparable to the electron collision rates at the temperature of maximum ionization of a specific ion and they become stronger at higher temperatures. However, for all calculated models, the proton collision rates have no effect on the atmosphere and synthetic spectrum.

In the databases, there are only proton collision data for the ionization stages Ne VII, Mg IX, Al X, for Si X to Si XI, S IX, S XI to S XII, and for Fe XVII to XXIII. In the atmosphere layers where these elements are abundant the temperature is too low for the proton collision rates to be larger or comparable to the electron collision rates (compare figures 7.30 and 7.33 to 7.38). Therefore, there are no contributions from proton collisions in model atmospheres with effective temperatures between $T_{\text{eff}} = 1.0 \times 10^5$ K and $T_{\text{eff}} = 1.0 \times 10^6$ K.

The effects from the two-photon continuum emission on the atmosphere and the spectrum has been examined. For model atmospheres with high temperatures and with solar and non-solar abundances, there are no effects from this process. In section 6.6 the importance of two-photon continuum emission in the ultraviolet spectral range has been described. Considering these results, the temperatures and densities of the model atmospheres in this work are too large for two-photon continuum emission to be important.

7.2 Models with non-solar abundances

7.2.1 Fits to the observations

In section 7.1.3 the observations of nova V4743 Sgr have been fitted with solar abundance models. In Petz et al. (2005c) the first models from Petz et al. (2005a) have been calculated with non-solar abundances and the obtained spectra have been fitted to the March 2003 observation of nova V4743 Sgr (figure 7.55, taken from Petz et al. 2005c). The model atmosphere has an effective temperature of $T_{\text{eff}} = 5.8 \times 10^5$ K and the spectrum can be fitted with $n_h = 4.9 \times 10^{21}\,\text{cm}^{-2}$. This T_{eff} is equal to the effective temperature obtained with the first fit with solar abundances (figure 7.23, Petz et al. 2005a) and n_h is higher ($n_h = 4.0 \times 10^{21}\,\text{cm}^{-2}$ in the first fit with solar abundances). The abundances which are obtained from the fit in figure 7.55 are a carbon abundance of 1.25 times the solar value and abundances of

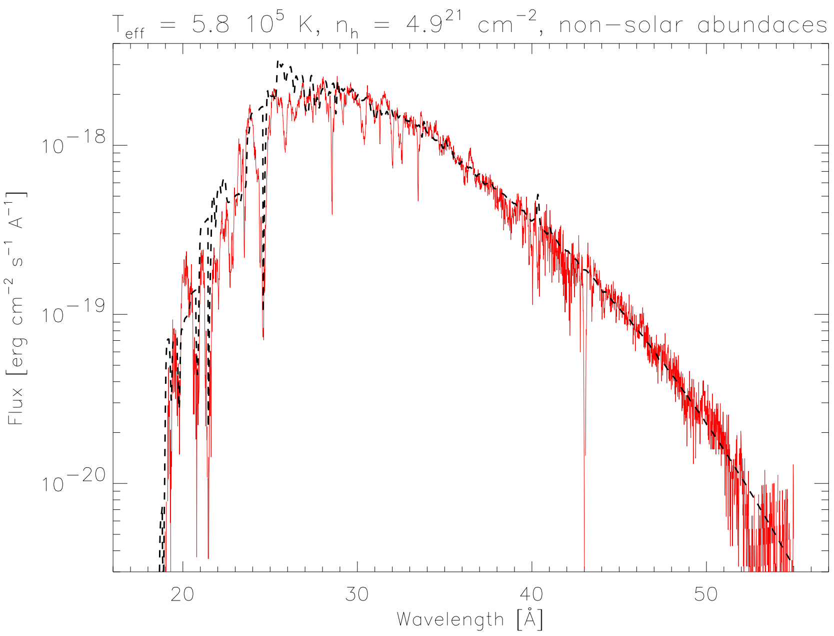

Figure 7.55: First fit with non-solar abundances to the March 2003 observation of nova V4743 Sgr (Petz et al. 2005c, figure 1, right panel). The abundance of carbon is 1.25 times the solar value and the abundances of nitrogen and oxygen are both 22 times the solar value.

nitrogen and oxygen which are both 22 times the solar value. Accordingly, the ratio between the oxygen and nitrogen abundance is equal to the solar value.

The fit with non-solar abundances is much improved than the fit with solar abundances but the model contains not all species from table 7.3. As explained in section 7.1.3, the first models of Petz et al. (2005a) and Petz et al. (2005c) contain only all ions of hydrogen, helium, carbon, nitrogen, and oxygen, and the ions Fe XXI - Fe XXVI. For an improved analysis, the models which are described section 7.1 must be calculated with non-solar abundances and the synthetic spectra have to be fitted to the observations.

As shown in section 7.1.2, the strongest contributions to the spectrum are from carbon, nitrogen, oxygen, and iron. Accordingly, the abundances of these elements have to be varied. If the strengths of the synthetic spectral lines are compared with the observations, it can be seen from the fits with solar abundances (figures 7.24 to 7.26) that the lines from carbon, nitrogen, and oxygen are too weak and the iron lines are too strong in the models. Therefore, the abundances of carbon, nitrogen, and oxygen must be increased and the abundance of iron must be decreased.

Calculations with different abundances of helium have shown that the continuum flux below $\lambda \sim 25\,\text{Å}$ is strongly affected by the abundance of helium and this abundance has to be varied, too. Furthermore, there are spectral lines of silicon and sulfur in the synthetic spectrum which are not found in the observations. Hence, the silicon and sodium abundances both have been reduced by a factor of 10 in respect to the solar values. The abundances of neon, magnesium, and aluminum also have been varied but they do not have strong effects on the spectrum. In the following they will be set equal the solar values.

In order to obtain good fits to the observations, test calculations have shown that it is necessary to vary the abundances of helium, carbon, nitrogen, oxygen, and iron simultaneously and to fit the continuum and lines simultaneously, too (Petz et al. 2005b). In addition, T_{eff} and n_h must be fitted. Therefore, seven parameters have to be varied simultaneously and a large grid of models is necessary to find spectra which fit to the observations. In the first models with non-solar abundance from Petz et al. (2005c) the ionization stages from iron below Fe XX have not been included. In this case, it has not been necessary to vary the iron and helium abundances to obtain a good fit.

Figures 7.56 to 7.59 show the best fits to the observations from March 2003, July 2003, September 2003, and February 2004 of nova V4743 Sgr. The atmosphere structures (temperature, gas density, and partial pressures) of the best fitting models for the March and July 2003 observations are shown in appendix B. All spectra have been fitted by eye. In general, the quality of a fit is determined, e. g., by the statistical χ^2-method to obtain the best fit parameters. But due to the missing lines in the modeled spectrum and due to the lines which are too weak in the model, the statistics would produce much worse results than a fit by eye.

The fits are better than the fit from Petz et al. (2005c). The modeled continuum flux fits very well to the observations, except around $\lambda \sim 20\,\text{Å}$ where it is too low and around $\lambda \sim 23\,\text{Å}$ here it is too high.

The oxygen line at $\lambda \sim 21.6\,\text{Å}$ and the nitrogen line at $\lambda \sim 24.8\,\text{Å}$ are the two strongest lines and their line strengths are modeled as accurate as possible. In contrast, the modeled nitrogen line at $\lambda \sim 20.9\,\text{Å}$ has only an accurate line strength in the fit for July and September 2003 and the nitrogen line at $\lambda \sim 19.8\,\text{Å}$ in the fit for July 2003. Otherwise, they are modeled too weak. All other lines are always too weak in the model spectrum. Particularly, there are no carbon and iron lines with modeled line strengths which fit the observations. But changing the abundances of carbon and iron does change the continuum flux so much that a good fit cannot be obtained any more. The change of the continuum flux and the spectral lines

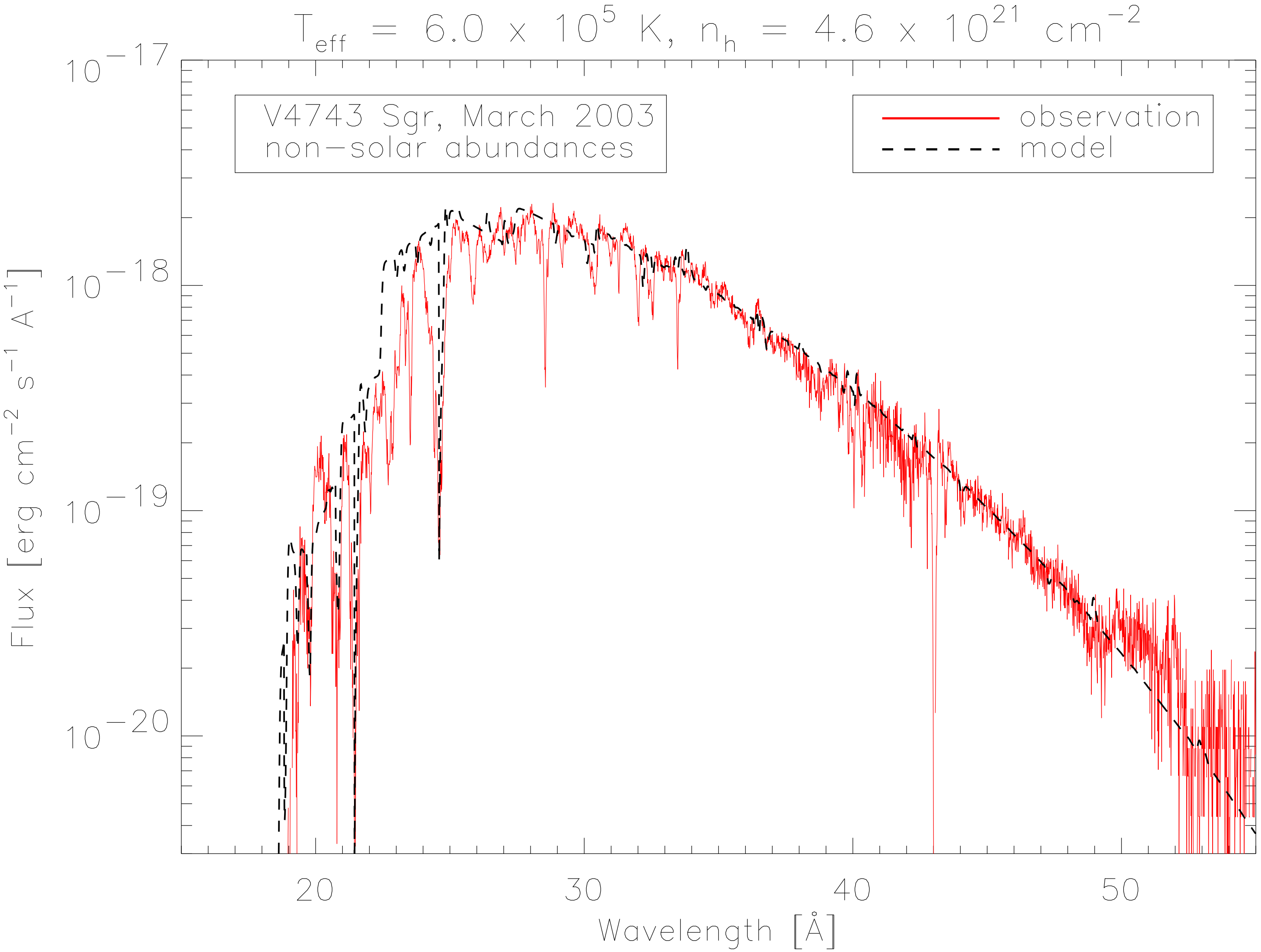

Figure 7.56: Fit of a model spectrum (dashed line) with non-solar abundances for the March 2003 observation of nova V4743 Sgr (solid line). The model atmosphere has $T_{\mathrm{eff}} = 6.0 \times 10^5\,\mathrm{K}$ and from the fit $n_h = 4.6 \times 10^{21}\,\mathrm{cm}^{-2}$ is obtained.

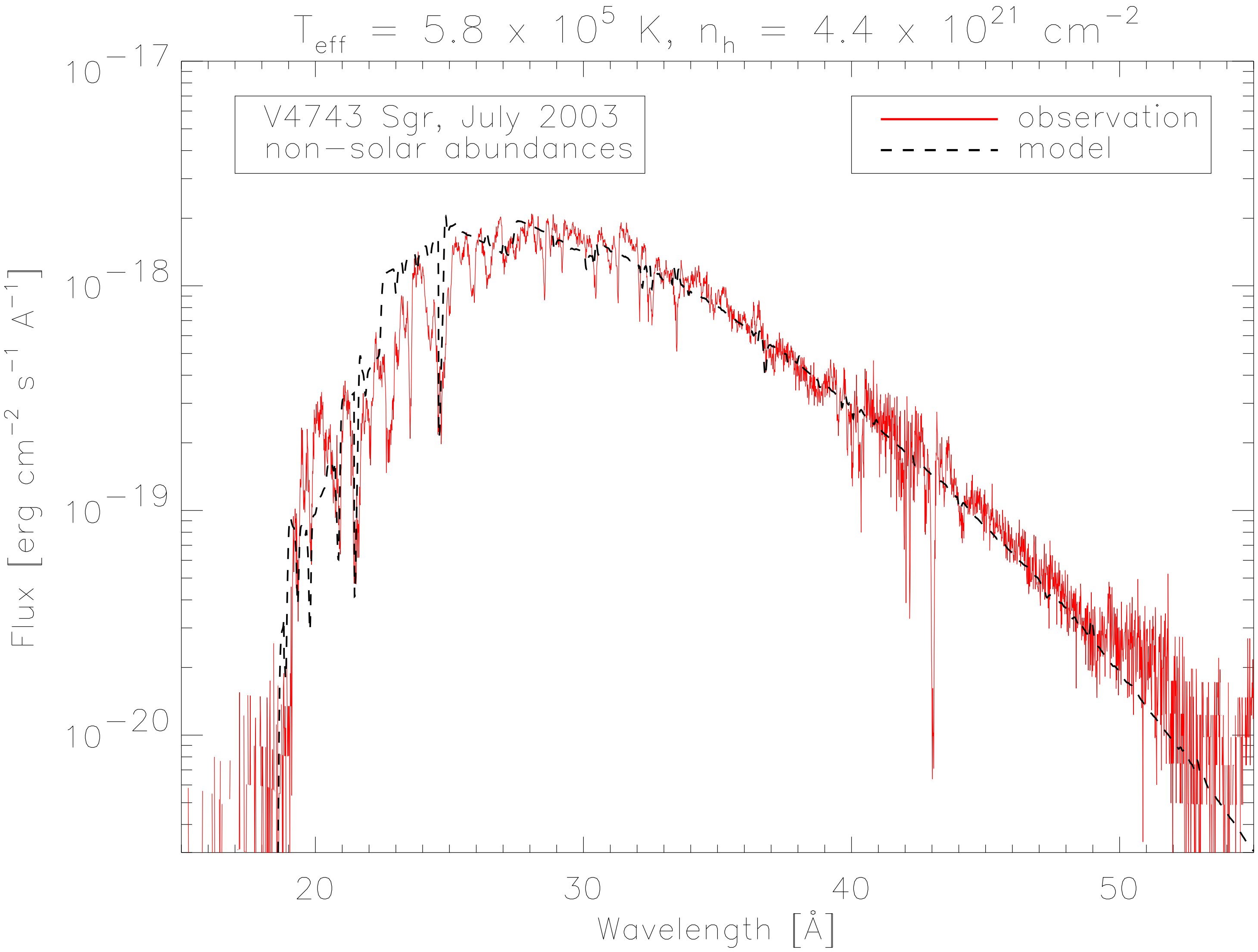

Figure 7.57: Fit of a model spectrum (dashed line) with non-solar abundances for the July 2003 observation of nova V4743 Sgr (solid line). The model atmosphere has $T_{\mathrm{eff}} = 5.8 \times 10^5\,\mathrm{K}$ and from the fit $n_h = 4.4 \times 10^{21}\,\mathrm{cm}^{-2}$ is obtained.

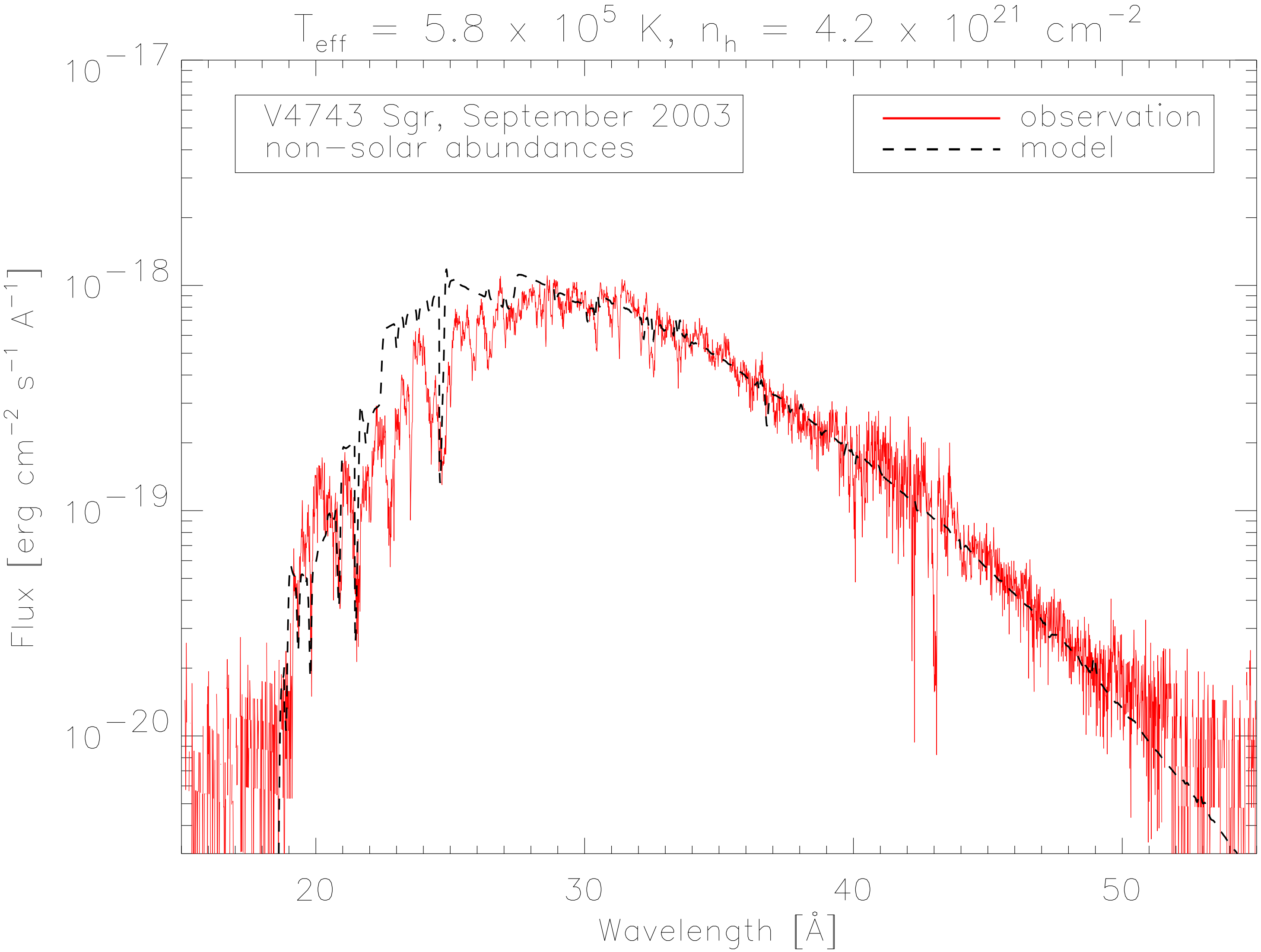

Figure 7.58: Fit of a model spectrum (dashed line) with non-solar abundances for the September 2003 observation of nova V4743 Sgr (solid line). The model atmosphere has $T_{\text{eff}} = 5.8 \times 10^5\,\text{K}$ and from the fit $n_h = 4.2 \times 10^{21}\,\text{cm}^{-2}$ is obtained.

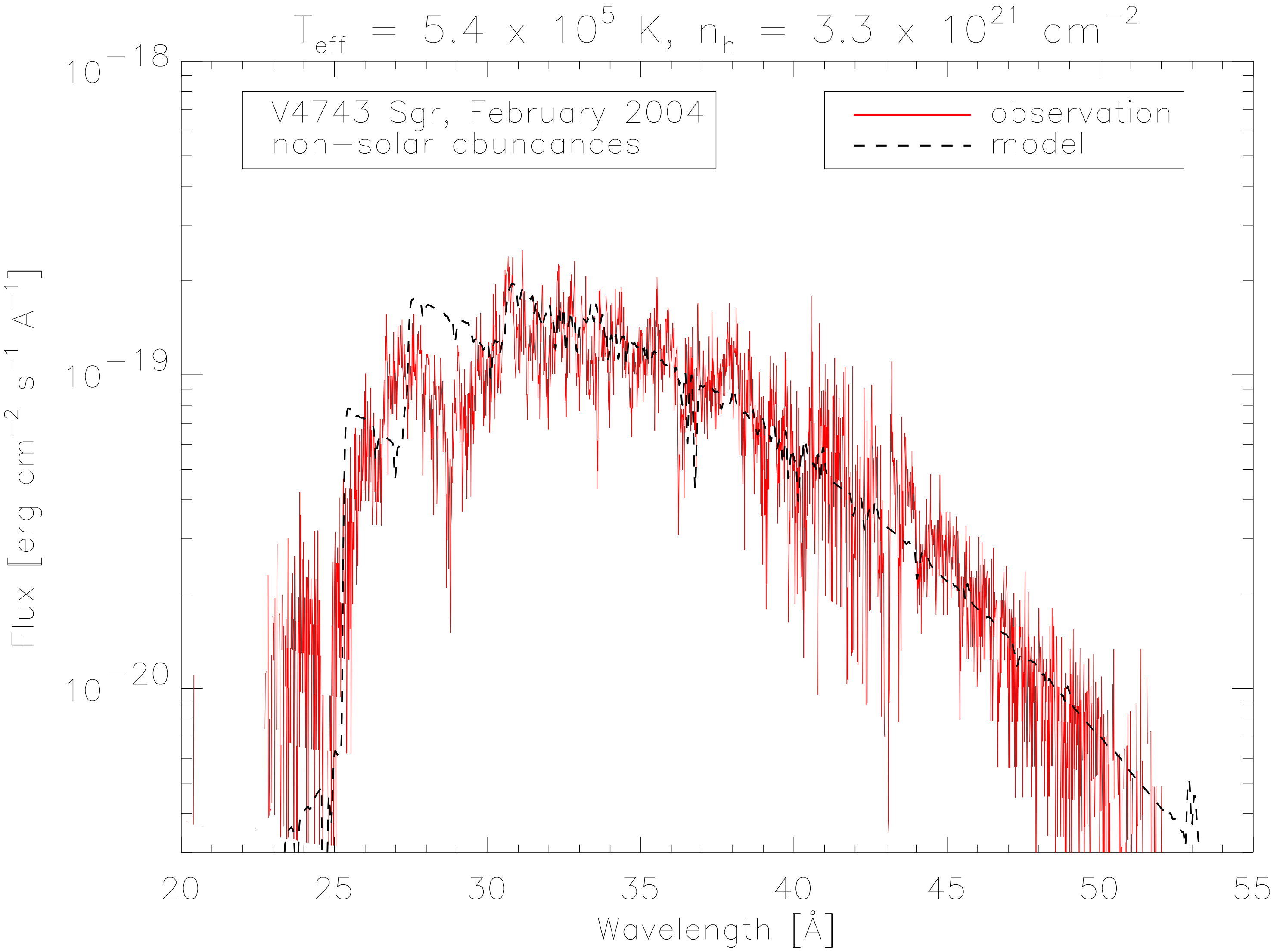

Figure 7.59: Fit of a model spectrum (dashed line) with non-solar abundances for the February 2004 observation of nova V4743 Sgr (solid line). The model atmosphere has $T_{\rm eff} = 5.4 \times 10^5$ K and from the fit $n_h = 3.3 \times 10^{21}$ cm^{-2} is obtained.

Parameter	March 2003	July 2003	Sept. 2003	Feb. 2004
$T_{\rm eff}$ in 10^5 K	6.00 ± 0.05	5.80 ± 0.05	5.80 ± 0.05	5.40 ± 0.20
n_h in $10^{21}\,{\rm cm}^{-2}$	4.60 ± 0.05	4.40 ± 0.05	4.20 ± 0.05	3.30 ± 0.20
He-abundance in $\odot$	7.5 ± 0.5	3.0 ± 0.1	3.0 ± 0.1	3.0 ± 0.5
C-abundance in $\odot$	2.5 ± 0.1	3.0 ± 0.1	3.0 ± 0.1	3.0 ± 0.5
N-abundance in $\odot$	17.0 ± 0.5	27.0 ± 0.5	26.0 ± 0.5	26.0 ± 5.0
O-abundance in $\odot$	12.0 ± 0.5	2.5 ± 0.1	2.5 ± 0.1	2.5 ± 0.5
Fe-abundance in $\odot$	0.1 ± 0.1	0.1 ± 0.1	0.1 ± 0.1	0.1 ± 0.1

Table 7.6: Parameters for the best fits to the observations from March 2003, July 2003, September 2003, and February 2004 of nova V4743 Sgr. The abundances are relative to the solar values.

in calculations with different abundances will be shown below.

The discrepancies in the modeled line strengths can be explained, e. g., with the run of the temperature inside the atmosphere. Lines are formed at certain optical depths and their line strengths are very sensitive to the temperature. Therefore, the abundance grids have been calculated for different $T_{\rm eff}$ but no better fits can be obtained. A possible explanation is a second component in the nova shell. `PHOENIX` calculates atmospheres which consist of one component. A second component can have a different temperature structure than the modeled component and can affect the strength of the spectral lines and the continuum flux. Another possible explanation for the discrepancies is an inhomogeneous medium which has density clumps that absorb flux at certain wavelengths and weaken the corresponding spectral lines. The effects of multiple components and inhomogeneities change the abundances determined from the fits.

The modeled spectral lines are too narrow. In order to model the expansion of the medium, the observed value of $v_{\rm out} = 2500\,{\rm km\ s}^{-1}$ has been used (section 3.2). Models with higher velocities do not solve the problem. The strengths and widths of the lines are affected by the velocity field. Models with different β-wind laws (equation 4.1) may produce spectra which fit better to the observations. The effects of inhomogeneities and a β-wind law must be considered in future work.

The parameters of the fitted models are shown in table 7.6. The errors arise from the determination of the parameters by fitting the observations by eye, e. g., the relative errors of the iron abundances are very large. The observed iron lines are relatively weak and an abundance determination with the continuum flux is not as accurate as a determination with spectral lines.

For all fits, $T_{\rm eff}$ is larger than in the fits with solar abundances (figures 7.24

to 7.27). $T_{\rm eff}$ is slightly lower in the July and September 2003 observations than in March 2003 but there is no change between the July and September 2003 observations. In February 2004, $T_{\rm eff}$ is lower than in September 2003. The temperature of the nova atmosphere is essentially constant between March and September 2003 and is decreasing between September 2003 and February 2004. As expected, n_h is decreasing with time.

In the observations from July 2003, September 2003, and February 2004 the spectral lines are weaker than in March 2003. Either a change of the physical conditions in the nova wind or a change in the abundances can weaken the lines. The physical conditions in the wind are changed by the expansion of the medium but in order to weaken the spectral lines the wind has to become more optically thick. Anyway, models with the same abundances of the March 2003 observation but with different density gradients n, expansion velocities $v_{\rm out}$ (equation 5.2 and 5.3), and $T_{\rm eff}$ have been calculated. No synthetic spectra can be found which fit to the observations with a quality comparable to the fits in the figures 7.57 to 7.59 and the abundances may change by an evolution. Possible reasons for this evolution will be discussed in section 7.4.

For all four observations the abundance of iron is the same. Between March and July 2003, the abundances of helium and oxygen are decreasing and the abundances of carbon and nitrogen are increasing. Between July and September 2003 there is only a minor decrease in the abundance of nitrogen which is contrary to the evolution between March and July 2003. This may be due to the effects of inhomogeneities, as discussed above, and must not be related with an evolution. The observation in February 2004 can be fitted with the same abundances than the observation of September 2003 but the quality of the fit is much worse than the qualities of the other fits and the determined abundances are not very reliable. The errors in table 7.6 are large for the observation in February 2004.

The abundances from the fit in figure 7.56 are different to the abundances determined with the first models in Petz et al. (2005c). The abundance ratio between nitrogen and oxygen is no longer equal to the solar value and has been a random result in Petz et al. (2005c).

On the one hand the errors for the abundances are affected by fitting the observations by eye and on the other hand by the effects of a second atmosphere component, a different velocity field, and the lack of inhomogeneities in the nova shell simulations. On the other hand effects arise from the atomic data which are used to calculate the models. In section 7.3 best fits will be determined with data from the CHIANTI4 and CHIANTI5 databases and the obtained errors will be larger than in table 7.6. Therefore, the calculated grid does not have to be more detailed. The errors from effects of inhomogeneities and the velocity field cannot be determined because models which include such effects have not been calculated in this work. These errors may be higher than the errors in table 7.6.

In the following the effects on the spectrum, when the abundance of different elements are varied, will be shown for a model with $T_{\text{eff}} = 6.0\times10^5$ K.

7.2.2 Effects of different abundances on the spectrum

Figures 7.60 to 7.64 show model spectra which were calculated with different abundances. Two plots with two spectra in each plot are shown in each figure. One spectrum was calculated with the abundances of the best fit for the March 2003 observation of nova V4743 Sgr (dashed line). The other spectra were calculated with different abundances for one of the varied chemical elements (solid line), in the one plot with an abundance which is lower and in the other plot with an abundance which is higher than in the best fit. For an easier comparison with the best fit, all spectra are plotted with the $n_h = 4.6 \times 10^{21}\,\text{cm}^{-2}$ of the best fit.

Raising the abundance of an element increases the strength of the continuum absorption. Absorption and emission lines of these elements increase, too. The effects of the abundances of particular chemical elements will be examined in the following.

In figure 7.60 the effects of different helium abundances on the spectrum are shown. Helium abundances equal to the solar value and 10 times the solar value are compared with helium abundances of 7.5 times the solar value. Different helium abundances affect the continuum of the whole spectral range. For $\lambda \lesssim 22\,\text{Å}$ the effect is the greatest. The relative line strengths of the spectral lines are not affected. Different helium abundances affect only the continuum flux.

In figure 7.61 a carbon abundance which is equal to the solar value and 5 times the solar value is compared with a carbon abundance of 2.5 times the solar value. In contrast to the helium abundance, the abundance of carbon affects the continuum flux only for wavelengths below $\lambda \sim 25\,\text{Å}$. The ionization edge of C VI lies at this wavelength (table 7.5). The spectral lines of carbon (table 7.4) are not significantly changed.

Figure 7.62 compares a nitrogen abundance equal to the solar value and a nitrogen abundance which is 22 times higher than in the sun with a nitrogen abundance of 7 times the solar value. The abundance of nitrogen mainly affects the spectrum for $\lambda \lesssim 22\,\text{Å}$, below the ionization edge of N VI. The strengths of the lines from N VII at $\lambda \sim 19.4\,\text{Å}$, $\lambda \sim 19.8\,\text{Å}$, $\lambda \sim 20.9\,\text{Å}$, and $\lambda \sim 24.8\,\text{Å}$ depend very strongly on the nitrogen abundance.

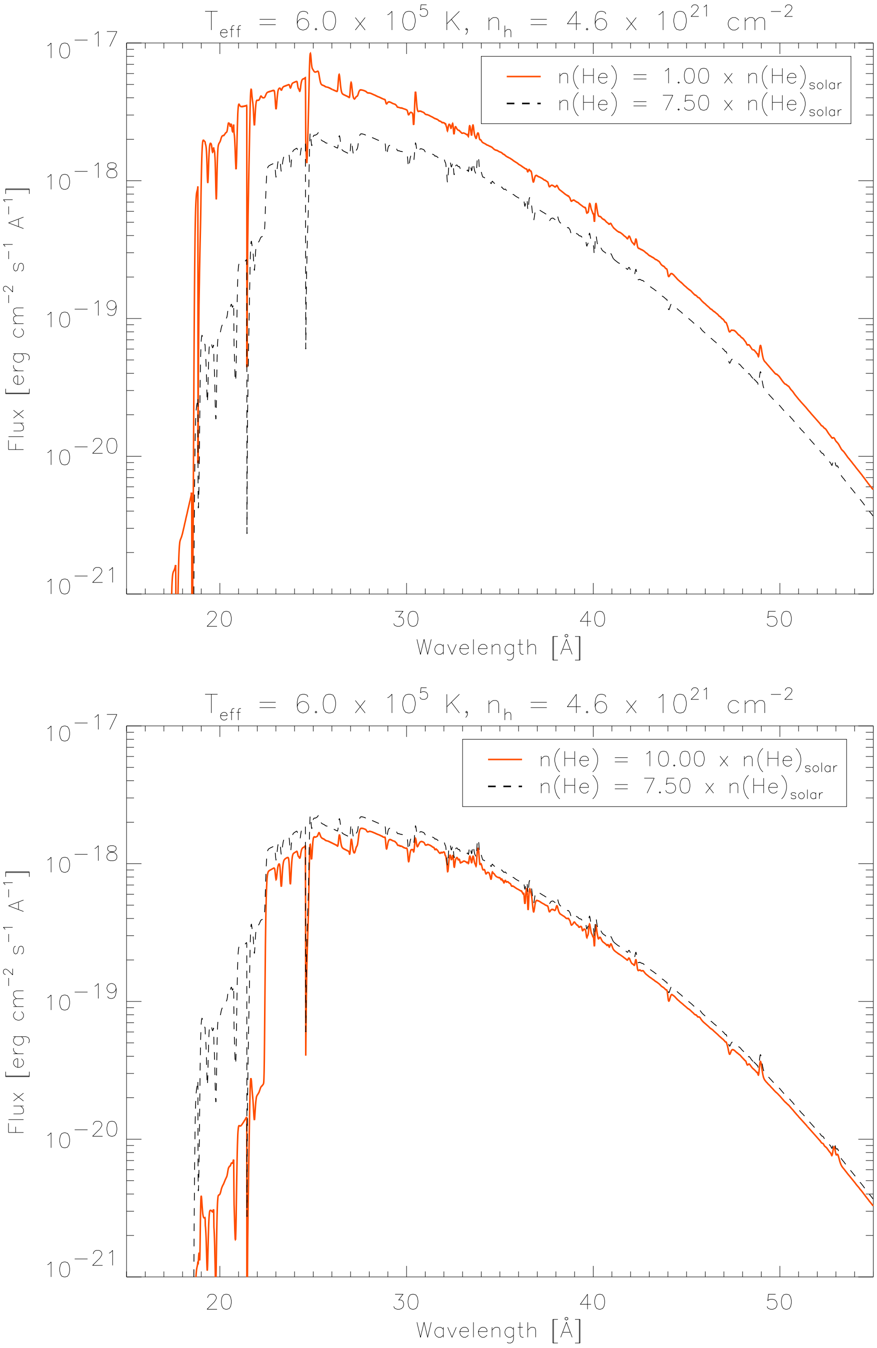

Figure 7.60: Model spectra calculated with different helium abundances. In the upper panel a helium abundance equal to the solar value and in the lower panel a helium abundance of 10 time the solar value are compared with a helium abundance of 7.5 times the solar value.

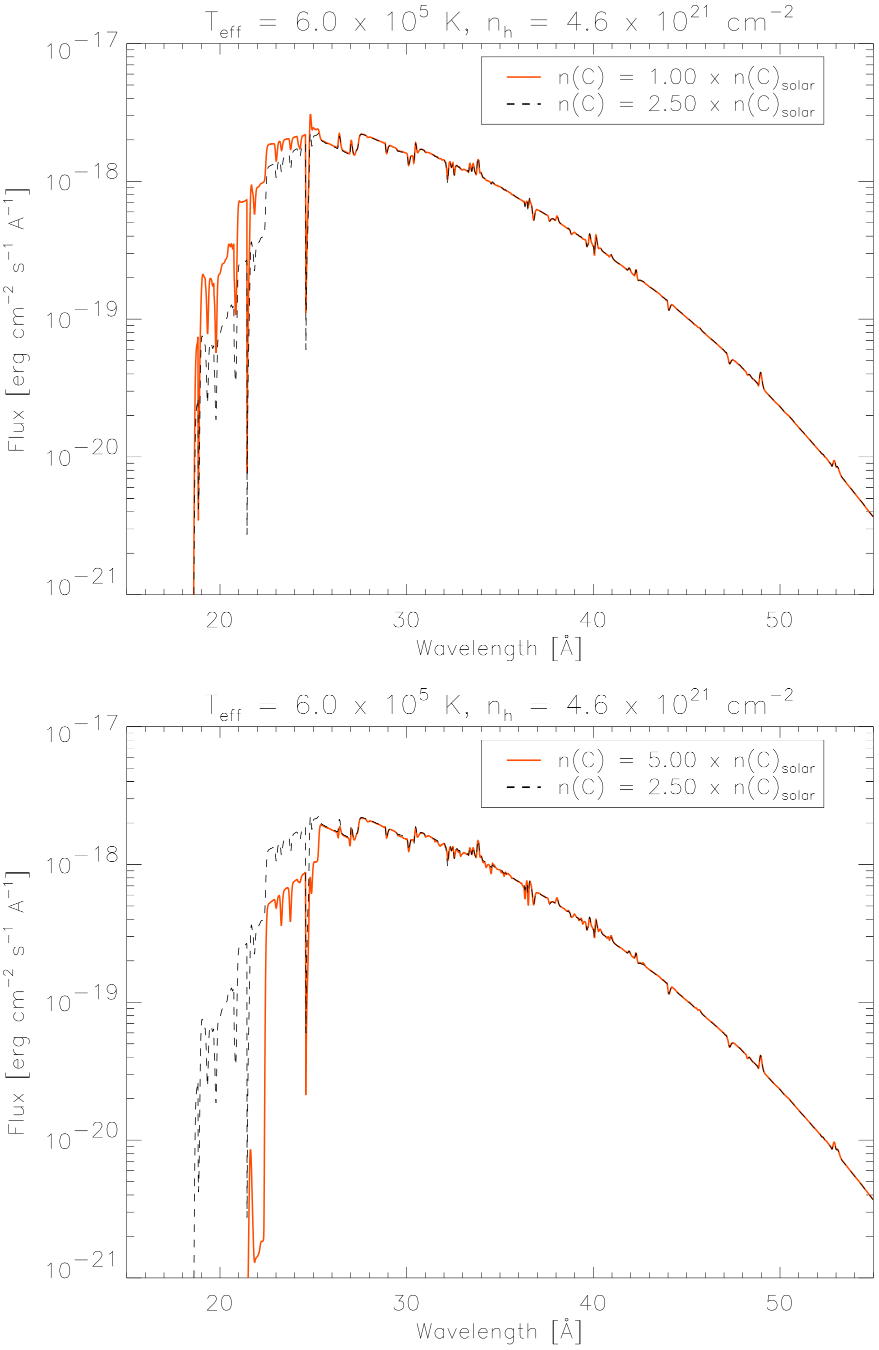

Figure 7.61: Model spectra calculated with different carbon abundances. In the upper panel a carbon abundance equal to the solar value and in the lower panel a carbon abundance of 5 times the solar value are compared with a carbon abundance of 2.5 times the solar value.

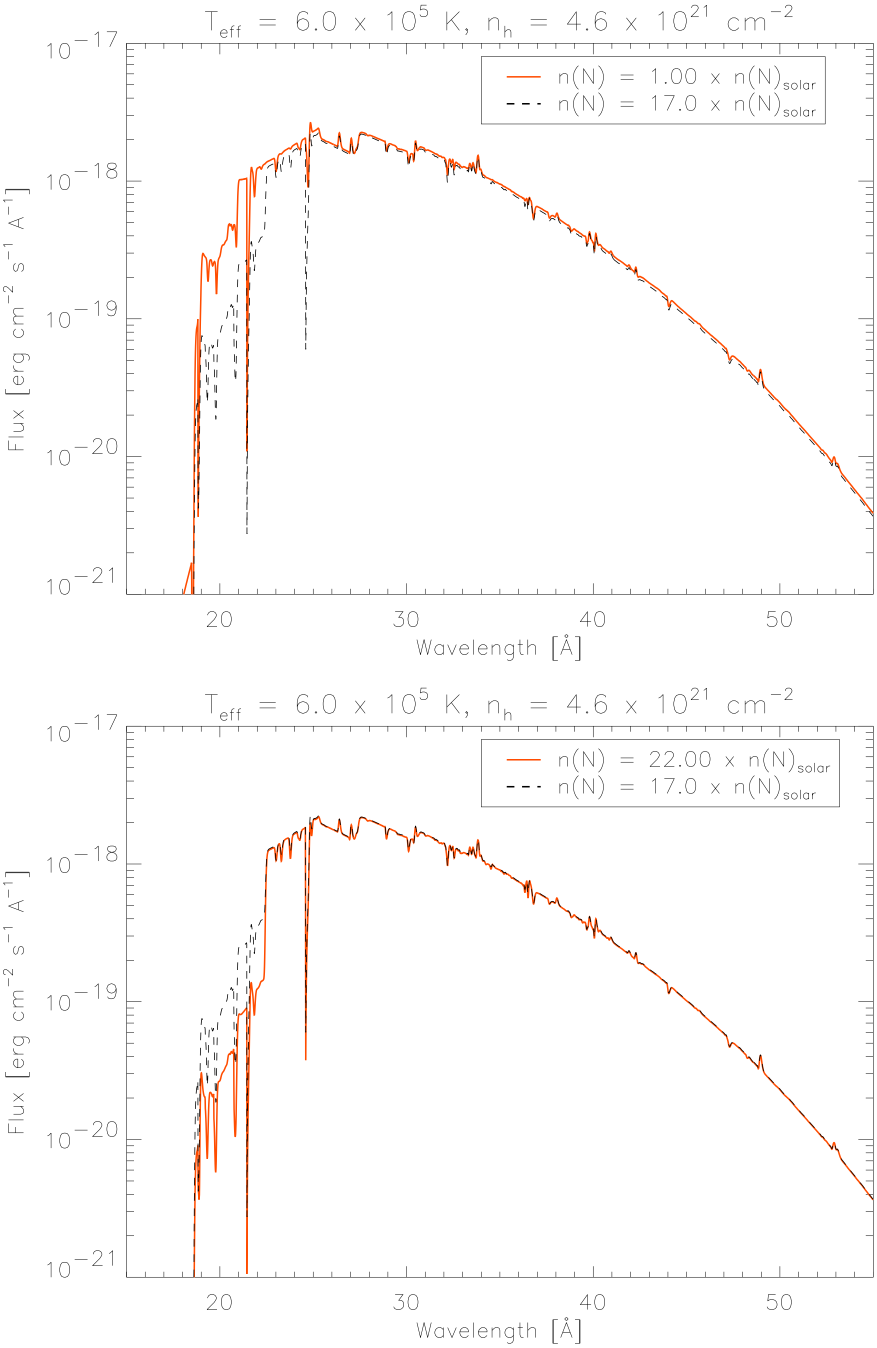

Figure 7.62: Model spectra calculated with different nitrogen abundances. In the upper panel a nitrogen abundance equal to the solar value and in the lower panel a nitrogen abundance of 22 times the solar value are compared with a nitrogen abundance of 17 times the solar value.

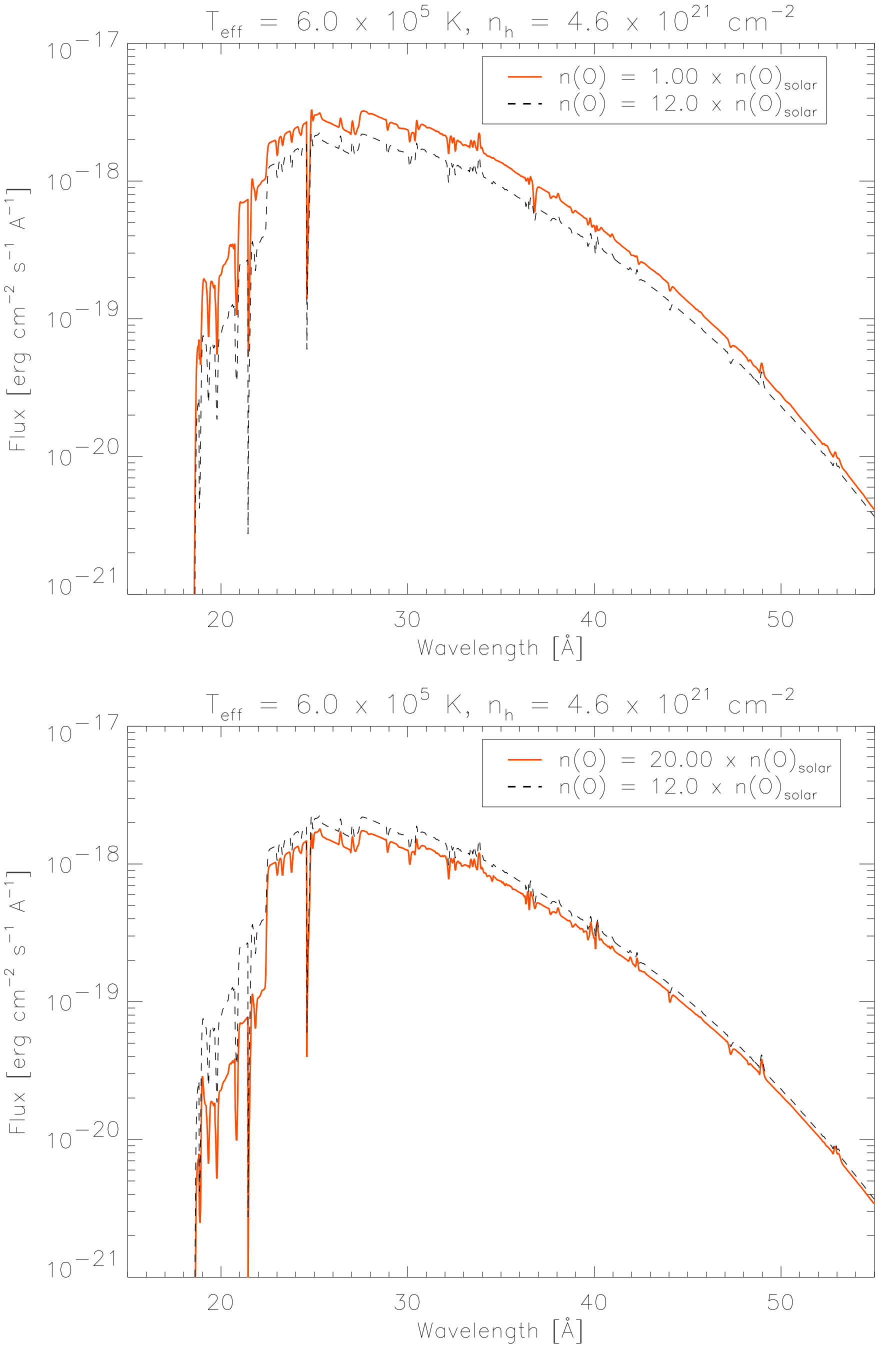

Figure 7.63: Model spectra calculated with different oxygen abundances. In the upper panel an oxygen abundance equal to the solar value and in the lower panel an oxygen abundance of 20 times the solar value are compared with an oxygen abundance of 12 times the solar value.

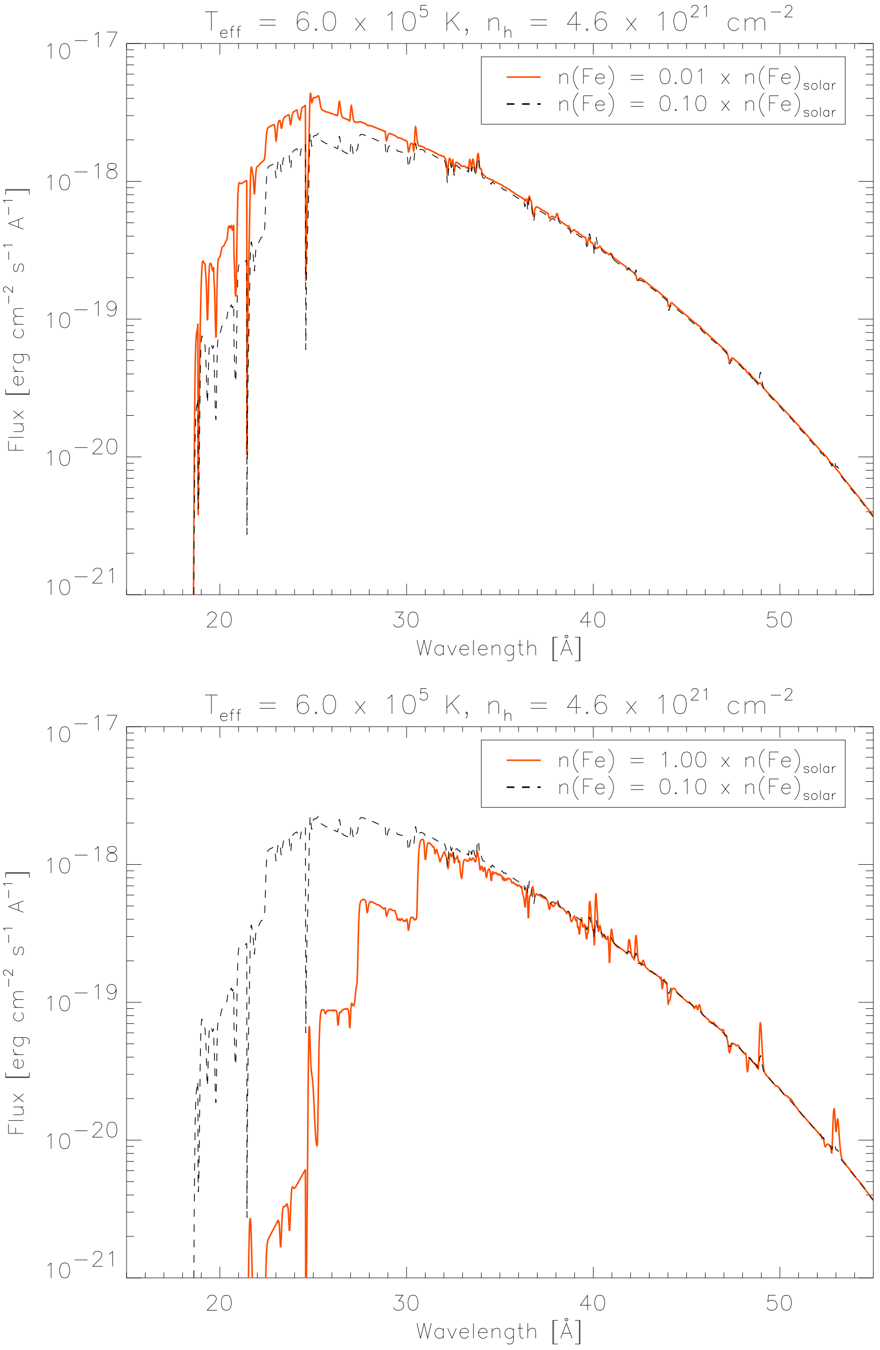

Figure 7.64: Model spectra calculated with different iron abundances. In the upper panel an iron abundance of 0.01 times the solar value and in the lower panel an iron abundance equal to the solar value are compared with an iron abundance of 0.1 times the solar value.

In order to examine the effects of the oxygen abundance, oxygen abundances equal to the solar value and 20 times the solar value are compared with an oxygen abundance which is 12 times higher than in the sun (figure 7.63). Like the helium abundance, the oxygen abundance has an effect on the whole spectrum which is strongest at $\lambda \lesssim 22\,\text{Å}$. The line relative strengths of the O VII lines at $\lambda \sim 21.6\,\text{Å}$ and $\lambda \sim 21.9\,\text{Å}$ and of the O VIII line at $\lambda \sim 19.0\,\text{Å}$ are strongly affected by the oxygen abundance.

Iron abundances of 0.01 times the solar value and equal to the solar value are compared with an iron abundance of 0.1 times the solar value in figure 7.64. The abundance of iron has a strong effect on the continuum, mainly below $\lambda \sim 30\,\text{Å}$. Many emission and absorption lines of iron in the spectrum are all affected by these abundances. There is no case where an iron line changes from an emission to an absorption line and vice versa.

7.3 Models with different atomic data

The CHIANTI4, CHIANTI5, and APED databases have been described in chapter 6. In the model calculations in section 7.1 and 7.2 data from the APED database have been used. Before a model for the emission and evolution of X-ray radiation in nova V4743 Sgr can be developed, the effects of the different atomic data on the synthetic spectra have to be be examined and the errors on the fit parameters must be determined.

7.3.1 Models with data from CHIANTI

The observations from March, July, and September 2003 of nova V4743 Sgr have been fitted with model spectra which were calculated with atomic data from CHIANTI. The quality of the observation from February 2004 is too bad for the analysis in this section and will not be considered. There are only minor differences between spectra calculated with data from CHIANTI4 and CHIANTI5. The Versions 4 and 5 of the CHIANTI databases are not distinguished in the following description.

The best fits to spectra which were calculated with CHIANTI data are plotted in the figures 7.65 to 7.67 for the observations from March, July, and September 2003. Compared with the fitted spectra which were calculated with APED (figures 7.56 to 7.58), the effective temperatures T_{eff} of the model atmospheres are the same. n_h is only different in the fits for the observation from September 2003. A hydrogen column density of $n_h = 4.2 \times 10^{21}\,\text{cm}^{-2}$ is obtained for a fit with a spectrum calculated with APED and for a fit with a spectrum calculated with CHIANTI, $n_h = 4.0 \times 10^{21}\,\text{cm}^{-2}$ is obtained (table

Parameter	March 2003	July 2003	Sept. 2003
$T_{\rm eff}$ in 10^5 K	6.00 ± 0.05	5.80 ± 0.05	5.80 ± 0.05
n_h in 10^{21} cm^{-2}	4.60 ± 0.05	4.40 ± 0.05	4.00 ± 0.05 (4.20)
He-abundance in $\odot$	7.5 ± 0.5	2.0 ± 0.1 (3.0)	2.0 ± 0.1 (3.0)
C-abundance in $\odot$	2.5 ± 0.1	1.5 ± 0.1 (3.0)	1.5 ± 0.1 (3.0)
N-abundance in $\odot$	12.0 ± 0.5 (17.0)	18.0 ± 0.5 (27.0)	17.0 ± 0.5 (26.0)
O-abundance in $\odot$	23.0 ± 0.5 (12.0)	3.0 ± 0.1 (2.5)	3.0 ± 0.1 (2.5)
Fe-abundance in $\odot$	0.1 ± 0.1	0.1 ± 0.1	0.1 ± 0.1

Table 7.7: $T_{\rm eff}$, n_h, and abundances for the best fits of synthetic spectra, calculated with atomic data from CHIANTI4, to the observations from March, July, and September 2003 of nova V4743 Sgr. The abundances are relative to the solar values. The values in brackets are the abundances determined with models calculated with APED data (table 7.6). They are only noted if differences do exist.

7.7). In both cases the n_h is lower than in the fits for the observations from March and July 2003, as expected from the expansion of the shell.

More important is the strong change in the determined abundances if different atomic data is used in the calculations. The abundances are shown in table 7.7, together with the errors obtained from a fit by eye. If there are differences compared to abundances determined with APED data, these values are given in brackets. These differences will be examined in the following.

In the fits for the March 2003 observation (figure 7.56 and 7.65) only the abundances of nitrogen and oxygen change. In figure 7.65 (fit of a synthetic spectrum calculated with data from CHIANTI) the relative strength of the N VII triplet at $\lambda \sim 24.8$ Å increases. The abundance of nitrogen must be decreased to fit the observed line strength. Below $\lambda \sim 22$ Å,the continuum flux increases in the model calculated with CHIANTI. If the abundance of nitrogen will be decreased, the continuum flux will be increased stronger (figure 7.62). Therefore, the nitrogen abundance was decreased and the higher continuum flux was lowered by increasing the oxygen abundance. This produces differences of 42% in the nitrogen and 48% in the oxygen abundance compared to calculations with APED data.

In the fits for the observation from July (figure 7.57 and 7.66) and September 2003 (figure 7.58 and 7.67) all abundances, except the iron abundance, do change if models are calculated with CHIANTI in contrast to APED. The shifts of the abundances are the same for both observations (in times the solar abundance): -1 for helium, -1,5 for carbon, -9 for nitrogen, and +0.5 for the oxygen abundance. Again, the nitrogen abundance must be decreased

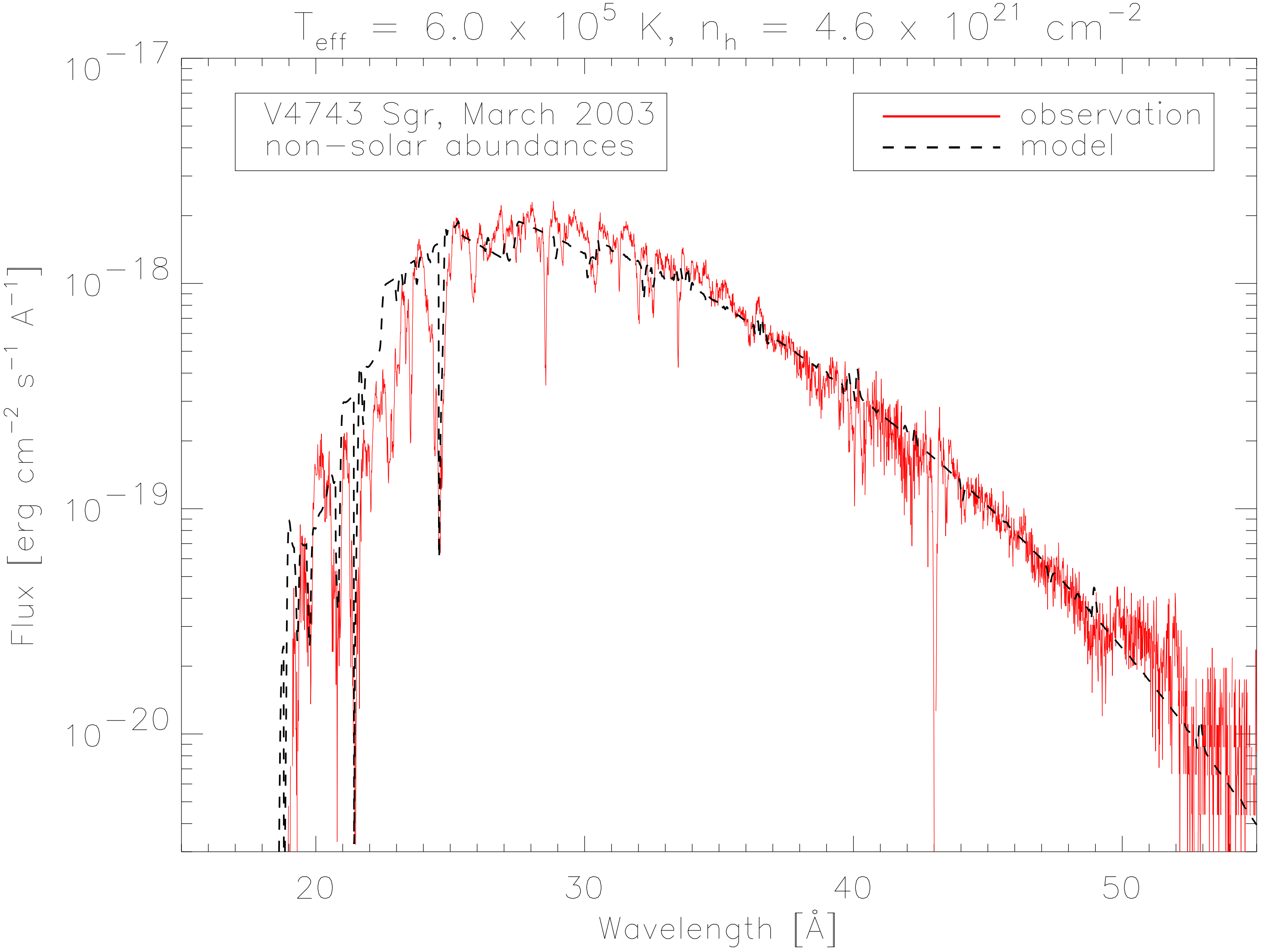

Figure 7.65: Fit of a model spectrum (dashed line) with non-solar abundances which was calculated with data from CHIANTI4 for the March 2003 observations of nova V4743 Sgr (solid line). The model atmosphere has $T_{\rm eff} = 6.0 \times 10^5\,{\rm K}$ and from the fit $n_h = 4.6 \times 10^{21}\,{\rm cm}^{-2}$ is obtained.

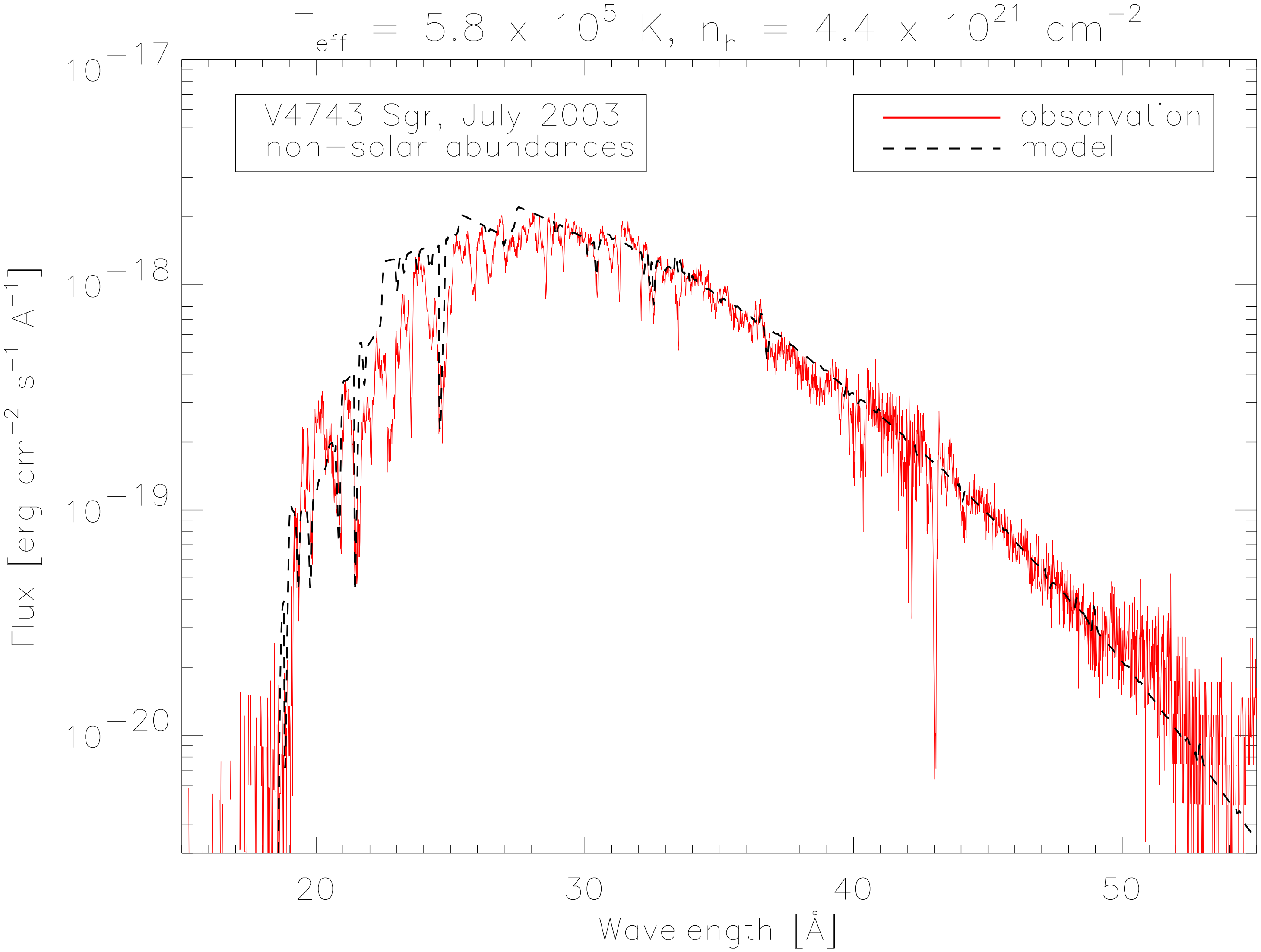

Figure 7.66: Fit of a model spectrum (dashed line) with non-solar abundances which was calculated with data from CHIANTI4 for the July 2003 observations of nova V4743 Sgr (solid line). The model atmosphere has $T_{\rm eff} = 5.8 \times 10^5$ K and from the fit $n_h = 4.4 \times 10^{21}\,\mathrm{cm}^{-2}$ is obtained.

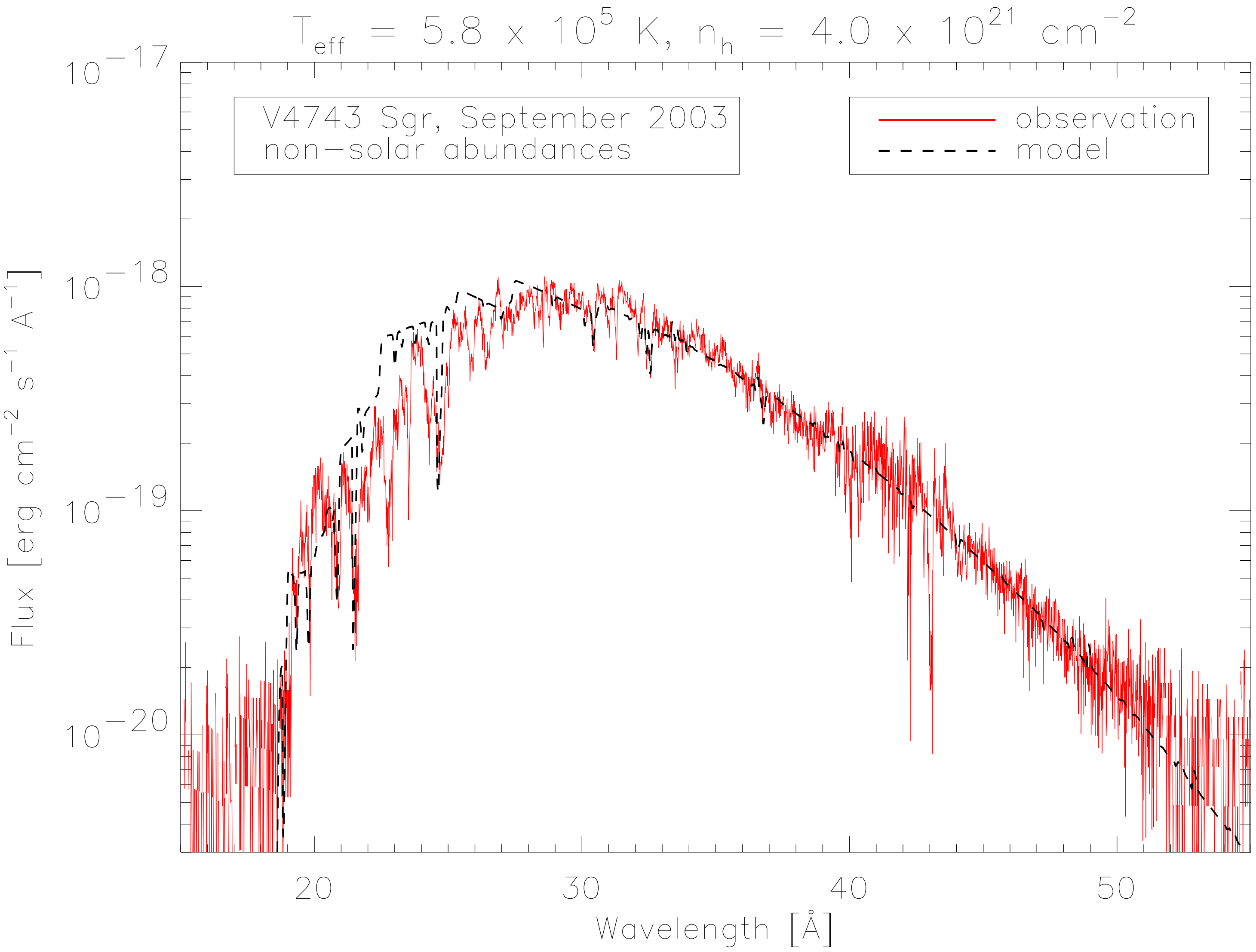

Figure 7.67: Fit of a model spectrum (dashed line) with non-solar abundances which was calculated with data from CHIANTI4 for the September 2003 observations of nova V4743 Sgr (solid line). The model atmosphere has $T_{\mathrm{eff}} = 5.8 \times 10^5\,\mathrm{K}$ and from the fit $n_h = 4.0 \times 10^{21}\,\mathrm{cm}^{-2}$ is obtained.

and the abundance of oxygen must be increased but with another ratio than before. The behavior of the changes in the spectra due to the use of different atomic data is more complex for July and September 2003 than for March 2003 because the abundances of helium and carbon also must be changed if different atomic data are used.

In general it can be concluded that the differences in the abundances are larger if the abundances depart more from the solar values. Due to the strong dependence of the determined abundances on the atomic data the abundance analysis contains big errors and is not reliable. But the run of the abundances between different observations which are fitted with spectra which were calculated with the same atomic database, is consistent within the errors which are obtained by fitting the observations by eye (e.g. the nitrogen abundance changes in all three fits and the oxygen abundance changes only between March and July 2003, independent from the atomic data used to calculate the models). A model for the time evolution of the abundances which does not deal with absolute values is independent of the atomic data. This model will be developed in section 7.4.

The cause of the differences in the spectra which were calculated with different atomic data must be examined. Therefore, radiative rates and collision rates for bound-bound transitions which where calculated with data from CHIANTI4 and APED are compared. The data of the N VII triplet at $\lambda \sim 24.8$ Å is examined in more detail because there are strong differences of the relative line strengths.

The line is formed from three transitions from the ground state (first level) to the second, third, and fourth level of N VII (triplet, table 7.4). The wavelengths of these transitions lie very close together and the single lines cannot be distinguished from each other because the Doppler effect broadens each line. In figure 7.68 the bound-bound radiative and collision rates for the three transitions calculated with data from APED (solid lines) and data from CHIANTI4 (dashed lines) are shown. In all three cases the collision rates are consistent. Differences in the radiative rates are negligible for the transition to the third level and they are small for the transition to the fourth level but for the transition to the second level they are large.

In order to examine if the difference in the radiative rates of the transition to the second level is responsible for the different strengths of the N VII line, the Einstein A-values of the transitions must be compared (table 7.8). The differences in the radiative rates can be reproduced with the differences in the A-values. For the transition from the ground state to the second level the A-values are different by about three orders of magnitude but the absolute value of the larger A-value for this transition lies around six to seven orders of magnitudes below the A-values of the other transitions and cannot be

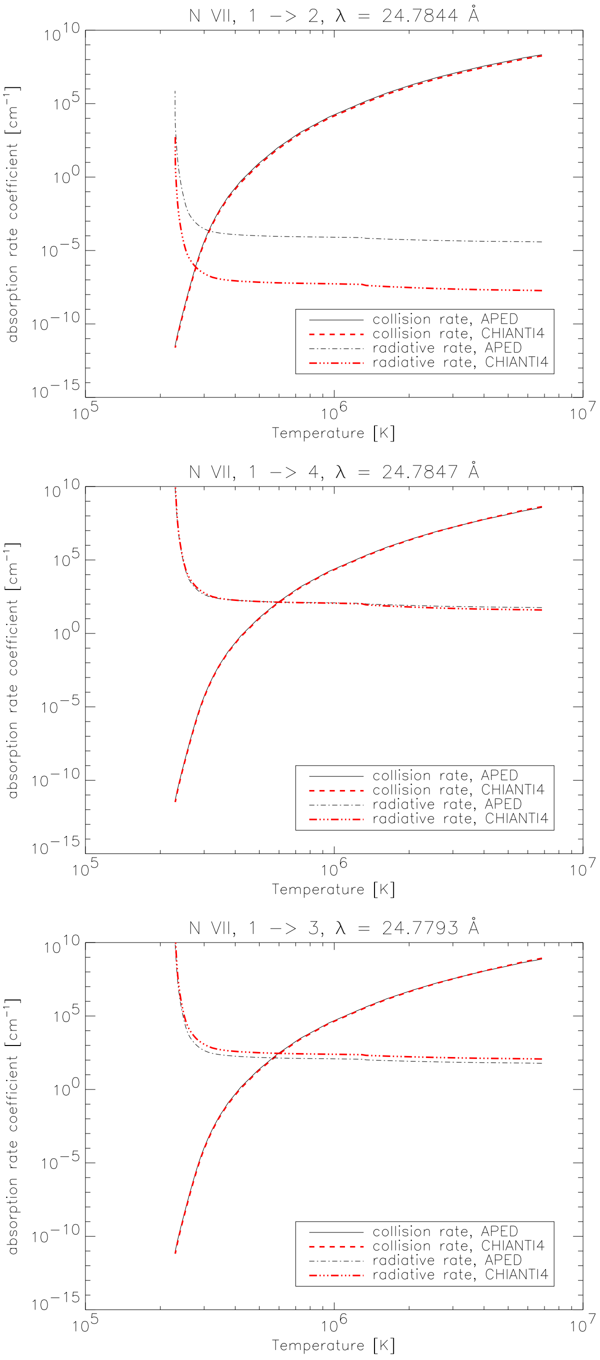

Figure 7.68: Bound-bound collision and radiative rates for the transitions of N VII from the ground state (first level) to the second, third, and fourth level calculated with data from CHIANTI4 and APED. The wavelengths of the transitions are given in the plots.

transition	λ in Å	A-value in s^{-1} (APED data)	A-value in s^{-1} (CHIANTI4 data)
$1 \rightarrow 2$	24.7844	9.87×10^5	7.07×10^2
$1 \rightarrow 3$	24.7847	1.48×10^{12}	1.51×10^{12}
$1 \rightarrow 4$	24.7793	7.40×10^{11}	1.51×10^{12}

Table 7.8: Einstein A-values for the transition triplet of N VII at $\lambda \sim 24.8$ Å from the APED and CHIANTI database. The transitions take place between the ground level (first level) and the second, third, and fourth level in N VII.

responsible for the different strengths of the N VII line. The results from comparisons of the rates for other strong transitions of different elements and ionization stages are qualitatively the same.

If the collision and radiative rates of the bound-bound transitions are not responsible for the different line strengths of the N VII line at $\lambda \sim 24.8$ Å, a change in the continuum flux must influence the relative line strength. This is also the case for the flux at $\lambda \lesssim 22$ Å and can be explained by different continuum rates or by a different background opacity from spectral lines or electron collisions which are different in number or have different rates in the two databases.

In order to determine from which chemical element these effects are produced the databases have been "mixed". It is assumed that either nitrogen or oxygen or both elements are responsible for these effects because only the nitrogen and oxygen abundances do change if different databases are used. Therefore, models with data from CHIANTI has been calculated but APED was used for the data of nitrogen, oxygen or for both elements simultaneously. The calculated spectra are compared in the figures 7.69 to 7.71 with the spectrum which fits best to the March 2003 observation and which was calculated with APED data.

If the data of nitrogen were changed from CHIANTI to APED (figure 7.69), the N VII line at $\lambda \sim 24.8$ Å and the O VII line at $\lambda \sim 21.6$ Å are still weaker than in the spectrum which was calculated with APED data but the continuum fluxes at $\lambda \lesssim 22$ Å agree better. If oxygen was calculated with APED data instead of CHIANTI data (figure 7.70), the strengths of the nitrogen line agree very good but the continuum fluxes and the line strengths of the O VII line do not. If the combined effects of nitrogen and oxygen are examined (figure 7.71) there are still discrepancies in the line strengths of the N VII and O VII lines and in the continuum fluxes.

Therefore, the data of carbon and iron were also changed from CHIANTI

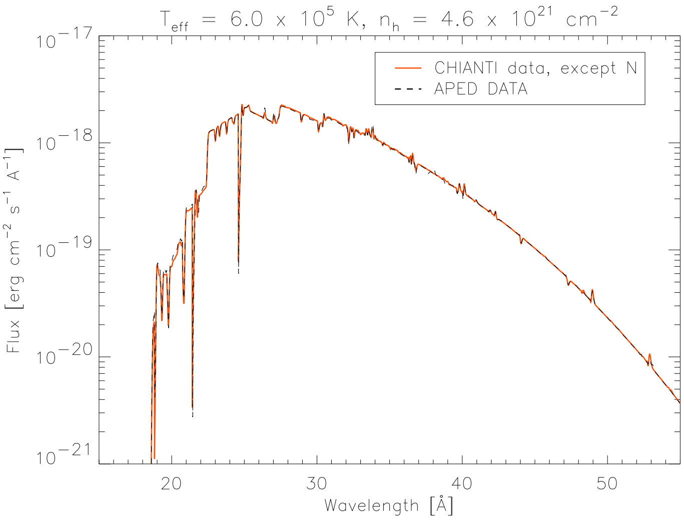

Figure 7.69: Comparison of model spectra. The spectrum which is plotted with the bold line was calculated with CHIANTI data, whereas nitrogen was calculated with APED data, and the spectrum which is plotted with the dashed line was completely calculated with data from APED.

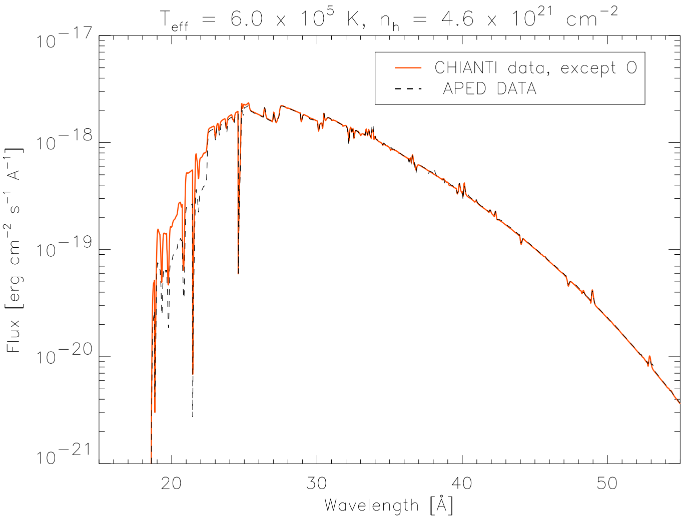

Figure 7.70: Comparison of model spectra. The spectrum which is plotted with the bold line was calculated with CHIANTI data, whereas oxygen was calculated with APED data, and the spectrum which is plotted with the dashed line was completely calculated with data from APED.

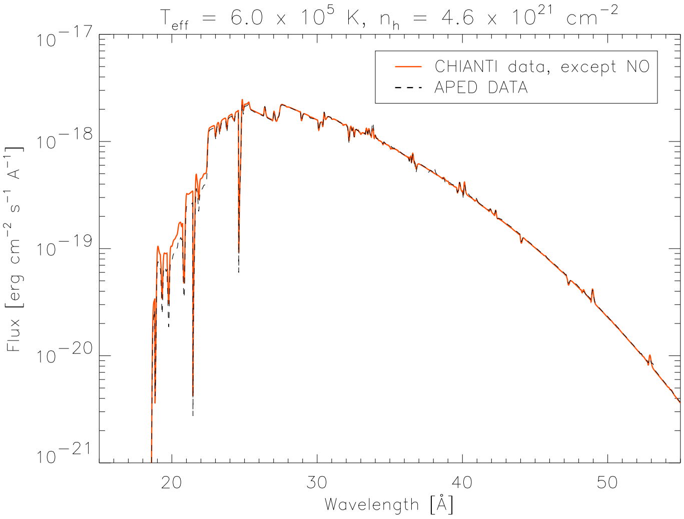

Figure 7.71: Comparison of model spectra. The spectrum which is plotted with the bold line was calculated with CHIANTI data, whereas nitrogen and oxygen were calculated with APED data, and the spectrum which is plotted with the dashed line was completely calculated with data from APED.

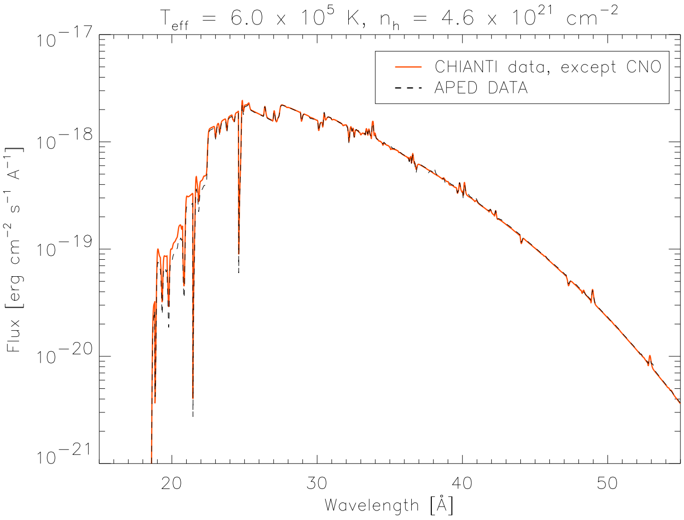

Figure 7.72: Comparison of model spectra. The spectrum which is plotted with the bold line was calculated with CHIANTI data, whereas carbon, nitrogen, and oxygen were calculated with APED data, and the spectrum which is plotted with the dashed line was completely calculated with data from APED.

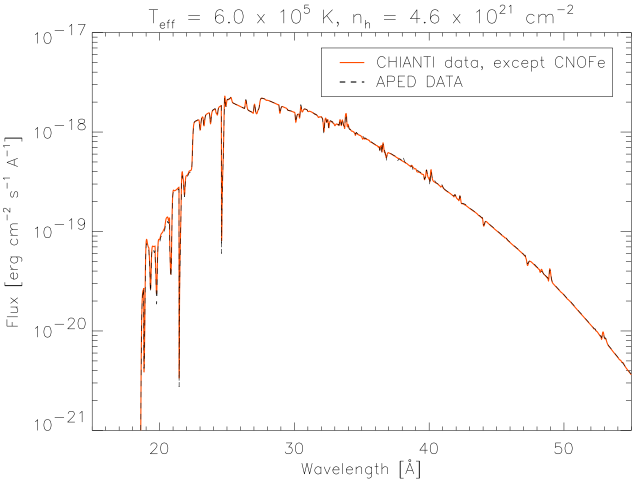

Figure 7.73: Comparison of model spectra. The spectrum which is plotted with the bold line was calculated with CHIANTI data, whereas carbon, nitrogen, oxygen, and iron were calculated with APED data, and the spectrum which is plotted with the dashed line was completely calculated with data from APED.

to APED (figure 7.72 and 7.73). There are still discrepancies between the spectra but they are much smaller now. The discrepancies must be an overall effect of the radiative and collision rates of all elements which are included in the calculations caused by different background and continuum opacities from different number of lines in the databases. The strongest effects are from carbon, nitrogen, oxygen, and iron.

7.3.2 Models with data from APED

As explained in section 6.2, there are multiple sets of atomic data in APED. In table 7.9 the ions with different datasets are shown. For all other ions there is only one dataset. The identification (ID) and the literature reference of the datasets are given. The datasets with the IDs which are printed in bold face are used in the “standard dataset”[2] of APED. All models in section 7.1 and 7.2 are calculated with the “standard dataset”.

Most of the datasets have no effect on the quality of the fit. Different model spectra are only obtained from datasets with the ID 'chi1'. These data are taken from the CHIANTI database. The effects of data from CHIANTI on the model spectra have already been examined in section 7.3.1.

---

[2] dataset of APED which is used for most of the calculations

Ion	ID	Ref.
He I	**qub1**	6
	qub2	6
C V	**mix1**	16
	mix2	16
	mix3	3,5
C VI	**mix1**	1
	mix2	1
	mix3	3,1
N VI	**int1**	4
	int2	4
	int3	3,5
N VII	**int1**	14
	int2	14
	int3	3,1
	int4	3,1
O VII	**mix1**	16
	mix2	16
	mix3	3,5
O VIII	**mix1**	1
	mix2	1
	mix3	3,1
	mix4	3,1
Ne VIII	chi1	15
	mix1	11,13,12
Ne IX	**mix1**	16
	mix2	16
	mix3	3,5
Ne X	**mix1**	1
	mix2	1
	mix3	3,1
	mix4	3,1
Mg X	chi1	15
	mix1	13,12
Mg XI	**mix1**	16
	mix2	16
	mix3	3,5
Mg XII	**mix1**	1
	mix2	1
	mix3	3,1
	mix4	3,1
Al XII	**mix1**	4
	mix2	4
	mix3	3,5
Al XIII	**mix1**	14
	mix2	14
	mix3	3,1
	mix4	3,1
	mix5	3,1
Si XII	chi1	15
	mix1	13,12
Si XIII	**mix1**	16
	mix2	16
	mix3	3,5
Si XIV	**mix1**	1
	mix2	1
	mix3	3,1
	mix4	3,1
S XIV	chi1	15
	mix1	13,12
S XV	**mix1**	16
	mix2	16
	mix3	3,5
S XVI	**mix1**	1
	mix2	1
	mix3	1,3
	mix4	1,3
Fe XVII	chi1	15
	mix2	9
	zer1	8
Fe XVIII	chi1	15
	mix2	9
	zer1	8
Fe XIX	chi1	15
	mix2	9
	zer1	8
Fe XX	chi1	15
	mix2	9
	zer1	8
Fe XXI	chi1	15
	mix4	9
	zer1	8
Fe XXII	chi1	15
	mix4	9
	zer1	8
Fe XXIII	chi1	15
	mix2	9
	zer1	8
Fe XXIV	chi1	15
	mix2	9
	zer1	8
Fe XXV	**mix1**	16
	mix2	16
	mix3	3,5
Fe XXVI	**mix1**	1
	mix2	1
	mix3	3,1
	mix4	3,1

References	1	J. Shapiro, G. Breit (1959), Phys.Rev. 113, 179
	2	W. J. Boardman (1964), ApJS 9, 185
	3	D. H. Sampson, S. J. Goett, R. E. H. Clark (1983), ADNDT, 29, 467
	4	J. A. Fernley, M. J. Seaton, K. T. Taylor (1987), JPhysB 20, 6457
	5	G. W. Drake (1988), CaJPh 66, 586
	6	P. M. J. Sawey, K. A. Berrington (1993), ADNDT 55, 81
	7	D. A. Verner, D. G. Yakovlev (1995), A&AS 109, 125
	8	L. Hullac (1997), unpublished
	9	L. Liedahl (1997), unpublished
	10	L. Liedahl (2000), unpublished
	11	APED (2002), unpublished
	12	L. Liedahl (2002), unpublished
	13	P. Podobed (2002), unpublished
	14	APED Approximation
	15	CHIANTI Database
	16	NIST Database

Table 7.9: Multiple line data in the APED database. For each ion with multiple data the identification of the datafile (ID) and the references are given. The ID is part of the filenames in APED where the data are saved. The datasets with the IDs which are printed in bold face are used in the "standard dataset".

7.4 The X-ray emission of nova V4743 Sgr

In this section the results of the models of nova V4743 Sgr will be summarized and a model for the emission and evolution of X-rays from nova V4743 Sgr will be developed.

The structure of the atmosphere has been examined in section 7.1.4. The results which are obtained from models for the X-ray range are consistent with the results of models for the previous nova atmospheres from `PHOENIX` (section 5.2). The atmosphere is geometrically extended ($R_{\rm out}/R_{\rm in} = 2074$ for a model atmosphere with $T_{\rm eff} = 6.0 \times 10^5\,{\rm K}$) and the range of temperatures inside the atmosphere is large ($T = 2.4 \times 10^5\,{\rm K}$ to $T = 6.8 \times 10^6\,{\rm K}$ for a model atmosphere with $T_{\rm eff} = 6.0 \times 10^5\,{\rm K}$). The temperature decrease in the inner part of the atmosphere (for $R/R_{\rm in} \sim 10$) is very steep and it is flat in the outer part.

Only the highest ionization stages of the chemical elements are present in the atmosphere. This is shown in the figures 7.3 and 7.31 to 7.38. In figure 7.43 the run of the gas density in the atmosphere is examined. As in the case of the temperature structure, there is a steep decrease of the density in the inner part of the atmosphere. In the regions with high temperatures, the density is relatively high ($\rho \sim 10^{18}\,{\rm cm}^{-2}$ for a model atmosphere with $T_{\rm eff} = 6.0 \times 10^5\,{\rm K}$). In the line forming regions, the radiative rates dominate the collision rates (figure 7.68) and the departures from LTE are large. The strength of the departures from LTE can be shown with the NLTE departure coefficients in the figures 7.44 to 7.54.

The NLTE effects on the temperature structure are small (figure 7.30) but they can be observed in the model spectra (figure 7.5 to 7.21) and in the partial pressures (figure 7.39 to 7.42). The comparison of the partial pressures for models calculated in LTE and in NLTE shows under- and overionization effects because the Saha-Boltzmann equation is no longer valid in NLTE. Carbon, nitrogen, oxygen, and iron show the strongest NLTE effects.

The NLTE effects change the ionization balances and the continuum flux increases. This effect is strongest below $\lambda \lesssim 25\,$Å, the ionization edge of C VI. The strongest NLTE effects on the continuum arise from the edges of C VI, N VI, N VII, and O VII. The strength of effects from the iron edges cannot be determined because there exists a “forest of spectral lines” from Fe XVII to Fe IXX in the X-ray spectral range. Therefore, it is impossible to distinguish between line and continuum absorption from iron. The effects of line blanketing from weak spectral lines are very important and have to be included into the calculations.

NLTE effects also influence the strengths of spectral lines. Absorption and emission lines are always weaker if they are treated in NLTE. Furthermore, NLTE can turn emission lines into absorption and vice versa.

As in the previous nova model atmospheres, there is very little dependence of the spectrum on the bolometric luminosity. The relative strength and shape of the spectral lines do not change significantly but the total flux does. Hence, it is not possible to determine the distance to the nova with the models because the modeled flux has to be scaled to the observed flux by a constant factor when the model spectra are fitted to the observations.

It is impossible to determine L_{bol} with the `PHOENIX` models and, therefore, the distance to the nova. The radius of the shell depends on L_{bol} and T_{eff} and the mass loss rate depends on the shell radius (equation 5.3). Therefore, with an unknown L_{bol} or distance, the shell radius and the mass loss rate cannot be determined.

In section 7.1.1 it has been shown that the bremsstrahlung emission is the dominant continuum emission process for X-rays in classical novae of the kind of V4743 Sgr. Observations can only be fitted with spectra calculated with the 'new bremsstrahlung' (section 6.5, figure 7.2). Figure 7.1 shows that bremsstrahlung is primarily emitted in the deeper layers of the atmospheres. This is near to the surface of the WD where the CNO burning is still 'on' (section 2.2). The material is highly ionized in these layers and a strong bremsstrahlung continuum can be produced.

The optically thick nova wind is like an absorber for the continuum emission and strong spectral lines are formed. The continuum is absorbed strongest below $\lambda \sim 25\,\mathrm{\AA}$. The strongest effects are from carbon, nitrogen, oxygen, and iron absorption (figures 7.8 to 7.10 and 7.20 to 7.21). Lines are formed from highly ionized elements because in the line forming region the temperatures are very high. The strongest lines arise from carbon, nitrogen, and oxygen, the same elements which affect the continuum flux the most. From the expansion of the medium the spectral lines are broadened via the Doppler effect.

It is resumed that *the X-ray spectrum of nova V4743 Sgr is formed by a thermal bremsstrahlung continuum emission from the hot atmosphere surrounding the WD and by a strong absorption in continuum and lines from the hot, optical thick, expanding medium.* Therefore, the theory for the X-ray emission mechanism from hot circumstellar material in section 2.2 can be confirmed with the `PHOENIX` models. The importance of shocks cannot be determined because shock processes are not included in the code. But from fitting models and observations they seem to be unimportant in the shell of nova V4743 Sgr.

The element abundances in the shell affect the continuum and line absorption very strongly. In the figures 7.60 to 7.64 spectra calculated with different abundances of helium, carbon, nitrogen, oxygen and iron are compared.

The observations of nova V4743 Sgr from March 2003, July 2003, September 2003, and February 2004 are fitted with model spectra. The synthetic spectra first have been calculated with solar abundances (figures 7.24 to 7.27). There are discrepancies in the fits to the continuum and in the fitted line strengths. These can be explained by the use of solar abundances which are wrong for nova atmospheres (section 2.1.6). In the models, the lines of carbon, nitrogen, and oxygen are too weak and the iron lines are too strong. Therefore, models with abundances of carbon, nitrogen, and oxygen which are greater than in the sun and with an iron abundance which is lower than the solar value are calculated. Best fits with non-solar abundances are shown in the figures 7.56 to 7.59 for the four observations of V4743 Sgr.

T_{eff}, n_h and the abundances of helium, carbon, nitrogen, oxygen, and iron have been determined from the fits. With the different observations the time evolution of these parameters can be examined. The parameters of the fits are given in table 7.6. Between the observations from March and July 2003 the effective temperature of the nova atmosphere is changing from $T_{\text{eff}} = 6.0 \times 10^5\,\text{K}$ to $T_{\text{eff}} = 5.8 \times 10^5\,\text{K}$ and there is no change between July and September 2003. In February 2004, the effective temperature is $T_{\text{eff}} = 5.4 \times 10^5\,\text{K}$ which is cooler than in 2003. *The effective temperature of the nova is essentially constant between March and September 2003 but it becomes lower between September 2003 and February 2004. The n_h of the fit decreases in all observations because the nova shell is expanding and the circumstellar material becomes thinner.* The values of n_h are always higher than the value from Dickey & Lockman (1990) which includes only interstellar and no circumstellar absorption which is important in nova atmospheres.

The spectral lines in the July 2003, September 2003, and February 2004 observations are weaker than in the observation from March 2003. Either there is a change in the nova wind or there is a change in the abundances which absorbs the continuum flux stronger (possible errors in the observations must always be assumed).

The density gradient n (equation 5.2) and the the mass loss rate $\dot{M}$ (v_{out}, equation 5.3) may change. For a stronger line absorption the wind has to become optically thicker. Different synthetic spectra which have been calculated with the same set of abundances as used in the fit for the observation from March 2003 but with different n, v_{out}, and T_{eff} do not fit to the observations as well as the model spectra which are fitted in figure 7.56 to 7.59. Models with different n will be presented in section 8.2.

A change in the element abundances may be caused by material which is ejected from the WD surface into the wind during the evolution of the nova. Due to the ongoing CNO burning on the top of the WD this material may has different abundances of helium, carbon, nitrogen, and oxygen.

Two problems are complicating the abundance analysis. *On the one hand the absolute abundance analysis strongly depends on the atomic data* (Errors from fitting the observation by eye are much smaller). On the other hand there exist only three observations for which the abundances can be determined (The quality of the February 2004 observation is very poor). Three datapoints are not statistically significant. The abundances in table 7.6 are determined with models which were calculated with atomic data from APED and the abundances in table 7.7 were determined with atomic data from the CHIANTI database (There are no differences in the synthetic spectra which were calculated with CHIANTI4 and CHIANTI5).

If there are changes in the element abundances between March and July 2003, the abundance of nitrogen increase, the abundances of helium and oxygen decrease and the abundance of iron stays the same. In the case of APED data the abundance of carbon increases and it decreases for data from CHIANTI. Between July and September 2003 the nitrogen abundance decreases but only about one times the solar abundance for both databases. This can arise from observation errors. Therefore, between July and September 2003 the abundances are essentially constant. In the fits of the observation from March 2003 the nitrogen and oxygen abundances are changing if APED or CHIANTI is used and in fits of the July and September 2003 observations all abundances, except the abundance of iron, are changing when different data are used in the models.

The determination of absolute values for the abundances is very inaccurate but the evolution of the abundances between different observations is independent from the atomic data. A possible theory of the evolution which does not deal with absolute abundance values is also independent from the atomic data.

If an evolution in the abundances exists, the abundances of helium, carbon, nitrogen, and oxygen change only between March and July 2003. According to the assumption above, no more matter will be ejected from the WD surface into the nova wind after July 2003. The CNO-burning on the WD slows after September 2003 and T_{eff} *is lower in the observation in February 2004.*

A constraint on the evolution of the CNO burning is a constant number of CNO atoms with time. This is much better fulfilled for the abundances determined with APED than with CHIANTI data. From equilibrium CNO burning it is assumed that the abundance of nitrogen has to increase and the abundance of carbon must decrease. An increase of the nitrogen abundance between March and July 2003 is obtained with the APED and CHIANTI data but a decrease of the carbon abundance is only obtained with the CHIANTI data and it stays constant for the APED data. From an evolution theory of the abundances *it cannot be determined which kind of atomic data is better.*

More sources of errors of the abundance analysis exist which can explain the discrepancies between the models and observations. In `PHOENIX` the nova shell is treated as a homogeneous medium. Density clumps absorb flux at distinct wavelengths and influence or form absorption lines. Multiple components with different temperature structures can exist in the nova shell. The line strength strongly depends on the temperature in the line forming region and different components can form lines at different wavelengths or affect lines from other components. This can explain the lines which are too weak or missing in the synthetic spectra.

The line widths in the synthetic spectra are too small and models with higher expansion velocities cannot solve this problem. The expansion velocity of $v_{\rm out} = 2500\,{\rm km\ s^{-1}}$ from the observations (section 3.2) is used in the calculations. The shape and strength of the spectral lines can be affected by the velocity law. A velocity field from a β-wind law (equation 4.1) may alter the spectrum and the determined abundances. Models with different velocity laws and inhomogeneities must be calculated in the future.

7.5 Comparison of results from `PHOENIX` with `TMAP`

Rauch et al. (2005) have modeled the atmosphere of nova V4743 Sgr and compared their model spectra with a X-ray spectrum observed with XMM-Newton. The observation was obtained on 2003 April 4, 16 days after the first LETGS observation with CHANDRA (section 3.2).

Rauch et al. (2005) used TMAP, the Tübingen NLTE Model Atmosphere Package (Werner et al. 2003; Rauch & Deetjen 2003) to model the spectrum. The models are calculated plane parallel, static, and in NLTE. In order to consider the expansion of the medium, the synthetic spectra are shifted in wavelength after they have been calculated. This shift is equal to the amount which the expansion would shift the observed spectrum. In the models for V4743 Sgr, 332 individual line transitions between 208 levels of hydrogen, helium, carbon, nitrogen, oxygen, neon, magnesium, and sulfur in NLTE and 409 levels in LTE are considered.

The best fits to the XMM observation are shown in figure 1 of Rauch et al. (2005). If the observation is fitted with a spectrum which was calculated with solar abundances, $T_{\rm eff} = 7.05\times10^5$ K is obtained. From models with non-solar abundances Rauch et al. (2005) obtained the best fit for a model atmosphere with a lower effective temperature of $T_{\rm eff} = 6.1 \times 10^5$ K and for abundance ratios of H:He:C:N:O = 18.9:75.1:0.0006:0.016:5.96. These abundances are

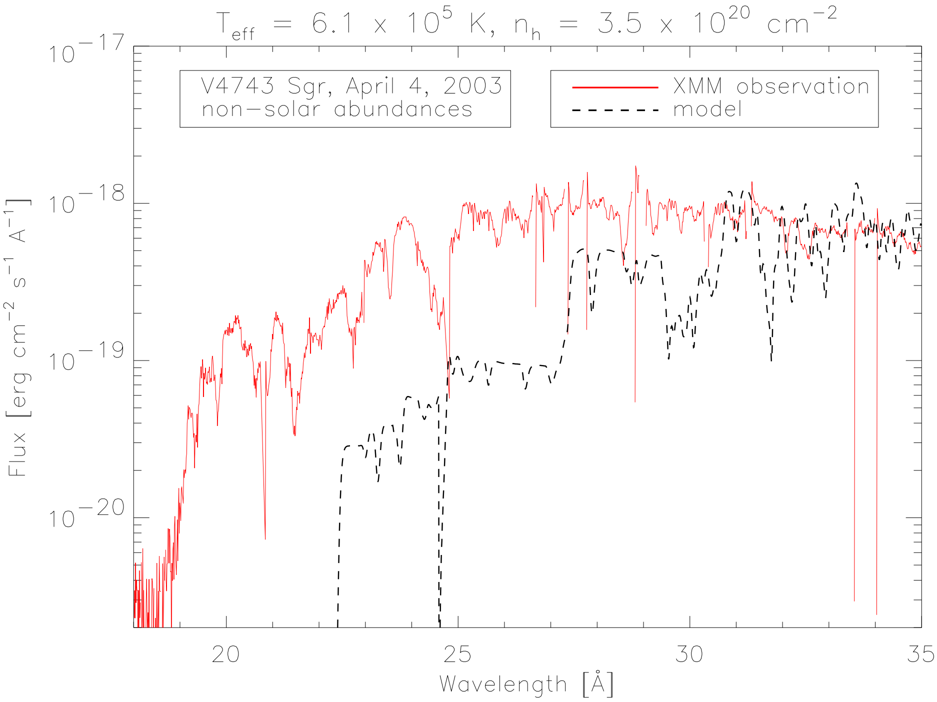

Figure 7.74: Fit for a model spectrum to the XMM observation of nova V4743 Sgr from 2003 April 4. The spectrum was calculated with `PHOENIX`. The same $T_{\rm eff}$, n_h, and the same set of abundances like in Rauch et al. (2005) was used in the calculations.

different to the results from `PHOENIX`.

The hydrogen column density of the best fit from Rauch et al. (2005) was determined with $n_h = 3.47 \times 10^{20}\,{\rm cm}^{-2}$. It is lower than $n_h = 1.41 \times 10^{21}\,{\rm cm}^{-2}$ from Dickey & Lockman (1990) which is obtained for interstellar absorption. This is unreliable because the n_h to fit the spectrum of a nova atmosphere must also contain the circumstellar absorption and has to be higher than the n_h obtained from interstellar absorption alone.

A spectrum with the same abundance ratio and $T_{\rm eff}$ was calculated with `PHOENIX` and fitted to the XMM observation, using the same n_h (figure 7.74). The `PHOENIX` model does not fit to the observation. The differences may be caused by the use of different physical conditions like an expanding, spherically symmetric atmosphere in `PHOENIX` models instead of a static, plane parallel atmosphere in models from TMAP. In section 7.3 the existence of large effects of different atomic data on the synthetic spectra has been shown. TMAP does not use CHIANTI and APED in the model calculations but an own database for atomic data (Rauch & Deetjen 2003).

Chapter 8

Model atmospheres for other supersoft X-ray sources

The model atmospheres which have been calculated for other supersoft X-ray sources (SSS) are presented in this chapter. Fits to the observation of nova V1494 Aquilae (V1494 Aql) on 2000 September 28 with CHANDRA's LETGS are shown in section 8.1. Discrepancies between the models and the observation are discussed.

Models for the CHANDRA observations of the supersoft X-ray binary sources (SSBS) CAL 83 and CAL 87 are presented in section 8.3. Before, models with different density gradients n are shown in section 8.2 because the nature of SSBS is different to CNe and spectra of these models have been tested to fit the observations of CAL 83 and CAL 87.

8.1 Models of V1494 Aql

Model atmospheres of the observation of V1494 Aql on 2000 September 28 with CHANDRA have been calculated with `PHOENIX`. The observation has been presented in section 2.3. Two possible interpretations of the observed spectrum have been discussed. On the one hand it is assumed that the spectrum is dominated by a strong soft continuum component with superimposed emission features which cannot yet be identified with any known emission lines. On the other hand it can be interpreted as an absorption spectrum with less absorption where the emission features appear.

The nature of the spectrum must be determined with fits of synthetic spectra to the observation. As in the case of nova V4743 Sgr a very large model grid with different T_{eff} and different sets of abundances of elements like helium, carbon, nitrogen, oxygen, and iron must be calculated. Two different

Parameter	Figure 8.1 (emission)	Figure 8.2 (absorption)
T_{eff} in 10^5 K	5.8 ± 0.2	5.8
n_h in $10^{21}\,\mathrm{cm}^{-2}$	7.0 ± 0.1	3.0
He-abundance in $\odot$	3.0 ± 0.5	3.0
C-abundance in $\odot$	1.0 ± 0.5	2.0
N-abundance in $\odot$	30.0 ± 3.0	20.0
O-abundance in $\odot$	20.0 ± 3.0	10.0
Fe-abundance in $\odot$	0.1 ± 0.1	0.1

Table 8.1: Parameters for the fits to the observation from September 2000 of nova V1494 Aql in the figures 8.1 and 8.2. The abundances are relative to the solar values.

fits to the observation with the parameters from table 8.1 are shown in the figures 8.1 and 8.2. If the nature of the observation is an emission spectrum and if strong discrepancies between model and observation are considered, the model may be of the kind of the first fit. To fit a possible absorption spectrum, the second fit has been found.

In the first fit (figure 8.1), the continuum component is modeled relatively well but the emission lines are missing in the synthetic spectrum because the emission features are formed in an other atmosphere component which is not included in the model. This component is at larger radii, less optically thick, and colder than the modeled component. Therefore, the observation could be an emission line spectrum. The emission features cannot be identified with the synthetic spectra.

In the second fit (figure 8.2), the modeled continuum flux is too high nearly everywhere. If the synthetic spectrum should fit an absorption spectrum, nearly all absorption features are missing in the model. However, this fit is much worse than the first and it is more likely that the observed spectrum is dominated by emission instead of absorption.

The quality of both fits is not so good as the quality of the fits for nova V4743 Sgr. Due to the quality of the first fit the determined abundances are not very accurate and the errors are large (table 8.1). The quality of the second fit is such bad that the abundances which were determined from this fit are not useful. No errors are given for these abundances.

From the first fit (figure 8.1) $n_h = 7.0 \times 10^{21}\,\mathrm{cm}^{-2}$ is determined which is higher than the hydrogen column density of $n_h = 3.0 \times 10^{21}\,\mathrm{cm}^{-2}$ from the second fit (figure 8.2). There is a literature value of $n_h = 4.02 \times 10^{21}\,\mathrm{cm}^{-2}$ for V1494 Aql from Dickey & Lockman (1990) which only includes the inter-

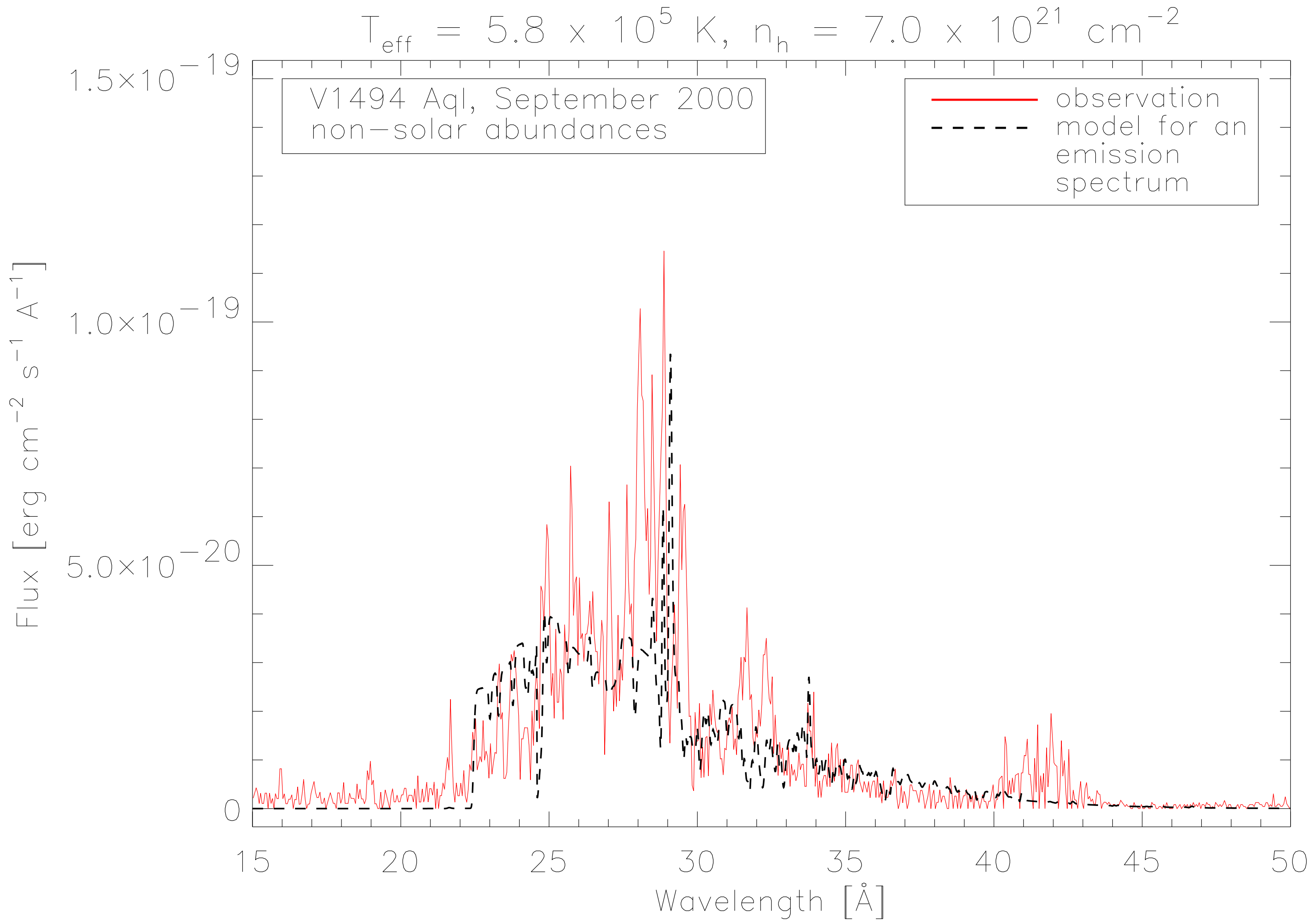

Figure 8.1: Fit of a model spectrum (dashed line) to the observation of nova V1494 Aql of September 2000 (solid line). The parameters are shown in table 8.1. If strong discrepancies between model and observation are assumed, this fit could confirm the possible emission nature of the observation.

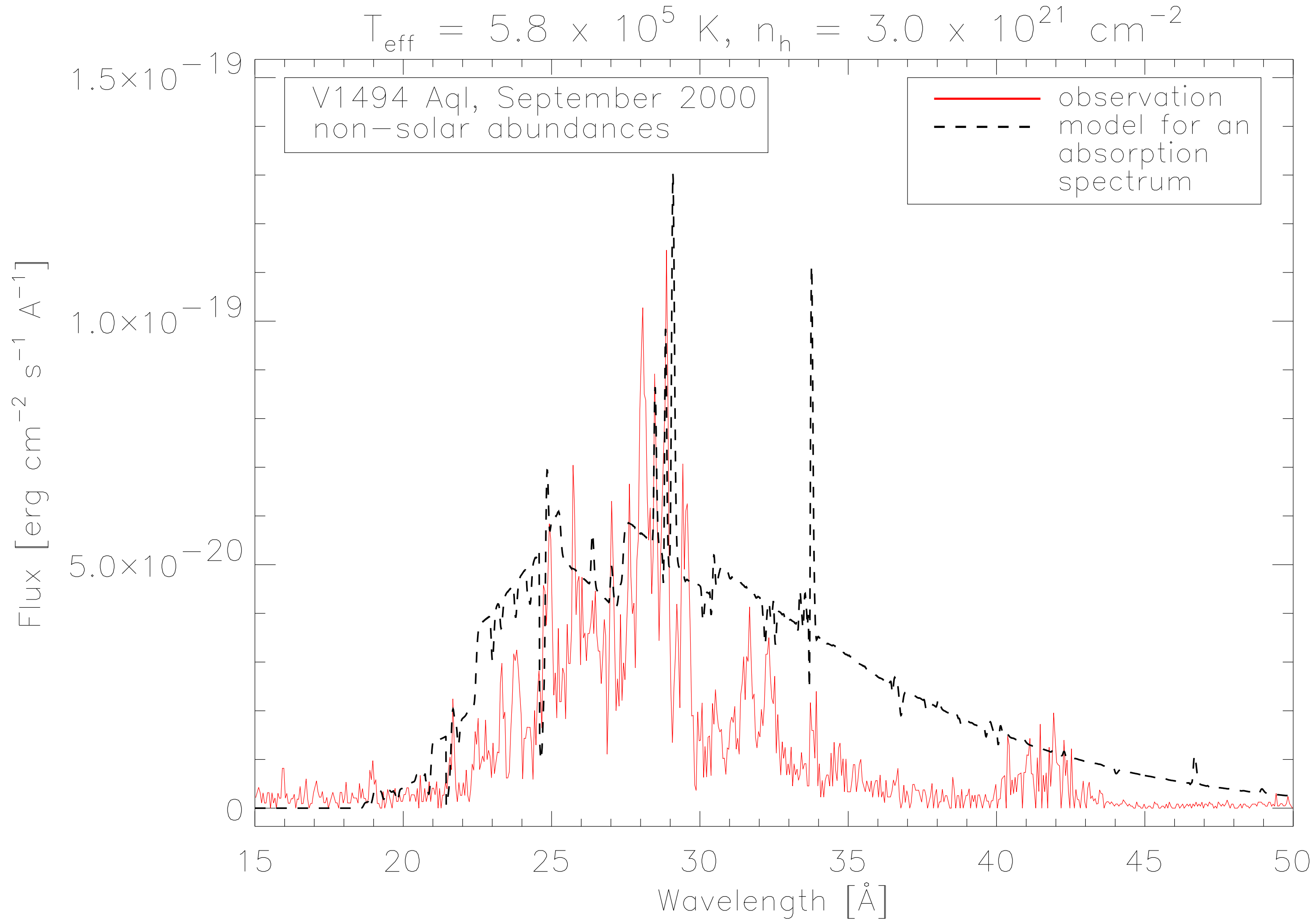

Figure 8.2: Fit of a model spectrum (dashed line) to the observation of nova V1494 Aql of September 2000 (solid line). The parameters are shown in table 8.1. This fit has been found if the observation is an absorption spectrum. It is much worse than the fit for an emission spectrum (figure 8.1).

stellar and not the circumstellar absorption. The n_h of the fist fit is larger and the n_h of the second fit is smaller than this value. This supports the first fit because the above assumed outer atmosphere component is missing in the model. In this case this component provides an additional strong contribution to n_h via circumstellar absorption.

Nova V1494 Aql is more evolved than nova V4743 Sgr. In the inner part of the atmosphere there is still continuum emission from thermal bremsstrahlung as in nova V4743 Sgr. If the observation of V1494 Aql is an emission spectrum, V1494 Aql has an optically thin nebular in the outer part in which the emission lines are formed. The shell of V1494 Aql is much larger than the shell of V4743 Sgr. In oder to include this part of the atmosphere, calculations with more optically thin atmospheric layers in the outer part of the atmosphere are necessary. The computation time will strongly increase. Due to the complexity of the model grid which is necessary to find the best fit, this could not be completed in this work and will be part of future model calculations.

8.2 Models with different density gradients n

The nature of SSBS is different to CNe and the assumption of $n = 3$ for the gradient of the density profile (equation 5.2) is no longer valid. Before the fits of synthetic spectra to the observations of the SSBS CAL 83 and CAL 87 are shown, models with different density gradients n are presented.

In the figures 8.3 and 8.4 models which were calculated with solar abundances and $n = 3$, $n = 4$, $n = 5$, and $n = 6$ are shown. The model atmospheres have an effective temperature of $T_{\text{eff}} = 6.0 \times 10^5\,\text{K}$ and are in full NLTE. With increasing n the atmosphere becomes more compact (the outer pressure is equal to $p_{\text{out}} = 10^{-1}\,\text{dyn cm}^{-2}$ in all models). The continuum flux increases and the atmosphere appears hotter. The continuum flux in the spectrum calculated with $n = 6$ and $T_{\text{eff}} = 6.0 \times 10^5\,\text{K}$ is very similar to continuum flux in the spectrum which has been calculated with $n = 3$ and $T_{\text{eff}} = 9.0 \times 10^5\,\text{K}$. In figure 8.5 these two spectra are compared. The flux of the spectrum which has been calculated with $n = 3$ was scaled by a factor of 230 which is the same as calculating this spectrum with a higher bolometric luminosity. The bolometric luminosity does not change the shape of the spectrum but the total flux (section 7.1).

Most of the spectral lines are weakening with increasing n. This is also the case of spectra if T_{eff} increases and n stays constant (figures A.1 to A.7). From the shape of the continuum flux it cannot be distinguished between different n if T_{eff} is unknown. But if models with different sets of element abundances

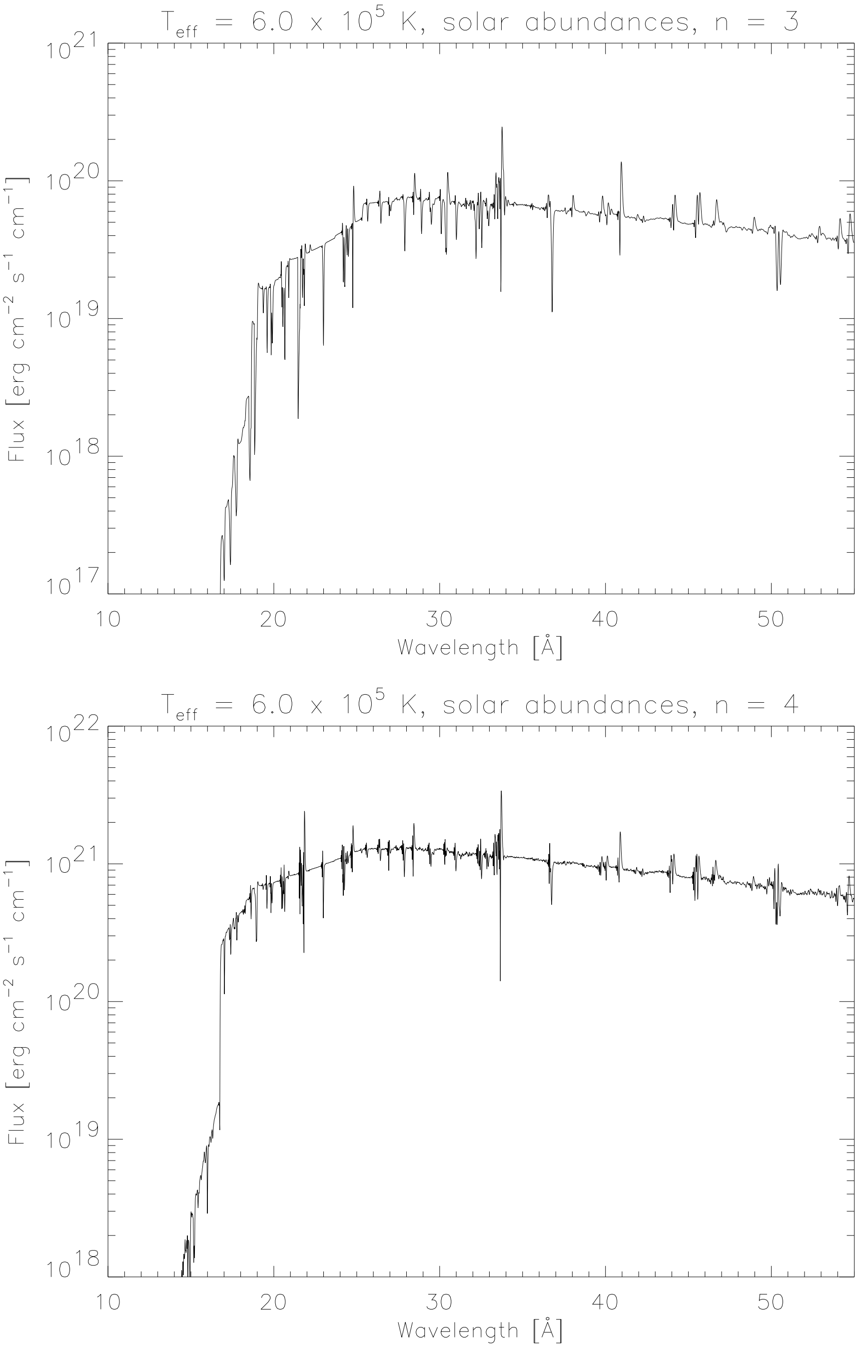

Figure 8.3: Synthetic spectra which have been calculated with solar abundances and density gradients $n = 3$ and $n = 4$. The models are calculated with $T_{\rm eff} = 6.0 \times 10^5\,$K and in full NLTE.

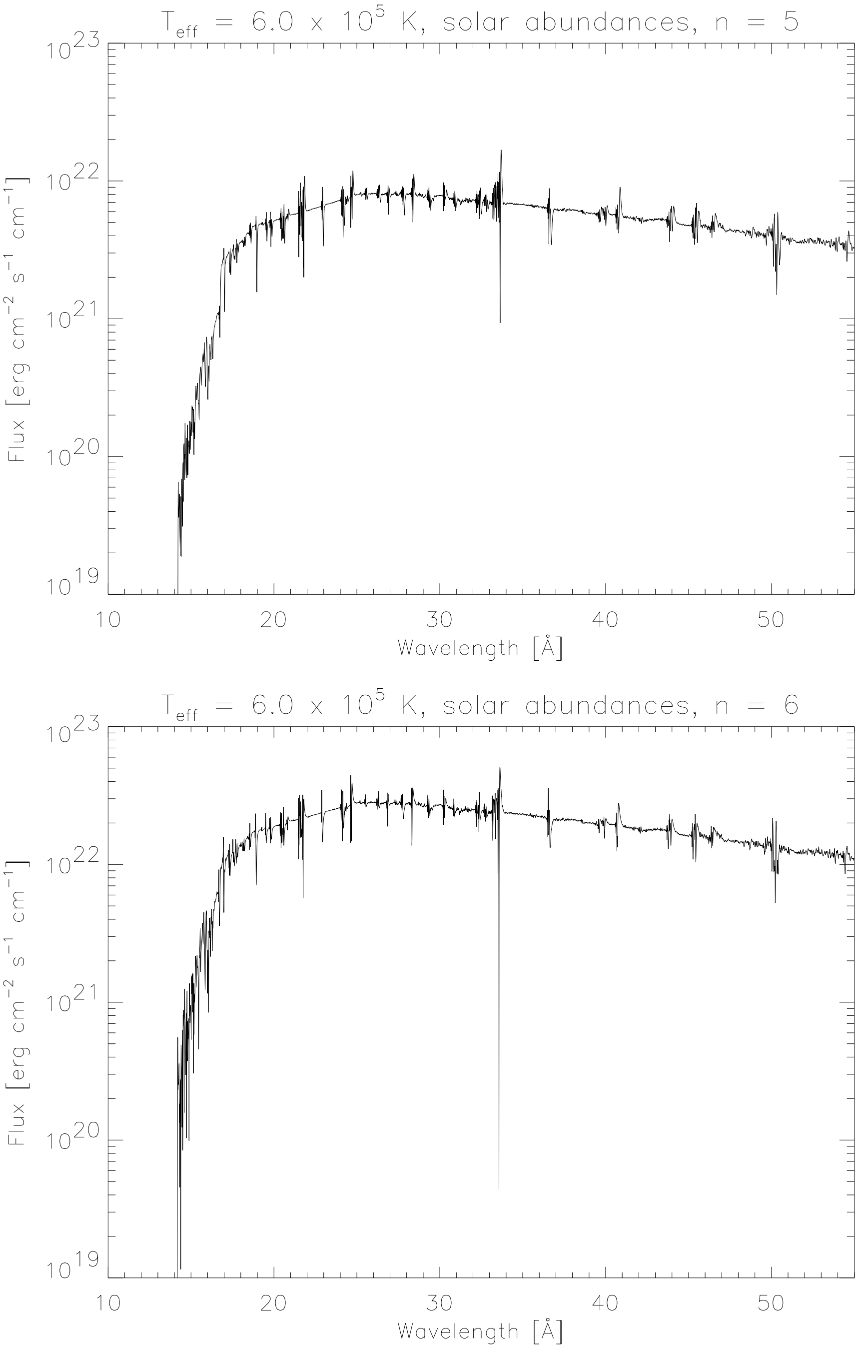

Figure 8.4: Synthetic spectra which have been calculated with solar abundances and density gradients $n = 5$ and $n = 6$. The models are calculated with $T_{\text{eff}} = 6.0 \times 10^5\,\text{K}$ and in full NLTE.

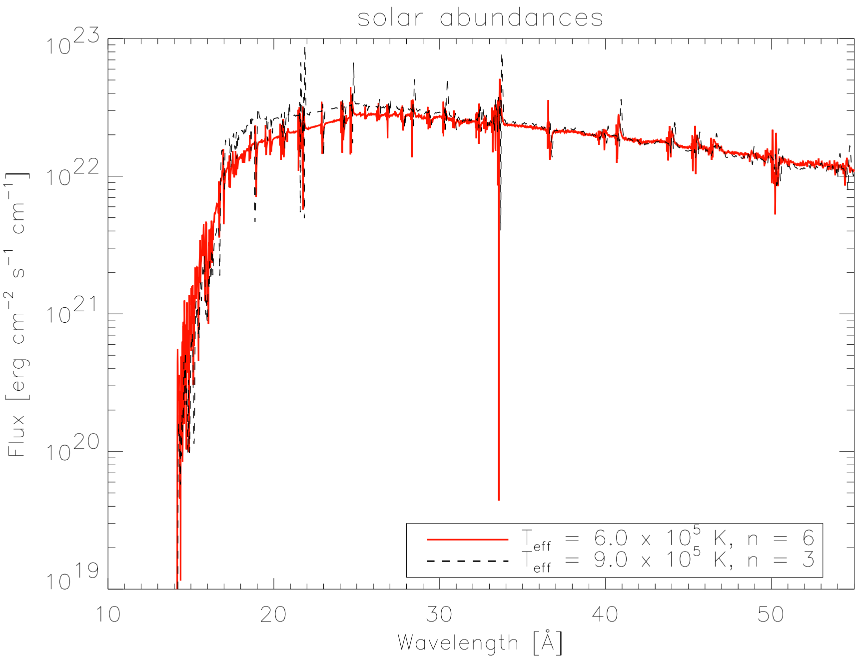

Figure 8.5: Comparison of synthetic spectra which have been calculated with solar abundances and different n and T_{eff}. The spectrum which is plotted with the dashed curve is scaled by a factor of 230.

are calculated, the changes in the relative strengths of the spectral lines show different behavior for models with different n and T_{eff}. From fitting the continuum flux and the spectral lines simultaneously, it can be determined which n has to be used in the calculations to obtain the best fit.

The temperature and gas density structure of models which have been calculated with $T_{\mathrm{eff}} = 6.0 \times 10^5\,\mathrm{K}$ and $n = 3$, $n = 4$, $n = 5$, and $n = 6$ are shown in figure 8.7 and 8.6. With increasing n the atmosphere becomes more compact. R_{out}, R_{in}, and $R_{\mathrm{out}}/R_{\mathrm{in}}$ of the models are shown in table 8.2. $R_{\mathrm{out}}/R_{\mathrm{in}}$ shrinks by a factor of 46 between models with $n = 3$ and $n = 6$. The atmosphere is heating in the inner part and cooling in the outer part if n is increasing (see table 8.2 for T_{in} and T_{out}), and the fall of the temperature is steeper in the inner part of the atmosphere (figure 8.6). If n is changing, the density values at the outer and inner edge of the atmosphere are changing only slightly (figure 8.7) but the run of the density is much steeper with increasing n.

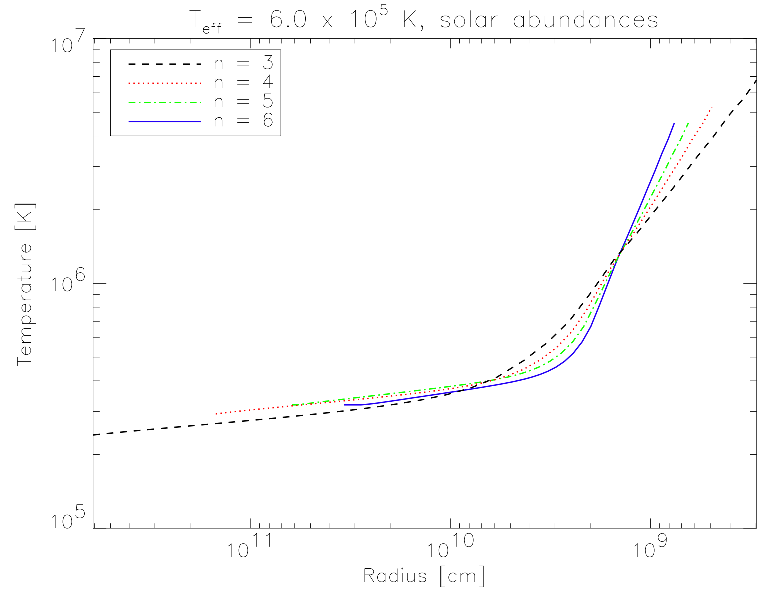

Figure 8.6: Temperature structure of model atmospheres which have been calculated with $T_{\rm eff} = 6.0 \times 10^5$ K and $n = 3$, $n = 4$, $n = 5$, and $n = 6$. The models are in full NLTE with solar abundances.

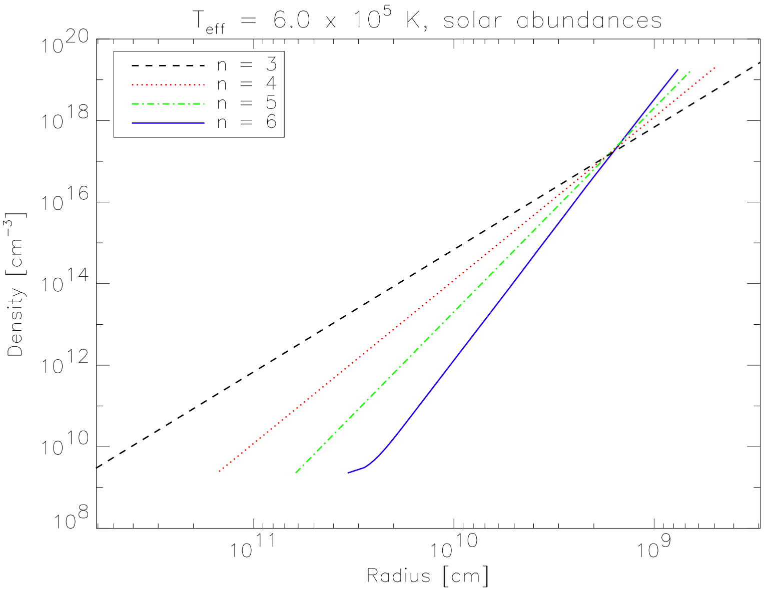

Figure 8.7: Gas density structure of model atmospheres which have been calculated with $T_{\rm eff} = 6.0 \times 10^5$ K and $n = 3$, $n = 4$, $n = 5$, and $n = 6$. The models are in full NLTE with solar abundances.

n	$R_{\rm out}$ [cm]	$R_{\rm in}$ [cm]	$R_{\rm out}/R_{\rm in}$	$T_{\rm in}$ [K]	$T_{\rm out}$ [K]
3	6.11×10^{11}	2.95×10^{8}	2074	6.78×10^{6}	2.40×10^{5}
4	1.49×10^{11}	4.93×10^{8}	302	5.25×10^{6}	2.93×10^{5}
5	6.17×10^{10}	6.46×10^{8}	96	4.52×10^{6}	3.19×10^{5}
6	3.39×10^{10}	7.59×10^{8}	45	4.10×10^{6}	3.39×10^{5}

Table 8.2: $R_{\rm out}$, $R_{\rm in}$, $R_{\rm out}/R_{\rm in}$, $T_{\rm in}$, and $T_{\rm out}$ of the models in the figures 8.6 and 8.7. n is the density gradient.

8.3 Models of CAL 83 and CAL 87

The `PHOENIX`-models for CNe in X-ray have been applied to the SSBS CAL 83 and CAL 87. Starrfield et al. (2004) have modeled semi-steady burning evolutionary sequences for these sources. The accretion of material from a companion star onto a massive WD which does not suffer a TNR was modeled but it was assumed that the CV had undergone several CN outbursts before and the WD had not yet cooled to low luminosities. Therefore, Starrfield et al. (2004) proposed that CNe and SSBS are two different phases of the evolution of the same CV. The expanding material from the previous nova outbursts should still exist. If the `PHOENIX`-models which were developed for CNe in X-ray can fit the observations of CAL 83 and CAL 87, a connection between CNe and SSBS which result in an SN Ia explosion may exist.

Models with different $T_{\rm eff}$, different density gradients n, and different grids of abundances have been calculated. CAL 83 and CAL 87 are in the Large Magellanic Cloud (LMC). The LMC has a different metallicity in comparison with the milkyway and, therefore, the metallicity has been changed in the models, too.

If the maximum of a synthetic spectrum which has been calculated with $n = 3$ should fit to the maximum of the observed spectrum of CAL 87, the effective temperature of the model atmosphere have to be higher than $T_{\rm eff} = 1.0 \times 10^6$ K. Considering the results by Parmar et al. (1997) such high $T_{\rm eff}$ are unlikely. In order to decrease $T_{\rm eff}$, n has to be increased (section 8.2). The observed maximum can be fitted with a model which has been calculated with $n = 6$ and $T_{\rm eff} = 7.0 \times 10^5$ K. This $T_{\rm eff}$ is inside the determined range from Parmar et al. (1997). Consequently, the model atmosphere would be less geometrically extended in contrast to an atmosphere with $n = 3$ (table 8.2) and should correspond rather to an extended atmosphere of a hot giant than to a nova shell. However, none of the `PHOENIX` models can fit the observations of CAL 83 and CAL 87.

As an example, a comparison of the August 2001 observation of CAL 87 and a synthetic spectrum which was calculated with $T_{\rm eff} = 7.0 \times 10^5\,$K, $n = 6$, and non-solar abundances[1] is shown in figure 8.8. The modeled continuum flux is too high but the maximum of the synthetic spectrum fits to the maximum in the observation at $\lambda \sim 19\,$Å. At $\lambda \sim 42\,$Å there is an additional maximum in the observation which may correspond to emission from a cooler component.

The model atmospheres from `PHOENIX`, calculated for CNe in X-ray which are in the constant bolometric luminosity phase and which have an optically thick wind cannot fit the observations of the SSBS CAL 83 and CAL 87. If it is assumed that the element abundances of the atmospheres of CAL 83 and CAL 87 are not very exotic and lie inside the modeled abundance grid, the above assumption from Starrfield et al. (2004) is excluded for CAL 83 and CAL 87. The second idea of Starrfield et al. (2004), an accreting, CNO burning, hot WD which is not ejecting matter, is more likely. This supports the results from Lanz et al. (2005) who have modeled static atmospheres of hot WDs. `PHOENIX`-models of static atmospheres for hot WDs with an additional layer of accreted material (this resembles an atmosphere of a hot giant star) are beyond the scope of this work and will be calculated in the future.

---

[1] $n(He) = 5 \times n(He)_\odot$, $n(C) = 2 \times n(C)_\odot$, $n(N) = 10 \times n(N)_\odot$, $n(O) = 10 \times n(O)_\odot$, $n(Fe) = 0.01 \times n(Fe)_\odot$

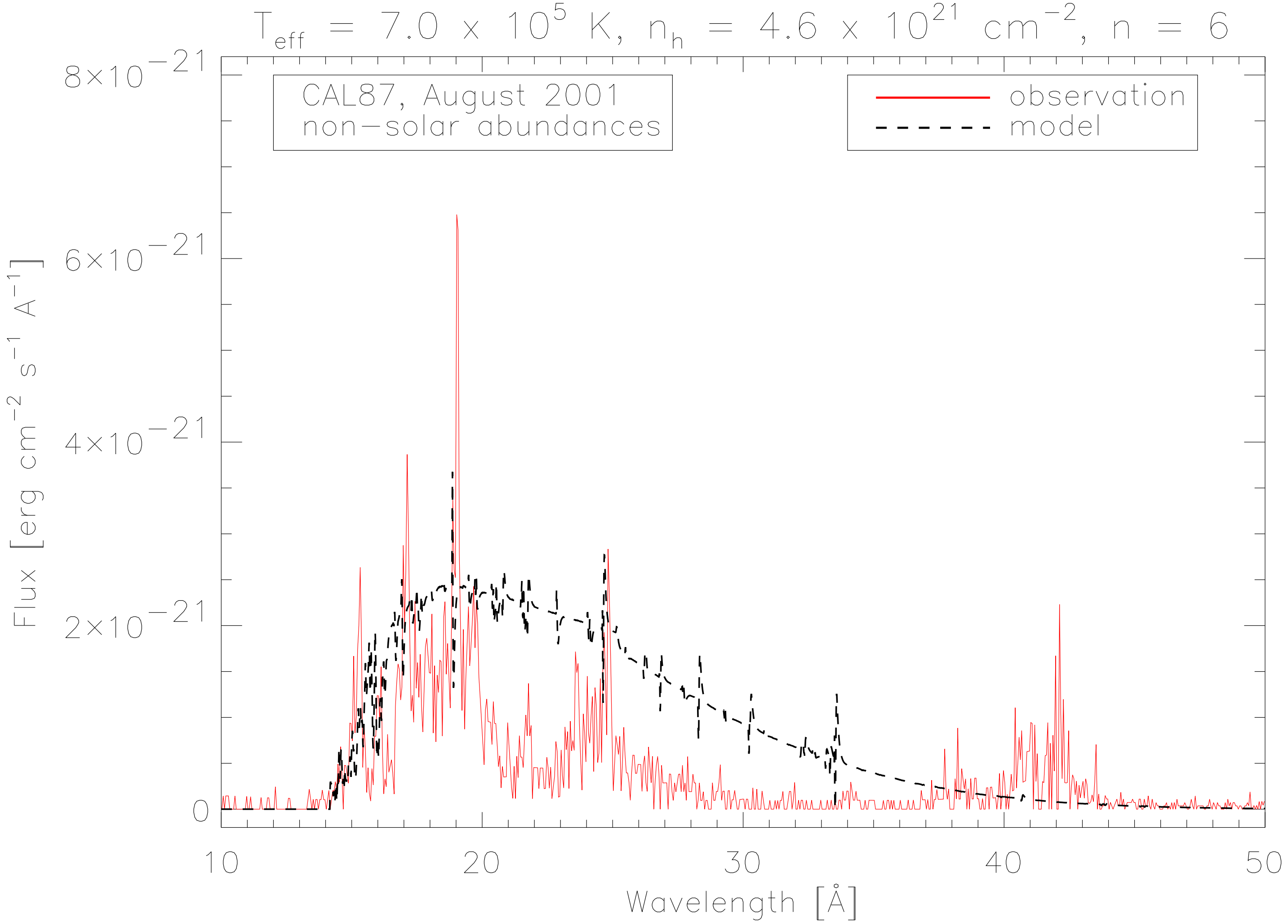

Figure 8.8: Comparison of a synthetic spectrum (dashed line) with the August 2001 observation of CAL 87 (solid line). The model has been calculated with $T_{\rm eff} = 7.0 \times 10^5\,$K, $n = 6$, and non-solar abundances. The hydrogen column density is determined with $n_h = 6.0 \times 10^{21}\,\rm cm^{-2}$ from the fit.

Chapter 9

Outlook

In section 7.4 the results of the calculations of model atmospheres for nova V4743 Sgr have been summarized. The discrepancies between the synthetic spectra and the observations can be explained by the following:

- Models are calculated for one atmosphere component and not for a multicomponent nova shell.
- Inhomogeneities are missing in the models
- Related to the second point, the models are one-dimensional.
- The models are calculated with a standard velocity field (equation 5.3) but the assumption of a β-wind law may be better for late nova shells.

In the calculation of a multicomponent atmosphere the interaction of the different components has to be considered. The radiation transport and the hydrodynamic have to be calculated for the interaction. This has not been implemented in the code yet. The different components of the atmosphere have different temperature structures and this will influence the modeled line strengths.

Inhomogeneities also modify the modeled line strengths and the errors on the abundances which are determined by the models may become large. In order to treat inhomogeneities in a one-dimensional atmosphere model, filling factors can be assumed. The density in a certain layer depends on the filling factor for this layer. The use of filling factors is not as exact as the calculation of inhomogeneities in three-dimensional model atmospheres in which the densities can be varied in certain points of the shell. Radiation transport in three-dimensions has been developed by Hauschildt & Baron (2006) for `PHOENIX`. In order to calculate a three-dimensional nova model atmosphere a much larger cluster of supercomputers is needed than it is available today. For this work supercomputers and clusters like Nathan and Seneca[1] from the Hamburg observatory, Seaborg from NERSC[2] and the HLRN[3] in Hannover and Berlin (Germany) have been used. Today, these clusters (especially Seaborg) belong to the largest and fastest in the world. However, for 3D calculations they have not enough memory and they are too slow.

The `PHOENIX`-code contains a mode for calculate a β-wind law (equation 4.1). This has been developed by Aufdenberg (2000) and model atmospheres with different β have been calculated for hot, luminous stars and for CNe to fit observations in the UV (Aufdenberg 2001). In future work the mode must be tested for nova model atmospheres in X-rays. The velocity law can affect the shape of the spectral lines in the synthetic spectra and better fits of the observations may be obtained by determining the best values for β and v_{out} from equation (4.1).

In addition, dielectronic recombination and the inverse process, autoionization, can be implemented in the `PHOENIX`-code with data from CHIANTI Version 5 (chapter 6). These processes may be important in the X-ray spectral range because they form satellite lines. CHIANTI5 was available for only a few weeks before this work was completed and there was no time to implement these data in the `PHOENIX`-code.

Atmosphere models have also been calculated for nova V1494 Aql and for the SSBS CAL 83 and CAL 87. Fits of such a good quality as compared to nova V4743 Sgr could not be made. For V1494 Aql, model atmospheres with more layers in the optically thin part have to be calculated to consider the outer thin nebular which forms the emission lines. In order to fit the observations of CAL 83 and CAL 87 static atmospheres, similar to hot giants, have to be calculated because the observations of SSBS cannot be fitted with nova model atmospheres. On the other hand CN and SSBS can have very exotic abundances and a larger model grid may be necessary.

In section 7.4 a model for the emission and evolution of X-rays in nova V4743 Sgr has been developed. In order to confirm this model more observations for V4743 Sgr are necessary but the nova emits no longer in X-rays. Maybe models for observations of other novae with CHANDRA may help to confirm this theory. Therefore, more observations of CNe and SSBS with CHANDRA are necessary which provide spectra of a good quality.

---

[1] `http://www.hs.uni-hamburg.de/phoenix` , Nathan has 50 1.8 GHz Opteron CPUs with 2 GB memory per CPU and Seneca has 52 2 GHz Apple G5 CPUs with 3 GB memory per CPU.

[2] National Energy Research Scientific Computing Center, `http://www.nersc.gov` , 6656 375 MHz Power 3 CPUs with 16-65 GB memory per CPU

[3] Höchstleistungsrechner Nord, `http://www.hlrn.de` , 1024 1.3 GHz Power 4 CPUs with 64-256 GB memory per CPU

Appendix A

Model spectra with solar abundances

Model spectra which have been calculated with solar abundances and different T_{eff} are shown here.

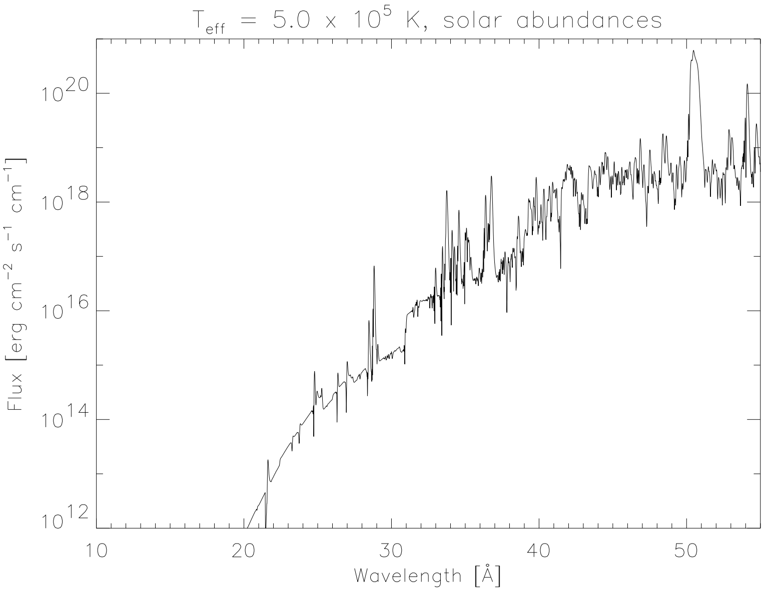

Figure A.1: Spectrum of a model atmosphere with $T_{\text{eff}} = 5.0 \times 10^5\,\text{K}$ in full NLTE, calculated with solar abundances.

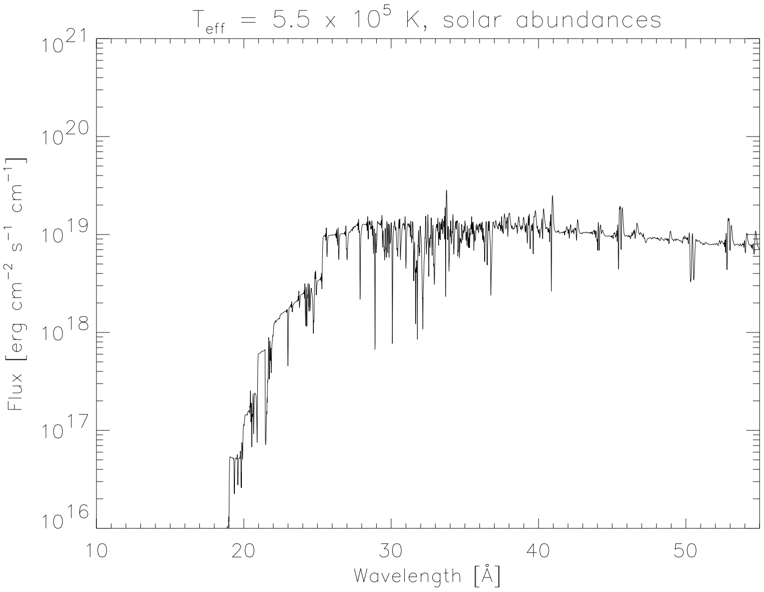

Figure A.2: Spectrum of a model atmosphere with $T_{\rm eff} = 5.5 \times 10^5\,$K in full NLTE, calculated with solar abundances.

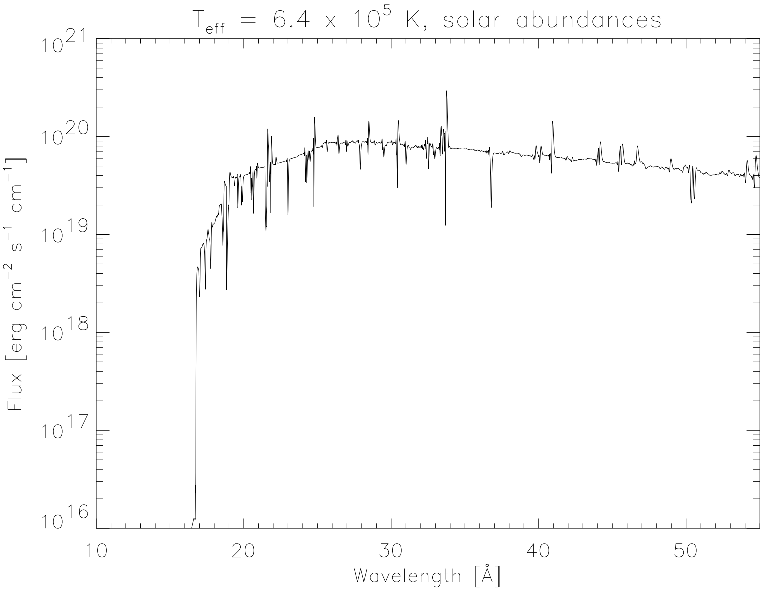

Figure A.3: Spectrum of a model atmosphere with $T_{\rm eff} = 6.4 \times 10^5\,$K in full NLTE, calculated with solar abundances.

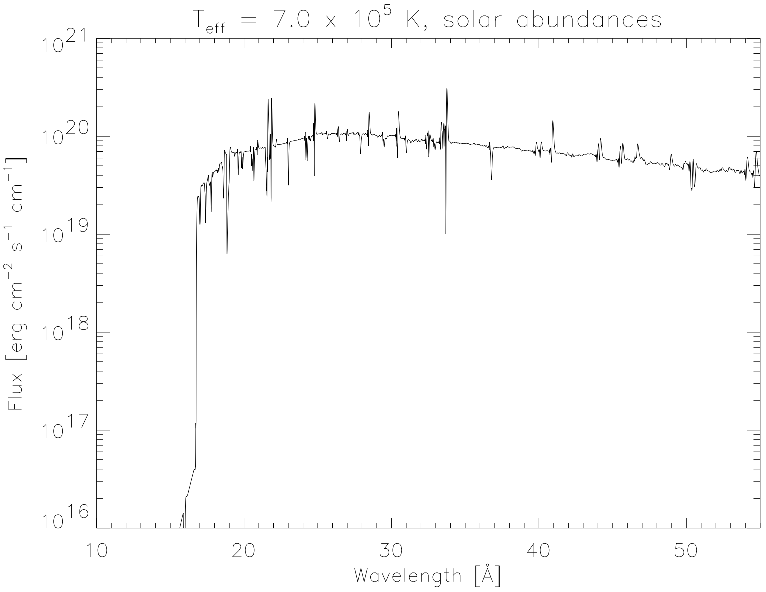

Figure A.4: Spectrum of a model atmosphere with $T_{\mathrm{eff}} = 7.0 \times 10^5\,\mathrm{K}$ in full NLTE, calculated with solar abundances.

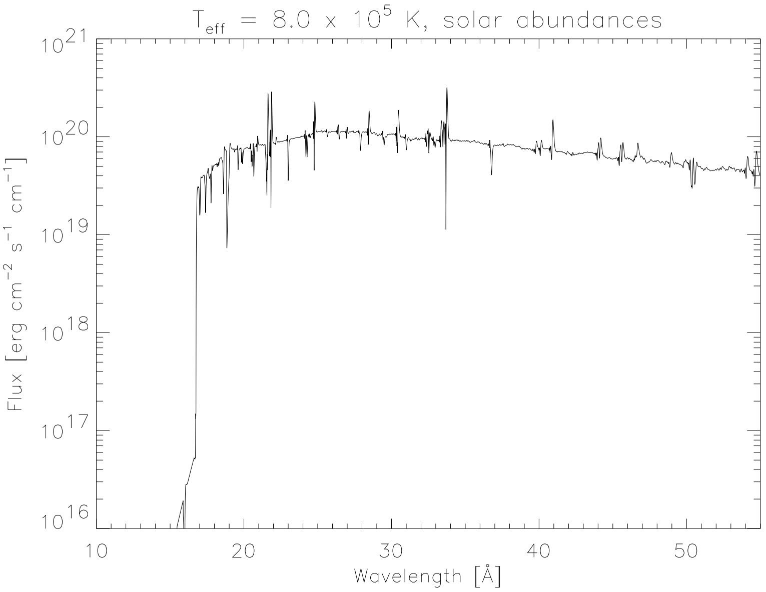

Figure A.5: Spectrum of a model atmosphere with $T_{\mathrm{eff}} = 8.0 \times 10^5\,\mathrm{K}$ in full NLTE, calculated with solar abundances.

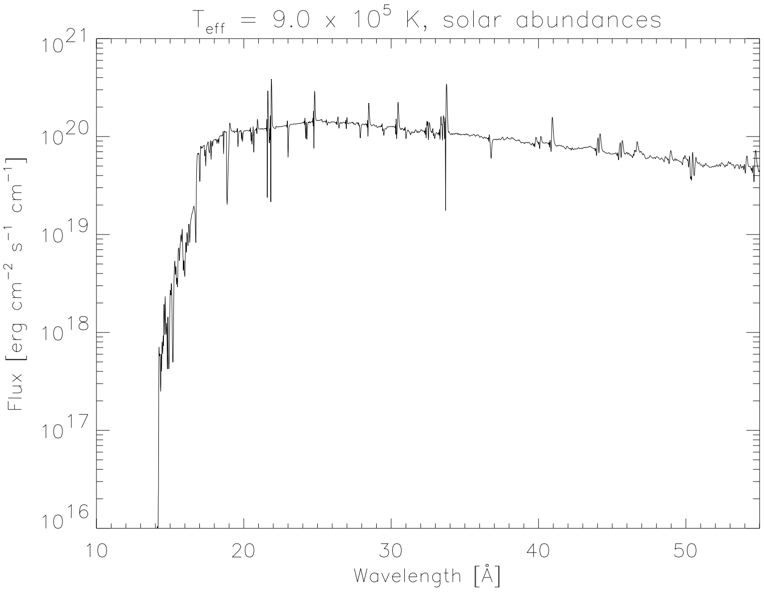

Figure A.6: Spectrum of a model atmosphere with $T_{\text{eff}} = 9.0 \times 10^5\,\text{K}$ in full NLTE, calculated with solar abundances.

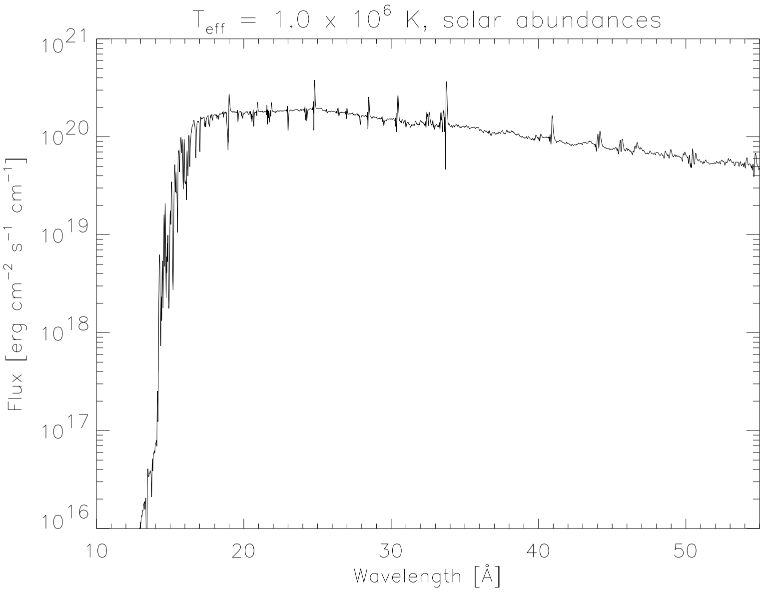

Figure A.7: Spectrum of a model atmosphere with $T_{\text{eff}} = 1.0 \times 10^6\,\text{K}$ in full NLTE, calculated with solar abundances.

Appendix B

Atmosphere structure

The temperature structure, the gas density and the partial pressures of helium, carbon, nitrogen, and oxygen of the the models which have been calculated with non-solar abundances and fitted to the observations of March and July 2003 of nova V4743 Sgr are presented here. Differences in the partial pressures between the best fitting models and a model which has been calculated with solar abundances and the same T_{eff} are compared.

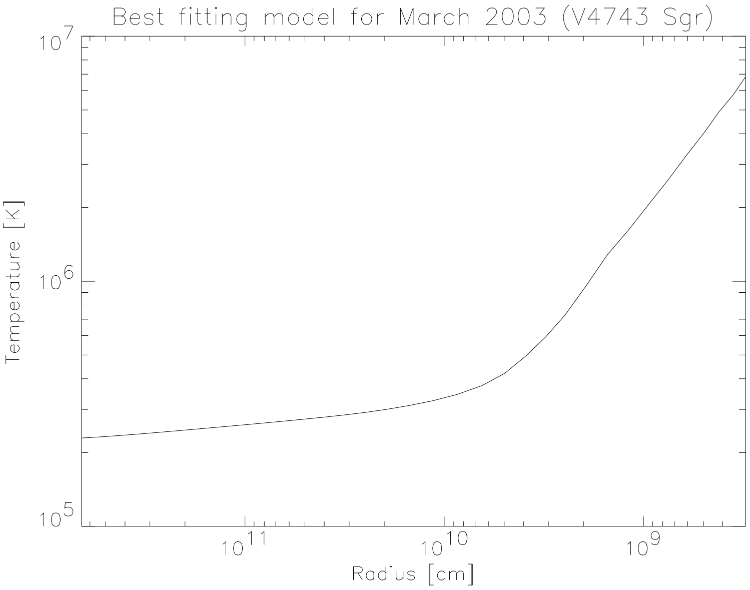

Figure B.1: Temperature structure of the best fitting model of the observation in March 2003 of V4743 Sgr (figure 7.56).

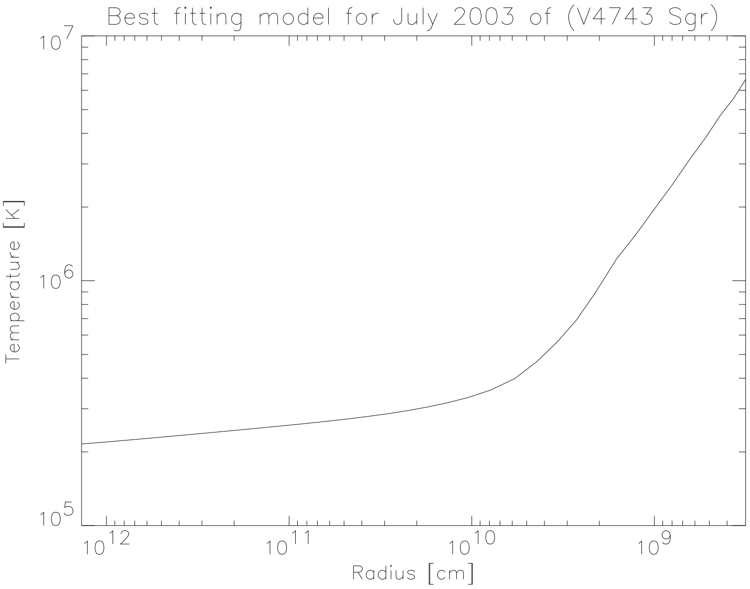

Figure B.2: Temperature structure of the best fitting model of the observation in July 2003 of V4743 Sgr (figure 7.57).

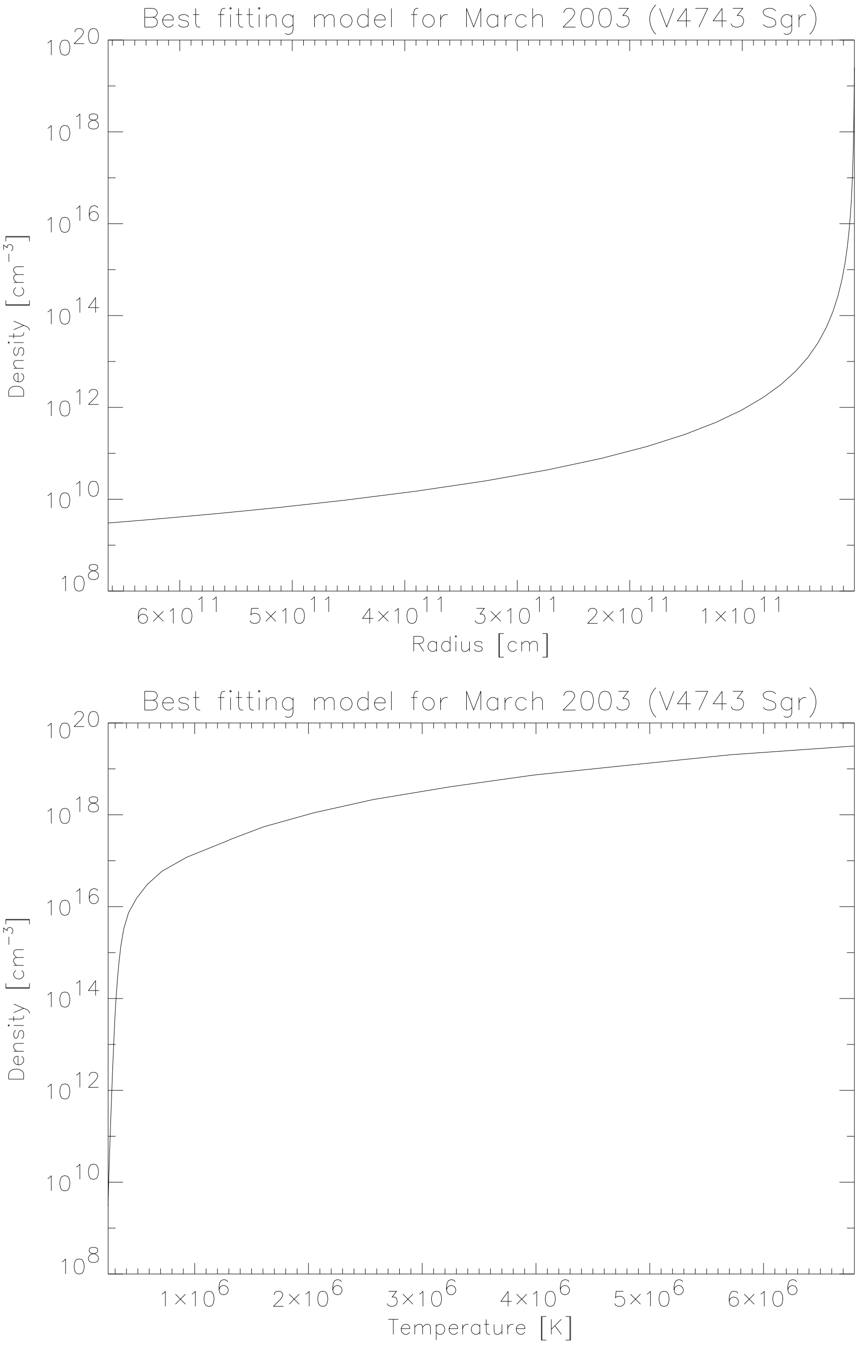

Figure B.3: Gas density of the best fitting model of the observation in March 2003 of V4743 Sgr (figure 7.56)

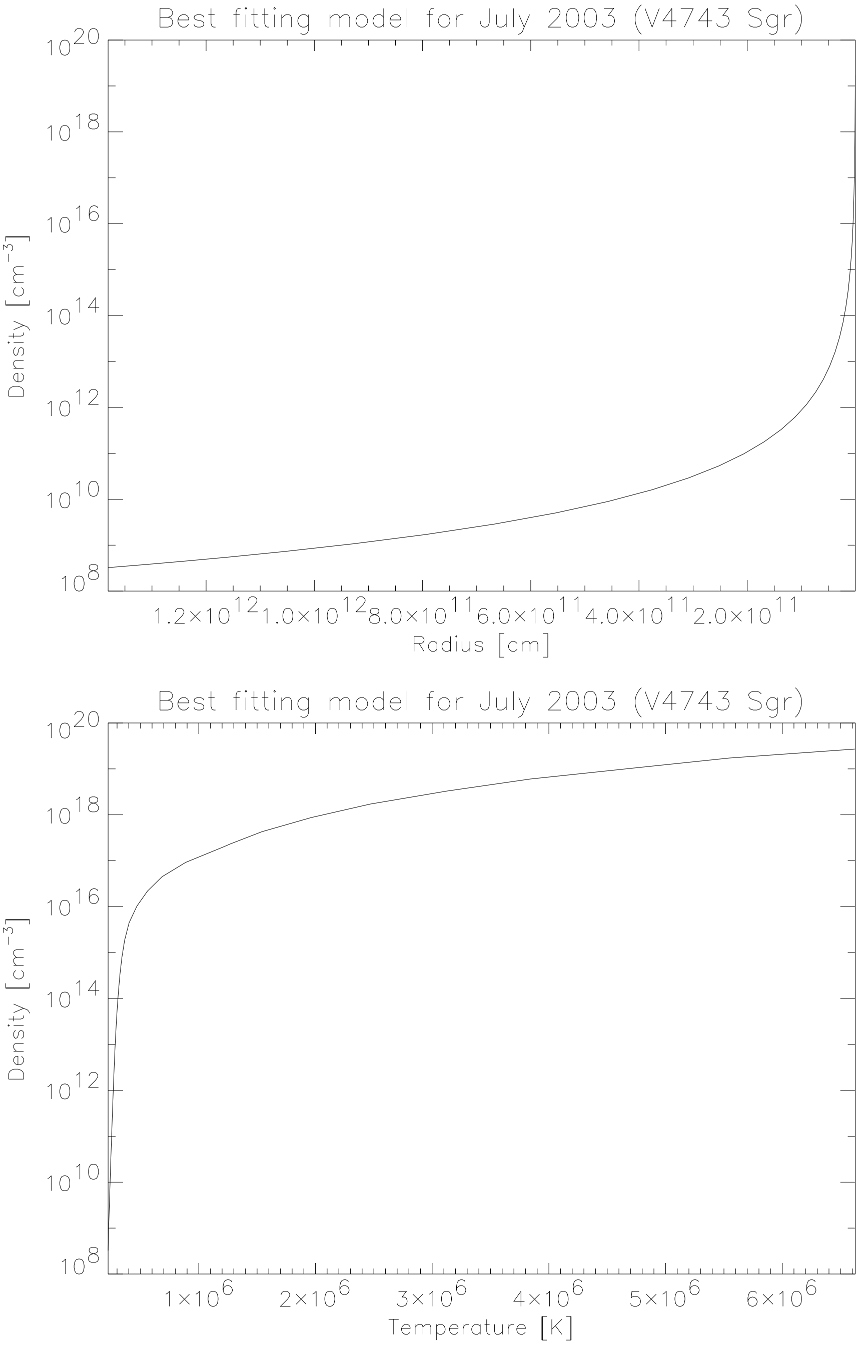

Figure B.4: Gas density of the best fitting model of the observation in July 2003 of V4743 Sgr (figure 7.57).

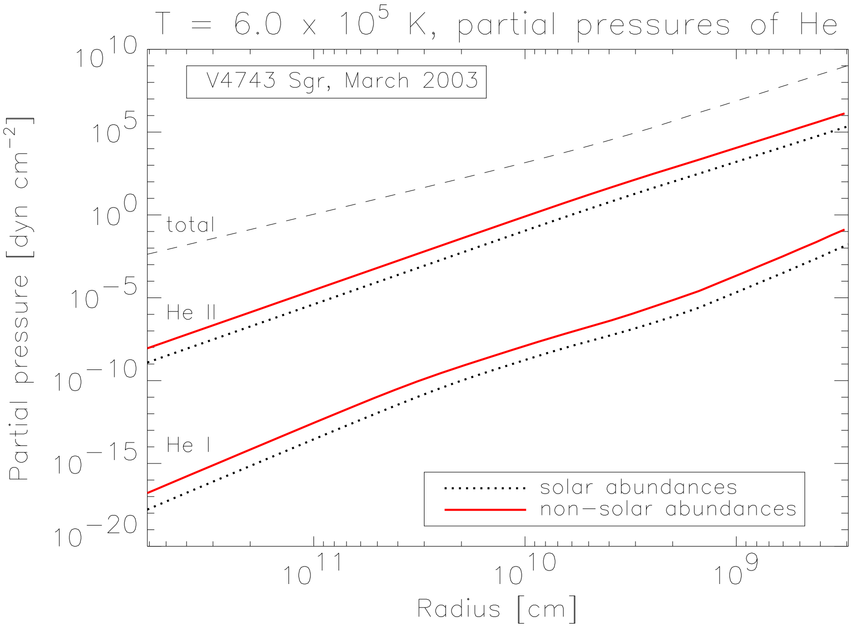

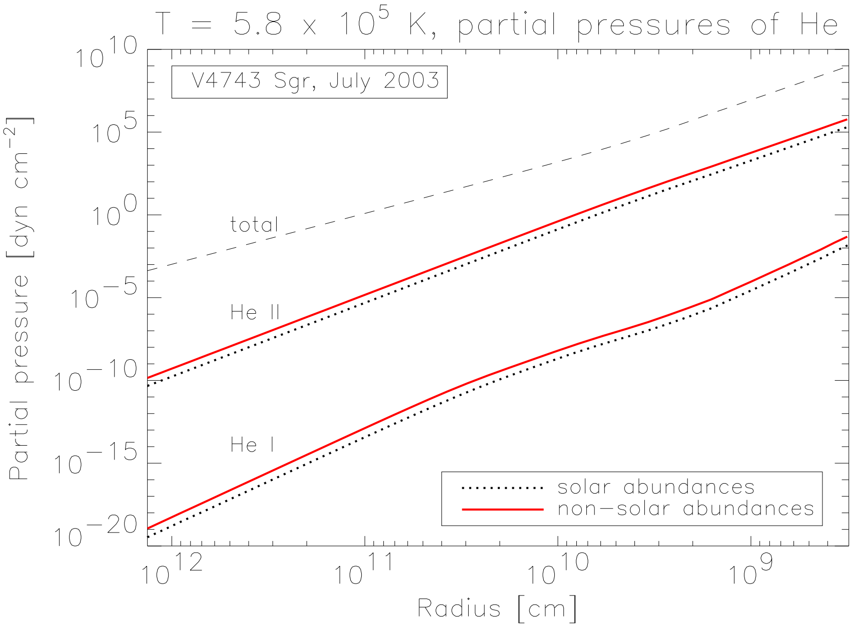

Figure B.5: Partial pressures of helium of the best fitting models of the observation in March and July 2003 of V4743 Sgr (solid lines) compared with partial pressures of a model which has been calculated with the same T_{eff} and with solar abundances (dotted lines). The total pressure is from the model with solar abundances (dashed line).

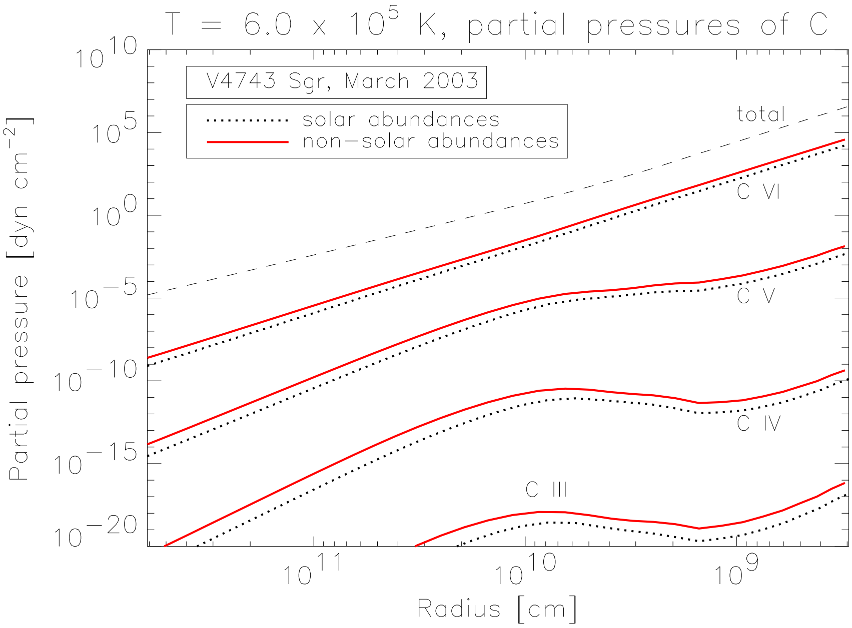

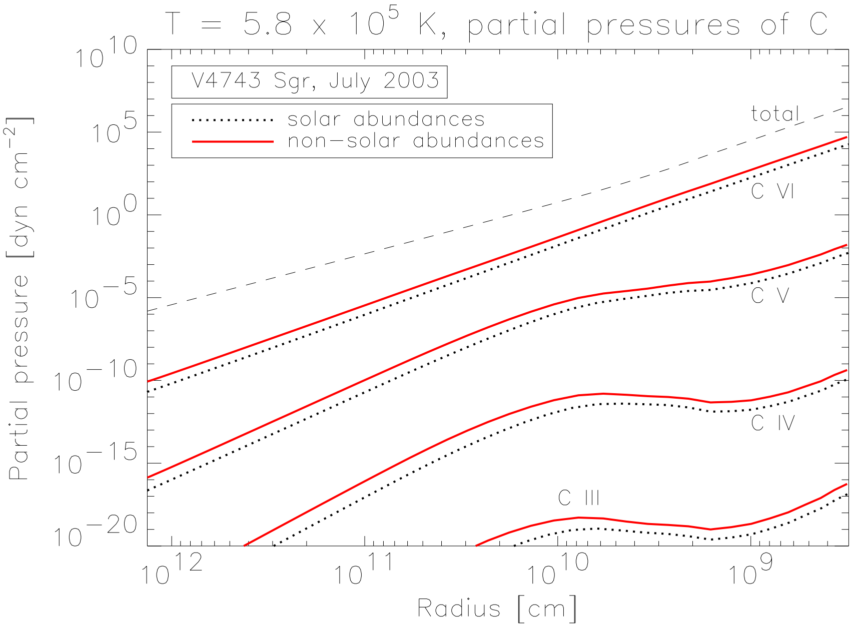

Figure B.6: Partial pressures of carbon of the best fitting models of the observation in March and July 2003 of V4743 Sgr (solid lines) compared with partial pressures of a model which has been calculated with the same $T_{\rm eff}$ and with solar abundances (dotted lines). The total pressure is from the model with solar abundances (dashed line).

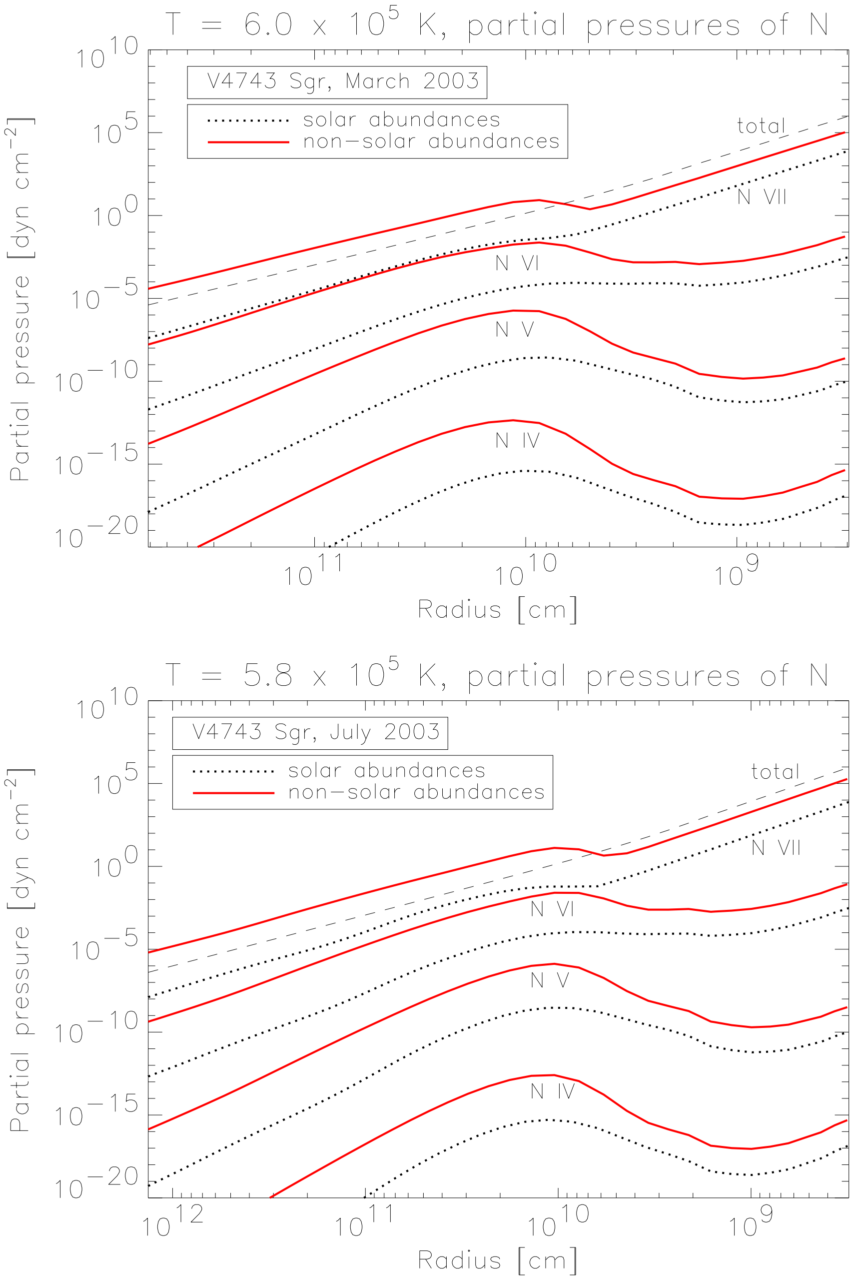

Figure B.7: Partial pressures of nitrogen of the best fitting models of the observation in March and July 2003 of V4743 Sgr (solid lines) compared with partial pressures of a model which has been calculated with the same $T_{\rm eff}$ and with solar abundances (dotted lines). The total pressure is from the model with solar abundances (dashed line).

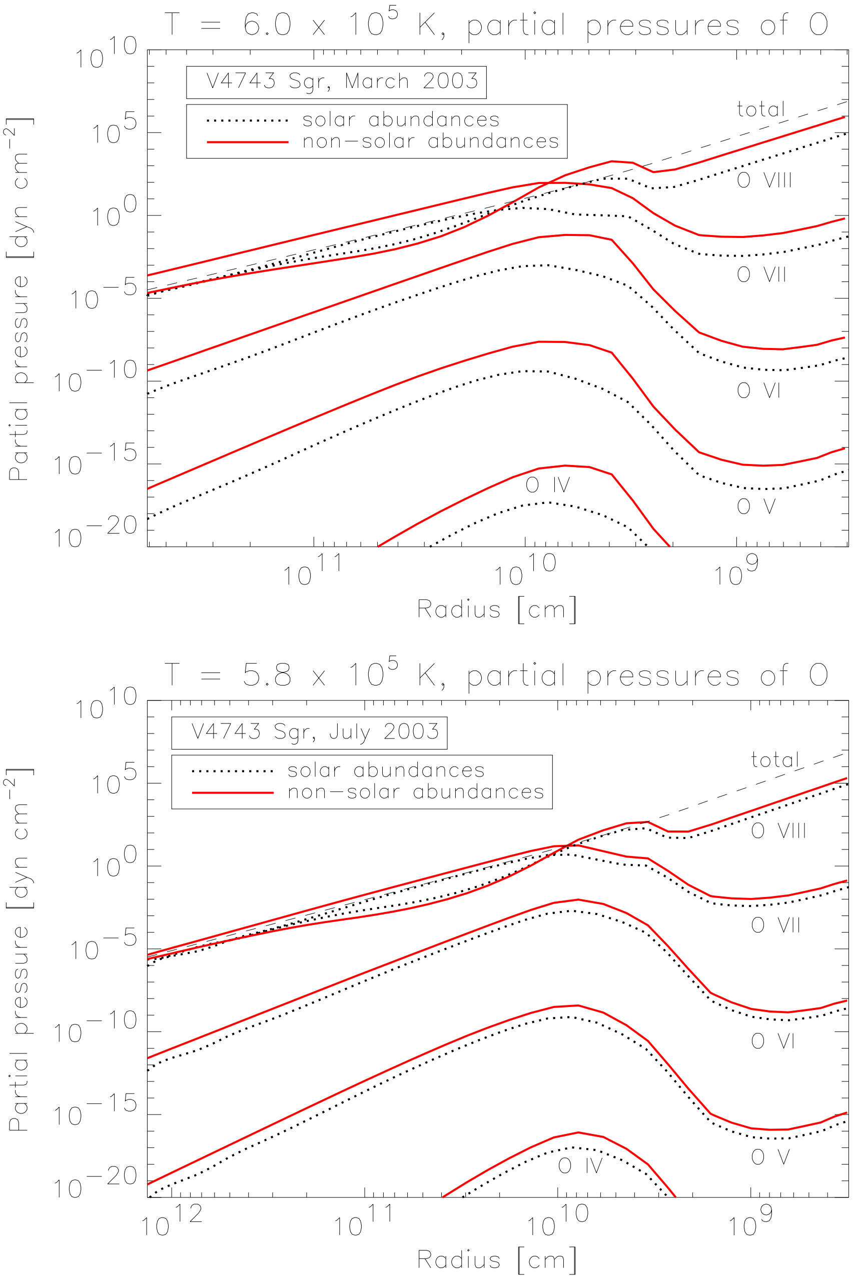

Figure B.8: Partial pressures of oxygen of the best fitting models of the observation in March and July 2003 of V4743 Sgr (solid lines) compared with partial pressures of a model which has been calculated with the same $T_{\rm eff}$ and with solar abundances (dotted lines). The total pressure is from the model with solar abundances (dashed line).

Bibliography

Alcock, C., Allsman, R. A., Alves, D., et al. 1997, MNRAS, 286, 483

Alexakis, A., Calder, A. C., Dursi, L. J., et al. 2003, AAS/High Energy Astrophysics Division, 7, 1808

Allard, F., Hauschildt, P. H., & Schweitzer, A. 2000, ApJ, 539, 366

Allen, C. W. 1954, MNRAS, 114, 387

Anders, E. & Grevesse, N. 1989, GeCoA, 53, 197

Andrea, J., Drechsel, H., & Starrfield, S. 1993, A&A, 291, 869

Anupama, G. C. 1995, in ASSL Vol. 205: Cataclysmic Variables, ed. A. Bianchini, M. della Valle, & M. Orio (Dordrecht: Kluwer), 49

Arp, H. C. 1956, AJ, 61, 15

Aschenbach, B., Braeuninger, H., Briel, U., et al. 1981, SSRv, 30, 569

Asplund, M., Grevesse, N., & Sauval, A. J. 2005, in ASP Conf. Ser. 336: Cosmic Abundances as Records of Stellar Evolution and Nucleosynthesis, ed. T. G. Barnes & F. N. Bash (San Francisco: Astronomical Society of the Pacific), 25

Aufdenberg, J. P. 2000, PhDT

Aufdenberg, J. P. 2001, in ASP Conf. Ser. 231: Tetons 4: Galactic Structure, Stars and the Interstellar Medium, ed. C. E. Woodward, M. D. Bicay, & J. M. Shull (San Francisco: Astronomical Society of the Pacific), 539

Balman, S. & Krautter, J. 2001, MNRAS, 326, 1441

Balman, S., Krautter, J., & Oegelman, H. 1998, ApJ, 499, 395

Barman, T. S., Hauschildt, P. H., & Allard, F. 2001, ApJ, 556, 885

Barman, T. S., Hauschildt, P. H., Short, C. I., & Baron, E. 2000, ApJ, 537, 946

Baron, E. & Hauschildt, P. H. 1998, ApJ, 495, 370

Baron, E. & Hauschildt, P. H. 2004, A&A, 427, 987

Bath, G. T. & Shaviv, G. 1976, MNRAS, 175, 305

Bautista, M. A. & Kallman, T. R. 2001, ApJS, 134, 139

Bode, M. F. & Evans, A. 1989, in Classical Novae, ed. M. F. Bode & A. Evans (Chichester: Wiley), 163

Boehm-Vitense, E. 1989, Introduction to stellar astrophysics. Volume 2 - Stellar atmospheres (Cambridge and New York: Cambridge University Press)

Bradt, H. V. D., Ohashi, T., & K. A.Pounds, K. A. 1992, ARA&A, 30, 391

Burgess, A. & Tully, J. A. 1992, A&A, 254, 436

Burwitz, V., Starrfield, S., Krautter, J., & Ness, J. U. 2002, in AIP Conf. Proc. 637: Classical Nova Explosions, ed. M. Hernanz & J. Jose (Melville, New York: American Institute of Physics), 377

Cassatella, A. & Gonzalez-Riestra, R. 1990, in Lecture Notes in Physics 369: Physics of Classical Novae, ed. A. Cassatella & R. Viotti (Berlin: Springer), 115

Chandrasekhar, S. 1967, An introduction to the study of stellar structure (New York: Dover)

Cohen, J. G. 1985, ApJ, 292, 90

Crampton, D., Cowley, A. P., Hutchings, J. B., et al. 1987, ApJ, 321, 745

della Valle, M. 2002, in AIP Conf. Proc. 637: Classical Nova Explosions, ed. M. Hernanz & J. Jose (Melville, New York: American Institute of Physics), 443

Dere, K. P., Landi, E., Mason, H. E., Fossi, B. C. M., & Young, P. R. 1997, A&AS, 125, 149

Dere, K. P., Landi, E., Young, P. R., & Zanna, G. D. 2001, ApJS, 134, 331

Dickey, J. M. & Lockman, F. J. 1990, ARA&A, 28, 215

Drake, G. W. F. 1986, PhRv, 34, 2871

Drake, G. W. F., Victor, G. A., & Dalgarno, A. 1969, PhRv, 180, 25

Drake, J. J., Wagner, R. M., Starrfield, S., et al. 2003, ApJ, 584, 448

Drake, S. A. & Ulrich, R. K. 1981, ApJ, 248, 380

Fujimoto, M. Y. 1982, ApJ, 257, 752

Gallagher, J. S. & Starrfield, S. 1978, ARA&A, 16, 171

Gaposchkin, C. H. P. 1964, The galactic novae (New York, Interscience Publishers: Amsterdam, North-Holland Pub. Co.)

Gehrz, R. D. 1988, ARA&A, 26, 377

Gehrz, R. D., Truran, J. W., Williams, R. E., & Starrfield, S. 1998, PASP, 110, 3

Giacconi, R., Branduardi, G., Briel, U., et al. 1979, ApJ, 230, 540

Goldman, S. P. & Drake, G. W. F. 1981, PhRvA, 24, 183

Greiner, J. 1995, in ASSL Vol. 205: Cataclysmic Variables, ed. A. Bianchini, M. della Valle, & M. Orio (Dordrecht: Kluwer), 443

Greiner, J. & Stefano, R. D. 2002, A&A, 387, 944

Grinin, V. P. 2001, Ap, 44, 402

Hachisu, I., Kato, M., & Nomoto, K. 1996, ApJ, 470, L97

Haseda, K., West, D., Yamaoka, H., & Masi, G. 2002, IAUC, 7975, 1

Hauschildt, P. H. 1992, JQSRT, 47, 433

Hauschildt, P. H. 1993, JQSRT, 50, 301

Hauschildt, P. H., Barman, T., Baron, E., & Allard, F. 2003, in ASP Conf. Ser. 288: Stellar Atmosphere Modeling, ed. I. Hubeny, D. Mihalas, & K. Werner (San Francisco: Astronomical Society of the Pacific), 227

Hauschildt, P. H. & Baron, E. 1995, JQSRT, 54, 987

Hauschildt, P. H. & Baron, E. 1999, JCAM, 109, 41

Hauschildt, P. H. & Baron, E. 2006, A&A, in press

Hauschildt, P. H., Baron, E., & Allard, F. 1997a, ApJ, 483, 390

Hauschildt, P. H., Baron, E., Starrfield, S., & Allard, F. 1996, ApJ, 462, 386

Hauschildt, P. H., Lowenthal, D., & Baron, E. 2001, ApJS, 134, 323

Hauschildt, P. H., Shore, S. N., Schwarz, G., et al. 1997b, ApJ, 490, 803

Hauschildt, P. H. & Starrfield, S. 1994, AJ, 108, 1008

Hauschildt, P. H. & Starrfield, S. 1995, ApJ, 447, 829

Hauschildt, P. H., Starrfield, S., Austin, S., et al. 1994, ApJ, 422, 831

Hauschildt, P. H., Wehrse, R., Starrfield, S., & Shaviv, G. 1992, ApJ, 393, 307

Hillebrandt, W. & Niemeyer, J. C. 2000, ARA&A, 38, 191

Itoh, N., Sakamoto, T., Kusano, S., Nozawa, S., & Kohyama, Y. 2000, ApJS, 128, 125

Jansen, F., Lumb, D., Altieri, B., et al. 2001, A&A, 365, L1

Kahabka, P. 1998, A&A, 331, 328

Kahabka, P., Haberl, F., Parmar, A. N., & Greiner, J. 1996, IAUC, 6467, 2

Kahabka, P. & van den Heuvel, E. P. J. 1997, ARA&A, 35, 69

Kato, M. & Hachisu, I. 1994, ApJ, 437, 802

Kato, T., Fujii, M., & Ayani, K. 2002, IAUC, 7975, 2

King, A. R. 1989, in Classical Novae, ed. M. F. Bode & A. Evans (Chichester: Wiley), 17

Kraft, R. P. 1964, ApJ, 139, 457

Krautter, J. 2002, in AIP Conf. Proc. 637: Classical Nova Explosions, ed. M. Hernanz & J. Jose (Melville, New York: American Institute of Physics), 345

Krautter, J., Oegelman, H., Starrfield, S., Wichmann, R., & Pfeffermann, E. 1996, ApJ, 456, 788

Krautter, J., Woodward, C. E., Schuster, M. T., et al. 2002, AJ, 124, 2888

Kurucz, R. L. & Bell, B. 1995, Atomic line list, Kurucz CD-ROM No. 23

Landi, E., Zanna, G. D., Young, P. R., et al. 2006, ApJS, in press

Lang, K. R. 1999, Astrophysical Formulae - Volume I: Radiation, Gas Processes and High Energy Astrophysics (New York: Springer)

Lanz, T., Telis, G. A., Audard, M., et al. 2005, ApJ, 619, 517

Leibundgut, B. 2001, ARA&A, 39, 67

Li, X. D. & van den Heuvel, E. P. J. 1997, A&A, 322, L9

Livio, M. 1995, in ASP Conf. Ser. 85: Magnetic Cataclysmic Variables, ed. D. A. H. Buckley & B. Warner (San Francisco: Astronomical Society of the Pacific), 80

Lloyd, H. M., O'Brien, T. J., Bode, M. F., et al. 1992, Nature, 356, 222

Lyke, J. E., Kelly, M. S., Gehrz, R. D., & Woodward, C. E. 2002, in Bulletin of the American Astronomical Society 34, ed. R. W. Milkey (Washington: American Astronomical Society), 1161

MacDonald, J. 1983, ApJ, 267, 732

McLaughlin, D. B. 1960, in Stars and Stellar Systems - Volume VI: Stellar Atmospheres, ed. J. L. Greenstein (Chicago, Illinois: The University of Chicago Press), 585

Mihalas, D. 1978, Stellar atmospheres (2nd edition) (San Francisco: W. H. Freeman and Co.)

Mihalas, D. & Weibel-Mihalas, B. 1984, Foundations of radiation hydrodynamics (New York: Oxford University Press)

Minkowski, R. 1948, ApJ, 107, 106

Mukai, K. & Ishida, M. 2001, ApJ, 551, 1024

Ness, J. U. 2004, private communication

Ness, J. U., Starrfield, S., Burwitz, V., et al. 2003, ApJ, 594, L127

Ness, J. U., Starrfield, S., Petz, A., Hauschildt, P. H., & Drake, J. J. 2006, MNRAS, in preparation

Nielbock, M. & Schmidtobreik, L. 2003, A&A, 400, L5

Nomoto, K., Nariai, K., & Sugimoto, D. 1979, PASJ, 31, 287

Oegelman, H., Beuermann, K., & Krautter, J. 1984, ApJ, 287, L31

Oegelman, H. & Orio, M. 1995, in ASSL Vol. 205: Cataclysmic Variables, ed. A. Bianchini, M. della Valle, & M. Orio (Dordrecht: Kluwer), 11

Oegelman, H., Orio, M., Krautter, J., & Starrfield, S. 1993, Nature, 361, 331

Olson, G. L. & Kunasz, P. B. 1987, JQSRT, 38, 325

Orio, M., Balman, S., della Valle, M., Gallagher, J., & Oegelman, H. 1996, ApJ, 466, 410

Orio, M., Hartmann, W., M. Still, M., & Greiner, J. 2003, ApJ, 594, 435

Orio, M., Parmar, A. N., Greiner, J., et al. 2002, MNRAS, 333, L11

Parmar, A. N., Kahabka, P., Hartmann, H. W., et al. 1997, A&A, 323, L33

Parpia, F. A. & Johnson, W. R. 1982, PhRvA, 26, 1142

Petz, A., Hauschildt, P. H., Ness, J. U., & Starrfield, S. 2005a, A&A, 431, 321

Petz, A., Hauschildt, P. H., Ness, J. U., & Starrfield, S. 2005b, in ASP Conf. Ser. 330: The Astrophysics of Cataclysmic Variables and Related Objects, ed. J. M. Hameury & J. P. Lasota (San Francisco: Astronomical Society of the Pacific), 299

Petz, A., Hauschildt, P. H., Ness, J. U., & Starrfield, S. 2005c, in AIP Conf. Proc. 774: X-ray Diagnostics of Astrophysical Plasmas: Theory, Experiment, and Observation, ed. R. K. Smith (Melville, New York: American Institute of Physics), 357

Pistinner, S., Shaviv, G., Hauschildt, P. H., & Starrfield, S. 1995, ApJ, 451, 724

Politano, M., Starrfield, S., Truran, J. W., Weiss, A., & Sparks, W. M. 1995, ApJ, 448, 807

Rauch, T. & Deetjen, J. L. 2003, in ASP Conf. Ser. 288: Stellar Atmosphere Modeling, ed. I. Hubeny, D. Mihalas, & K. Werner (San Francisco: Astronomical Society of the Pacific), 103

Rauch, T., Werner, K., & Orio, M. 2005, in AIP Conf. Proc. 774: X-ray Diagnostics of Astrophysical Plasmas: Theory, Experiment, and Observation, ed. R. K. Smith (Melville, New York: American Institute of Physics), 361

Sala, G. 2004, PhDT

Schwarz, G. J., Hauschildt, P. H., Starrfield, S., et al. 1997, MNRAS, 284, 669

Seaquist, E. R. 1989, in Classical Novae, ed. M. F. Bode & A. Evans (Chichester: Wiley), 143

Seaton, M. J. 1964, MNRAS, 127, 191

Segretain, L., Chabrier, G., & Mochkovitch, R. 1997, ApJ, 481, 355

Shanley, L., Oegelman, H., Gallagher, J. S., Orio, M., & Krautter, J. 1995, ApJ, 483, L95

Shara, M. M. 1989, PASP, 101, 5

Shore, S. N., Bond, H. E., Downes, R., et al. 1999a, IAUC, 7192, 1

Shore, S. N., Bond, H. E., Downes, R., et al. 1999b, IAUC, 7261, 1

Short, C. I., Hauschildt, P. H., & Baron, E. 1999, ApJ, 525, 375

Short, C. I., Hauschildt, P. H., Starrfield, S., & Baron, E. 2001, ApJ, 547, 1057

Starrfield, S. 1989, in Classical Novae, ed. M. F. Bode & A. Evans (Chichester: Wiley), 39

Starrfield, S. 1993, in The realm of interacting binary stars (Astrophysics and Space Science Library, Volume 177), ed. J. Sahade, G. E. McCluskey, & Y. Kondo (Dordrecht: Kluwer), 209

Starrfield, S. 2003, in From Twilight to Highlight: The Physics of Supernovae, ed. W. Hillebrandt & B. Leibundgut (Berlin: Springer), 128

Starrfield, S., Drake, J., Wagner, R. M., et al. 2001, in Bulletin of the American Astronomical Society 33, ed. R. W. Milkey (Washington: American Astronomical Society), 804

Starrfield, S., Timmes, F. X., Hix, W. R., et al. 2004, in Cosmic explosions in three dimensions: asymmetries in supernovae and gamma-ray bursts, ed. P. Hoflich, P. Kumar, & J. C. Wheeler (Cambridge, UK: Cambridge University Press), 87

Starrfield, S., Truran, J. W., Sparks, W. M., & Kutter, G. S. 1972, ApJ, 176, 169

Starrfield, S., Truran, J. W., Wiescher, M. C., & Sparks, W. M. 1996, in ASP Conf. Ser. 99: Cosmic Abundances, ed. S. S. Holt & G. Sonneborn (San Francisco: Astronomical Society of the Pacific), 242

Starrfield, S., Truran, J. W., Wiescher, M. C., & Sparks, W. M. 1998, MNRAS, 296, 502

Sutherland, R. S. 1998, MNRAS, 300, 321

Szkody, P. & Hoard, D. W. 1994, ApJ, 429, 857

Tanaka, T., Nishimura, H., Garcia, J., et al. 2002, IAUC, 7975, 3

Verner, D. A., Ferland, G. J., Korista, K. T., & Yakovlev, D. G. 1996, ApJ, 465, 487

Verner, D. A. & Yakovlev, D. G. 1994, yCat (VizieR Online Data Catalog), 410, 90125

Verner, D. A. & Yakovlev, D. G. 1995, A&AS, 109, 125

Walker, M. F. 1954, PASP, 66, 230

Warner, B. 1989, in Classical Novae, ed. M. F. Bode & A. Evans (Chichester: Wiley), 1

Warner, B. 1995, Cataclysmic Variable Stars (Cambridge and New York: Cambridge Astrophysics Series: Cambridge University Press)

Webbink, R. F. 1984, ApJ, 277, 355

Weisskopf, M. C., Brinkman, B., Canizares, C., et al. 2002, PASP, 114, 1

Werner, K., Deetjen, J. L., Dreizler, S., et al. 2003, in ASP Conf. Ser. 288: Stellar Atmosphere Modeling, ed. I. Hubeny, D. Mihalas, & K. Werner (San Francisco: Astronomical Society of the Pacific), 31

Young, P. R., Zanna, G. D., Landi, E., et al. 2003, ApJS, 144, 135

Acknowledgments

First I am delighted to thank Prof. Peter H. Hauschildt for providing me with the very interesting topic and helping me with the successful execution of this work. Furthermore, I thank him for the travel support to the astrophysical meetings in Strasbourg and Cambridge, as well as for the research periods in Phoenix and Tübingen.

I thank Prof. Sumner Starrfield for reading my work as second referee and for the helpful and interesting discussions about nova physics we had as well as for the support of my fruitful research period at the ASU in Phoenix.

Thanks to the `PHOENIX` group in Hamburg - Ines Brott, Matthias Dehn, Birgit Fuhrmeister, Dennis Jack, Christine Johnas, Sebastian Knop, Daan van Rossum, Michael Schülke, Andreas Schweitzer, Alexander C. Wawrzyn - for the very nice incorporation into the working group, for the comfortable working atmosphere, for the always fruitful discussions, and for all the sweets on my desk. Special thanks to Matthias Dehn for the good humor in our office, to Christine Johnas, Sebastian Knop, and Andreas Schweitzer for reading my thesis very thoroughly, and to Andreas Schweitzer for the support if the queuing system and the computers did not work according to my expectations.

I thank the whole CHANDRA X-ray team for providing me with observational data. Special thanks to Jan-Uwe Ness for the explanations and the support of the observations and the CHANDRA detectors. I thank the `PHOENIX` collaborators outside of Hamburg for the parts of the `PHOENIX`-code I have needed for my model calculations and for fruitful discussions. Furthermore I thank Klaus Werner and Thomas Rauch from Tübingen and Joachim Krautter from Heidelberg for the discussion of my results and Joachim Krautter for presenting my first fits at CHANDRA meetings.

Thanks to all researchers and the administrative personnel of the Hamburger Sternwarte who made my time there very agreeable, especially to the kitchen fraction of the “grosses Beamtenwohnhaus”. Thanks for all the parties and barbecues we had. In addition, I want to thank Birgit Fuhrmeister, Christian Schröder, and Uwe Wolter for the incorporation into the “Astronomie Werkstatt” carrying out courses for pupils.

A big part of this work was financially supported by the DFG (project number HA 3457/2–1) who shall receive my thanks. Some of the calculations presented in this work were performed at the Höchstleistungs Rechenzentrum Nord (HLRN) and at the National Energy Research Supercomputer Center (NERSC), supported by the U.S. DOE. I thank all these institutions for a generous allocation of computer time.

I thank my parents who made my studies and my thesis at the University of Hamburg possible. Very very special thanks to my lovely girlfriend Madlen Labahn who put up with me during hard working periods. Finally I thank all of my relatives and friends who helped me during my studies.